FACULTY OF ENGINEERING
AND ARCHITECTURE

Unravelling Fundamental and Application-Oriented Aspects of Plasma-Assisted Surface Activation of Polymeric Films and Nanofibers

Parinaz Saadat Esbah Tabaei

Doctoral dissertation submitted to obtain the academic degree of
Doctor of Engineering Physics

Supervisors
Prof. Nathalie De Geyter, PhD - Anton Nikiforov, PhD

Department of Applied Physics
Faculty of Engineering and Architecture, Ghent University

September 2021

GHENT
UNIVERSITY

FACULTY OF ENGINEERING
AND ARCHITECTURE

Unravelling Fundamental and Application-Oriented Aspects of Plasma-Assisted Surface Activation of Polymeric Films and Nanofibers

Parinaz Saadat Esbah Tabaei

Doctoral dissertation submitted to obtain the academic degree of
Doctor of Engineering Physics

Supervisors
Prof. Nathalie De Geyter, PhD - Anton Nikiforov, PhD

Department of Applied Physics
Faculty of Engineering and Architecture, Ghent University

September 2021

GHENT
UNIVERSITY

ISBN 978-94-6355-522-7
NUR 926, 971
Wettelijk depot: D/2021/10.500/70

Members of the Examination Board

Chair

Prof. Filip De Turck, PhD, Ghent University

Other members entitled to vote

Rouba Ghobeira, PhD, Ghent University
Prof. Christophe Leys, PhD, Ghent University
Prof. François Reniers, PhD, Université libre de Bruxelles
Prof. Andre Skirtach, PhD, Ghent University
Damien Thiry, PhD, Université de Mons

Supervisors

Prof. Nathalie De Geyter, PhD, Ghent University
Anton Nikiforov, PhD, Ghent University

Acknowledgements

My PhD was without a doubt one of the most remarkable experiences of my life. Now that I am on the tail-end of it, I can reflect on all that I have been through and many lessons that I have learnt: "PhD is a journey that one cannot finish without team work and support." Throughout my journey I have been extremely fortunate to have the support of many people in one way or another. And now I have an opportunity to express my gratitude and sincerest appreciation to them.

First, and most importantly, I would like to thank my promotor Prof. Nathalie De Geyter for giving me the opportunity to pursue this PhD project. I am so grateful for her instructive feedbacks that pushed me to sharpen my thinking and brought my work to a higher level. My sincere appreciation also goes to my co-promoter Dr. Anton Nikiforov for providing me insightful comments and encouragements during difficult times. I would like to thank you very much for your support and understanding.

Besides my promotors, I am also grateful to the head of our department Prof. Christophe Leys for giving me a chance to develop and improve my teaching skills in applied physics lab sessions. I would like to also express my gratitude to Prof. Rino Morent for giving me an opportunity to have many interesting international collaborations.

I would like to take a moment to thank all my committee members. Thank you for your time and valuable feedbacks. I feel proud and honored that you have agreed to be in my committee.

I wish to express my appreciation to Dr. Ghobeira for the unwavering guidance and scientific support. Rouba, I really appreciate your generosity, patience and friendly attitude. I gratefully acknowledge the efforts of Dr. Asadian not only for introducing the exciting world of tissue engineering to me, but also for welcoming me to her home with open arms when I started my PhD.

I would like to express my gratitude to Dr. Onyshchenko and Dr. Cools for generously teaching me their enormous XPS knowledge and experience. I really appreciate your efforts for training me to become XPS operator myself. I also wish to sincerely thank Prof. Pandiyaraj for so many international and prestigious collaborations.

A special thanks goes to the technical team of the department Tim Poelman, and Joris Peelman for maintaining and building the set-ups. Tim, Thank you for your availability, adapting the different experimental set-ups that I used, and kindly helping me when something was wrong with XPS.

I would also like to sincerely thank my colleagues in the Applied Physics department. Many thanks goes to Monica, Savita, Tim Egghe, Chuanlong, Laura, and Rim for the cherished time we spent together in the lab, and social settings. It was a very enjoyable experience to work with so many brilliant people, from different cultures and backgrounds.

Getting through my dissertation required more than academic support, and I have many, many people to thank for listening to me and, at times, having to tolerate me. I thank all my fantastic friends, specially my 3 musketeers: Parisa, Moazameh, and Behnaz. Thank you for always being there for me.

And my älskling Jesper, thanks for your love, understanding, unfailing support, and never-ending encouragement throughout my years of study and through the process of finalizing my thesis. Thank you azizam, you are amazing.

Finally, a few lines in Farsi to appreciate my family:

پدر، مادر، پریسا و پریدخت عزیزم

قطعا سخت ترین کاری که در زندگیم کردم دوری از شما ها بوده. این جایگاهی که الان دارم را مدیون شما هستم تا همیشه. امیدوارم توانسته باشم که باعث سرافرازی شما شوم.

Summary

Nowadays, synthetic polymers are constituting a vital component in diverse applied engineering fields that set up the pillars for most of the technological and biomedical advancements in the society. This is mainly due to their low processing costs, adaptability to ever-renewing manufacturing pathways, modulation ease of their mechanical performance and stability of their bulk properties. Nonetheless, their surface properties represent a limiting factor impeding their use in a big range of the intended applications. In order to solve this issue, intrinsically nonconformant surfaces are subjected to treatments post-processing in order to impart efficient chemical effects for a desirable functionality. Among the different surface modification approaches, non-thermal plasma surface activation has increasingly earned, in the last few decades, a high-flying position in several application fields. On the one hand, this supremacy of plasma activation over other surface treatments is attributed to its simplicity, versatility, time efficiency, non-invasive character restricted to a modification depth of a few nanometers and solvent-free aspect. On the other hand, numerous studies available in literature have recurrently proven the plasma ability to efficaciously enhance or optimize, amongst others, the surface wettability, bio- and cyto-compatibility, barrier properties, bonding characteristics and adhesiveness of polymers. Generally, plasma-induced effects result in cross-linking, etching and/or grafting of new functionalities on the treated polymeric surfaces. Nonetheless, the most targeted aim in the wide literature involving plasma surface activation is the insertion of chemically reactive functionalities onto non-reactive polymeric substrates. However, given the diversity of chemical reactions occurring between the surface and the multitude of active species present in plasma, a chaotic insertion of non-specific surface functional groups might befall. Therefore, achieving controlled surface chemistries is a challenging approach demanding excessive optimization of the working parameters. In fact, correlations between the used working parameters, the ensued plasma active species and the induced surface chemistry should be carefully drawn for a deeper fundamental understanding of the plasma-surface interactions. To do so, researchers have been employing a broad range of plasma diagnostic tools and surface analytical techniques such as optical emission spectroscopy (OES), laser-induced fluorescence, X-ray photoelectron spectroscopy (XPS) and Fourier-transform infrared spectroscopy. Amongst the different surface characterization techniques, XPS is the most widely used since

it accurately determines the surface chemical composition at a depth approximately equaling the region depth affected by the plasma activation (a few nanometers). Its general principle involves the detection and measurement of photoelectrons ejected from the surface of a material that has been initially irradiated with X-rays having a fixed energy. The extensive XPS results available in literature have revealed that oxygen-containing groups are always inevitably incorporated on surfaces exposed to plasma discharges generated in inert and reactive non-oxygen containing gases (He, Ar and N_2 discharges being the most popular ones). To date, two different scientific points of view exist on how this theoretically unexpected oxygen incorporation occurs. Some plasma scientists have reported that during exposure to plasmas sustained in an oxygen-free atmosphere, the active species would initially break some C-C and C-H bonds on the polymeric surface generating carbon radicals. Thereafter, upon exposure of the polymer to the ambient air post-plasma treatment, oxygen-containing functionalities would then be incorporated onto the polymer surface due to the reaction of the long-lived surface carbon radicals with reactive O_2 molecules present in the surrounding atmosphere. On the other hand, other researchers have claimed that oxygen functionalities are directly inserted on the polymer surface during plasma exposure due to small amounts of oxygen impurities lingering in the discharge atmosphere. In this case, post-plasma interactions are supposed to be of a reduced prominence. This continuous debate remains unresolved because of the fact that the big majority of XPS measurements on plasma-treated polymers were performed after exposing the treated samples to ambient air prior to XPS analysis, making it impossible to differentiate between in-plasma and post-plasma oxygen incorporation. Only very few studies have already dealt with the direct XPS characterization of plasma-modified polymer surfaces i.e. without air exposure between the performed plasma treatment and subsequent XPS analysis. This direct analysis was carried out either by making use of a transfer vessel or by connecting the plasma set-up directly to an XPS machine. Most of the studies involving *in situ* XPS analysis have reported that in-plasma oxidation processes stemming from highly reactive oxygen impurities inside plasma reactors largely contribute to the final surface oxygen content. Moreover, a careful comparison between different studies has shed the light on the crucial role that the reactor base pressure plays in determining the extent of in-plasma surface oxygen incorporation. The lower the reactor base pressure is, the less prominent the in-plasma oxygen-based functionalization becomes. Nonetheless, despite these interesting findings and the significant progress that has been made in unraveling plasma-surface interactions, 4 important fundamental aspects have not been yet examined and will constitute points of interest in this thesis. Firstly, literature has only focused so far on low pressure plasma treatments, totally neglecting the examination of plasma-surface interactions in case of high pressure plasmas. Secondly, a systematic study comparing between in-plasma and post-plasma surface chemical processes via the performance of both *in situ* and *ex situ* XPS analyses is also lacking. Post-plasma chemical surface interactions can be divided into short-term processes occurring immediately after the treatment and long-term processes responsible for the so-called "ageing effect" of plasma-activated surfaces. Thirdly, in the available studies focusing on *in situ* characterization of plasma-treated surfaces, OES diagnostics have been highly disregarded. Nonetheless, OES is known as a very practical and non-invasive diagnostic technique determining the nature of excited chemical species inside a discharge and helping to decorticate the insights into the implicated gas/plasma interactions. Therefore, correlating OES diagnostics with direct XPS investigations allows to shortlist the potential excited species that are specifically involved in the diverse surface chemical modifications. This can aid to fundamentally understand the relative importance of in-plasma and post-plasma reactions on polymeric surfaces. Finally, all reported *in situ* XPS analyses were focused on discerning surface chemistries induced by discharges sustained in pure gases such as N_2 and Ar. No study has investigated, to the best of our knowledge, in-plasma initiated oxidation processes by purposely admixing oxygen to different feed gases in order to elucidate its exclusive influence on the surface chemistry without the interference of post-plasma oxidation.

Recognizing the above discussion, the first fundamentally-oriented goal of the thesis is to distinctively sort out the relative implication of in-plasma and post-plasma surface interactions in sub-atmospheric pressure treatments operating in non-oxygen containing atmospheres (Chapter 6). To do so, ultrahigh molecular weight polyethylene (UHMWPE) films are subjected to a N_2 and Ar plasma activation using a dielectric barrier discharge (DBD) operating at a pressure of 5.0 kPa. For an accurate analysis, two challenges are practically surmounted: 1) oxygen contaminations inside the reactor are maximally eliminated by attaining a highly controlled gas environment via pre-pumping the plasma chamber to a base pressure of 10^{-7} kPa and 2) biased surface characterization caused by the exposure of plasma-treated samples to air is excluded by directly connecting the XPS machine to the DBD. A distinctive combination of OES diagnostics and *in situ* XPS is then used to characterize the in-plasma species/surface interactions. Post-plasma surface oxidation and ageing are unraveled by exposing plasma-treated samples to ambient air from 5 min to 21 days and performing comparative *ex situ* XPS measurements. Results reveal that Ar and N_2 discharges are predominantly composed of exited Ar and molecular N_2 and N_2^+ states respectively, with discernable low intensity OES emission lines attributed to OH radicals and excited N_2 molecules in the Ar discharge. *In situ* XPS analysis shows a remarkably high nitrogen incorporation (20.6 %) with only a negligible oxygen incorporation (1.1→ 2.8 %) on the polymer surface thus leading to a significantly enhanced N-selectivity when comparing to the current state-of-the-art. In fact, photons, electrons and nonreactive excited N_2 species present in the discharge are able to generate surface polymer radicals that in turn will react with the chemically active species such the exited N_2^+ ions thus grafting N-containing groups onto the surface. The used very low reactor base pressure of 10^{-7} kPa is actually behind the very low surface oxygen incorporation. More surface oxygen is however detected after Ar activation which is probably due to the high energy Ar metastables more efficiently breaking surface C-C and C-H bonds thus creating more surface radicals that can react with the highly reactive O_2 impurities. Moreover, Ar metastables can as well efficiently dissociate the H_2O molecules present in the feed gas thus producing OH radicals known to play a major role in the chemical processes leading to the incorporation of O-containing groups onto UHMWPE. Upon exposure to ambient air, particular post-plasma oxidation processes occur, producing more oxygen mainly in the form of O-C=O and N-C=O groups on N_2-activated surfaces and C-O groups on Ar-activated surfaces. Above a certain storage time, physical processes of surface polymeric chain reorientation prevail over chemical processes leading to the migration of some pre-induced oxygen and nitrogen-containing groups away from the surface.

The second fundamental goal of the thesis shifts towards the examination of in-plasma initiated oxidation processes occurring at UHMWPE surfaces when exposed to similar plasmas but with the feed gases (N_2 and Ar) admixed with different concentrations of O_2 (ranging from 6.2×10^{-3} % to 5 %) (Chapter 7). The OES results of the N_2/O_2 discharge show an additional emission of $NO\gamma$ peak when compared to the pure N_2 discharge. The OES results of the Ar/O_2 discharge reveal the disappearance of the excited N_2 emission lines that is compensated by the appearance of a small atomic O line. This atomic O was reported to be very powerful in initiating the surface functionalization by generating surface radicals. The *in situ* XPS analysis shows that when the N_2 discharge atmosphere contains less than 1 % of O_2, a steep increase in the surface O content is observed at the expenses of the N content. When the added O_2 in the feed gas exceeds 1 %, the nitrogen incorporation onto the surface becomes completely quenched. In this case, the surface radicals created by the non-reactive plasma species are probably rapidly reacting with the highly reactive O_2 molecules in a way overpowering the reactions with nitrogen species. The moment a small concentration of O_2 is added to the Ar gas flow, a sharp increase in the surface oxygen content is also detected. Thereafter, the evolution of the incorporated oxygen amount onto the surface runs in parallel with the amount of the extra O_2 added in the gas mixture. In fact when more O_2 is present in the discharge, more surface radicals are excepted to react with O_2 molecules instead of interacting with each other which eventually leads to more O-containing functionalities inserted on the surface with a lower degree of cross-linking.

After deeply uncovering the fundamentals of in-plasma and post-plasma chemical processes occurring at polymeric surfaces, the second part of thesis shifts towards an actual palpable application of plasma activation in one of the hottest topics within the scientific community: tissue engineering (TE). TE approaches aim at overcoming the limitations of standard transplantation methods via the biofabrication of substitute structures so-called scaffolds for the regeneration of damaged tissues. One of the most influential requirement ensuring effective cell-scaffold interactions is the mimicry of the nanofibrous extracellular matrix (ECM) governing a widespread range of crucial cellular performances such as adhesion, proliferation and maturation. As such, in order to biofabricate fibrous scaffolds, electrospinning has been widely used given its versatility, simplicity, cost effectiveness and ability to produce fibers with diameters going down to the nanometer scale. Nonetheless, appropriate topographical cues mimicking the ECM architecture are not enough to trigger the looked-for outcome. In fact, cells are not solely affected by the material topography but also by the surface biochemistry that has a complementary role in initiating proper cell behaviors. As such, a functionalization of the nanofibrous scaffolds should be carried out to promote the binding proteins onto the surface. Such proteins are recognized by cell receptors thus mediating the cell affinity towards the fibers. To do so, plasma activation can be performed and carefully optimized to obtain a desirable surface chemistry without altering the structure of the fibers. The biofabrication and plasma treatment of advanced bone TE scaffolds will constitute a final application-oriented goal of this thesis (Chapter 8). Bone TE is particularly chosen because of the interesting double role of plasma activation in enhancing bone regeneration. Firstly, the plasma-induced incorporation of polar functional groups onto the surface can promote “bone” cell affinity towards the treated fibers. Secondly, such functionalities can induce the nucleation and growth of bone-like apatitic calcium phosphate (CaP) nanocrystals on the fibers (biomineralization) which are quite essential for successful osteointegration, osseoinduction and osteoconduction. Moreover, the need of artificial bone grafts sufficiently enhancing bone regeneration is increasing because of the high alerting incidence of bone defects caused by bone fractures and osteo-degenerative diseases. Given the complex calcified nature of the fibrous bone tissue, an integrative approach merging specific topographical and biochemical cues is adopted in the last experimental chapter for the design of a novel bone tissue-engineered scaffold. To do so, natural coral having a bone-like Ca-enriched structure is added to electrospun chitosan (CS)/polyethylene oxide (PEO). Coral-free and coral-containing fibers are then subjected to plasma surface modifications using a DBD operating in Ar, air or N_2 at medium pressure (50 mbar) to further enhance the fibers osteo-bioactivity. *Ex situ* XPS results reveal that plasma treatments incorporate a variety of oxygen- and nitrogen-containing functionalities onto the fibers surface thus significantly enhancing their wettability. No morphological alterations of the fibers are visualized post-plasma treatments. The improved plasma-induced surface chemistry strikingly enhances the adhesion and proliferation of MC3T3 osteoblasts. Moreover, the interplay between plasma treatment and coral is shown to further boost the initial cell adhesion. The *in vivo* capacity of the fibers to trigger CaP growth onto their surface was predicted via the biomimetic immersion in simulated body fluid (SBF). Oxygen-containing functionalities mainly COOH groups are shown to constitute the main CaP nucleation sites. As such, globular nano-dimensional CaP crystals are deposited on air and N_2 plasma-treated CS/PEO NFs while thicker layers of flake-like CaP nanocrystals are fully and individually covering each plasma-treated Coral/CS/PEO fiber without blocking the pores of the fibrous mesh architecture. Fourier-transform infrared spectroscopy (FTIR) results indicate that the deposited CaP phase is the type B carbonate apatite occurring in normal bone calcification.

Overall, this thesis unravels novel fundamental and application-oriented aspects of plasma surface activation of polymers. Basic understandings of in-plasma and post-plasma processes occurring on the surface of UHMWPE subjected to Ar and N_2 plasma activation are reaped. The light is shed on the high reactivity of O_2 in N_2 and Ar plasmas via the observed extreme changes occurring in the surface elemental composition upon the deliberate addition of O_2 to the feed gas. As such, a delicate tuning of the plasma working parameters should run in parallel with accurate surface characterization to reach the optimal surface chemistry sought after in a particular end-application. The tailored plasma activation used in the specific bone TE application adopted in this thesis has actually led to the positive outcomes. The exclusive multifaceted scaffold made up of plasma-treated Coral/CS/PEO nanofibers is as such believed to effectively repair bone defects and revolutionize the field of bone TE. A future translation to *in vivo* studies is planned thus paving the way towards the clinical use of plasma-activated scaffolds in bone and other TE applications.

Samenvatting

Tegenwoordig vormen synthetische polymeren een essentieel onderdeel in diverse toegepaste ingenieurs gerelateerde gebieden. Het zijn de pijlers voor de grootste technologische en biomedische voortgang in onze samenleving. Dit is voornamelijk te danken aan hun lage verwerkingskost, hun groot aanpassingsvermogen aan de steeds vernieuwde productie routes, het gemak om hun mechanische prestaties te moduleren, en de stabiliteit van hun bulkeigenschappen. Desondanks, vormen hun oppervlakte eigenschappen een beperkende factor die hun gebruik ervan in een groot aantal van de beoogde toepassingen belemmert. Om dit probleem op te lossen worden de intrinsiek niet-conforme oppervlaktes onderworpen aan nabewerkingsbehandelingen om efficiënte chemische effecten te verkrijgen voor een gewenste functionaliteit.

Binnen de verschillende methodes voor oppervlakte modificatie heeft niet-thermische plasma oppervlakte activatie de afgelopen decennia aan terrein gewonnen in verschillende toepassingsgebieden. Enerzijds wordt deze overmacht van plasma activatie ten opzichte van de andere oppervlaktebehandelingen toegeschreven aan zijn eenvoud, veelzijdigheid, snelheid, het niet-invasief karakter beperkt tot een modificatie diepte van enkele nanometer en het oplosmiddelvrij aspect. Aan de andere kant hebben talrijke studies reeds herhaaldelijk het vermogen van plasma bewezen om, onder andere, de bevochtiging van het oppervlak, de bio en cytocompatibiliteit, de barrière eigenschappen, de bindingseigenschappen en de hechting van polymeren doeltreffende te verbeteren of te optimaliseren. In het algemeen resulteren plasma geïnduceerde effecten in verknoping, etsen en/of enten van nieuwe functionaliteiten op de behandelde oppervlakten van polymeren. Het belangrijkste doel in de brede literatuur met betrekking tot plasma oppervlakte activering is het inbrengen van chemisch reactieve functionaliteiten op niet reactieve polymeer substraten. Gezien de grote diversiteit aan chemische reacties die plaatsvinden tussen het oppervlak en de veelheid aan actieve species die aanwezig zijn in plasma, kan er echter een chaotische invoeging van niet specifieke functionele oppervlakte groepen plaatsvinden. Het bereiken van gecontroleerde oppervlaktechemie is een uitdagende taak die een grondige optimalisatie van de werkparameters vereist. Meer bepaald dienen er zorgvuldig correlaties gelegd te worden tussen de gebruikte werkparameters, de resulterende plasma actieve species en de geïnduceerde oppervlakte chemie om zo een beter begrip te krijgen van de plasma-oppervlakte interacties. Om dit te

doen, hebben onderzoekers een breed scala aan plasmadiagnostische hulpmiddelen en oppervlakte analysetechnieken gebruikt zoals optische emissiespectroscopie (OES), laser geïnduceerde fluorescentie, X-straal foto-elektron spectroscopie (XPS) en Fourier getransformeerde infraroodspectroscopie (FTIR). Binnen de verschillende oppervlakte karakteriseringstechnieken wordt XPS het meest aangewend, aangezien het de chemische samenstelling van het oppervlak nauwkeurig bepaald op een diepte die ongeveer gelijk is aan de diepte van het gebied dat wordt beïnvloed door plasma activering (enkele nanometers). Het algemene principe van XPS omvat de detectie en het opmeten van foto-elektronen die worden uitgestoten vanaf het oppervlak van een materiaal dat voordien was bestraald met X-stralen van een welbepaalde energie. De uitgebreide XPS resultaten die in de literatuur beschikbaar zijn, hebben aangetoond dat zuurstof bevattende groepen altijd onvermijdelijk worden ingebouwd op oppervlakken die worden blootgesteld aan plasma-ontladingen die worden gegenereerd in inerte en reactieve niet-zuurstof bevattende gassen (He-, Ar- en N_2 ontladingen zijn de meest populaire). Tot op heden bestaan er twee verschillende wetenschappelijke standpunten over hoe deze theoretische onverwachte zuurstofopname plaatsvindt. Sommige plasmawetenschappers zijn van mening dat tijdens de blootstelling aan plasma in een zuurstofvrije atmosfeer, de actieve species aanvankelijk enkele C-C en C-H verbindingen op het polymeer oppervlak zouden breken en koolstofradicalen zouden genereren. Hierna zouden, bij blootstelling van het polymeer aan de omgevingslucht, zuurstof bevattende functionaliteiten op het polymeeroppervlak worden opgenomen als gevolg van de reactie van de langlevende koolstofradicalen op het oppervlak met reactieve O_2 moleculen die aanwezig zijn in de omringende atmosfeer. Aan de andere kant beweren andere onderzoekers dat zuurstof functionaliteiten direct op het polymeeroppervlak worden ingebracht tijdens de blootstelling aan plasma vanwege kleine hoeveelheden zuurstof onzuiverheden die in de ontladingsatmosfeer blijven hangen. In dit geval wordt verondersteld dat post-plasma interacties minder belangrijk zijn. Dit voortdurende debat blijft echter onopgelost vanwege het feit dat de grote meerderheid van XPS metingen op de met plasma behandelde polymeren werd uitgevoerd na blootstelling van de behandelde monsters aan omgevingslucht voorafgaand aan de XPS analyse. Hierdoor is het onmogelijk om een onderscheid te maken tussen in-plasma en post-plasma zuurstof incorporatie. Slechts een klein aantal studies gebruiken directe XPS karakterisering van plasma gemodificeerde polymeer oppervlakken, d.w.z. zonder blootstelling aan de lucht tussen de uitgevoerde plasmabehandeling en de daaropvolgende XPS-analyse. Deze directe analyse werd uitgevoerd ofwel door gebruik te maken van een transfervat ofwel door de plasma opstelling rechtstreeks aan te sluiten op een XPS instrument. Uit deze onderzoeken met in situ XPS analyse kwam aan het licht dat in-plasma oxidatieprocessen, die het gevolg zijn van zeer reactieve zuurstof onzuiverheden in de plasmareactoren, grotendeels bijdragen aan het uiteindelijke zuurstofgehalte aan het oppervlak. Bovendien heeft een zorgvuldige vergelijking tussen verschillende onderzoeken licht geworpen op de cruciale rol die de reactorbasisdruk speelt bij het bepalen van de in-plasma oppervlaktezuurstof opname. Hoe lager de reactorbasisdruk is, hoe minder prominent de in-plasma zuurstofgebaseerde functionalisering wordt. Ondanks deze interessante bevindingen en de aanzienlijke vooruitgang in het ontrafelen van plasma-oppervlakte interacties, zijn 4 belangrijke fundamentele aspecten nog niet onderzocht geweest. Deze zullen de aandachtspunten vormen in dit proefschrift. In eerste instantie heeft de literatuur zich tot nu toe alleen gericht op lage druk plasma behandelingen, waarbij het onderzoek van plasma-oppervlakte interacties in het geval van hoge druk plasma's volledig werd verwaarloosd. Ten tweede ontbreekt er op dit moment ook een systematische studie waarin in-plasma en post-plasma oppervlakte chemische processen worden vergeleken door zowel in situ als ex situ XPS analyses uit te voeren. Post-plasma chemische oppervlakte interacties kunnen worden onderverdeeld in korte termijn processen die onmiddellijk na de behandeling plaatsvinden en lange termijn processen die verantwoordelijk zijn voor het zogenaamde "verouderingseffect" van plasma geactiveerde oppervlakken. Ten derde, in de beschikbare studies die zich richten op in situ karakterisering van de met plasma behandelde oppervlakken, is OES diagnostiek in de meeste studies buiten beschouwing gelaten. Desalniettemin staat OES bekend als een zeer praktische en niet invasieve diagnostische techniek die de aard van de geëxciteerde chemische species in een ontlading bepaalt en helpt om inzichten in de betrokken gas/plasma interacties te krijgen. Daarom maakt het correleren van OES-diagnostiek met direct XPS onderzoek het mogelijk om de potentiele geëxciteerde species op te lijsten die specifiek betrokken zijn bij de diverse chemische oppervlakte modificaties. Dit kan helpen om fundamentele inzichten te verwerven in het relatieve belang van in-plasma en post-plasma reacties op polymeer oppervlakken. Tot slot zijn alle gerapporteerde in situ XPS analyses gericht op het onderscheiden van oppervlakte chemie die wordt veroorzaakt door ontladingen in zuivere gassen zoals N_2 en Ar. Voor zover wij weten, is er nog geen enkele in situ plasma studie geweest die het geïnitieerde oxidatieproces onderzocht door opzettelijk zuurstof aan verschillende gassen toe te voegen om de invloed ervan op de oppervlakte chemie op te helderen zonder de interferentie van post-plasma oxidatie.

Het eerste fundamenteel georiënteerde doel van dit proefschrift is het bepalen van de relatieve implicatie van in-plasma en post-plasma oppervlakte interacties in sub- atmosferische drukbehandelingen in niet-zuurstof bevattende atmosferen (Hoofdstuk 6). Om dit te doen, worden films van polyethyleen met een ultrahoog moleculair gewicht (UHMWPE) onderworpen aan een N_2 en Ar-plasma activering met behulp van een diëlektrische barrière ontlading (DBD) die werkt bij een druk van 5,0 kPa. Voor een nauwkeurige analyse dienen 2 praktische uitdagingen overwonnen te worden: 1) zuurstofverontreinigingen in de reactor worden maximaal geëlimineerd door een zeer gecontroleerde gasomgeving te creëren door de plasmakamer voor te pompen tot een basisdruk van 10^{-7} kPa en 2) vooringenomen oppervlakte karakterisering veroorzaakt door blootstelling van de met plasma behandelde stalen aan lucht wordt uitgesloten door het XPS instrument rechtstreeks op de DBD reactor aan te sluiten. Een combinatie van OES diagnostiek en in situ XPS metingen wordt vervolgens gebruikt voor de karakterisatie van de in-plasma species/oppervlakte interacties. Post-plasma oppervlakte oxidatie en veroudering worden onderzocht door de met plasma behandelde monsters gedurende 5 minuten tot 21 dagen bloot te stellen aan omgevingslucht en vergelijkende ex situ XPS metingen uit te voeren. Uit de resultaten bleek dat Ar en N_2 ontladingen voornamelijk bestaan uit respectievelijk geëxciteerde Ar en moleculaire N_2 en N_2^+ toestanden. De waarneembare OES emissielijnen met lage intensiteit worden toegeschreven aan OH-radicalen en geëxciteerde N_2 moleculen in de Ar ontlading. In situ XPS analyse toont een opmerkelijk hoge stikstofopname (20,5%) en slechts een verwaarloosbare zuurstofopname (1.1→ 2.8 %) op het polymeeroppervlak, wat leidt tot een aanzienlijk verhoogde N selectiviteit in vergelijking met de huidige data beschikbaar in de literatuur. Het zijn in feite de fotonen, elektronen en niet-reactieve geëxciteerde N_2 species die aanwezig zijn in de ontlading die in staat zijn om oppervlakte polymeerradicalen te genereren. Deze kunnen dan op hun beurt reageren met de chemisch actieve species, zoals de geëxciteerde N_2^+ ionen die uiteindelijk de N-bevattende groepen op het oppervlak introduceren. De zeer lage basisdruk van de reactor (10^{-7} kPa) is wellicht de reden voor de zeer lage zuurstof opname aan het oppervlak. Er wordt meer oppervlakte zuurstof gedetecteerd na Ar activering, wat waarschijnlijk te wijten is aan de hoogenergetische Ar metastabielen die de C-C en C-H bindingen op het oppervlak efficiënter breken waardoor er meer oppervlakte radicalen ontstaan die kunnen reageren met de zeer reactieve O_2 onzuiverheden. Bovendien kunnen de Ar-metastabielen de H_2O moleculen die aanwezig zijn in het gas ook efficiënt dissociëren waardoor er OH-radicalen worden geproduceerd waarvan bekend is dat ze een belangrijke rol spelen in de chemische processen die leiden tot de opname van O-bevattende groepen op UHMWPE. Bij blootstelling aan omgevingslucht vinden bepaalde post-plasma oxidatie processen plaats waarbij meer zuurstof wordt geproduceerd, voornamelijk in de vorm van O-C=O- en N-C=O- groepen op N_2 geactiveerde oppervlakken en C-O- groepen op Ar-geactiveerde oppervlakken. Boven een bepaalde opslagtijd prevaleren fysieke processen van heroriëntatie van de polymeerketen aan het oppervlak boven de chemische processen die leiden tot de migratie van sommige vooraf geïnduceerde zuurstof en stikstof bevattende groepen aan het oppervlak.

In het 2^de^ fundamentele doel van dit proefschrift verschuift het onderzoek naar de in-plasma geïnitieerde oxidatie processen die optreden op UHMWPE oppervlakken bij blootstelling aan vergelijkbare plasma's maar met de voedingsgassen N_2 en Ar gemengd met verschillende concentraties O_2 (variërend van 6.2×10^{-3} % to 5 %) (Hoofdstuk 7). De OES resultaten van de N_2/O_2 ontlading tonen een extra emissie van NOγ in vergelijking met de zuivere N_2 ontlading. De OES resultaten van de Ar/O_2 ontlading onthullen het verdwijnen van de geëxciteerde N_2 emissielijnen die gecompenseerd worden door het verschijnen van een kleine atomaire O-lijn. Deze atomaire O bleek zeer krachtig te zijn in het initiëren van de oppervlakte functionalisering door oppervlakte radicalen te genereren. De in situ XPS analyse toont aan dat wanneer de N_2 ontladingsatmosfeer minder dan 1% O_2 bevat, er een sterke toename van het O-gehalte aan het oppervlak wordt waargenomen ten koste van het N-gehalte. Wanneer het toegevoegde O_2 in het voedingsgas de 1% overschrijdt, wordt de stikstof opname op het oppervlak volledig uitgedoofd. In dit geval reageren de oppervlakte radicalen die worden gecreëerd door de niet-reactieve plasma species waarschijnlijk snel met de zeer reactieve en elektronegatieve O_2 moleculen op een manier die de reacties met de stikstof species overmeestert. Op het moment dat er een kleine concentratie O_2 aan de Ar gasstroom wordt toegevoegd, wordt er ook een sterke toename van het zuurstofgehalte aan het oppervlak gedetecteerd. Hierna loopt de ontwikkeling van de opgenomen hoeveelheid zuurstof op het oppervlak parallel met de hoeveelheid extra O_2 die aan het gasmengsel wordt toegevoegd. Als er meer O_2 in de ontlading aanwezig is, zullen er meer oppervlakte radicalen reageren met O_2 moleculen in plaats van met elkaar in wisselwerking te treden. Dit zal uiteindelijk leiden tot meer O-bevattende functionaliteiten die op het oppervlak worden ingebracht met een lagere mate van verknoping.

Na het verwerven van deze fundamentele inzichten van in-plasma en post-plasma chemische processen die plaatsvinden op polymeer oppervlakken, verschuift het 2de deel van dit proefschrift naar een daadwerkelijk tastbare toepassing van plasma activering in één van de meest populaire onderwerpen binnen de wetenschappelijke gemeenschap: *tissue engineering* (TE). TE benaderingen zijn gericht op het overwinnen van de beperkingen van standaard transplantatie methoden via de bi fabricage van vervangende structuren, zogenaamde scaffolds, voor de regeneratie van beschadigde weefsels. Één van de meest invloedrijke vereisten voor effectieve cel-scaffolds is de nabootsing van de nano vezelige extracellulaire matrix (EMC) die een scala aan cruciale cellulaire prestaties regelt, zoals adhesie, proliferatie en rijping. Om deze vezelachtige scaffolds te bio fabriceren, wordt elektrospinning op grote schaal gebruikt vanwege de veelzijdigheid, de eenvoud en de lage kost om efficiënt vezels te produceren met een diameter tot op nanometer schaal. Desalniettemin zijn geschikte topografische aanwijzingen die de ECM architectuur nabootsen niet voldoende om de gezochte uitkomst te activeren. In feite worden cellen niet alleen beïnvloed door de materiële topografie, maar ook door de biochemie van het oppervlak die een aanvullende rol speelt bij het initiëren van goed cel gedrag. Hiervoor moet een functionalisering van de nano vezelige scaffolds uitgevoerd worden om de binding eiwitten op het oppervlak te bevorderen. Dergelijke eiwitten worden herkend door de cel receptoren, waardoor de cel affiniteit voor de vezels wordt bevorderd. Om dit te doen, kan plasma activering worden uitgevoerd en zorgvuldig worden geoptimaliseerd om een gewenste oppervlakte chemie te verkrijgen zonder de structuur van de vezels te veranderen.

De bio fabricage en plasmabehandeling van geavanceerde bot TE scaffolds vormt het laatste toepassingsgericht doel van dit proefschrift (Hoofdstuk 8). Bot TE wordt met name gekozen vanwege de interessante dubbele rol van plasma activering bij het verbeteren van botregeneratie. Ten eerste kan de plasma-geïnduceerde opname van polaire functionele groepen op het oppervlak de affiniteit van “bot”-cellen voor de behandelde vezels bevorderen. Ten 2de kunnen dergelijke functionaliteiten de kiemvorming en de groei van botachtige apatitische calciumfosfaat (CaP) nanokristallen op de vezels (biomineralisatie) induceren die vrij essentieel zijn voor succesvolle osteo-integratie, osteo-inductie en osteo geleiding. Bovendien neemt de behoefte aan kunstmatige bottransplantaten die de botgeneratie voldoende verbeteren toe vanwege de toenemende incidentie van botdefecten veroorzaakt door botbreuken en osteodegeneratieve ziekten. Gezien de complexe verkalkte aard van het botweefsel, wordt in het laatste experimenteel hoofdstuk een combinatorische benadering toegepast waarbij specifieke topografische en biochemische aanwijzingen worden gecombineerd voor het ontwerp van een nieuw botweefsel engineered scaffold. Hiervoor wordt een natuurlijk koraal met een botachtige Ca verrijkte structuur toegevoegd aan electrospun chitosan (CS)/ polyethyleenoxide (PEO). De koraal vrije en koraal bevattende vezels worden vervolgens onderworpen aan plasma oppervlakte modificaties met behulp van een DBD die werk in Ar, lucht of N_2 bij een gemiddelde druk (50mbar) om de osteo-bioactiviteit van de vezels verder te verbeteren. De ex situ XPS resultaten laten zien dat de plasmabehandelingen een verscheidenheid aan zuurstof en stikstof bevattende functionaliteiten op het vezel oppervlak inbrengen, waardoor hun bevochtiging aanzienlijk wordt verbeterd. Na de plasmabehandelingen worden geen morfologische veranderingen van de vezels waargenomen. De verbeterde plasma geïnduceerde oppervlakte chemie verhoogd opvallend de adhesie en proliferatie van de MC3T3-osteoblasten. Hiernaast wordt de initiële cel adhesie versterkt door het samenspel van de plasmabehandeling en het koraal. Het in-vivo vermogen van de vezels om de groei van CaP op hun oppervlak te veroorzaken, werd voorspeld via de biomimetische onderdompeling in gesimuleerde lichaamsvloeistof (SBF). Zuurstof bevattende functionaliteiten, voornamelijk COOH-groepen, blijken de belangrijkste CaP kiemvormingsplaatsen te vormen. Als zodanig worden bolvormige nano dimensionele CaP kristallen afgezet op lucht en N_2 plasma behandelde CS/PEO NF's, terwijl dikkere lagen van vlokachtige CaP nano kristallen volledig de plasma-behandelde koraal/CS/PEO vezels bedekken zonder hierbij de poriën te blokkeren van de vezelachtige mesh-architectuur. De FTIR resultaten geven aan dat de gedeponeerde CaP fase het type B carbonaat apatiet is dat voorkomt bij normale botverkalking.

In conclusie, dit proefschrift geeft inzicht in nieuwe fundamentele en toepassingsgerichte aspecten van plasma oppervlakte activering van polymeren. Basis bevindingen van in-plasma en post-plasma processen die plaatsvinden op het oppervlak van UHMWPE dat wordt onderworpen aan Ar en N_2 plasma activering worden verkregen. Het licht wordt geworpen op de hoge reactiviteit van O_2 in N_2 en Ar-plasma's via de waargenomen extreme veranderingen die optreden in de samenstelling van de oppervlakte elementen na de opzettelijke toevoeging van O_2 aan het voedingsgas. Als zodanig moet een delicate afstemming van de plasma werkparameters parallel lopen met een nauwkeurige oppervlakte karakterisering om de optimale oppervlakte chemie te verkrijgen waarnaar wordt gezocht in een bepaalde eindtoepassing. De op maat gemaakte plasma activering die wordt gebruikt in de specifieke bot TE toepassing in dit proefschrift heeft geleid tot positieve resultaten. De exclusieve veelzijdige scaffolds bestaande uit de met plasma behandelde koraal/CS/PEO nano vezels wordt als zodanig verondersteld botdefecten effectief te herstellen en een revolutie teweeg te brengen in het gebied van bot-TE. Toekomstige in-vivo studies staan gepland waardoor de weg wordt geëffend naar het klinische gebruik van plasma geactiveerde scaffolds in bot en andere TE toepassingen.

List of Acronyms and Abbreviations

A

AC: Alternating Current

AFM: Atomic Force Microscopy

APPJ: Atmospheric Pressure Plasma Jet

ARXPS: Angle resolved X-ray Photoelectron Spectroscopy

B

BECM: Bone Extracellular Matrix

BTE: Bone Tissue Engineering

C

$CaCO_3$: Calcium Carbonate

CaP: Calcium Phosphate

CCD: Capacitively Coupled Discharges

CS/PEO: Chitosan/Polyethylene oxide

D

DC: Direct Current

DBD: Dielectric Barrier Discharge

E

ECM: Extracellular Matrix

EDS: Energy Dispersive Spectrometer

EEDF: Electron Energy Distribution Function

F

FTIR: Fourier Transform Infrared Spectroscopy

FWHM: Full Width at Half Maximum

G

GC-MS: Gas Chromatography Mass Spectrometry

I

ICD: Inductively Coupled Discharges

H

HA: Hydroxyapatite

HDPE: High-Density Polyethylene

He: Helium

HV: High Voltage

L

LDPE: Low Density Polyethylene

LTE: Local Thermodynamic Equilibrium

M

MW: Microwave

MTT: 3-(4,5-dimethylthiazol-2-yl)-2,5-diphenyltetrazolium bromide

N

NFs: Nanofibers

N_e: Electron Density

O

OES: Optical Emission Spectroscopy

P

PBS: Phosphate Buffered Saline

PCL: Poly(ε-caprolactone)

PDMS: Polydimethylsiloxane

PE: Polyethylene

PEEK: Poly(ether ether ketone)

PEOT/PBT: Poly(ethylene oxide terephthalate/poly(butylene terephthalate)

PLGA: Poly (lactide-co-glycolide)

PLLA: Poly(L-lactic acid)

PLTE: Partial Local Thermodynamic Equilibrium

PMMA: Poly(methyl methacrylate)

PP: Polypropylene

PS: Polystyrene

PTFE: Poly(tetrafluoroethylene)

PU: Polyurethane

PVA: Poly(vinyl alcohol)

R

RF: Radio Frequency

S

SBF: Simulated Body Fluid

SEM: Scanning Electron Microscopy

T

TE: Tissue Engineering

T_e: Electron Temperature

T_{exc} : Excitation Temperature

TCPS: Tissue Culture Polystyrene

TFAA: Trifluoroacetic Anhydride

TFBA: 4-(Trifluoromethyl)benzaldehyde

TFE: Trifluoroethanol

U

UHMWPE: Ultra High Molecular Weight Polyethylene

W

WCA: Water Contact Angle

X

XPS: X-ray Photoelectron Spectroscopy

XRD: X-ray Diffraction

List of publications

A1. Articles included in Web of Science indexes

(1) Mahtab Asadian, Iuliia Onyshchenko, Monica Thukkaram, **Parinaz Saadat Esbah Tabaei,** Joachim Van Guyse, Pieter Cools, Heidi Declercq, Richard Hoogenboom, Rino Morent, and Nathalie De Geyter. "Effects of a dielectric barrier discharge (DBD) treatment on chitosan/polyethylene oxide nanofibers and their cellular interactions." *Carbohydrate Polymers* 201: 402-415 (2018).

(2) K. Navaneetha Pandiyaraj, M. C. Ramkumar, A. Arun Kumar, D. Vasu, P. V. A. Padmanabhan, **Parinaz Saadat Esbah Tabaei,** Pieter Cools, Nathalie De Geyter, Rino Morent, and S. K. Jaganathan. "Development of phosphor containing functional coatings via cold atmospheric pressure plasma jet-Study of various operating parameters." *Applied Surface Science,* 488: 343-350 (2019).

(3) **Parinaz Saadat Esbah Tabaei,** Rouba Ghobeira, Pieter Cools, Fatemeh Rezaei, Anton Nikiforov, Rino Morent, and Nathalie De Geyter. "Comparative study between in-plasma and post-plasma chemical processes occurring at the surface of UHMWPE subjected to medium pressure Ar and N_2 plasma activation" *Polymer,* 193: 122383 (2020).

(4) Monica Thukkaram, Renee Coryn, Mahtab Asadian, **Parinaz Saadat Esbah Tabaei,** Petra Rigole, Naveenkumar Rajendhran, Anton Nikiforov, Jacob Sukumaran, Tom Coenye, Pascal Van Der Voort, Gijs Du Laing, Rino Morent, Alexander Van Tongel, Lieven De Wilde, Patrick De Baets, Kim Verbeken, Nathalie De Geyter. "Fabrication of microporous coatings on titanium implants with improved mechanical, antibacterial, and cell-interactive properties" *ACS Applied Materials & Interfaces,* 12(27): 30155-30169 (2020).

(5) K. Navaneetha Pandiyaraj, D. Vasu, Rouba Ghobeira, **Parinaz Saadat Esbah Tabaei,** Nathalie De Geyter, Rino Morent, M. Pichumani, P. V. A. Padmanabhanan, and R. R. Deshmukh. "Dye wastewater degradation by the synergetic effect of an atmospheric pressure plasma treatment and the photocatalytic activity of plasma-functionalized Cu–TiO_2 nanoparticles" *Journal of Hazardous Materials,* 124264 (2020).

(6) K. Navaneetha Pandiyaraj, D. Vasu, P. V. A. Padmanabhan, Rouba Ghobeira**, Parinaz Saadat Esbah Tabaei,** Pieter Cools, Nathalie De Geyter, Rino Morent, R. R. Deshmukh, and M. Pichumani. "Synergetic effect of the catalytic action of plasma jet deposited TiO_x coatings and atmospheric pressure plasma treatment on the degradation of RYRR." *Surface and Coatings Technology,* 389:125642 (2020).

(7) K. Navaneetha Pandiyaraja, D. Vasu, P. V. A. Padmanabhan, R. R. Deshmukh, V. Kandavelu, D. Saravanan, **Parinaz Saadat Esbah Tabaei,** Pieter Cools, Nathalie De Geyter, and Rino Morent. "Non-thermal atmospheric pressure plasma jet-assisted degradation of azo dye-acid orange 7 (AO7): influence of operating parameters and toxicity evaluation." *Desalination and Water Treatment,* 185: 344-354 (2020).

(8) **Parinaz Saadat Esbah Tabaei**, Mahtab Asadian, Rouba Ghobeira, Pieter Cools, Monica Thukkaram, Parviz Gohari Derakhshandeh, Sara Abednatanzi, Pascal Van Der Voort, Kim Verbeken, Chris Vercruysse, Heidi Declercq, Rino Morent and Nathalie De Geyter. "Combinatorial effects of coral addition and plasma treatment on the properties of chitosan/polyethylene oxide nanofibers intended for bone tissue engineering" *Carbohydrate Polymers*, 253: 117211 (2021).

(9) K. Navaneetha Pandiyaraj, D. Vasu, Rouba Ghobeira, **Parinaz Saadat Esbah Tabaei**, Pieter Cools, Nathalie De Geyter, Rino Morent and R. R. Deshmukh. “Non-thermal plasma jet assisted development of phosphorus containing functional coatings on 3D-printed PCL scaffolds intended for bone tissue engineering.” *Journal of Physics and Chemistry of Solids*, 3: 110025 (2021).

B2. Book chapter

(1) Pieter Cools, Laura Astoreca, **Parinaz Saadat Esbah Tabaei,** Monica Thukkaram, Herbert De Smet, Rino Morent, and Nathalie De Geyter. "Surface treatment of polymers by plasma". In: *Surface Modification of Polymers: Methods and Applications,* Jean Pinson and Damien Thiry (Eds) (Germany, Wiley-VCH) (2019): 31-65.

C1. Conference proceeding paper

(1) Laura Astoreca Alvarez, **Parinaz Saadat Esbah Tabaei**, David Schaubroeck, Maaike Op de Beeck, Rino Morent, Herbert De Smet, and

Nathalie De Geyter. "Visualizing the nucleation of ALD on polymers." In: *20th International Conference on Atomic Layer Deposition* (2020).

C4. Active conference participations

(1) Oral presentation at the “18th European Conference on Applications of Surface and Interface Analysis” (ECASIA), Dresden, Germany (2019).

(2) Oral presentation at the “16th International Conference on Plasma Surface Engineering” (PSE), Garmisch-Partenkirchen, Germany (2018).

(3) Poster presentation at the “Conference on Cold Plasma Sources and Applications” (COPSA), Ypres, Belgium (2018).

Table of Contents

List of Figures

List of Tables

Chapter 1. Introduction to Plasma

The literature study presented in Chapter 1 was published in a B2 book chapter:

Pieter Cools, Laura Astoreca, **Parinaz Saadat Esbah Tabaei,** Monica Thukkaram, Herbert De Smet, Rino Morent, and Nathalie De Geyter. "Surface Treatment of Polymers by Plasma". In: *Surface Modification of Polymers: Methods and Applications,* Jean Pinson and Damien Thiry (Eds) (Germany, Wiley-VCH) (2019): 31-65.

1. Plasma: an introduction

1.1 Definition

Plasma, generally referred to as the fourth state of matter, is often defined as a highly energetic quasi-neutral ionized gas that conducts electricity and is generated by imparting a certain amount of energy (in the form of heat or a strong electromagnetic field) to a gas. The supplied energy will result in highly energetic electrons, that transfer their energy to atoms through collisions, thus breaking down the atomic shell and ionizing the gas particles. Consequently, (partial) excitation, dissociation and ionization processes will take place as a result of those collisions, with an energy distribution that follows the Maxwell-Boltzmann distribution [1].

Plasma is characterized by more than its charge density and electric field alone though. It is a complex mixture consisting of active species such as electrons, reactive oxidative species, ions, photons, ultraviolet radiation, excited neutrals and radicals. Despite the fact that it can be characterized by a high charge density, the overall charge of a plasma is approximately zero, making it an electrically neutral medium. In fact, this quasi-neutrality is one of the main characteristics of plasmas, along with the collective behavior of the charged particles (a dynamic play of attractive and repelling electric forces). If the non-neutrality of a plasma becomes too high, the plasma will dissipate quickly due to electrostatic forces. There are examples of sustainable non-neutral plasmas (e.g. low-density electron beams), but they fall outside the scope of this thesis.

One of the most common ways to classify any plasma is by its degree of ionization, which is the ratio of the density of charged particles to the total density of species (equation 1.1), where *r* is the ionization degree, N_e the electron density, N_n the neutral density and N_i the ion density:

$$r = \frac{N_e}{N_n + \Sigma N_i} \qquad (1.1)$$

When $r \to \infty$, it is referred to as a completely ionized plasma. Typical examples of such fully ionized plasmas are thermonuclear plasmas (e.g. the sun), which are of little interest for polymer surface modifications and will therefore not be discussed further in this thesis. For $r < 10^{-2}$, plasma is considered to be weakly ionized. In those cases, the ionization degree of plasma is weak and the collision frequency of electrons to ions is less than the collision frequency of electrons to neutrals (e.g. neon lights). In a fully ionized gas, the dominating particle interactions sustaining the plasma will be Coulomb-type collisions (elastic collisions between two charged particles). On the other hand, when the gas is weakly ionized, these Coulomb collisions are no longer dominant and the particle interactions are largely controlled by inelastic collisions [2].

1.2 Thermal vs non-thermal plasma

Strongly correlated with the degree of ionization are the relative temperatures of the ions, neutrals and electrons, allowing plasmas to be classified into two categories: thermal plasma (also referred to as equilibrium plasma), usually more strongly ionized, and non-thermal plasma (non-equilibrium plasma), normally weakly ionized. In thermal discharges, the heavy particle temperature (T_{ion} + T_{neutral}) is close to the electron temperature (T_{electron}), which is usually several thousand Kelvin ($T_{\text{ion}} \approx T_{\text{neutral}} \approx T_{\text{electron}}$). For this reason, thermal discharges are also called equilibrium discharges. The best-known examples of thermal plasmas are plasma flames, electric arcs, nuclear fusion reactors and interstellar gases, which make up more than 99 % of the known universe (Figure 1.1). As already mentioned, these high temperatures prevent the use of thermal plasmas in the processing of polymers and are therefore not the focus of this thesis.

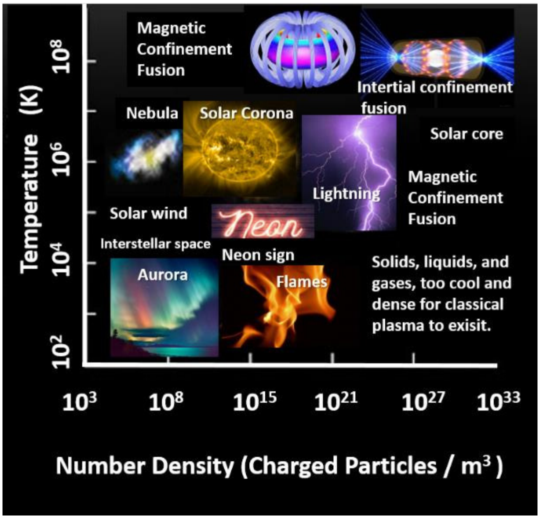

Figure 1.1 Characteristics of typical plasmas according to their temperature and density.

Non-thermal plasmas are generated and maintained by introducing a non-equilibrium between the temperatures of the electrons and ions. The heavy particles temperature remains at room temperature ($T_{\text{ion}} \approx T_{\text{neutral}} \sim 0.025$ eV), while the electron temperature is increased to several electron volts of kinetic energy ($T_{\text{electron}} \sim$ 1-10 eV), resulting in a (partial) ionization and the breakage of covalent bonds. Such non-equilibrium plasmas are usually generated through the application of a short pulsed direct current discharge (DC), or by applying a rapidly alternating (AC), radio frequency (RF) or microwave (MW) voltage which will be discussed in more detail further on [3]. As the overall non-equilibrium plasma temperature can be tuned towards ambient temperatures, thermo-sensitive polymer processing becomes feasible.

1.3 The formation of non-thermal plasma

Non-equilibrium discharges can be categorized into (1) avalanche Townsend discharges, (2) streamer discharges and (3) glow discharges, depending on the input current and potential used to ignite and maintain the plasma. The Townsend discharge type results in a large number of successive electron avalanches, whereas the streamer mechanism results in a single rapid micro-discharge but is sustained by secondary electron emission at the cathode. Moreover, a further increase in the electrical current through the gas results in the formation of a glow discharge. At this point, the voltage will exceed the breakdown voltage threshold (Figure 1.2).

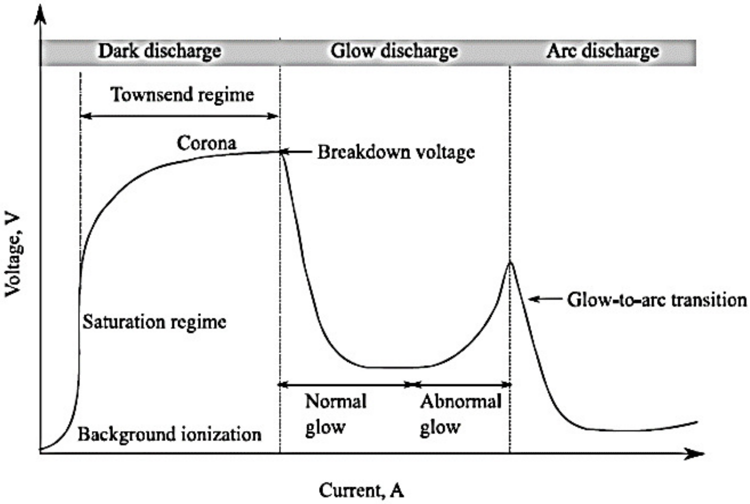

Figure 1.2 The different discharge regions for a DC discharge. The figure is reproduced with permission of IOP [1].

Figure 1.3 schematically presents the general transition process from an electron avalanche (Townsend) towards a streamer-type discharge. By applying a low-current electric field between two electrodes, free electrons will start accelerating from the cathode towards the anode, consequently colliding with the background particles and ionizing them (impact ionization). This process results in the formation of electron avalanches. The formation of the primary avalanche is presented in Figure 1.3(a). This electron avalanche propagates throughout the discharge gas and moves forward (Figure 1.3(b)) until it reaches the anode, becoming more intense as it propagates. In this case, the electrons of the main avalanche will mostly be transferred to the anode. After the initial avalanche reaches the anode, the charge density will start increasing, giving cause to photon radiation and eventually leading to the formation of secondary electron avalanches (Figure 1.3(c)). As a result, a large number of ionized particles will start to accumulate around the discharge anode. Due to this accumulation, a plasma column and a streamer head with an active zone will form (Figure 1.3(d)), resulting in multiple electron avalanches that are attracted to the head of the streamer and participate in the formation of a plasma channel. In this case, the local ionization is much higher than the electron avalanche. The next step occurs when electrons from the avalanche's neutralizing head are transformed into a new streamer head (Figure 1.3(e)). This formation and rapid propagation of the highly ionized region is actually called a streamer (Figure 1.3(f)). It is worth mentioning that this entire process takes place in the range of nanoseconds [4,5].

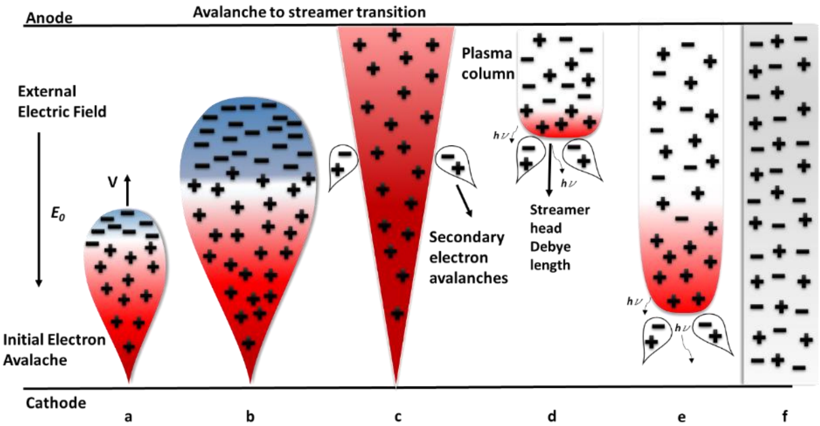

Figure 1.3 Avalanche to streamer transition: (a) Initial electron avalanche (b) avalanche development, (c) secondary electron avalanches, (d) appearance of plasma, (e) streamer propagation and (f) formation of streamer.

1.4 Plasma generation and operating conditions

Plasmas can be generated in a wide range of pressures going from a few Pa up to atmospheric pressure. Generating plasmas at low and medium pressures has the advantage of larger plasma volumes, thus allowing the surface modification of bigger objects with complex surface geometries. The plasma chemistry under those conditions is dominantly driven by radical or atomic interactions that are relatively well but not fully understood, thus permitting a fairly good control over the surface chemistry. Moreover, since the plasma is generated in a closed environment, it enables the use of toxic and/or air-sensitive chemicals. Although working with a low pressure plasma gives some great advantages, operating a plasma in a vacuum environment is expensive and time-consuming. On the other hand, atmospheric pressure plasmas have been broadly studied due to the possibility of in-line integration in continuous production processes and their reduced cost, which are important drives in industry. As a result, atmospheric pressure plasma systems have attracted considerable interest in a wide range of environmental, biomedical and industrial applications [8– 10]. However, the fundamental knowledge on the atmospheric pressure plasma chemistry and plasma physics remains limited. Finally, as the particle density at atmospheric pressures is considerably higher, it can be challenging to find the proper plasma parameters to avoid operating in the filamentary mode.

1.5 Different methods of plasma generation

The energy needed for generating a plasma can be obtained by applying an external electric field to a neutral gas. The charged particles are therefore accelerated within the electrical field and couple their energy in plasma through collisions with other particles, resulting in the electrical breakdown of the neutral gas (as presented and discussed in Figure 1.3). Since electrons have a small mass, they keep a considerable amount of their energy when interacting with molecules and atoms through elastic collisions, primarily transferring their energy via inelastic collisions. Such types of discharges are typically generated within high voltage electricity, microwaves or pumped lasers [1]. Within a research environment, the power sources most commonly used to generate plasmas are DC-based (which can be operated continuously or in pulsed mode), AC-based, RF-based (inductively coupled discharges (ICD) and capacitively coupled discharges (CCD)) and MW-based. The RF discharges are operated at a frequency range between 1 -100 MHz [1,9] while MW-based discharges are most commonly driven at a frequency of 2.45 GHz [1]. In the following paragraphs the non-thermal plasma source that has been used in this thesis will be discussed in more detail.

1.5.1 Dielectric barrier discharges (DBDs)

The silent discharge or DBD plasma, used for ozone production in the treatment of drinking water more than 100 years ago [5], is now successfully used for a variety of industrial applications. Extensive research on DBDs has widen its applications in many fields such as surface modification, thin film deposition, gas reforming, water treatment, creation of excimer ultraviolet lamps, sterilization and cleaning the surfaces of materials such as polymers and semiconductors [10–14]. A DBD is a controlled discharge between two electrodes of which at least one is covered by a dielectric layer. The configuration of the electrodes comes in many variations. One of the most common configurations (the parallel-plate) is schematically presented in Figure 1.4(a) and consists of two flat electrodes that are separated by a few mm up to a few cm, with the gas flowing in-between them [15]. The gap size between the electrodes is depending on the application, chamber pressure and used discharge gas, with a rule-of-thumb stating that the larger the gap size, the more difficult it becomes to maintain a homogeneous (pseudo)glow discharge (the one typically used for polymer treatment).

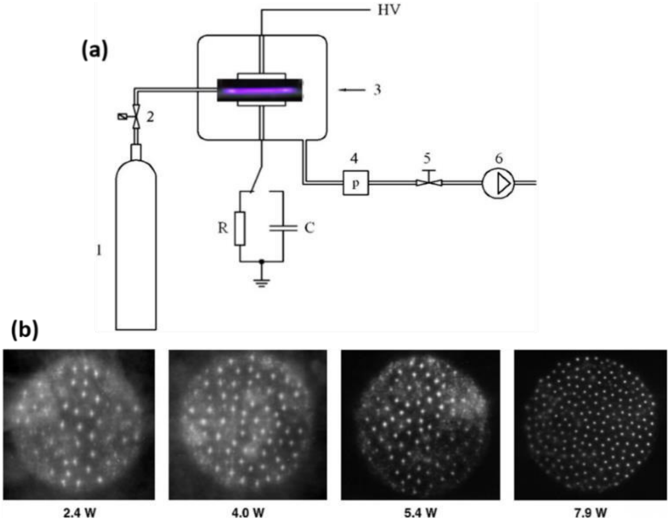

Figure 1.4 (a): Schematic representation of a DBD reactor (1: gas bottle; 2: mass flow controller; 3: DBD plate reactor; 4: manometer; 5: pressure valve, 6: vacuum pump) [53]. *(b): Lichtenberg figures of a DBD at different discharge powers. Figure is reproduced with permission from* [16].

As shown in Figure 1.4(a), one of the electrodes is connected to a high voltage source and the other is grounded with a controlled gas flow in between.

The two main modes in which a DBD can operate are the filamentary and glow mode:

In filamentary mode, the DBD consists of many separate current filaments referred to as micro-discharges. These micro-discharges are formed by channel streamers and are extremely short-living. When applying a sufficiently high discharge potential, the micro-discharges can be visualized as they continuously strike at the same place, appearing to the eye as bright filaments. Figure 1.4(b) shows that by increasing the discharge power, more micro-discharges can be observed [16]. The most important characteristic of a DBD is the dynamic of the electron energy distribution function (EEDF) in the micro-discharge. The effectiveness of this process is the direct electron impact dissociation, which can be calculated through data obtained from Langmuir probes. The streamers in DBD plasmas are capable of producing highly energetic electrons, as the electric field in the streamer is by far greater than the applied electric field itself [5]. The potency of direct electron impact dissociation in the discharge determines the overall efficiency of the treatment.

A glow discharge mode is characterized by a single current pulse with durations up to a few µs [17]. In this mode, plasma is formed homogeneously once every half cycle of the voltage. In addition to filamentary and glow mode, the transition from glow to filamentary is realized by the so-called pseudo-glow mode [18–20]. The indication of the operational mode can be also confirmed by the visual appearance of the plasma: a homogenous glow discharge is uniformly distributed throughout the discharge volume. On the other hand, the filamentary discharge consists of a set of separate filaments arbitrarily distributed across the electrode surface.

1.6 Non-thermal plasma for polymer surface treatment

For any industrial application requiring a surface modification step of a polymer, including surface cleaning, functionalization and/or coating, an overall processing temperature close to room temperature is highly desired, as it avoids damaging the underlying thermo-sensitive substrate. It is well described in literature that the active species in non-thermal plasmas can have a significant impact on the substrate’s surface chemistry and topography without altering the bulk properties of the polymer material [21–24]. The interactions that are responsible for those changes will be discussed in more detail in the following paragraphs.

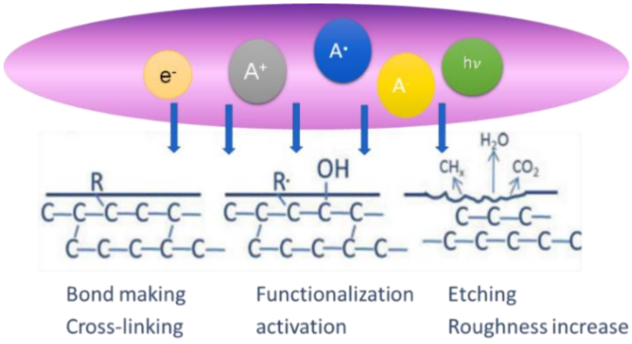

Figure 1.5 Schematic overview of the different plasma-surface interactions (where A refers to Anions, e: electrons, and hυ: photons).

Major competing molecular reactions will take place on the surface of polymers upon their exposure to a non-thermal plasma: (1) etching, (2) plasma functionalization and (3) cross-linking (Figure 1.5) [9]. The effect of each type of reaction is largely controlled by the discharge physical properties (see above), the discharge chemistry and the used process variables:

- **Plasma ablation/etching** is the collective name for the abstraction of atoms/ions/molecular fragments from a polymeric substrate through ion bombardment and energetic electron impact. When operating at reduced pressures, these species are subsequently pumped away from the surface. A clear distinction must be made between chemical and physical etching. During chemical etching, the plasma-activated gases will attack the surface by forming gases that are easy to evaporate. In physical etching, the plasma-generated ions are accelerated towards the surface, transferring their momentum to the surface and ejecting surface contaminants. These plasma treatments are mainly applied for surface cleaning, especially the removal of organic contaminants through their transformation into volatiles. It is worth mentioning that, depending on the crystallinity of the plasma-treated substrate, parts of the polymer itself can also be actively etched away, which usually results in a (slight) alteration of the surface topography [25].

- **Plasma functionalization** is the process of introducing new functional groups onto the surface (amines, alcohols, ketones, esters…) and can be divided into plasma activation and plasma passivation.

  Plasma activation is the general term used for the plasma treatments that result in an increase in the surface free energy through the incorporation/substitution of surface atoms and molecules. A clear distinction must be made between plasmas generated in inert gases (Ar, He, Ne, Xe…) and those created in reactive gases (O_2, N_2, CO_2, NH_3...). In case of reactive plasmas, two types of active species are present in the plasma active region. The first group consists of reactive species such as, depending on the used gas, nitrogen ions and oxygen and nitrogen radicals. These species can be incorporated directly onto the surface as new functional groups [26]. The second group consists of photons, electrons, non-reactive ions, non-reactive excited atoms and non-reactive molecules. Such species have no direct effect on the exposed substrate but can break covalent bonds on the polymeric surface, which in turn leads to the creation of radicals. For plasmas generated in inert gases, only the second group of species are present. Although those species cannot directly incorporate new functional groups, the radicals they generate on the surface can quickly react with oxygen/water when exposed to the ambient environment, leading to the incorporation of oxygen-containing functional groups onto the surface of the polymer. Alternatively, when interchanging ambient air with another reactive atmosphere, other functional groups can also be grafted onto the surface [27].

  Plasma passivation is the collective term for all plasma functionalization processes that result in the reduction of the surface free energy by making it (chemically) inert [25]. The best-known example of plasma passivation is fluorine-based plasma functionalization (CF_4), resulting in Teflon-like surfaces [28].

- **Cross-linking** is the **bonding** of two or more parallel polymer chains. Cross-linking is a side-effect of bombarding the surface with species generated in inert gases like Ar and He. As mentioned earlier, Ar or He plasma cannot directly introduce new functional groups onto the surface [26]. Nevertheless, the formed He and Ar ions that are thermodynamically unstable are capable of subtracting H-atoms from the polymer chains, resulting in the formation of reactive radicals on those chains. The spawned radicals are in their turn able to generate new covalent bonds between two polymer chains, resulting in a stable cross-linked network on the surface.

1.7 Scope and strategic methodology of the thesis

In the past few decades, plasma activation of polymers has particularly established a prominent place in a widespread and dynamic field of surface treatments. Nonetheless, despite the wide literature involving profound basic investigations and diverse applications of plasma activation, some uncertainties about the exact mechanisms of plasma activation still linger. Researchers have actually attempted to decorticate all fundamental aspects linked to the exact plasma-surface chemical interactions by employing a wide range of surface analytical techniques. Given the fact that plasma site of action is limited to the top few nanometers of the treated substrate, the number of techniques that can be used becomes very restricted to the ones detecting the top surface chemistry. As such, a supremacy of the X-ray photoelectron spectroscopy (XPS) technique having an analysis depth approximately equaling the region depth affected by the plasma activation is observed over other techniques. However, in the big majority of the literature studies, XPS measurements were carried out post-exposure of the treated samples to ambient air thus making it impossible to draw definite conclusions and make clear distinctions between in-plasma and post-plasma surface interactions. Only very few studies have already dealt with the direct XPS characterization of plasma-modified polymer surfaces which was carried out either by making use of a transfer vessel or by connecting the plasma set-up directly to an XPS machine. In this way, no exposure to the ambient air occurs prior to the XPS analysis, thus eliminating the effects of post-plasma oxidation. Several non-tackled important aspects in the literature involving *in situ* XPS analyses have left some question marks around some fundamental pathways. For instance, studies were only focused on low pressure plasma treatments, totally neglecting the examination of exclusive in-plasma processes in case of high pressure plasmas. Moreover, a systematic study comparing between in-plasma and post-plasma surface chemical processes via the performance of both *in situ* and *ex situ* XPS analyses is also lacking. Additionally, in the available studies focusing on *in situ* characterization of plasma-treated surfaces, plasma diagnostics have been highly disregarded. This sets up some limits for useful plasma diagnostics/surface analysis correlations that can very accurately determine the potential excited species that are specifically involved in the ensuing surface chemical modifications. Finally, no study has investigated, to the best of our knowledge, in-plasma initiated oxidation processes by purposely admixing oxygen to different non-oxygen containing feed gases in order to elucidate its influence on the surface chemistry without the interference of post-plasma oxidation.

In view of the above, the first part of the thesis will be focused on acquiring novel fundamental acquaintances and filling some basic gaps found in the field of non-thermal plasma activation of polymers. Firstly, the relative implication of in-plasma and post-plasma surface interactions will be distinctively sort out in sub-atmospheric pressure treatments. Thereafter, exclusive in-plasma initiated oxidation processes occurring at polymeric surfaces upon O_2 admixtures to medium pressure non-oxygen containing DBD treatments will be profoundly investigated.

After deeply uncovering the fundamentals of plasma-surface chemical interactions, the reaped knowledge will be used in an eventual application-orientated pathway. As such, the second part of the thesis is focused on an actual palpable application of plasma activation in one of the hottest topics within the scientific community: tissue engineering (TE). Bone TE is in particular selected because of the high alerting incidence of bone defects occurring nowadays which triggers an urgent need for artificial implants sufficiently enhancing bone regeneration. Plasma activation can have an interesting double role in boosting bone regeneration: 1) the improvement of the cell-surface interactions and 2) the enhancement of the scaffold's biomineralization that is essential for successful osteointegration, osseoinduction and osteoconduction.

After setting up both the fundamental and application-oriented goals, an evolutionary step-by-step approach is adopted in the writing of the thesis. As such, the reader is placed in the frame of the current state-of-the-art involving plasma activation of polymers in general, *ex situ* and *in situ* XPS surface analyses associated with plasma-activated surfaces and the use of plasma in bone TE. Based on the pitfalls found in literature, the thesis will evolve towards finding solutions in the performed experimental studies.

Overall, the thesis is divided into 4 parts formulated in the following way:

Part 1: Literature overview

Chapter 2 is dedicated to provide an extensive overview on the different XPS measurement capabilities applied to chemically characterize plasma-activated polymeric surfaces. Beside the typical measurements determining the surface elemental composition, more advanced XPS analyses will be discussed such as XPS mapping, peak fitting and angle resolved XPS. The limitations associated with some of the reported XPS analyses are also comprehensively discussed. Several acquaintances on plasma surface interactions are as such reaped. Overall, Chapter 2 constitutes a perfect-picture reference for all future studies involving a plasma activation of polymers.

The XPS results reported in **Chapter 2** were all carried out within a short time range post-exposure of the treated samples to the ambient air. Therefore, in-plasma processes and the well-known ageing effect of plasma-activated surfaces occurring upon longer storage periods were not tackled. As such, **Chapter 3** is specifically devoted to provide the reader with a profound knowledge on in-plasma surface interactions and surface ageing processes via a literature overview involving XPS analyses undertaken *in situ* or *ex situ* after relatively prolonged storage times.

The last chapter of the literature study (**Chapter 4**) shifts towards the application of plasma activation in bone TE. The first part of the chapter gives the reader an overview of scaffold-based TE approaches and their main existing pitfalls. The subsequent part provides an extensive overview on how recent progresses in the plasma activation of electrospun bone TE scaffolds have mostly enhanced bone tissue regeneration. This chapter serves as an excellent reference that can be used to further improve bone TE scaffolds for better outcomes.

Part 2: Materials and Methods

Chapter 5 is dedicated to the description of the experimental setups, materials and methods used in this thesis. Plasma treatments, electrical and optical characterization techniques, surface analysis techniques, biofabrication methods, *in vitro* cell tests and calcium phosphate (CaP) deposition will be described with their different operating parameters.

Part 3: Experimental results

As already mentioned, the relative implication of in-plasma and post-plasma surface interactions are not yet distinctively decorticated especially in sub-atmospheric pressure treatments. As such, the first experimental chapter

(**Chapter 6**) profoundly highlights such phenomena together with the exact reasons behind oxygen incorporation on surfaces subjected to a plasma activation operating in a non-oxygen containing atmosphere. To do so, ultra-high molecular weight polyethylene (UHMWPE) films are treated with N_2 and Ar DBDs at a medium pressure of 5.0 kPa. Thereafter, *in situ* XPS analysis is combined with optical emission spectroscopy (OES) measurements to precisely understand in-plasma surface interactions and link them back to the excited species present in the different discharges. Post-plasma chemical processes and surface ageing behavior are then unraveled by performing comparative *ex situ* XPS measurements upon exposure to air for times ranging from 5 min to 21 days.

Chapter 7 further advances in complexity by tackling in-plasma initiated oxidation processes occurring when exposing UHMWPE surfaces to similar plasmas but with the feed gases (N_2 and Ar) admixed with different concentrations of O_2 (ranging from 6.2×10^{-3} % to 5 %). An extensive comparative study is also conducted by performing careful correlations between OES and *in situ* XPS results.

The last experimental chapter of this thesis (**Chapter 8**), is actually directed towards reaching the application-oriented goal of the thesis: plasma activation of advanced scaffolds for an enhanced bone regeneration. To do so, an integrative approach merging specific topographical and biochemical cues is adopted in the design of a novel bone TE scaffold. Natural coral having a bone-like calcium-enriched structure is added to electrospun chitosan (CS)/polyethylene oxide (PEO) nanofibrous scaffolds mimicking the bone extracellular matrix (ECM) architecture. In order to further enhance the scaffolds osseoinduction, osteoconduction and osteointegration, coral-free and coral-containing fibers are subjected to plasma surface modifications using Ar, air or N_2 DBD operating at medium pressure (5.0 kPa). To the best of our knowledge, these exclusive multifaceted nanofibers adopting a finely selected combination of coral addition and plasma treatment were never investigated in the broad literature involving electrospinning, plasma surface functionalization or TE. A profound comparative study of the physicochemical surface properties, cytocompatibility and CaP growth capacity is performed.

Part 4: Conclusion

Chapter 9 gives a general conclusion of the performed work and an outlook on future considerations and perspectives.

Chapter 2. Chemical characterization of plasma-activated polymeric surfaces via XPS analyses

2.1 Introduction

During the last few decades, non-thermal plasma surface functionalization of polymeric materials has increasingly earned a high-flying position in a wide range of application fields [7,13,21,29–31]. On the one hand, the acquired supremacy of plasma treatments over other surface modification techniques is due to their versatility, simplicity, time efficiency, non-invasive character restricted to a modification depth of a few nanometers and solvent-free aspect [13,32,33]. On the other hand, numerous studies have redundantly demonstrated the plasma aptitude to successfully enhance or optimize, amongst others, the surface wettability, bio- and cyto-compatibility, printability, barrier properties, optical absorbance, bonding characteristics and adhesiveness of polymers [21,30,31,34–38]. As such, plasma-treated surfaces have constituted one of the main topics in the field of applied physics. Generally, plasma-induced effects result, as stated in the previous chapter, in cross-linking, etching and/or grafting of new functionalities (activation/passivation) on the treated polymeric surfaces. These diverse reactions can actually happen concurrently, yet depending on the pre-determined experimental conditions, the effect of one can become more significant than the other [39]. Nonetheless, in the wide literature involving plasma surface modifications, the insertion of chemically reactive functionalities onto non-reactive polymeric substrates is most commonly targeted [34–38]. Such functionalities result in an increase in the surface energy which subsequently improves its hydrophilicity, a characteristic that is highly desirable for the creation of bio-interfaces [33–38,40,41]. However, one of the major limitations of plasma activation is the diversity of functional groups that are produced on the surface because of the multitudes of chemical reactions occurring in the plasma region. In fact, plenty of active species having a significant impact on the surface chemistry of the polymer are present in the ignited plasma. When such active species collide with a surface, various chemical bond dissociations and ionizations as well as secondary collisions befall [17,20,34]. Despite all the advanced fundamental studies aiming at deeply understanding the reactions occurring on polymeric surfaces upon and post-modification, some uncertainties about the exact mechanisms of plasma activation still linger [34]. It is however assumed that the most probable scenario could be a series of chemical reactions initiated by the creation of surface radicals and followed, depending on the used working gas, by different pathways [20,39,42]. In fact, when the treatment is sustained in an inert gas such as helium or argon, the ensuing surface radicals should theoretically interact with each other leading to a polymer topology change illustrated by the formation of a cross-linked network. When plasma is ignited in a chemically reactive atmosphere such as oxygen or nitrogen, the plasma-induced surface radicals will interact with the plasma reactive species leading to a surface functionalization hypothetically characterized by a selective insertion of oxygen- or nitrogen-containing functionalities respectively [15,34]. Nonetheless, most of the conducted studies have shown that these hypotheses are biased by an inevitable incorporation of oxygen-containing groups on surfaces exposed to plasma discharges generated in inert and reactive non-oxygen containing gases [20,42]. Several possible reasons can stand behind this unexpected oxygen incorporation such as the presence of water vapor and oxygen contaminations in the plasma reactor, the impurity of the used gas that might contain oxygen traces, the plasma-induced desorption of oxygen-containing gaseous components from the reactor wall and post-plasma treatment oxidation upon exposure of the polymer to the ambient air [20,33]. Therefore, grafting well-defined chemical functionalities onto a plasma-activated surface and achieving controlled surface chemistries is a challenging approach that demands excessive optimization of the working parameters. In fact, deeper understandings of the plasma-surface interactions illustrating the relation between the different parameters and the spawned surface chemistry should be unravelled by effective chemical surface characterizations. This safeguards for a fine-tuned control over the surface chemistry to perfectly match the requirements of the desired end application. For instance, the control of surface chemistry is highly important in the biomedical field as the optimization of the number and types of surface functionalities dictates cell attachment but also cell spreading, which are important mechanisms affecting cell division, gene expression and differentiation [40]. Nonetheless, some scientific papers aiming at enhancing bio-interfacial interactions via plasma surface treatments underappreciated the necessity of surface characterizations. The focus was instead directed towards the immediate use of plasma-treated surfaces as an intermediate bonding layer for the immobilization of biomolecules to obtain specific biological responses [43–46]. Such responses could have been highly improved with a prior fundamental knowledge on the plasma-surface interactions and optimization of the ensuing surface chemistry.

To cope with this issue, analysis techniques are being used to qualitatively and quantitatively detect and characterize plasma-induced chemical surface modifications [35,37]. Given that the plasma site of action is limited to the top few nanometers of the treated substrate, the number of techniques that can be used becomes very restricted to the ones detecting the top surface chemistry. As such, a supremacy of the XPS technique is observed over other techniques in the wide literature involving surface characterizations following plasma treatments [15,16,47–50]. Therefore, in what follows, a brief synopsis of the used techniques will be first given. Thereafter, a description of the XPS technique together with its utilities in the characterization of the plasma-induced effects on polymeric surfaces will be highlighted in a framework limited to non-thermal plasma activation.

2.2 Surface characterization of plasma-treated surfaces

Many research groups have studied the chemical and physical interactions of various plasma atmospheres with a range of polymeric substrates. To do so, atomic force microscopy (AFM) and scanning electron microscopy (SEM) were mainly employed to get an insight on the plasma-induced topographical changes and water contact angle (WCA) analysis and XPS were most widely considered for chemical characterizations as they truly are surface specific [15,20,35]. WCA measurements are actually known to be affected by a surface thickness of approximately 0.5 nm. Such measurements give accurate information on the wettability of the treated surface that can become more water-attracting (more hydrophilic) or more water-repellent (more hydrophobic) upon and post-exposure to plasma [20,39,51]. This can be experimentally very easily quantified by measuring the angle between a small water droplet deposited on the surface and the surface itself after drawing a tangential line on the liquid side passing through a point where the liquid, gas and solid phase meet. Normally, strong interactions occur between a hydrophilic surface and the water drop thus giving a contact angle lower than 90°. In contrast, limited interactions with the water drop befall if the surface is hydrophobic which leads to a contact angle higher than 90° [51,52]. Despite being very simple and cost-effective, the WCA technique does not provide any information on the specific surface chemical elements and functionalities responsible for the enhanced hydrophilicity or hydrophobicity. Moreover, the obtained value does not solely reflect the chemical polarity of the surface but is also affected by the surface roughness [33,53]. In fact, when the roughness of a surface is relatively high, air might be trapped inside the roughness grooves; a phenomenon that prevents water infiltration and amplifies the WCA. This behaviour that was portrayed by the Cassie-Baxter equation is known as “heterogeneous wetting” [54,55]. In contrast, an opposite behaviour was also described by the Wenzel equation that was formulated on a basis stating that water tends to infiltrate in the roughness furrows present on the surface. This trend known as “homogeneous wetting” leads to a reduced WCA. This competition between heterogeneous and homogeneous wetting aiming at minimizing the Gibbs energy is affected by both the surface topography and chemistry [33,56]. Therefore, a purely chemical characterization technique is required to complement WCA measurements. Secondary ion mass spectrometry (SIMS) was thus used in some studies to qualitatively detect plasma-grafted surface functionalities as it is typically not quantitative without standards. Therefore, some authors have combined it with other techniques for more detailed and complementary information to XPS analysis [47,57,58]. The use of Fourier-transform infrared spectroscopy (FTIR) has also faced the restriction of its analysis depth going way beyond a few nanometers to reach several hundreds of nanometers. This technique was therefore mainly utilized to qualitatively determine functional groups on relatively thick coatings deposited upon plasma polymerization processes that fall outside the scope of this thesis [59]. As such, the XPS technique, being distinguished by an analysis depth approximately equaling the region depth affected by the plasma activation (a few nanometers), is an excellent alternative determining the surface chemical composition and functionalities [15,16,47–50]. It is somewhat a young technique that started to be used in the 1980s after the Swedish physicist Kai M. Siegbhan was awarded the Nobel Prize for his discoveries in X-ray spectroscopy in 1981 [60]. The decade that followed has marked the emergence of a few research articles per year in which “plasma” and “XPS” were combined in their topic. Thereafter, a steep rise in the number of such publications has followed to reach more than 200, 500 and 600 articles in 2000, 2010 and 2020 respectively (Figure 2.1, Source: *Web of Science*). These publications that were growing in parallel with the increase in the commercially available XPS machines have progressively decorticated the unknown in chemical plasma-surface interactions [15,16,47–50,61–64]. Besides determining the surface elemental composition on defined points, XPS offers some more advanced measurement capabilities. For instance, XPS mapping discerns the distribution of elements across a surface [41], high resolution spectral measurement enables the recognition of surface chemical bonds through peak deconvolution [16,17,65,66], XPS combined with specialized sputtering guns such as a the Buckminster fullerene (C_{60}) ion gun and Ar-ion gun is able to provide advanced chemical depth profiling [47,59,67,68] and angle resolved XPS can also acquire chemical information as a function of depth in a less destructive manner but with a more limited depth range [66]. These techniques with some of their corresponding applications involving plasma activation of polymers will be discussed elaborately later on after a brief description of the XPS principle. In fact, choosing an appropriate XPS measurement is also crucial to better comprehend the plasma-induced effects on polymeric surfaces.

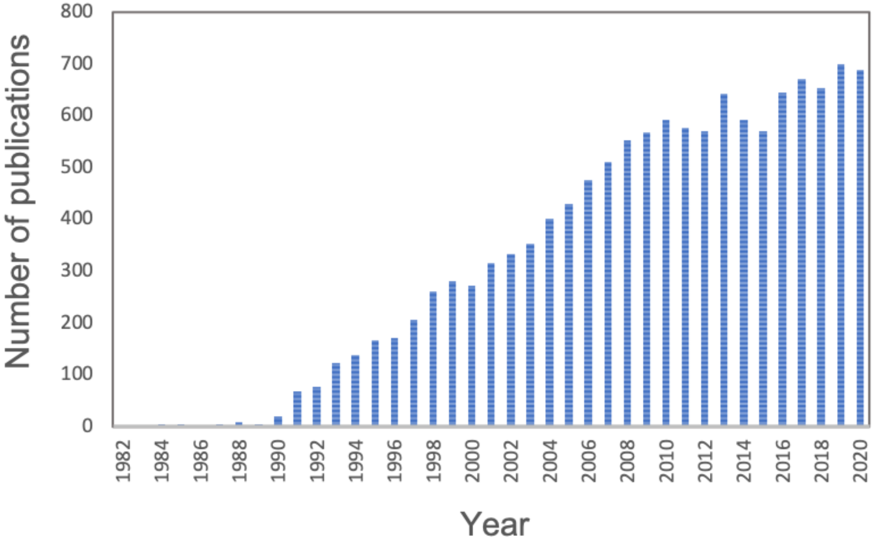

Figure 2.1 Number of articles implicating "plasma" and "XPS" in their topic as a function of the publication year (Source: Web of Science®).

2.3 XPS principle

As already mentioned, XPS is a highly powerful and superior analysis technique employed for both the qualitative and quantitative determinations of chemical states in the top surface regions (a few nanometers). It detects the elemental surface composition and can sort out different types of surface chemical bonds [13,20,61–64].

The principle of XPS involves the detection and measurement of photoelectrons ejected from the surface of a material which has been initially irradiated with X-rays originating from a monochromatic source and having a fixed energy *($h\nu$)*. The ejection of electrons or the so-called photoionization process happens either from a tightly bounded core electron (similar to atomic orbitals) or from a more weakly bounded valance electron of low binding energies levels. The expelled photoelectrons are then focused and directed towards an electron energy analyzer that is able to disperse them based on their kinetic energy (E_{kin}) and then measure the different electron fluxes having particular energies [69]. The measured kinetic energies of the photoelectrons are then converted to binding energies (E_b) via the following equation:

$$E_b = hv - E_{kin} - W_f \qquad (2.1)$$

where W_f is the work function which is the minimum energy that should be conferred to an electron to release it from the surface of a material [69].

The obtained binding energies will then permit the atoms on the surface to be detected. In fact, each binding energy is characteristic of a core atomic orbital meaning that every atom will generate a characteristic group of peaks in the binding energy spectrum [70].

It should be noted that photoelectrons that are only generated near the surface can escape without losing too much of their energies, whereas those generated deeper in the material lose some energy via elastic and inelastic collisions. Such photoelectrons are not able to be detected with XPS as they only will become part of the background or will diverge from the detection line. This can therefore explain why an XPS spectrum only provides chemical information in provenance of the surface top atomic layers (≈ 20-40 atomic layers or 5-10 nm) [20,35].

An important requirement of XPS is the execution of the measurements at an ultra-high vacuum ($<10^{-6}$ Pa) in order to avoid any surface contamination of the measured sample and obviate as much as possible collisions between the ejected electrons and the background gas [70,71].

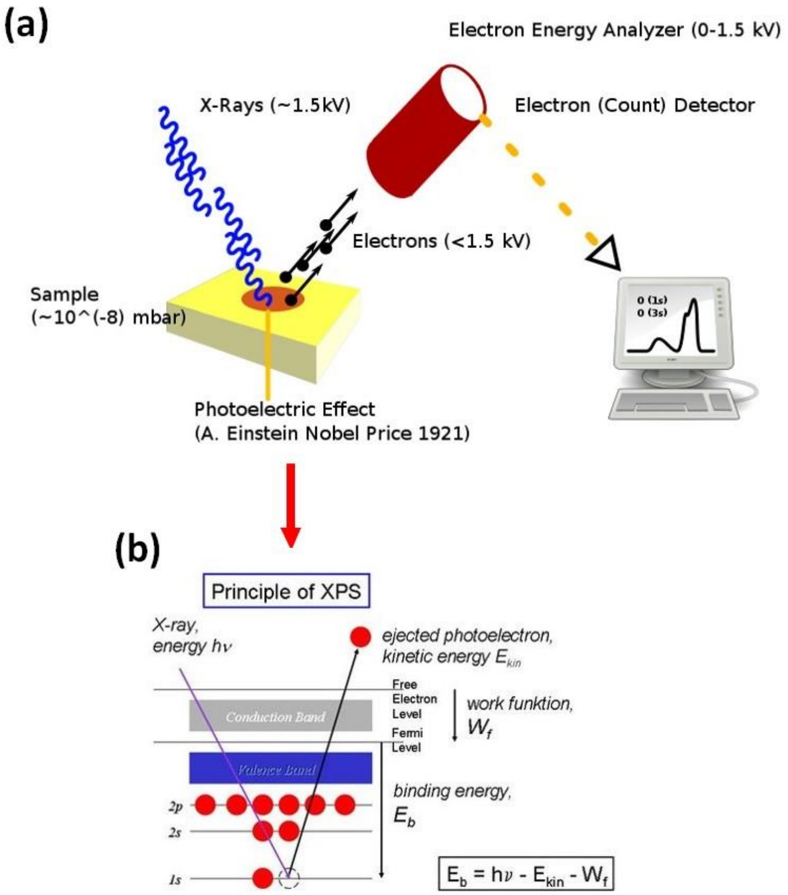

Figure 2.2 (a) Schematic illustration of the XPS mechanism; (b) Diagram of the photoionization process.

The use of XPS has increasingly advanced the field of plasma surface modification via the continual improvement of technologies that are associated with the XPS instrumentation. Some of the novelties reside in the development of new electron detectors, the use of different X-ray source (e.g. conventional soft X-ray source (Al Kα, Mg Kα), hard X-ray source (Cr Kα) with different energy values or even the combination of both Al Kα and Cr Kα monochomators (dual scanning monochromatic X-ray source)). In fact, the energy value is related to the photon energy of the monochromatic X-ray source. For example, the photon energy of a conventional monochromatic soft X-ray source (Al Kα) is 1486.6 eV while the photon energy used in hard X-ray source Cr Kα monochromators is 5 to 8 keV [72]. Due to the higher energy of the primary X-ray source compared to soft sources, information from deeper sampling depths can be obtained. And last but not the least the improvement in the electron energy analyzer. Further enhancements in XPS instrumentation can be find in previous review articles [64,73].

2.4. XPS characterization of plasma-activated polymeric surfaces

2.4.1 Determination of the surface elemental composition

In order to determine the surface elemental composition of a polymer pre- and post-plasma treatment, an XPS spectrum with a broad binding energy range (0-1100 eV) is normally recorded at a relatively low resolution (Figure 2.3). After the identification of the characteristic peaks in this so-called survey scan, the quantitative analysis is done based on the relative peak intensities expressed by the peak areas. Such data and most of the looked-for information are actually delivered by the core level binding energies [69,71]. An example is depicted in figure 2.3 that shows the XPS survey scans of a polyethylene terephthalate (PET) surface before and after air and ammonia plasma treatments in a study performed by Zheng et al.. The spectrum of the untreated sample clearly revealed the existence of 2 peaks at binding energies of 284.8 eV and 531.7 eV corresponding respectively to C1s and O1s peaks. After ammonia plasma, a new peak arose at a binding energy of 399.0 eV attributed to the N1s peak. A significant increase of the O1s peak accompanied with a moderate increase of the N1s peak were detected after air plasma treatment. When taking a look at the quantitative analysis, one can conclude that the incorporation of surface oxygen (≈ 5 % increment) upon air plasma was considerably higher than the nitrogen incorporation upon both ammonia (2.8 %) and air (0.8 %) treatments [74]. In fact, XPS results in the plethora of studies aiming at incorporating polar groups onto polymeric substrates upon exposure to nitrogen- and oxygen-containing plasmas have consistently revealed that oxygen is more abundantly and easily grafted onto the surface than nitrogen [15,20,75,76]. The work conducted by Pandiyaraj et al. who have also subjected PET films to a low pressure glow discharge operating in air is a good example confirming this deduction. The XPS survey scan results in their study have indeed shown that the surface oxygen content increased from 25.1 % to 30.1 % after 20 min of treatment while only 0.7 % of nitrogen was incorporated onto the surface [77].

Such observations have shed the light on the extremely higher reactivity of the active species derived from oxygen compared to the ones derived from nitrogen present in air. Even when plasma is sustained in N_2 or ammonia, the effectiveness of surface nitrogen functionalization can still be impeded by only water and/or oxygen traces in the reactor. As a matter of fact, working in a fully air/oxygen-free atmosphere is very hard if not impossibly achievable even at ultra-high vacuum conditions [15]. Nonetheless, the surface density of the implanted groups is greatly dependent on a wide range of process parameters such as the discharge power, the treatment time, the used plasma source, the reactor configuration, the working pressure, the discharge gas, the gas flow rate… For instance, López-Santos et al. have conducted a comparative study to examine the extent of nitrogen functionalization on low density polyethylene (LDPE) surfaces upon exposure to DBD or MW plasmas sustained in N_2 or a mixture of NH_3 + Ar at a reduced pressure. XPS results have indicated that the DBD NH_3 + Ar treatment was the most efficient in N incorporation (≈ 8 %) compared to the DBD N_2, MW NH_3 + Ar and MW N_2 treatments that have led to a surface N increase of approximately 3 %, 2% and 3 % respectively. Nonetheless, the 4 treatments have caused a significant surface oxidation illustrated by a surface oxygen content increasing from 4 % to 23 %, 32 %, 14 % and 30 % for the DBD NH_3 + Ar, DBD N_2, MW NH_3 + Ar and MW N_2 treatments respectively. This considerable oxidation was observed even after performing a pre-plasma flushing step aiming at removing the air traces by maintaining the different gas mixtures flowing for 30 min in the reactor [78]. Similar trends were spotted when replacing LDPE with PET and performing the same treatments. However, the overall surface nitrogen content was lower with, for instance, less than 1 % incorporated after DBD N_2, thus underlining the marked influence of the polymer nature on the plasma-induced chemical effects [79]. Recently, Cheng et al. have demonstrated via XPS measurements that an NH_3 + He DBD treatment conducted at medium pressure is also slightly superior than its N_2 counterpart in nitrogenizing polycaprolactone (PCL) surfaces. This is presumably due to the fact that N_2 is a weakly ionizable gas in comparison to NH_3, which results in the generation of more ions in NH_3 plasmas than in N_2 plasmas. The highly energetic ion bombardment in NH_3 plasma will in turn cause the creation of more free radicals on the polymer surface, thus explaining the more prominent nitrogen incorporation compared to N_2 plasma. Moreover, the plasma-induced dissociation of NH_3 into hydrogen atoms that end up reacting with oxygen in plasma is probably diminishing the extent of surface oxidation [11,80]. Tatoulian et al. have also detected a more pronounced nitrogen uptake on polypropylene (PP) substrates subjected to an

RF NH_3 plasma activation compared to N_2 plasma [81]. Nevertheless, despite this reported lower efficiency of N_2 plasma in nitrogen functionalization, Morent et al. were able to achieve a significant surface N amount exceeding 10 % upon exposure of PP surfaces to a N_2 DBD plasma at sub-atmospheric pressure. They have actually followed a good multi-step strategy involving pumping and flushing the plasma chamber pre-treatment to create as much as possible a reproducible N_2 environment with a low concentration of residual oxygen [15]. Vesel et al. could also incorporate more than 14 % of nitrogen versus 5 % of oxygen onto the surface of PET films after an N_2 plasma activation in an RF reactor at low pressure. When replacing the working gas with O_2, the surface oxygen was increased by more than 21 % with evidently no nitrogen incorporation [82].

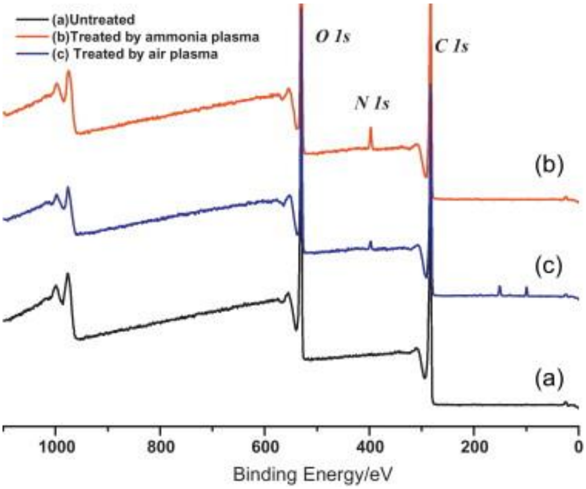

Figure 2.3 XPS survey scan spectra of PET surfaces pre- and post-plasma treatment sustained in air and ammonia [74].

Numerous authors have used noble gases with a particular dominance of argon and helium to generate plasma and treat polymeric substrates. In theory, such plasmas should create surface radicals followed by the formation of a cross-linked network. Nonetheless, XPS measurements performed in the preponderance of studies have again shed the light on the unavoidable surface oxidation occurring in- and/or post-plasma activation [20]. Jacobs et al. have indeed shown that a relatively high concentration of oxygen (≈ 10 %) could be grafted onto the surface of polylactic acid (PLA) when subjected to helium or argon DBD treatment at medium pressure. This was again attributed to the unescapable presence of oxygen traces in the reactor. The very influential role of these oxygen traces could be clearly elucidated by the fact that the exact same oxygen concentration was as well detected when the treatment was performed using air as working gas [83]. In a more recent study, Fang et al. have interestingly studied the influence of oxygen content in an argon DBD plasma by purposely adding 0.3 % and 1 % of O_2 to the feeding gas. XPS results have surprisingly revealed that the surface of PET subjected to the Ar + 0.3 % O_2 treatment presented a higher oxygen content (≈ 37 %) compared to the surface treated with Ar + 1% O_2 that exhibited an oxygen content of approximately 30 %. These results were complemented with OES measurements for a better understanding of the underlying reason. In fact, OES spectra have shown that the intensity of emission lines attributed to oxygen radicals decreased when the oxygen admixture was above 0.3 %. This was presumably due to the fact that O_2 is an electronegative gas able to adsorb electrons via attachment processes which leads to the loss of electrons in-plasma. Therefore, when the O_2 content in the discharge is larger than a certain threshold, the electron density declines considerably. As a result, the direct electron impact that generates argon metastables (capable of breaking chemical bonds) and oxygen radicals (functionalizing the surface) is depleted, thus explaining the reduced O content at high O_2 admixture [84]. Besides the use of a DBD, Wang et al. have compared the effects of a helium and an argon plasma jet on the surface chemical properties of polymethyl methacrylate (PMMA). XPS measurements have indicated an increase in the surface oxygen content from 30 % for the untreated substrate to approximately 35 % and 36 % post-exposure to argon and helium plasma respectively. A distinguished nitrogen incorporation was also detected with concentrations of approximately 2 % and 4 % on argon and helium plasma-treated PMMA respectively. OES measurements have actually shown the presence of emission lines corresponding to N_2 and N_2^+ species that were generated by the penning effect of Ar or He metastables. A higher intensity of such emission lines was observed in the He plasma due to the higher energy of He metastables compared to Ar metastables, which explained the higher potential of He plasma in nitrogenizing the surface [85].

The induced surface functionalization in all the aforementioned plasma treatments sustained in noble or reactive oxygen- and nitrogen-containing gases eventually leads to an enhanced hydrophilicity. Yet, increasing the hydrophobicity of polymeric substrates finds important applications involving, amongst others, micro fluidic devices, barrier or antifouling surfaces needed in the biomedical field, water repellent textiles, protective clothing or packaging… [86–88]. To reach this purpose, fluorine-containing plasmas can be employed and can lead, depending on the F/C ratio in the discharge, to a surface functionalization or a coating deposition via plasma polymerization of fluorocarbons. When the F/C ratio is higher than 3, plasma activation prevails over polymerization. Therefore, discharges sustained in CF_4, SF_6 and C_2F_6 gases have been used to functionalize polymers [86,88]. The effectiveness of such treatments has been recurrently validated by performing XPS measurements. For instance, Resnik et al. have compared the effects of different RF plasma treatments sustained in CF_4 and SF_6 at different pressures on the surface chemical composition of PET films. XPS results have revealed that a pressure below 130 Pa is optimal to incorporate a high amount of fluorine on the surface (46 %) subjected to the CF_4 treatment while a pressure up to 200 Pa can still graft a similar fluorine content on the surface treated with SF_6 [88].

Overall, one can conclude that a delicate tuning of the numerous working parameters should run in parallel with XPS measurements to better comprehend plasma-surface interactions on the one hand and to reach the optimal surface chemistry sought after in a particular end-application on the other hand. Table 2.1 presents a picture-perfect overview depicting the XPS surface chemical composition of polymeric substrates pre- and post-plasma treatments as acquired in some papers. The corresponding most influential parameters that have led to the reported XPS results are also displayed.

Table 2.1 Overview of literature on the surface elemental composition of polymers pre- and post-plasma activation as acquired through XPS measurements (not discussed in the text).

Authors (Year)	**Polymeric substrate**	**Reactor and working pressure**	**Working gas/ gas mixture**	**Discharge power (W)**	**XPS results: Surface chemical composition (%)**	
					Pre-plasma activation	**Post-plasma activation**
Dhayal et al. (2005) [89]	Polystyrene (PS)	RF, 2 Pa	Ar	20	C: 98.5 O: 1.5 N: 0	C: 91.98 O: 8.02 N: 0
Morent et al. (2007) [66]	Polydimethylsiloxane (PDMS)	DBD, 5 kPa	Air	6.6	C: 41.1 O: 28.1 Si: 30.8	C: 32.5 O: 36.9 Si: 30.6
Vandencasteele et al. (2008) [90]	Poly(tetrafluoroethylene) (PTFE)	RF, 6 Pa	O_2	20-70	C: 33.3 O: 0 F: 66.7	C: 45.7 O: 4.5 F: 49.8
Vesel et al. (2008) [91]	PTFE	RF, 75 Pa	N_2	200	C: 32.0 O: 0 F: 68.0	C: 35.4 O: 0.8 F: 61.1

					N: 0	N: 2.8
			O_2			C: 31.7 O: 0.5 F: 67.8 N: -
De Geyter et al. (2010) [17]	PLA	DBD, 5 kPa	Air	4.54	C: 68.2 O: 31.8 N: 0	C: 62.2 O: 37.8 N: 0
			N_2	4.84		C: 62.1 O: 31.1 N: 6.8
			Ar	1.12		C: 65.1 O: 34.9 N: 0
			He	0.82		C: 66.9 O: 30.4 N: 2.7
Shao et al. (2010) [38]	Polyimide	DBD, atmospheric pressure	Air	-	C: 75.37 O: 19.93 N: 6.7	C: 64.39 O: 27.48 N: 8.13

Vasile et al. (2011) [92]	Polyvinylidene fluoride (PVDF)	MW, 15 Pa	CO_2	50	C: 53.8 O: 2.4 N: 0.2 F: 43.2	C: 81.3 O: 7.5 N: 0.4 F: 8.8
			N_2			C: 66.1 O: 5.62 N: 2.3 F: 16.6
			N_2/H_2			C: 69.8 O: 9.05 N: 1.25 F: 21.55
Cho et al. (2011) [93]	Polyamide	MW, not specified (ns)	N_2	400	C: 75.6 O: 20.1 N: 4.3	C: 64.4 O: 29.1 N: 6.6
Hnilica et al. (2013) [94]	Polyamide 12	MW plasma jet, atmospheric pressure	Ar	150 - 350	C: 70.8 O: 24.2 N: 3.9	C: 69.6 O: 25.8 N: 4.6
			$Ar+O_2$			C: 60.9 O: 34.2 N: 4.5

			Ar+N_2			C: 56.8 O: 35.9 N: 5.5
Wang et al. (2015) [87]	PMMA	RF plasma jet, Atmospheric pressure	Ar/CF_4	3	C: 74.18 O: 24.14 F: 0	C: 68.43 O: 24.75 F: 2.24
Aziz et al. (2015) [76]	UHMWPE	DBD, 5 kPa	He	1.2	C: 99.2 O: 0.8 N: 0	C: 83.7 O: 16.2 N: 0
			N_2	11.3		C: 74.1 O: 12.6 N: 13.2
			Ar	1.2		C: 81.9 O: 18.0 N: 0
			Air	9.0		C: 81.6 O: 18.3 N: 0
Van Vrekhem et al. (2015) [65]	UHMWPE	DBD, 5 kPa	N_2	1.89	C: 95.2 O: 4.8 N: 0	C: 78.4 O: 19.3 N: 2.3

			Air	2.00		C: 75.8 O: 22.7 N: 1.5
			He	0.65		C: 83.9 O: 16.1 N: 0
			Ar	1.12		C: 76.4 O: 23.6 N: 0
Ba et al. (2016) [95]	PS	RF, 3 Pa	O_2	100-300	C: 95 O: 5 N: 0	C: 84.0 O: 16.0 N: 0
			N_2			C: 84.7 O: 13.7 N: 1.6
Terpilowski et al. (2018) [96]	Polyetheretherketone (PEEK)	(ns), 20 Pa	N_2	400	C: 84 O: 13.8 N: 0.9	C: 74.9 O: 22.0 N: 2.6
Cools et al. (2018) [97]		DBD, 5 kPa	Dry air	3	C: 76.4 O: 23.6	C: 66.8 O: 33.2 N: 0

	Poly(ethylene oxide terephthalate)/poly(butylene terephthalate) (PEOT/PBT)		Ar	3	N: 0	C: 69.5 O: 30.5 N: 0
			He	6		C: 71.4 O: 28.6 N: 0
			N_2	6		C: 65.4 O: 30.9 N: 3.7
Esbah Tabaei et al. (2020) [20]	UHMWPE	DBD, 5 kPa	N_2	0.16	C: 98.9 O: 1.1 N: 0	C: 76.6 O: 2.8 N: 20.6
			Ar	0.25		C: 94.1 O: 5.9 N: 0
Ma et al. (2021) [51]	PET	RF, atmospheric pressure	Ar	30	C: 77.3 O: 22.7 N: 0	C: 67.3 O: 31.4 N: 1.3

2.4.2 Identification of surface chemical bonds via curve fitting

In addition to the rudimentary determination and quantification of the surface elemental composition, XPS is characterized by a strength implicating the identification of chemical state changes occurring at a surface of a sample [16,17,65,66]. In fact, the exact core level binding energy varies for each atom depending on its local bonding situation that engenders chemical shifts. These shifts, usually ranging between fractions of an eV to a few eV, are due to the electron transfer occurring between 2 atoms forming a bond with one of them becoming more negative and the other more positive. This results in the broadening of the XPS peaks that can be fitted to extract information on the nature of bonds present on the surface [13,20,33,98,99]. A curve fitting model is in general delineated by several component peaks and a background algorithm. The component peaks are defined making use of lineshapes and a number of fitting parameters that can modify a component peak in different ways. The lineshapes are mathematical functions such as the Lorentzian, Gaussian or the mix of both “Gauss-Lorentzian” functions [100,101]. The differences and the followed ways to choose between these functions are elaborately described in a previously published book [101]. The fitting parameters of importance include the full width at half maximum (FWHM), position, area, Lorentzian character and/or Gaussian character and degree of asymmetry of each component peak. The photoemission peaks can exhibit different lineshapes ranging from narrow, symmetric and simple structures to wide and more complex structures typically reflecting a number of oxidation states. The series of component peaks are combined and adjoined to a background to approximate the initial data envelope. For an accurate identification of surface chemical bonds, a narrow binding energy frame localized around a particular XPS peak of a certain element is recorded with a high resolution and small binding energy step size. The quantitative characterization of the identified chemical states implies the measurement of the relative area of each corresponding component peak. Some requirements accompany these calculations such as the need to separate the zero energy-loss signals from the inelastically scattered background [100,102]

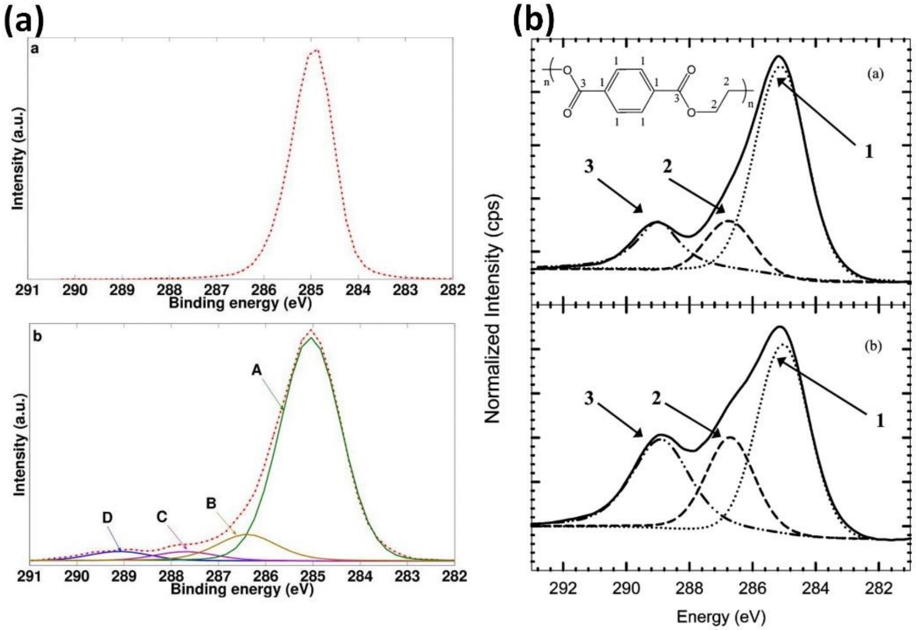

Figure 2.4 Fitting of high resolution C1s peaks of (a) UHMWPE pre- and post-Ar DBD plasma treatment and (b) PET pre- and post-He/O_2 RF plasma treatment (top C1s curves: untreated surfaces; bottom C1s curves: plasma-treated surfaces) [76,103].

Given the multifaceted plasma environment leading to the surface incorporation of several functional groups, a treated polymeric surface tends to involve an intricate chemical environment producing a complex envelope. Depending on the used plasma atmosphere and the initial substrate chemistry, diverse chemical shifts and large differences in component peak intensities of the high resolution carbon (C1s) spectrum can occur [34,76,103]. An example of such chemical shifts and peak intensity differences can be discerned in Figure 2.4 (a) and (b) respectively. Figure 2.4 (a) depicts the C1s curves of an untreated UHMWPE surface and its counterpart subjected to an argon DBD plasma ignited at medium pressure (50 mbar) as was shown in a study of Aziz et al.. The C1s curve of the untreated surface exhibited a relatively narrow peak centered at 285.0 eV corresponding to the C-C/C-H bonds. After Ar plasma, a broadening of the curve accompanied with the occurrence of new component peaks corresponding to C-O, C=O and O-C=O bonds could be perceived. The C1s curve fitting results have revealed a decrease in the relative concentration of C-C bonds and a higher concentration of newly formed C-O bonds compared to C=O and O-C=O bonds [76]. Figure 2.4 (b) shows the C1s curve fitting of PET surfaces as analyzed by

Gonzalez et al. pre- and post-plasma treatment performed using a He/O_2 RF reactor operating at atmospheric pressure. A decreased relative amount of C-C/C-H bonds with parallel increased amounts of C-O and O-C=O bonds were detected after treatment. It is worth mentioning that the fitting did not show any component peak attributed to C=O bonds which can be due to the initial exclusion of this peak during the fitting process or to its actual absence in the PET surface structure post-treatment [103]. This second assumption would be more credible since De Geyter et al. have purposely shed the light on the fact that PET surfaces, unlike PP surfaces, could not incorporate C=O bonds after subjecting them to air, He and Ar DBD treatments at medium pressure. This observation have elucidated the fact that the nature of functional groups grafted onto a surface upon plasma treatment is highly dependent on the used type of polymer. The C1s curve fitting results is this afore-introduced comparative study have helped De Geyter et al. to draw some conclusions and gain some deeper understandings on the surface chemical interactions leading to the incorporation of the detected bonds on PP surfaces. Firstly, air plasma treatment could lead to a higher incorporation of oxygen-containing functionalities namely C-O and O-C=O onto PET surfaces and C-O, C=O and O-C=O onto PP surfaces than Ar and He plasmas. This observation was evidently accompanied with a decrease in the concentration of C-C/C-H bonds which is mainly due to the fact that UV photons, OH radicals and oxygen atoms formed in air plasma can abstract secondary hydrogen from the PP chains atoms forming alkyl radicals. Such radicals can then interact with ozone and atomic oxygen triggering the formation of alkoxyl radicals. The alkoxyl radicals will then in their turn react with reactive molecular and atomic species engendering the generation of C–O, C=O and O-C=O bonds on the PP surface. The exact mechanisms leading to the surface oxidation of PET films without exhibiting the grafting of C=O bonds was not known in detail [34]. Nonetheless, plasma-induced surface radicals will generally follow, depending on the polymer nature and the plasma parameters, different oxidation pathways in which they interact with chemically reactive species. This will therefore lead to the incorporation of different functional groups at different surface densities [20,34,75,76,103,104]. Slightly different chemical pathways normally occur in plasmas ignited in inert gases such as He and Ar. A first comparable step involves the formation of carbon radicals via the breakage of C-C or C-H bonds by the ions and UV photons present in the discharge. Given the existence of oxygen traces into the reactor, the expected cross-linking reactions between the formed radicals will be combined with surface oxidation pathways. This cross-linking will enter in a competition with the oxidation, leading to a slower incorporation of oxygen-containing groups, which can explain their lower concentrations on He and Ar plasma-treated PP and PET compared to their air-treated counterparts [26,34,42]. For all plasma treatments, an easier incorporation of C-O bonds was detected on both the PP and PET surfaces compared to O-C=O and C=O (only for PP) bonds that exhibited lower concentrations [34]. This trend was recurrently detected via C1s curve fittings when subjecting PET, PP and other polymers such as PCL, UHMWPE and LDPE to a low, medium or atmospheric pressure DBD, plasma jet or RF treatment operating in air, O_2, argon or helium [33,53,65,84,105–109]. However, an opposite trend implicating the incorporation of more O-C=O and/or C=O bonds compared to C-O bonds was perceived mainly for other plasma-treated polymers such as PLA, PEOT/PBT and PMMA but also for some of the previously mentioned polymers subjected to different plasma conditions [83,97,110–113]. These observations can again highlight the dependency of the surface oxidation processes on the initial polymer structure on the one hand and the use of various plasma parameters on the other hand. For instance, Cools et al. have concluded after performing C1s analyses that the C-O surface content of PEOT/PBT films subjected to air, Ar and He DBD plasmas remained constant or even decreased while the relative concentrations of O-C=O and C=O increased. This was therefore presumably attributed to a rivalry between the incorporation of newly-formed C-O bonds and the preferential plasma etching of the soft PEOT segment triggering a C-O bond depletion from its backbone [97]. Another example involves the MW plasma treatment of PMMA using Ar + H_2O at atmospheric pressure which incorporated a much higher concentration of surface O-C=O bonds compared to C-O bonds. Based on the performed C1s analyses, the author Adbel-Fattah has anticipated and portrayed some possible plasma-surface reactions leading to the chain scission and functionalization processes of PMMA (Figure 2.5) [111]. It is worth mentioning that the C1s curve fittings of the last 2 afore-cited articles have included an additional component peak at binding energies of 285.8 and 286.0 eV corresponding to C-C=O bonds that were very rarely considered in other studies [97,111]. In a study conducted by Ghobeira et al., the insertion of a component peak due to C-COO at 286.5 eV in the fitting of C1s spectra measured on PCL films subjected to an air DBD treatment has provided some extra interesting information. In fact, at extended treatment times, the relative concentration of O-C=O bonds have significantly exceeded that of C-COO bonds which confirmed the pronounced random chain scissions and was indicative of PCL degradation [114].

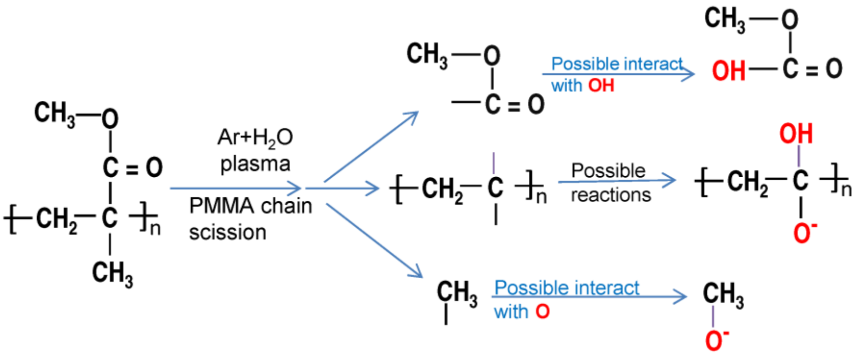

Figure 2.5 Possible chemical pathways occurring at the surface of PMMA upon exposure to an MW Ar + H_2O plasma treatment [111].

This unsystematic inclusion or exclusion of the C-COO component peak in the fitting of the C1s spectrum is one example underlining the absence of a distinctive clear-cut method to perform XPS fitting. Another prominent example highlighting curve fitting inconsistencies in literature is the positioning of the same component peaks at different binding energies within the C1s envelope. Table 2.2 depicts such big discrepancies in the binding energies attributed to different chemical bonds and adopted in a number of papers implicating the curve fitting of C1s spectra measured on plasma-activated polymers. It can be also clearly noted from the table that the peak positions of carbon-nitrogen bonds are very close or mostly overlapping with carbon-oxygen bonds which makes their mathematical separation in a good fitting model within decent error bars impossible. Given the inevitable surface oxygen incorporation upon treatment in nitrogen-containing discharges such as N_2 and NH_3, a decisive answer to define the grafted functionalities from C1s fittings is not as straightforward [15,82]. Some authors have over-simplified the fitting process by attributing only one peak to C–N, C=N, C–O and C≡N bonds and another peak to C=O and N-C=O, while others have considered 2 separate peaks for C-N and C-O bonds [11,17,20,99]. Figure 2.6 depicts a good example in which the C1s curve of PCL substrates subjected to relatively similar N_2 and NH_3/He DBD treatments have been fitted with a different number of component peaks and slightly different peak positions [11,99]. It is also very challenging to draw indubitable conclusions about the surface chemical processes leading to the grafting of nitrogen functionalities from the fitting of the N1s curve. In fact, an N1s spectrum is typically composed of one broad symmetric peak located at a binding energy of approximately 399.7 eV, which can be accredited to several nitrogen states such as C-N, O=C-N, C-N, C≡N… Nonetheless, given the fact that nitrogen cannot be easily incorporated onto surfaces upon their exposure to plasma, some authors have assumed that it is only existent under the form of single bonding to carbon (C-N) [15,82]. Other authors have supposed that surface nitrogen is also present under the form of amides that can be generated in-plasma or via post-plasma interactions with the surrounding O_2 [20,79,92]. In fact, it is believed that nitrogen-containing discharges engender, like other discharges, the breakage of C-H and C-C bonds thus forming surface radicals that will in turn interact with atomic and metastable nitrogen states to form nitrogen-containing functionalities namely amine groups. The continuous C-C cleavage would then lead to the generation of radicals at the α-amino carbons. The formed radicals are expected to interact with the surrounding O_2 triggering the formation of peroxy radicals that can recombine in pairs thus generating amides [20].

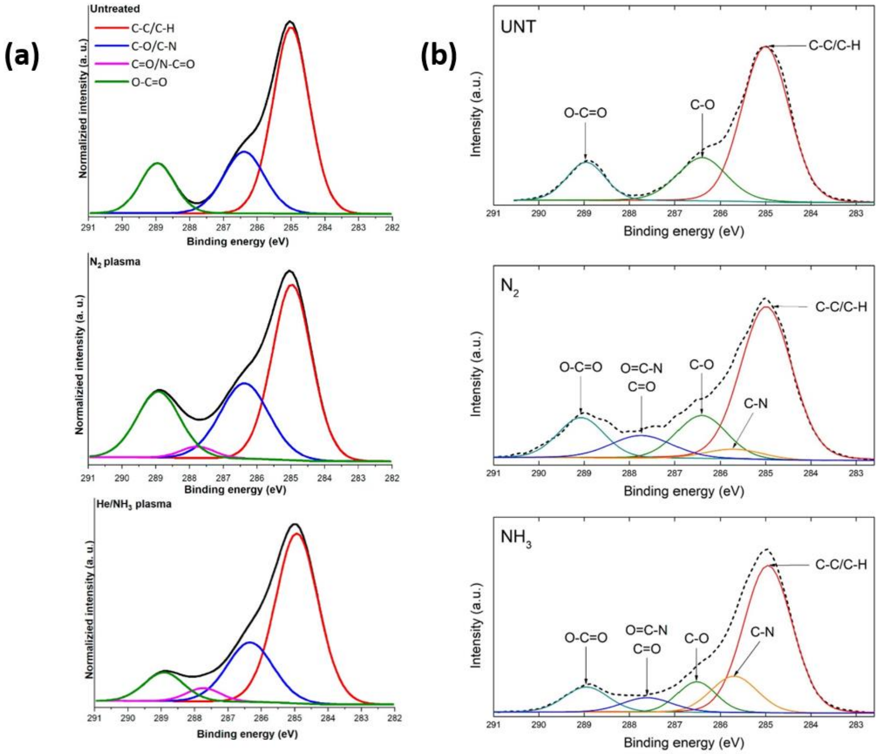

Figure 2.6 Different peak fitting methodology applied to high resolution C1s curves of untreated, N_2 plasma-treated and NH_3/He plasma-treated PCL [11,99].

When taking a look at the C1s curve fittings that were conducted in literature for polymers subjected to a fluorine-containing plasma passivation, similar complications could be faced. First of all, large binding energy divergences can be perceived for the numerous fluorine-containing carbon groups that can be grafted onto the surface. Secondly, many possible CF_n, $C\text{-}CF_n$ and $CF_n\text{-}CF_n$ combinations can be present. Thirdly, an accurate separation between C-F and $C\text{-}CF_n$ component peaks and oxygen-containing peaks can be quasi-impossible due to some overlapping. Nonetheless, CF_2 and CF_3 peaks might be more easily distinguished since their binding energies are generally above 290 eV which is the range that does not interfere with most of the plasma-induced oxygen functionalities [86,88,115,116].

To sum up, despite all recent computational advancements and the generation of several superior software resources, it has been very problematic to develop a chemically eloquent curve fitting methodology. This has inevitably led to the publication of biased conclusions about plasma-induced surface chemistry. A recent publication presenting some guidelines on how to avoid the erroneous application of XPS curve fittings has reported that roughly 70 % of the papers that have performed XPS measurements have included some kind of curve fitting. Based on the extensive literature overview performed in this chapter, a similar or even a higher percentage could be extrapolated to papers involving plasma activation of polymeric surfaces. Moreover, it was reported in the XPS guide that bad curve-fitting practices accompanied with misconceptions were detected in more than 30 % of the checked papers [100].

A proposed route to resolve the ambiguities associated with XPS curve fittings and facilitate the interpretation of XPS spectra can be usage of valence band spectra [69,117]. Additionally, chemical derivatization prior to XPS measurements can be as well a very useful solution triggering a more precise identification of surface functional groups and their relative concentrations. This approach is commonly used in literature as a complementary technique for the characterization of plasma-activated polymers and will therefore be the subject of the next paragraph.

Table 2.2 Binding energies of C1s component peaks as attributed to different chemical bonds upon surface plasma activation in literature.

C1s binding energy (eV)	Corresponding chemical bond	Reference
284.6	$\underline{\mathrm{C}}$-C/$\underline{\mathrm{C}}$-H	[95]
284.7	$\underline{\mathrm{C}}$-C/$\underline{\mathrm{C}}$-H	[38,98]
284.8	$\underline{\mathrm{C}}$-C/$\underline{\mathrm{C}}$-H	[88]
285.0	$\underline{\mathrm{C}}$-C/$\underline{\mathrm{C}}$-H	[13,14,114,16,20,33, 47,75,76,97,99]
285.3	$\underline{\mathrm{C}}$-C/$\underline{\mathrm{C}}$-H	[49]
285.5	$\underline{\mathrm{C}}$-COO	[114]
285.6	$\underline{\mathrm{C}}$-N	[38]
285.9	$\underline{\mathrm{C}}$-N	[14]
286.0	$\underline{\mathrm{C}}$-O	[47]
286.0	$\underline{\mathrm{C}}$-C=O	[97]
286.1	$\underline{\mathrm{C}}$-N/$\underline{\mathrm{C}}$-O	[13,62]
286.2	$\underline{\mathrm{C}}$-O	[95]
286.3	$\underline{\mathrm{C}}$-O/$\underline{\mathrm{C}}$-N	[38,76,98]
286.8	$\underline{\mathrm{C}}$-O/$\underline{\mathrm{C}}$-N	[97]
286.4	$\underline{\mathrm{C}}$-O	[99]
286.5	$\underline{\mathrm{C}}$-O	[14,33,75,88,114]
286.5	$\underline{\mathrm{C}}$-CF	[88]
286.5	$\underline{\mathrm{C}}\equiv\mathrm{N}$/ $\underline{\mathrm{C}}=\mathrm{N}$	[14]
286.6	$\underline{\mathrm{C}}\text{-CF}_n$	[115]
286.7	$\underline{\mathrm{C}}$-O	[13,49]
287.1	$\underline{\mathrm{C}}\text{-CF}_n$	[116]

287.4	$\underline{C}$=N	[62]
287.5	$\underline{C}$=O	[62]
287.7	$\underline{C}$=O	[33,114]
287.8	$\underline{C}$=O/$\underline{C}$F	[76,98,115]
287.9	$\underline{C}$=O	[47,99]
288.0	$\underline{C}$=O/O-$\underline{C}$-O	[13,49]
288.0	$\underline{C}$=O/ N-$\underline{C}$=O	[14]
288.3	$\underline{C}$=O/ $\underline{C}$=N/ N-$\underline{C}$=O/ O-$\underline{C}$-O	[20]
288.6	$\underline{C}$=O	[38]
288.9	O-$\underline{C}$=O	[62]
289.0	O-$\underline{C}$=O	[16,47,76,88,98]
289.0	$\underline{C}$F	[88]
289.0	N-$\underline{C}$=O	[97]
289.1	O-$\underline{C}$=O	[13,33,114]
289.2	O-$\underline{C}$=O	[98]
289.3	$\underline{C}$F-CF$_n$	[115]
289.5	$\underline{C}$-F	[116]
289.6	O-$\underline{C}$=O	[104]
291.2	$\underline{C}F_2$	[115]
291.3	$\underline{C}F_2$	[88]
293.0	$\underline{C}F_3$	[88]
293.6	$\underline{C}F_3$	[115]

2.4.7 Detection of protein immobilization via XPS analyses

Plasma-activated polymeric surfaces have earned a prominent place within the biomedical field for their ability to immobilize biologically active molecules [99,118]. In fact, some of the plasma-induced functionalities such as carboxyl, hydroxyl, amine and aldehyde groups were proven to possess a great potential to covalently bind proteins [119]. Some proteins are well-known to act as binding sites for cell receptors thus promoting cell adhesion on the underlying surface and subsequent crucial cell performances such as growth, proliferation, migration and differentiation [99]. A protein is a series of amino acids synthesized within the cell and folded inside or outside the cell depending on its complexity and size. The functionality of a certain protein is determined by its amino acid structure and spatial configuration [120]. The interactions that can occur between functional groups present on the surface of proteins and the ones present on a plasma-activated surface are eventually responsible for the immobilization of the proteins on the surface. Nonetheless, the density of plasma-induced functional groups should be carefully controlled as an excessive density can result in an unfolding of the characteristic structure of the protein and thus the loss of its biological role [99]. For instance, it was previously reported that surfaces solely enriched with oxygen-containing functionalities and exhibiting a moderate hydrophilicity are deemed to trigger a more effective protein adsorption compared to surfaces enriched with both nitrogen- and oxygen-containing functionalities and exhibiting a super-hydrophilicity [99]. XPS analyses were therefore frequently conducted to detect the density of grafted functional groups on plasma-activated polymeric surfaces pre-immobilization of proteins [99,118]. Nonetheless, in order to make sure that proteins are successfully bound to such plasma-induced functional molecules, few researchers have again performed XPS measurements post-protein immobilization [90,92,121]. For instance, Kasálková et al. have immersed untreated and argon plasma-treated PLA and PE surfaces into a solution of bovine serum albumin (BSA) in an attempt to evaluate the efficiency of protein attachment on the different surfaces. To do so, XPS measurements were conducted pre- and post-immersion into the protein solution. Results have revealed a significantly increased and comparable nitrogen content on both plasma-treated PLA and PE surfaces post-BSA immersion which actually confirmed the successful BSA grafting onto the surface. XPS spectra of untreated surfaces did not exhibit an N1s signal thus highlighting the failure in protein attachment. As such, these observations could corroborate the importance of plasma-induced functionalities in binding proteins onto a surface and therefore stimulating cell attachment and proliferation [121]. Vasile et al. have subjected hydrophobic polyvinylidene fluoride (PVDF) films to N_2, N_2/H_2 and CO_2 plasmas in order to incorporate carboxylic and amino groups onto their surface and as such enhance protein immobilization. Two proteins namely triglycine (TG) and protein A were then chemically immobilized via 1-ethyl-3-(-dimethylaminopropyl) carbodiimide/*N*-hydroxysuccinimide (EDC/NHS) coupling chemistry reactions or simply adsorbed onto plasma-treated surfaces. The changes in the N1s and O1s signals depicted by XPS survey scans and the variations in the component peaks corresponding to C-N, O=C-N and O=C-O groups detected upon fitting of high resolution C1s spectra highlighted the effective immobilization of both proteins. It was however perceived that TG was better grafted on N_2/H_2 plasma-activated surfaces, while protein A was more firmly anchored on N_2 and CO_2 plasma-treated surfaces. These interesting results have drawn the attention to the fact that a distinctive surface chemistry is required for the optimal immobilization of every protein type [92]. An opposing interest in generating antifouling surfaces having protein-resistant properties has grown in parallel within the biomedical field given the frequent use of such surfaces in several applications requiring, amongst others, a repelled cellular and bacterial adhesion [87,90,122]. Polymeric surfaces exhibiting a super-hydrophobicity are normally adopted in such applications. For instance, in order to obtain a protein-resistant surface, Vandencasteele et al. have firstly selected the polymer PTFE having a fully fluorinated backbone prompting its native hydrophobicity. In an attempt to further enhance the polymer hydrophobicity, a carefully controlled O_2 plasma treatment aiming at only increasing the surface roughness via etching processes was then performed. Nonetheless, O_2 plasma was accompanied with a high risk of changing the surface chemical composition, decreasing the hydrophobicity and eventually promoting protein adhesion. Therefore, in order to probe the treatment efficiency in repelling proteins, untreated and plasma-treated surfaces were immersed in a BSA solution. XPS measurements could detect the occurrence of BSA adsorption via 3 observations: 1) a decrease in the fluorine content and an increase in the oxygen content, 2) the appearance of an N1s signal originating from the protein structure and 3) the emergence of protein-related component peaks corresponding to C–N, C–O and N–C=O bonds in the C1s spectra. Results suggested that surfaces treated with low plasma powers could adsorb slightly more proteins (N: 5 at.%) compared to untreated surfaces (N: 3 at.%). However, a less pronounced protein adsorption (N: 1-2 at.%) was detected on surfaces treated with high plasma powers because of a marked etching effect and a resulting increase in roughness [90].

To sum up, this chapter was dedicated to provide an extensive overview on the different XPS measurement capabilities applied to chemically characterize plasma-activated polymeric surfaces. The limitations associated with some of the reported XPS analyses were also comprehensively discussed. Several acquaintances on plasma-surface interactions were as such reaped. Overall, this chapter constitutes a perfect-picture reference for all future studies involving a plasma activation of polymers. Nonetheless, in all the reported papers, XPS measurements were carried out post-exposure of the treated samples to ambient air thus making it impossible to draw definite conclusions and to make clear distinctions between in-plasma and post-plasma surface interactions. Moreover, all discussed XPS results were obtained within a short time range post-plasma treatment. Therefore, the well-known ageing effect of plasma-activated surfaces occurring upon longer storage periods was not yet deeply tackled. In view of the above, the following chapter will be specifically devoted to provide the reader with a profound knowledge on in-plasma surface interactions and surface ageing processes via a literature overview involving XPS analyses undertaken *in situ* or after relatively prolonged storage times.

Chapter 3. Characterization of exclusive in-plasma processes versus ageing processes occurring at plasma-treated polymeric surfaces via *in situ* and *ex situ* XPS analyses

3.1 *In situ* XPS measurements

In order to better comprehend plasma-polymer surface interactions, numerous research groups have been extensively employing, amongst other plasma diagnostic tools and surface analytical techniques, XPS analyses. This has led, as already reported in Chapter 2, to the potential identification and quantification of chemical interactions occurring between various plasma discharges and a selection of polymeric substrates with a varying amount of success [15,32,33,37,41,47,99,123,124]. To date, there are still two different scientific points of view on how the majority of oxygen is incorporated onto a polymeric surface after treatment with plasma discharges that do not contain oxygen (helium, argon and N_2 discharges being the most popular ones). Some literature has reported that during plasma exposure in an oxygen-free atmosphere, the active species in the plasma would primarily produce carbon radicals on the polymer surface through hydrogen abstraction. Following plasma treatment, oxygen-containing functionalities would then be incorporated onto the polymer surface due to the reaction of those surface carbon radicals with reactive oxygen molecules (O_2 and H_2O) during exposure to ambient air [47,61,62,125]. On the other hand, other researchers have argued that oxygen functionalities are directly built in on the polymer surface during plasma exposure due to small oxygen impurities being present in the discharge atmosphere, suggesting that post-plasma interactions are of less importance [15,26,34]. For example, Massines et al. have observed that by adding only 0.2 % of oxygen to an N_2 plasma, the oxygen incorporation on a PP surface doubled while the nitrogen incorporation significantly decreased [42]. In a first attempt to clarify this, Borcia et al. have examined the effect of a nitrogen DBD treatment on the surface of UHMWPE in a controlled atmospheric pressure gaseous environment, unsuccessfully trying to overcome the dominant effect of reactive oxygen plasma species which are typically present in the discharge region due to air contamination. They have concluded that the incorporation of oxygen directly occurred on the UHMWPE surface during plasma exposure due to the very high reactivity of unwanted oxygen species in the discharge, even at very low concentrations. Consequently, these researchers have also concluded that post-plasma reactions are unlikely to occur [75].

In most available literature on plasma activation of polymers, almost all XPS measurements of plasma-treated polymers were carried out after exposing the treated samples to ambient air prior to XPS analysis, hence making it impossible to distinguish between in-plasma and post-plasma oxygen incorporation. At this moment, there are only very few studies in literature dealing with the direct XPS characterization of plasma-modified polymer surfaces i.e. without air exposure between the performed plasma treatment and subsequent XPS analysis. In this limited amount of studies, direct XPS analysis was conducted either by making use of a transfer vessel or by connecting the plasma set-up directly to an XPS machine [47,48,58,61,62,89,126–128]. Additionally, these studies have also mainly focused on low pressure plasma activation of polymers. For example, Mutel et al. have treated the surface of PP with a low pressure pure N_2 MW plasma after which the plasma-modified PP samples were directly analyzed in an XPS machine without exposure to ambient air (base pressure of the plasma reactor: 2 Pa). The authors have observed a high nitrogen content (≈16 at%) on the PP surfaces in combination with an even higher oxygen content (≈ 22 at%). Based on their results, the authors have concluded that oxygen incorporation occurred during the nitrogen plasma treatment step because of the presence of oxygen-containing impurities in the nitrogen flow, on the reactor walls and/or in the commercial PP film [126]. Shi et al. have also performed a low pressure N_2 MW plasma activation of PET that initially contains oxygen in its backbone (base pressure of the plasma reactor: 1.3×10^{-3} Pa). *In situ* XPS results have revealed that this "pure" N_2 plasma did not trigger a significant incorporation of surface nitrogen (≈4 at%). In fact, C1s curve fittings have demonstrated the simultaneous occurrence of a plasma-induced destruction of original oxygen-containing functionalities (mainly ester and ether groups) and a formation of amide and amine groups. Nitrogen atoms were actually proven to favorably attach to oxygen bonded carbon sites leading to the formation of amide structures. Nonetheless, the density of the newly incorporated functional groups was negligible compared with that of the removed ester and ether groups. This observation has indicated that the loss of oxygen functionalities took place mainly through the elimination of the entire groups containing nitrogen, hence the final low surface nitrogen content [128]. In 2 earlier studies, Gerenser has employed a low pressure (6.7 Pa) plasma sustained in Ar, O_2, and N_2 atmospheres (base pressure of the plasma reactor: 6.7×10^{-7} Pa) to modify the surface properties of different polymers. Based on the obtained *in situ* XPS results, the author has reported that the performed Ar plasma treatment did not introduce new chemical species onto the polymer surfaces, but could induce a surface degradation and a rearrangement of polymeric chains. On the other hand, both O_2 and N_2 plasma treatments led to the formation of new chemical species which noticeably altered the chemical reactivity of the polymer surfaces. For example, it was observed that on a PS surface, oxygen and nitrogen plasma treatment resulted in the incorporation of 18 at% of oxygen and 15 at% of nitrogen respectively [61,62]. After subjecting HDPE to an Ar RF plasma activation (base pressure of the plasma reactor: 10^{-6} Pa), Øiseth et al. have as well performed a comparative study between in-plasma and post-plasma surface modification via *in situ and ex situ* analyses. [47]. The *in situ* XPS characterization has confirmed the Ar plasma ability to achieve a clean modification without oxygen incorporation, similar to what was observed by Gerenser. On the contrary, *ex situ* XPS results have demonstrated that by exposing Ar plasma-modified samples to ambient air, the surface oxygen content could reach 13 % thus highlighting the pronounced effect of post-plasma oxidation [47]. In a later study, Dhayal et al. have also carried out *in situ* XPS analysis of Ar plasma-modified PS surfaces (base pressure of the plasma reactor: 5 x 10^{-3} Pa) [89]. These authors observed, in contrast to Gerenser and Øiseth et al., a significant oxygen incorporation on the PS surface due to the Ar plasma exposure. Based on this literature overview, it seems that the base pressure of the plasma reactor plays a crucial role in whether oxygen incorporation at the polymer surface directly occurs during plasma exposure. At considerably low plasma reactor base pressures (order 10^{-6}-10^{-7} Pa), oxygen is not incorporated during plasma treatment in Ar or N_2, while at higher base pressures (10^{-3} Pa, 2 Pa), oxygen incorporation directly occurs during Ar/N_2 plasma exposure.

Nonetheless, despite the use of a MW reactor with a relatively high base pressure (10^{-3} Pa), Lianos et al. have attempted to precisely unravel the exact oxidation mechanisms occurring on the surface of O_2 plasma-treated surfaces without the interference of the surrounding air. To do so, *in situ* XPS measurements were executed on the surface of three different treated polymers namely LDPE, PS and PMMA. Based on the obtained results, the authors have discerned the fundamental role of ground state atomic oxygen O(^{3}P) in initiating surface polymeric oxidation. These species are responsible for the formation of free radicals that most likely react with singlet state molecular oxygen to graft highly oxidized functionalities on the polymer surface [127].

3.2 Ageing effect processes post-plasma activation of polymers

Once plasma-activated, polymeric surfaces were evidenced to possess a tendency to retrogress towards their initial untreated state by lowering their surface free energy in a well-recognized phenomenon: the so-called "ageing effect" or "hydrophobic recovery" [26,129,130]. Nonetheless, the few available comparisons between *in situ* and *ex situ* XPS results have validated the foreseeable immediate occurrence of particular post-plasma oxidation processes upon exposure to ambient air, which actually increase the surface energy [20,47]. These pronounced short-term processes leading to a further incorporation of more surface oxygen functionalities were actually attributed to reactions between O_2 and other oxygen-containing molecules present in the surrounding atmosphere and plasma-induced carbon-centered radicals [20,47]. Above a certain storage time, physical processes start progressively overcoming chemical processes thus eventually triggering a retrogressed surface polarity or ageing. In fact, pre-induced oxygen- and nitrogen-containing groups have a propensity to migrate away from the surface via chain reorientation or diffusion towards the material bulk in order to adopt more energetically stable locations [47,129]. Several authors have actually corroborated these physical incidents occurring between the surface and sub-surface regions by performing ARXPS measurements at different post-treatment storage times [131–133]. For instance, Wang et al. have subjected chitosan membranes to a low pressure oxygen plasma treatment after which they have analyzed the distribution of the induced polar groups within the sub-surface region at day 15 post-treatment. Firstly, initial XPS measurements have elucidated the presence of a pronounced ageing effect illustrated by a significant decrease in the C-O bond intensity on aged samples compared to their freshly-treated counterparts. Thereafter, ARXPS measurements have been performed on the aged samples with take-off angles ranging from 15° to 90° in order to unravel the exact causes behind this behavior. C1s curve fittings have revealed that when decreasing the take-off angle, a progressive decrease in the C-O bond concentration accompanied with an increase in the C-C bond density occurred (Figure 3.1). These analyses could therefore lead to the assumption that a redistribution of C-O groups towards the bulk of the membranes is responsible for the ageing effect [131]. A similar conclusion was also drawn by Haïdopoulos et al. who have carried out comparative ARXPS measurements on freshly O_2 plasma-treated and one week aged PS substrates. A loss in the oxygen content was observed at the topmost surfaces of the aged samples that in fact exhibited more oxygen in deeper locations compared to the fresh samples [132]. Kim et al. have interestingly established a direct correlation between the crystallinity of plasma-treated surfaces and their ageing behaviors via ARXPS analyses. A pronounced ageing effect illustrated by a significant and rapid decrease in the topmost surface concentration of C-O bonds was detected on O_2 plasma-treated LDPE substrates of low crystallinity (quenched LDPE). Nonetheless, annealed LDPE substrates characterized by a higher crystallinity underwent a slower and less prominent movement of C-O groups towards the bulk. This was basically accredited to the smaller free volume limiting the mobility of plasma-induced functionalities and as such their diffusion and/or reorientation towards the bulk [133].

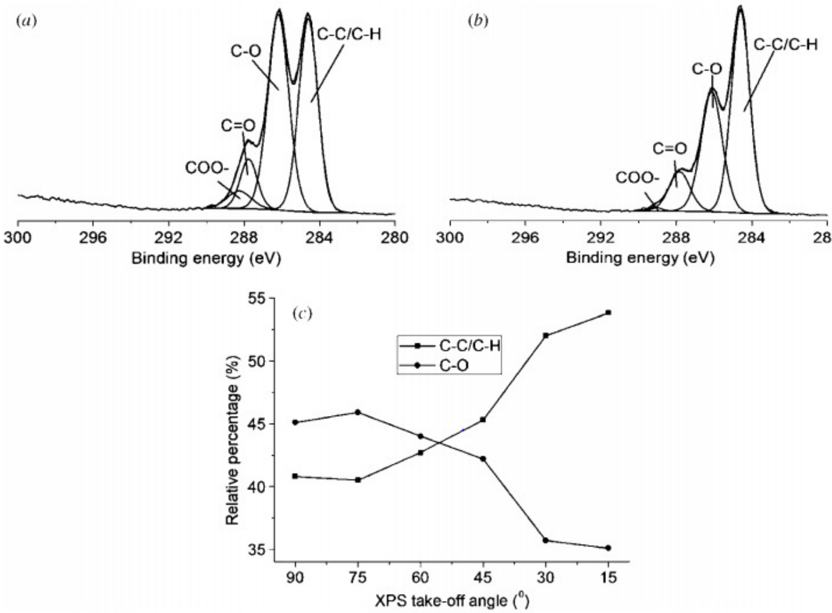

Figure 3.1 High resolution C1s curve fitting results of aged chitosan membranes 15 days post-oxygen plasma treatment. (a) Take-off angle of 90°; (b) Take-off angle of 30°; (c) Evolution of C-C and C-O relative percentages as a function of the XPS take-off angle [131].

In contrast to what was observed in most of the ageing studies involving ARXPS measurements, Dufour et al. have perceived a uniform loss in oxygen as a function of depth in He/O_2 plasma-activated HDPE surfaces one month post-treatment. This outcome has implied that the ageing was not caused by a rearrangement of the polar groups in deeper layers but by an opposite upward diffusion of plasma-induced low molecular weight oxidation materials (LMWOMs) towards the surface. Such small fragments, being likely volatile, were most probably detached from the surface and lost in the ambient air [134]. In an earlier study, a quite similar out-diffusion of free chains was as well presumably causing the ageing effect of air plasma-modified PDMS films. In fact, XPS depth profiles have indicated that a large fraction of plasma-induced silanol functionalities was still present in the initially modified region. As such, the ageing behavior was not due to the reorientation or inward diffusion of silanol groups, but to an opposite migration of free PDMS chains into the oxidized layers [66].

In two subsequent studies, Morent at al. have elucidated the influence of the working gas used during the plasma activation of polymeric surfaces on their eventual ageing behavior. To do so, 3 different polymers namely PP, PET and PLA were subjected to a DBD plasma treatment operating in air, helium and argon at medium pressure. XPS measurements demonstrated a loss in the treatment efficiency of 29 %, 34 % and 39 % for argon, helium and air plasma-treated PET and 25 %, 35 % and 47 % for argon, helium and air plasma-treated PP respectively. A similar trend in ageing prominence was as well detected on PLA surfaces. These significant differences were associated with the different cross-linking degrees triggered by the different discharge gases on the polymeric surfaces. In fact, argon plasma treatment instigated the highest cross-linking degree which restricted the plasma-induced chain movements and thus obviated their reorientation towards the material bulk. Helium plasma treatment exhibited a slightly lower cross-linking degree leading to more mobile groups translating in the sub-surface region. Finally, air plasma treatment known for its low cross-linking degree provoked a pronounced ageing behavior because of the high number of mobile plasma-induced functionalities [26,129]. In a more recent study, Ghobeira et al. have obtained comparable results when investigating the ageing behaviors of PCL films subjected to argon and air DBD treatments. Next to the discharge gas importance, the authors have highlighted the significant and simultaneous influence of the plasma exposure time on the eventual ageing process. In fact, a slight increase in the air plasma exposure time leading to the same initial surface elemental composition could slightly curtail the pronounced ageing effect. This was attributed to the potential ability of air plasma to trigger a higher cross-linking with time. An inverse effect was however detected upon prolonged argon plasma treatment times that heightened the loss in treatment efficiency. This outcome was probably due to a relaxation of the plasma-induced chains that experienced a prior cross-linking at lower treatment times [114]. In 2 successive studies, Ghobeira et al. have additionally drew the attention on the less pronounced surface ageing behavior of electrospun PCL NFs subjected to a similar argon DBD treatment as the treated PCL films. Moreover, when comparing highly aligned and randomly deposited fibers having different diameters, the authors could still distinguish variances in the loss of treatment efficiency over 7 days post-treatment. XPS measurements have actually indicated a gradually more prominent decline in the oxygen content as the fiber diameter increased. Likewise, random fibers were revealed to withstand ageing less efficiently than aligned fibers that underwent a milder hydrophobic recovery (Figure 3.2). These results were accredited to the distinctive highly packed arrangement of the macromolecular chains that are driven to compactly accommodate small regions to fit into NFs. This initial dense positioning of the chains with shrunken free spaces in between is believed to impede the practicability of plasma-induced polar chains to migrate towards the fibers bulk. In particular, the molecular chains adopt a more aligned conformation with an even higher packing density in aligned and thinner fibers thus further hindering polar group reorientation [33,135]. The resulting trifling ageing effect constitutes a positive feature of plasma-treated NFs that are frequently used in the rapidly evolving TE field. In the next chapter, the application of plasma treatment on electrospun fibers particularly used in bone tissue engineering (BTE) will be tackled as a palpable exemplification of the plasma surface activation benefits in a hot topic.

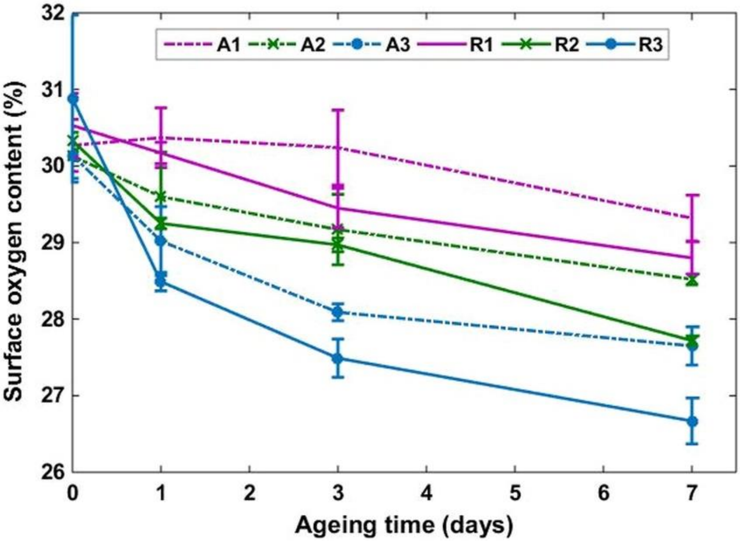

Figure 3.2 Evolution of the surface oxygen content of argon plasma-activated PCL NFs having different diameters and orientations as a function of ageing time post-treatment (A: aligned fibers with diameters of 225 nm (A1), 482 nm (A2) and 1173 nm (A3); R: random fibers with diameters of 232 nm (R1), 500 nm (R2) and 1272 nm (R3) [33].

Chapter 4. Applicability of plasma activation in scaffold-based bone tissue engineering approaches

4.1 Introduction to scaffold-based tissue engineering

After deeply uncovering the fundamentals of plasma-surface chemical interactions via the extensive literature overview provided in the first 3 chapters, the current chapter shifts towards an actual palpable application of plasma activation in one of the hottest topics within the scientific community: tissue engineering. TE approaches aim at surmounting the frequent limitations of standard transplantation methods via, amongst others, the biofabrication of substitute structures so-called scaffolds for the regeneration of damaged tissues and organs [13,36,49,96,136,137]. This scaffold-based TE methodology is currently gathering a lot of attention because of the emerging advanced technologies affording the scaffolds with adequate physical, chemical and biological properties ensuring a perfectly harmonized interaction between the cells and the material [13,55,138]. In fact, several prerequisites must be fulfilled by the scaffolds such as their biodegradability, non-toxicity and mechanical properties matching those of the native tissue to be repaired [137,139,140]. One of the most influential requirements ensuring effective cell-scaffold interactions is the mimicry of the fibrillary arrangement of the ECM. In the body, a widespread range of crucial cellular performances such as adhesion, metabolic activity, growth, proliferation, maturation, differentiation, migration and gene expression is actually governed by ECM/cell interactions [141–146]. Several physical, electrostatic, thermal and chemical techniques were established to produce fibrous scaffolds such as liquid-liquid phase separation, template synthesis, vapor-phase polymerization, self-assembly and electrostatic spinning [29,147–149]. This latter technique, also known as electrospinning, is characterized by several attractive strengths such as versatility, simplicity and cost effectiveness thus making it by far the preferred technique in the TE field. Moreover, electrospinning has an ability to produce fibers with easily adjustable fiber diameters going down to the characteristic nanometer scale of the ECM [33,55]. Solution-related parameters (i.e. polymer concentration, viscosity, surface tension…), process-related parameters (applied electric field, polymer flow rate, collector-to-needle distance…) and environmental parameters (i.e. temperature and relative humidity) can be straightforwardly fine-tuned to obtain the desired fiber diameter, morphology orientation and uniformity [55,150,151]. Nonetheless, appropriate topographical cues mimicking the ECM fibrous architecture are not enough to trigger the looked-for outcome. This is mainly attributed to the fact that cells are not solely affected by the material topography but also by the surface biochemistry that has a complementary role in initiating proper cell behaviors [32,33,152,153]. As such, a biofunctionalization of the nanofibrous scaffolds should be carried out by binding or promoting the binding of growth factors and proteins recognized by cell receptors thus mediating the cell affinity towards the fibers [99,119,154]. To do so, a surface chemical modification creating polar groups acting as binding sites for proteins can be carried out. However, given the fact that NFs are delicate structures, selecting a surface modification technique not damaging the scaffold's structure is quite challenging. Ozone oxidation, gamma and ion beam radiations were employed for their ability to graft reactive chemical groups on polymeric surfaces [29,139]. However, such modifications are accompanied with a potential degradation of the polymer structure and an alteration of the mechanical stability which rapidly compromise the fibers [155–157]. Traditional wet chemical treatments were as well frequently adopted to promote the density of polar groups on biomaterials. For instance, surface hydrolysis with NaOH solution or aminolysis with nitrogen-containing solutions can lead to the surface incorporation of COOH and NH_2 groups respectively [158–160]. Nonetheless, despite the highly controlled selectivity of such wet treatments, they are associated with many drawbacks. Firstly, surface modifications using chemicals are very harsh which frequently triggers a decline in the polymer mechanical performance, an acceleration in its degradation rate and therefore a high risk of fiber destruction. Secondly, many authors have revealed that this kind of surface modifications can lead to pronounced undesirable etching effects drastically damaging NFs. Moreover, the implementation of such techniques is quite time-consuming as it requires multi-step purification for long periods of time ranging from 1 day to a few days with typically low yields [161], demands a high labor-intensity and produces hazardous chemical waste [119,162]. As alternative, plasma surface activation is a much more versatile, simple, fast, dry, cost-effective, one-step process and environmentally friendly method (not generating toxic chemical waste) that can incorporate functional groups on electrospun scaffolds. A fine-tuning of different plasma process parameters can be carried out to obtain a desirable surface chemistry without altering the structure of the fibers [59]. Moreover, plasma treatment is a gas-based surface modification approach and is as such capable of homogenously treating the surface of porous biomaterials, hence NFs [13,33,49,59,163].

Acknowledging these advantages, the subsequent paragraphs will give an overview on the plasma treatment of electrospun nanofibrous specifically used in BTE. The choice of BTE in particular stemmed from two main reasons:

1) The high alerting incidence of bone defects caused by bone fractures and osteo-degenerative diseases which eventually increases the need of artificial bone grafts to restore serious injuries [137,142,148].
2) The double synergistic role of plasma treatment in promoting “bone” cell affinity towards the treated scaffold surface and the fibers biomineralization that is quite essential for successful osteointegration, osseoinduction and osteoconduction [13,45,46].

4.2 Plasma activation of electrospun nanofibrous scaffolds intended for bone tissue engineering

4.2.1. Improvement of cell performances

In the last 2 decades, several researchers have underlined the high promises of the plasma-assisted development of electrospun scaffolds in boosting bone repair via considerable improvements in seeded cell performances [45,164–166]. For instance, Yan et al. have cultured mouse osteoblasts (MC3T3-E1) on PCL NFs exposed to different low pressure RF plasmas and have published 2 papers in which cell behavior was studied. In the first paper, aligned and random NFs were treated with NH_3/O_2 plasma while in the second paper the authors tackled only random fibers exposed to N_2/H_2, NH_3/O_2 and Ar/O_2 plasmas. In all cases, XPS measurements indicated an increase in the surface oxygen that was grafted under the form of C-O and C=O functionalities. Furthermore, newly-incorporated N-containing groups were perceived after N_2/H_2 and NH_3/O_2 plasma exposures. An amine titration test showed that amines were only grafted on the N_2/H_2 plasma-treated fibers. These plasma-induced polar groups have led to a considerable decline in the WCA from approximately 135° to 0°. As a result of such chemical changes, an enhanced cell adhesion, growth and proliferation were detected via a 3-(4,5-dimethylthiazol-2-yl)-2,5-diphenyltetrazolium bromide) (MTT) assay and SEM imaging. When seeded on the aligned NFs, osteoblasts adopted well spread aligned morphologies as a response to the underlying architecture [163,167]. In a more recent study, Sankar et al. have electrospun PCL micro- and NFs and have subsequently subjected them to nitrogen and argon low pressure plasmas. XPS measurements indicated that argon plasma led to the incorporation of OH, C-O and C=O groups while nitrogen plasma grafted OH and NH functionalities on the fibers. Boosted adhesion, proliferation and spreading of human mesenchymal stem cells (hMSCs) were perceived on all treated fibers. The cell differentiation towards osteogenic lineages was investigated by a quantification of the alkaline phosphatase (ALP) activity. A superior differentiation towards osteoblasts was detected on plasma-treated fibers compared to their untreated counterparts [145]. Other interesting studies that have also depicted quite similar findings related to plasma-treated NFs intended for BTE applications are summarized in Table 4.1.

Table 4.1 Overview of literature studies involving plasma activation of electrospun NFs intended for BTE applications.

Authors (Year)	**Polymeric base material of the electrospun fibers**	**Plasma reactor and working gas**	**Plasma-induced surface chemical properties**	**Seeded cell type**	**Plasma-induced cyto-responsive properties**
Martins et al. (2009) [164]	PCL	RF, O_2 and Ar	- Incorporation of oxygen-containing groups, mainly –OH and –C=O. -Enhanced surface wettability	Osteoblasts (Saos-2 cell lines)	Improved cell viability, adhesion and proliferation
Seyedjafari et al. (2010) [45]	PLLA	RF, O_2	Enhanced surface wettability	Unrestricted somatic stem cells (USSCs)	Enhanced cell attachment, spreading and proliferation
Paletta (2010) et al. [165]	PLLA	RF, O_2	-Incorporation of carboxyl groups -Reduced surface hydrophobicity	hMSCs	Improved expression of genes associated with osteoblast lineage

Ardeshirylajimi at al. (2013) [166]	Polyethersulfone (PES)	MW, O_2	Enhanced surface wettability	Human induced pluripotent stem cells (iPSCs)	-*In vitro* assays: Enhanced cell proliferation and osteogenesis -*In vivo* study in rats: extensive bone reconstruction
Nandakumar et al. (2013) [168]	Polyactive®	RF,O_2	-Incorporation of oxygen containing functionalities (C-O and O-C=O) -Improved surface hydrophilicity -Pronounced adsorption of BSA	hMSCs	-Enhanced cell attachment with a spindle-like morphology -Significant upregulation of bone sialoprotein and osteonectin gene expression
Unalan et al. (2016) [169]	Poly(3-hydroxybutyrate-co-3-hydroxyvalerate) (PHBV)	RF, N_2,O_2	-Incorporation of oxygen- or nitrogen-containing functional groups (C-O,C-N and C=N)	Human primary osteosarcoma cells (Saos-2)	-N_2 plasma: improved osteoblastic cell viability -O_2 plasma: enhanced mineral formation but poor cell viability

			-Enhanced surface hydrophilicity		
Birhanu (2017) et al. [170]	PLLA	ns, Air	Improved, surface hydrophilicity	hMSCs	Enhanced cell proliferation and ALP activity
Wang (2019) et al. [171]	Polyvinyl alcohol (PVA)/ (PLLA)	ns, Air	Improved surface hydrophilicity	MSCs	Improved cell attachment, proliferation and ALP activity or osteoinductivity
Esbah Tabaei et al. (2020) [13]	CS/PEO and Coral/CS/PEO	DBD, Air, N_2, Ar	-Incorporation of oxygen- and nitrogen-containing functionalities (C-O, C-N, C=O, O=C-NH, O-C-O and O-C=O) -Enhanced surface wettability	MC3T3 cells	Enhanced cell adhesion, metabolic activity and proliferation

4.2.2. Stimulation of the scaffolds biomineralization

Next to the enhancement of cell-material interactions, an appropriate surface chemistry concurrently inducing the nucleation and growth of bone-like apatitic CaP nanocrystals is imperative for an effective bone repair [172]. In fact, the natural biomineralization process forming the bone is initiated on well-dispersed bone ECM (bECM) proteins with definitive functional groups based on amino acid side chains establishing apatite-binding sites [173]. A mimicry of this natural process via a plasma surface functionalization of NFs is believed to trigger the formation of a biologically active apatite layer. This layer is vital for typical bone-related activities such as osseoinduction, osteoconduction and osteointegration or intimate bone-bonding ability of the tissue-engineered scaffold [45,174–176]. Several researchers have immersed metallic and polymeric pre-functionalized bone implants in simulated body fluid (SBF) as a validated biomimetic method to predict the *in vivo* osteo-bioactivity by examining the ability of apatite to grow on the surface [35,172,177–179]. For instance, Van Vrekhem et al. have submerged UHMWPE films into SBF after exposing them to an argon plasma jet treatment. Results revealed a more prominent and uniform CaP deposition on plasma-treated films compared to untreated films. This was attributed to the presence of plasma-induced oxygen-functionalities namely C-O and O-C=O groups that initiated the nucleation and growth of CaP onto the surface. A careful analysis of FTIR data indicated that the formed CaP crystals were under the form of apatite type B [35]. However, a scarce amount of research has been conducted on fibrous scaffolds given the large challenge in obtaining homogeneous apatite nanocrystal growth around the fine fibers without blocking the pores and completely hindering the envisioned bECM-like structure. For example, Ito et al. have reported that electrospun PHBV fibers, normally displaying a compatible surface for apatite layer deposition, were fully covered on the outside without any sign of porosity or nanostructure when soaked in SBF [180]. Therefore, a very cautious optimization of the plasma treatment parameters and the SBF immersion time should be carried out to avoid pores blockage by CaP. In an effort to enhance the CaP deposition on PCL NFs while retaining their porous and fibrous structures, Yang et al. have performed an argon plasma treatment followed by an immersion in 10 x concentrated SBF (SBF10) for varying time periods. Plasma-induced COOH groups that were grafted on the surface were presumably turning into carboxyl anions when in contact with SBF10. Such negatively charged groups are able to induce the chelation of calcium and phosphate ions thus stimulating surface nucleation. In fact, PCL fibers were found to be uniformly mineralized with nano-textured flake-like CaP crystals only after a 2 hour immersion in SBF. However, when prolonging the immersion time to 6 hours, PCL scaffolds became fully covered with a CaP coating and the porous structure was lost (Figure 4.1). FTIR measurements revealed that the coating consisted of a mixture of dicalcium phosphate dihydrate and nano-apatite. When continuously immersing the treated fibers in a classical non concentrated SBF for 7 days, the inter-fibrous pores were not blocked and the homogeneously formed CaP crystals were shown to be deposited under the form of pure calcium deficient type B carbonate apatite which is similar to the biological apatite [46].

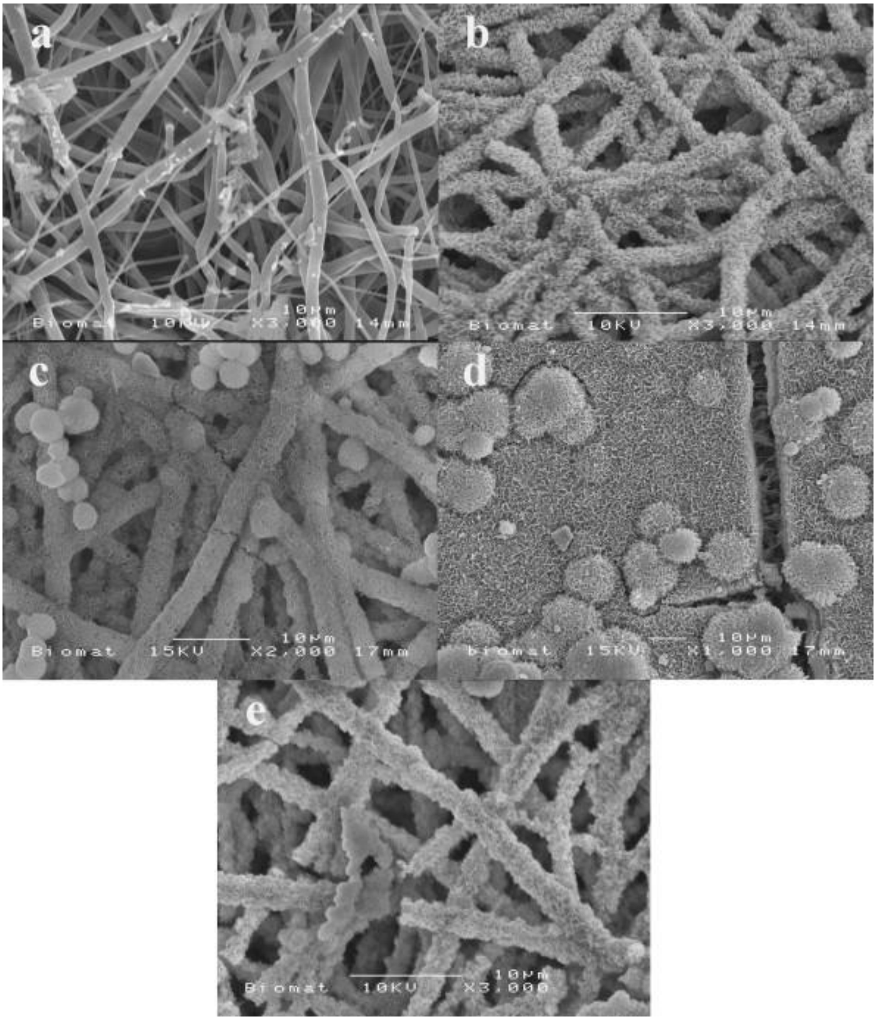

Figure 4.1 SEM images of plasma-treated PCL fibers after immersion in 10 x concentrated SBF for 1 h (a), 2 h (b), 3 h (c) and 6 h (d) and in classical SBF for 7 days (e) [46]

Chapter 5. Materials and methods: plasma treatments, surface characterization and biofabrication

5.1 Plasma treatment

5.1.1 Dielectric barrier discharge set-up

The schematic of the medium pressure parallel-plate DBD system used in this thesis is presented in Figure 5.1. The discharge was generated between two circular electrodes (Figure 5.1 (12; 16)). The upper electrode (Figure 5.1 (12)) was a copper plate (Ø: 48 mm) covered with an Al_2O_3 layer with a thickness of 3 mm and was connected to a custom-made power supply (Figure 5.1 (11)) providing a sinusoidal wave high voltage at a fixed frequency of 20 kHz. The lower stainless-steel electrode (Ø: 25 mm) (Figure 5.1 (16)), on which the polymer sample was directly placed, was grounded through a 10 nF capacitor (Figure 5.1 (18)). To control the distance between the 2 electrodes and to ease the process of transferring the sample to an XPS device, both electrodes were adjustable in height. As mentioned in Chapter 1, one of the objectives of this thesis is to investigate the polymer surface composition directly after plasma treatment without any air exposure between the plasma modification and the XPS characterization steps. To do so, the DBD plasma chamber was directly connected to an XPS machine (Figure 5.1 (13)) and the lower electrode with the polymer sample on top was transferred straight into the XPS introduction chamber using a transfer arm (Figure 5.1 (17)).

In an effort to minimize the level of oxygen contamination inside the plasma reactor, the plasma chamber was continuously kept at high vacuum (pressure of approximately 5×10^{-7} kPa) using an Edwards turbo pump (EXT 75DX) (Figure 5.1 (6)) directly connected to the plasma chamber. In addition, the polymer samples were introduced into the plasma reactor by first placing them into the introduction chamber of the XPS device. As such, the plasma chamber did not need to be brought to atmospheric pressure to introduce the polymer samples. The low volume intro chamber of the XPS can be easily filled with N_2 to bring it to atmospheric pressure, after which the polymer sample on top of the lower electrode was placed inside the intro chamber. Afterwards, the intro chamber was pumped down to 10^{-3} kPa using the designated rough pump of the XPS machine prior to transferring the sample + electrode into the plasma chamber. After introducing the sample (polymeric films of fibers) in the plasma reactor, the reactor was pumped down to a pressure of 10^{-3} kPa using a rotary vane pump (Edwards, RV3) (Figure 5.1 (3)). For a further reduction of the reactor base pressure, two additional turbo pumps were then switched on: (1) the turbo pump directly connected to the plasma reactor (Edwards, EXT 75DX) (Figure 5.1 (6)) and (2) the turbo pump used for evacuating the intro chamber of the XPS device

(Pfeiffer vacuum, HiPace 80). By simultaneously using these two turbo pumps, a base plasma reactor pressure of 1 x 10^{-7} kPa could be obtained. Two manometers were used for pressure readings: (1) a Pirani Thyracont VD85 compact vacuum meter (Figure 5.1(7)) for measuring plasma chamber pressures in the range 10^{2} to 10^{-5} kPa and (2) an Edwards active inverted magnetron gauge (AIM-X-DB40CF) (Figure 5.1(8)) for accurate measurements of reactor pressures below 10^{-5} kPa. After reaching the desirable base pressure of 1 x 10^{-7} kPa, the plasma reactor was filled with the working gas (Ar or N_2) for 3 minutes using a fixed gas flow rate of 3000 standard cubic centimeters per minute (sccm) making use of a gas mass flow controller (Bronkhorst, El-Flow®) (Figure 5.1(2)). As a result of this flushing step, the chamber pressure increased to approximately 30 kPa. In a next step, the gas flow rate was reduced to 800 sccm and the plasma reactor was pumped down to 5.0 kPa, after which the plasma was ignited by turning on the high voltage power source.

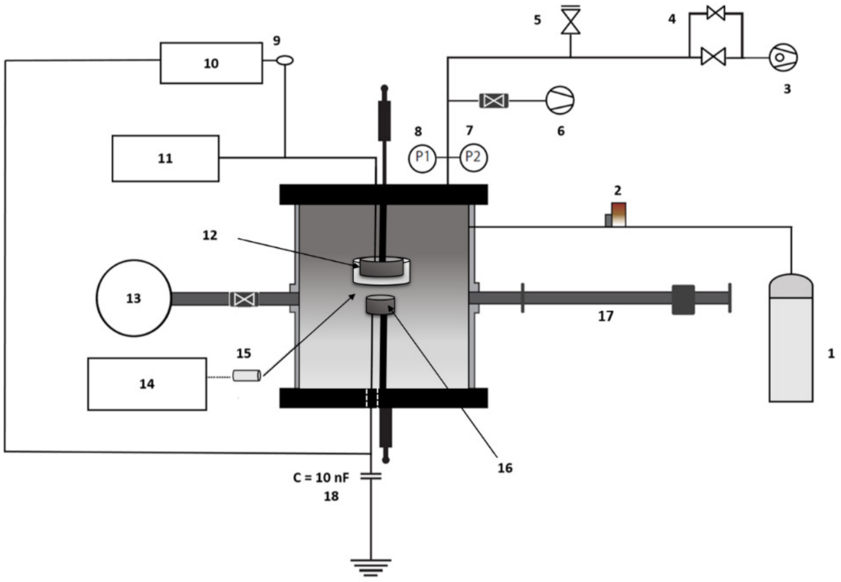

Figure 5.1 Schematic of the experimental plasma set-up: (1) gas bottle; (2) mass flow controller; (3) rotary vane pump; (4) needle valve; (5) vent; (6) turbomolecular pump; (7) Pirani gauge; (8) active inverted magnetron gauge; (9) high voltage probe; (10) oscilloscope; (11) AC power supply; (12) adjustable powered electrode; (13) XPS machine; (14) optical emission spectrometer; (15) optical fiber; (16) movable substrate holder (bottom electrode); (17) electrode + sample transfer arm; (18) capacitor.

5.2 Electrical and optical characterization techniques

5.2.1 Electrical characterization

The voltage applied to the top electrode of the reactor was measured using a 1000:1 high voltage probe (Tekronix P6015A) (Figure 5.1 (9)), whereas the charge generated on the electrodes was obtained by measuring the voltage over the 10 nF capacitor, connected in series with the discharge reactor to the ground (Figure 5.1). The obtained charge-voltage waveforms (also known as Lissajous figures) were recorded with a Picoscope 3204A digital oscilloscope (Figure 5.1 (10)), after which the power consumed by the discharge was calculated from these waveforms by using equation 5.1 as described in [53]:

$$P = f * \int V(t)C(t)dt \tag{5.1}$$

where f is the discharge frequency, V(t) the applied high voltage and C(t) the charge on the electrodes as a function of time.

To be able to objectively compare the surface activation results when using different gas discharges, energy density values (J/cm^2) were calculated and the results will be presented in this work as a function of this parameter instead of as a function of treatment time. The energy density was calculated by multiplying the plasma discharge power with the plasma exposure time and by dividing this value by the area of the bottom electrode (Ø: 25 mm) [34].

5.2.2 Optical characterization

The optical emission spectra of the N_2, N_2/O_2, Ar, and Ar/O_2 plasmas were recorded using an optical spectrometer (Ocean Optics, S1000) (Figure 5.1 (14)) with a spectral resolution of 0.7 nm in the wavelength range 200 to 900 nm to obtain information on the excited state species present in the discharge. The optical fiber (Figure 5.1 (15)) was mounted close to the front window of the reactor and was located 20 cm away from the center of the discharge. OES analysis of the different discharges was carried out as described by Deng et al. [181].

The obtained OES spectra of the different plasmas were used to estimate some basic physical characteristics of the discharges under study. In this work, assuming partial local thermodynamic equilibrium (pLTE), the electron temperature (T_e) has been determined from the relative intensities of the emitted lines in corona approximation [182]. Considering that the excited levels are in pLTE, each T_e could be approximated by the electron excitation temperature (T_{exc}), which was determined by the Boltzmann plotting method. According to the Boltzmann distribution, the relative intensities of the emitted lines fulfill the following equation [181,183,184]:

$$ln\left(\frac{I\lambda}{g_k A_{kj}}\right) = -\frac{E_k}{k_B T_{exc}} + C \tag{5.2}$$

where I is the intensity of the line, λ its wavelength, g_k the statistical weight of the radiating level k of the transition, A_{kj} the transition probability for spontaneous emission from k to j, E_k the excitation energy of the k level, k_B the Boltzmann constant and C a normalization constant dealing with the ground state.

5.3 Fabrication of CS/PEO and Coral/CS/PEO NFs

5.3.1 Coral sizing and disinfection

Coral was obtained from Persian Gulf coral reefs and the sample was kindly provided by the group of Prof. Mirzadeh (Faculty of Polymer Engineering, Amirkabir University of Technology, Tehran, Iran). Coral pieces were grinded making use of high speed vibrational milling (HSVM). The grinding procedure was performed in a Fritsch Mini-Mill Pulverisette 23 in a 10 mL stainless steel grinding bowl with a 15 mm diameter grinding ball [185]. Thereafter, the coral micro-particles were disinfected by immersion in an aqueous sodium hypochlorite solution (6-14 % active chlorine) (Merck, Germany) for 30 h, followed by washing with distilled water (three times) and vacuum drying.

5.3.2 Polymer solution preparation

To prepare the CS/PEO polymer solution for electrospinning, a 3:1 mixture of CS (83.3 % deacetylated, medium molecular weight, Sigma-Aldrich) and PEO (MW = 400,000 Da, Sigma-Aldrich) was dissolved in a mixture of acetic acid (Carl Roth) and distilled water (9:1) in such a way that a 4 w/v % polymer solution was obtained. In a next step, to prepare the Coral/CS/PEO solution, coral powder was added to the 4 w/v % CS/PEO solution in a 1:1 (Coral:CS/PEO) weight ratio. The suspension was then continuously stirred until a homogeneous mixture was obtained.

5.3.3 Electrospinning

A customized Nanospinner 24 electrospinning machine (Inovenso), as schematically represented in Figure 5.2 (a), was used at room temperature to fabricate NFs and has been previously well described in literature [24,33,151]. Prepared CS/PEO and Coral/CS/PEO solutions were first loaded into a 10 mL standard syringe, which was subsequently placed inside a syringe pump (NE-300 Just Infusion™). Using this pump, a predefined flow rate of the CS/PEO or Coral/CS/PEO solution was pumped through a polyethylene tube (inner Ø: 2 mm) ending in a brass nozzle with an inner diameter of 0.8 mm. During the electrospinning process, the flow rate of the polymer solution was varied between 0.2 and 0.7 mL/h to maintain a stable jet during the electrospinning procedure. At the moment a polymer solution droplet came out of the nozzle, a DC voltage of 26 kV was supplied to the nozzle. The nozzle was placed vertically below a rotating (130 rpm) collector at a distance of 18.0 cm. As collector, a grounded cylinder with a 5 cm radius and a length of 28 cm was used. The NFs were deposited on glass coverslips (Ø: 12.0 mm) which were fixed on the collector by using conductive copper tape on an aluminum sheet wrapped around the collecting cylinder.

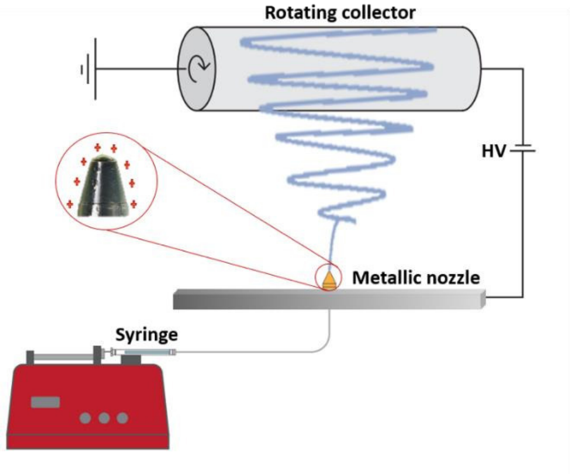

Figure 5.2 A schematic representation of the electrospinning set-up.

5.4 Surface analysis techniques

5.4.1 WCA measurements

WCA measurements were carried out at room temperature in ambient air to pinpoint the saturation region of the performed N_2 and Ar plasma treatments. Additionally, WCA analysis was also performed to determine possibly occurring changes in surface wettability after storing the plasma-treated samples in ambient air. Static WCA measurements were performed using a commercial Krüss Easy Drop system immediately after plasma treatment. The deposited water droplets (volume of 2.0 µL) were fitted using Laplace-Young curve fitting and 6 measurements over an extended area of a single sample were collected and averaged.

5.4.2 XPS measurements

XPS measurements were carried out on a PHI Versaprobe II spectrometer employing a monochromatic Al K_α X-ray source (hν = 1486.6 eV) operated at 25 W. All measurements were conducted in a vacuum of at least 10^{-9} kPa and the photoelectrons were detected with a hemispherical analyzer positioned at an angle of 45° with respect to the normal of the sample surface. Survey scans and individual high resolution spectra (C1s, O1s, N1s) were recorded with a pass energy of 187.85 eV (eV step = 0.8 eV) and 23.50 eV (eV step = 0.1 eV) respectively, using a 100 µm spot size. Elements present on the surfaces were identified from XPS survey scans and quantified with Multipak (Version 9.6.1) software using an iterated Shirley background and applying the relative sensitivity factors supplied by the manufacturer of the instrument. Multipak software was also used to curve fit the high resolution C1s peaks after calibration of the energy scale using the hydrocarbon component of the C1s spectrum (285.0 eV). The C1s and N1s peaks were deconvoluted using Gaussian-Lorentzian peak shapes (%Gaussian > 80 %) and the full-width at half maximum (FWHM) of each line shape was constrained below 1.5 eV. All fittings are optimized until a chi-square value below 2 is reached.

5.4.3 FTIR measurements

FTIR has been used to determine the type of functional groups that are incorporated onto a substrate within a depth of approximately 600 nm. Just as its name implies, FTIR employs a range of infrared (IR) wavelength radiations that can be partially absorbed by the chemical groups present on the substrate's surface. In this thesis, FTIR analysis was performed making use of a Spectrum Two spectrometer (Perkin Elmer Instruments). The spectra (32 scans) were recorded for wavelengths between 4000 and 450 cm^{-1} with a resolution of 1 cm^{-1}.

5.4.4 SEM measurements

To visualize the morphology of the CS/PEO and Coral/CS/PEO NFs before and after plasma treatment, a SEM device (JSM-6010 PLUS/LV, JEOL) was used. SEM images were acquired with an accelerating voltage of 7 kV at a working distance of 10 mm after coating the samples with a thin layer of gold for 25 s, making use of a sputter coater (JFC-1300 autofine coater, JEOL) operating at 20 mA to enhance sample conductivity. To determine the mean diameter of the CS/PEO and Coral/CS/PEO NFs, obtained SEM images were analyzed using ImageJ (V 1.48) software, which was applied to determine the diameter of 40 randomly selected NFs per sample condition.

5.4.5 Mechanical characterization of untreated and plasma-modified NFs

To gather information on the mechanical properties of the CS/PEO and coral/CS/PEO NFs, stress-strain curves have been recorded. For this purpose, 0.17 mm thick nanofibrous meshes were cut into 10 × 25 mm^2 rectangular shapes and their tensile properties were characterized making use of a Tinius Olsen tensile tester before and after plasma treatment on both groups of NFs. The samples were vertically mounted into two pneumatically actuated rubber grips, leaving a 20 mm gauge length for the mechanical loading. A fixed preload of 1 N was applied to the samples after which the displacement rate was set at 50 mm/min. Stress vs. strain curves of the NFs were subsequently constructed by measuring the force at the load cell as a function of the grips displacement. From these curves, the ultimate tensile strength defined as the maximum force divided by the sample cross section was determined. Additionally, the Young's modulus, which describes the tensile elasticity, was calculated as the slope of the linear part of the obtained stress-strain curves. Since all samples originated from the same electrospinning batch, thickness variations among the samples could be neglected.

5.4.6 X-ray diffraction (XRD) analysis

The crystalline structure of coral powder, SBF immersed CS/PEO NFs and Coral/CS/PEO NFs were studied using a powder XRD ARL X'TRA diffractometer (Thermo Scientific) equipped with a Cu Kα (λ = 1.5405 Å) source and operating at angles in the range of 5–80°. The integration time and the step size were fixed at 1.2 s and 0.02°, respectively. The analysis of the obtained XRD spectra was performed using the RRUFF database.

5.4.7 SEM and SEM-energy dispersive spectrometer (EDS) analyses

The surface morphology of coral powder was analyzed using a JEOL JSM-6010 PLUS/LV SEM device operated at an accelerating voltage of 7.0 kV and a working distance of 12.0 mm. In addition, the elemental composition and elemental mapping of coral particles were also obtained with an EDS present on the JSM-7600F FEG-SEM device.

5.5 Biological performance of CS/PEO and Coral/CS/PEO NFs

5.5.1 Cell seeding

The effect of plasma treatment on the cellular interactions (such as cell adhesion and proliferation) on both studied NF types was also examined. Prior to cell seeding, untreated and plasma-treated NFs were first sterilized by exposure to UV light (Sylvania; 254 nm wavelength) for 30 min because this was found to be the most effective sterilization method for plasma-treated NFs [114]. After sterilization, the samples were placed in a 24-well plate and MC3T3 osteoblast cells were seeded onto different samples at a density of 40,000 cells/mL of medium, using a total volume of 1 mL of medium per sample. Cell culturing was performed using Dulbecco’s modified Eagle glutamax medium (DMEM) (Gibco Invitrogen) enriched with 15 % foetal calf serum (Gibco Invitrogen), 2 mM L-glutamine (Sigma-Aldrich), 10 U/mL penicillin, 10 mg/mL streptomycin and 100 mM sodium-pyruvate (all from Gibco Invitrogen). The seeded samples were subsequently incubated at 37°C in a humidified atmosphere containing 5 % CO_2 for 1 and 7 days (time required for MC3T3s to adhere and proliferate on the NF surface). Cells were cultured on tissue culture polystyrene (TCPS) plates as positive control (considering a 100 % cell viability). All the data are in reference to TCPS 1 days and 7 days after culturing on untreated and plasma-treated NFs.

5.5.2 Live/dead assay by fluorescence microscopy

Cell viability was visualized 1 day and 7 days after cell seeding making use of fluorescence microscopy. In a first step, the supernatant was removed and the samples were rinsed twice with phosphate buffered saline (PBS). Thereafter, cell staining was performed by placing the samples in a mixture of 2 µL (1 mg/mL) calcein-acetylmethoxyester (Anaspec), 2 µl (1 mg/mL) propidium iodide (Sigma-Aldrich) and 1 mL PBS for 10 min in the dark at room temperature. Afterwards, the samples containing stained cells were removed from the solution, rinsed twice with PBS and then visualized with a fluorescence microscope (Olympus; IX 81).

5.5.3 Cell morphology visualization by SEM

To visualize the morphology of the MC3T3 cells, SEM analysis was performed to investigate the distribution, spreading and shape of attached cells on both CS/PEO and Coral/CS/PEO NFs, before and after plasma modifications. Preceding SEM analysis, the cell-seeded NFs were removed from the culture medium and rinsed 3 times with PBS to remove non-adhered cells. In a next step, the cells were fixed by incubating the samples in a fixative solution of 2.5 % glutaraldehyde in 0.1 M cacodylate buffer for 1 h at room temperature. Afterwards, cell dehydration was performed by immersing the NFs in increasing concentrations of ethanol (50 %, 75 %, 85 % and 95 %) for 10 min immersion per ethanol solution. The last dehydration step in 95 % ethanol was carried out twice, using a fresh ethanol solution in the second step. Afterwards, the cell-loaded NFs were immersed in a 100 % hexamethyldisilazane (HMDS) (Acros Organics) solution for 10 min, removed from the solution and subsequently immersed again in a fresh HMDS solution for 10 min. In a final step, the samples were set aside for evaporation under the fume hood and viewed with SEM, according to the procedure previously described in section 5.4.4.

5.5.4 MTT assay

To quantify the metabolic activity of MC3T3 cells on CS/PEO and Coral/CS/PEO NFs, a colorimetric MTT assay was carried out after 1 day and 7 days. The assay is based on the fact that the yellow tetrazolium dye 3-(4, 5-dimethyldiazol-2-yl)-2, 5-diphenyltetrazolium bromide (MTT, Merck Promega) turns into purple-blue formazan after mitochondrial dehydrogenases of living, metabolically active cells cause its reduction. In a first step, the culture medium was replaced by 0.5 mL (0.5 mg/mL) MTT reagent 1 day and 7 days after cell seeding. Subsequently, the samples were incubated at 37°C for 4 h, after which the samples were removed from the MTT reagent and placed in a lysis buffer (1 % Triton-X100 in isopropanol/ 0.04 N HCl) at 37°C for 30 min to dissolve the produced water-insoluble formazan. Finally, 200 µL of the formazan solution was transferred to a 96-well plate and the absorbance of the colored solution was measured at 580 nm using a spectrophotometer (Universal microplate reader EL 800, BioTek Instruments). Background absorbance at 750 nm was subtracted from the measured absorbance and the obtained optical density of the colored solution was reported as a percentage compared to the normalized TCPS positive control. Percentage data are presented as mean ± standard deviation and statistical analysis of the obtained values was performed making use of single factor ANOVA analysis of variance (Excel software) and a *P* value < 0.05 was considered as a statistically significant difference.

5.5.5 CaP deposition

It should be noted that bone regeneration is facilitated by the deposition of calcium ions, especially calcium phosphate minerals [45,46]. As such, it is of interest to incubate the nanofibrous samples in SBF, which is known to introduce an apatite layer (calcium ions or its minerals) onto the surface of NFs [186,187]. After incubation, the CaP deposition can be examined, which is an important parameter to evaluate the bioactivity of the electrospun nanofibrous meshes. This biomimetic mineral formation has already attracted extensive research interests as it is similar to the *in vivo* biological mineralization in bone [45,65,188,189]. In this thesis, the *in vitro* bioactivity of pristine and plasma-treated CS/PEO and Coral/CS/PEO NFs was investigated by immersing the samples in 2.0 SBF for 7, 14 and 30 days. Prior to immersion, the samples were subjected to 6 cycles of alternate dipping. Each cycle consists of the following steps:

- 60 s in 1000 mM Ca^{2+} ($CaCl_2 \cdot 2\ H_2O$; Merck 2382)
- 30 s in H_2O (for rinsing)
- 60 s in 600 mM HPO_4 ($Na_2HPO_4.2\ H_2O$; Merck 6580)
- 30 s in H_2O (for rinsing)

2.0 SBF was prepared using the following components: NaCl (VWR Prolabo 27810.295), $NaHCO_3$ (Merck 6329), KCl (Merck 4936), K_2HPO_4 (Merck 5104), $MgCl_2.6\ H_2O$ (Merck 5833), $CaCl_2 \cdot 2\ H_2O$ (Merck 2382), Na_2SO_4 (Merck 6647) and tris(hydroxymethyl) aminomethane (VWR Prolabo 103156X). These components were dissolved in deionized water as described in the protocol of Kokubo et al. [190] and the pH was adjusted to 7.4 with a 1 M HCl solution. For each condition, 5 samples were immersed in SBF and after SBF incubation, FTIR spectra of the created CaP-coatings were recorded according to the procedure previously described in section 5.4.3.

Chapter 6. Comparative study between in-plasma and post-plasma chemical processes occurring at the surface of UHMWPE subjected to medium pressure Ar and N_2 plasma activation

The results of Chapter 6 were published in the following peer-reviewed journal:

Parinaz Saadat Esbah Tabaei, Rouba Ghobeira, Pieter Cools, Fatemeh Rezaei, Anton Nikiforov, Rino Morent, and Nathalie De Geyter. "Comparative study between in-plasma and post-plasma chemical processes occurring at the surface of UHMWPE subjected to medium pressure Ar and N_2 plasma activation." *Polymer* 193: Art. No. 122383 (2020).

6.1 Introduction

Although considerable progress has been made in unravelling plasma-surface modifications, based on *in situ* XPS analyses, as can be noticed from chapter 3, some important research aspects have not yet been examined. First of all, literature so far only focused on low pressure plasma treatments, totally neglecting the examination of plasma-surface interactions in case of high pressure plasmas. Additionally, a systematic study examining the impact of post-plasma ambient air exposure on the surface chemical composition of polymers is also lacking. And, last but not least, in the available studies focusing on *in situ* characterization of plasma-treated surfaces, OES diagnostics have been highly underappreciated, although OES is known as a very practical and non-invasive diagnostic technique to determine the nature of excited chemical species inside a discharge. As such, correlating OES diagnostics with direct XPS investigations can aid to fundamentally understand the relative importance of in-plasma and post-plasma reactions on polymeric surfaces. This chapter aims to use a combination of OES and *in situ* XPS analysis to examine the relative importance of in-plasma and post-plasma oxygen incorporation on a polymer surface. For this purpose, in contrast to the available literature, a medium pressure plasma sustained in Ar and N_2 will be used, namely a DBD operated at a pressure of 5.0 kPa. Unlike atmospheric pressure plasmas, this medium pressure plasma still allows operating in a controlled gas environment and induces a uniform polymer surface treatment, permitting the study of plasma-surface interactions. In this work, UHMWPE is chosen as model polymer. Because of its simple chemical structure ($-(CH_2-)_n$) and high chemical inertness (little spontaneous surface oxidation or water adsorption), possible side-effects on the polymer surface will be limited, making it easier to identify and distinguish which surface phenomena are exactly taking place. Besides the direct XPS analysis, a detailed XPS study of the plasma-modified UHMWPE samples upon exposure to ambient air will also be conducted in this work. By doing so, it is intended to discern the relative importance of in-plasma and post-plasma incorporation of oxygen in case of a medium pressure plasma, to reveal the role of oxygen contamination inside the plasma reactor and to identify which polymer surface changes occur upon storage in ambient air.

6.2 Experimental conditions

All experimental details can be found in Chapter 5. The parameters that are specifically used in this chapter are summarized in Table 6.1.

Table 6.1 Specific experimental conditions adopted in this chapter.

Base material	UHMWPE
Plasma gas	Ar, N_2
Discharge power (W)	Ar: 0.25 N_2: 0.16
Treatment time (s)	Ar: 0-120 N_2: 0-90
Energy density at saturated point (J/cm^2)*	Ar: 3.05 N_2: 1.95
Gas flow rate (sccm)	800
Electrode distance (mm)	1
Frequency (kHz)	20
Base pressure (kPa)	10^{-7}
Working pressure (kPa)	5
Surface characterization techniques	WCA: - 2.0 µL-drops of distilled water - Reported value: average of 10 values measured on 2 different samples XPS: - Reported value: average of 6 measurements points for both *in situ* and *ex situ* XPS measurements

**the saturated point corresponds to the lowest attainable WCA value, which will be explained in detail in section 6.3.4.*

6.3 Results and discussion

6.3.1 Electrical measurements

The obtained time-averaged Lissajous figures over 15 voltage cycles for N_2 and Ar plasmas are shown in Figure 6.1. From these Lissajous figures, the discharge power can be calculated and the obtained results have been already given in Table 6.1: the calculated power for Ar plasma (0.25 W) is higher than that for N_2 plasma (0.16 W). It is well known that the chemically reactive species in the discharge not only depend on the working gas but also on the discharge operational regime [42]. As such, it is also important to reveal information on the operational mode of the DBDs applied in this work. According to literature, the shape of the parallelogram in case of the N_2 plasma depicted in Figure 6.1 (a) is an indication of a filamentary discharge [191]. In contrast, the Lissajous figure in case of the Ar plasma can be linked to a transition mode of the discharge, operating somewhere between a glow and filamentary mode, often referred to as a pseudo-glow mode [192]. The indication of the operational mode is also confirmed by the visual appearance of the plasma: a homogenous glow discharge uniformly distributed throughout the discharge volume can be seen when using Ar as discharge gas. On the other hand, the discharge in N_2 consists of a set of separate filaments arbitrarily distributed among the electrode surface, confirming the filamentary nature of the N_2 discharge.

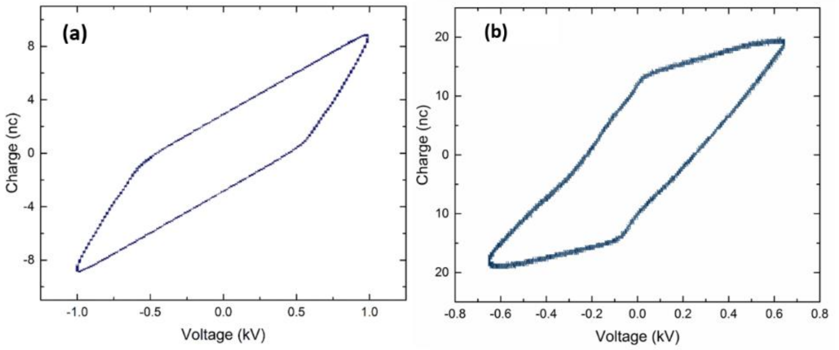

Figure 6.1 Lissajous figure at 5.0 kPa for (a) N_2 plasma at a discharge power of 0.16 W, (b) Ar plasma at a discharge power of 0.25 W.

6.3.2 OES study

The normalized OES spectra of the used N_2 and Ar plasmas are shown in Figure 6.2 (a) and (b) respectively and will be discussed in detail in the following paragraphs.

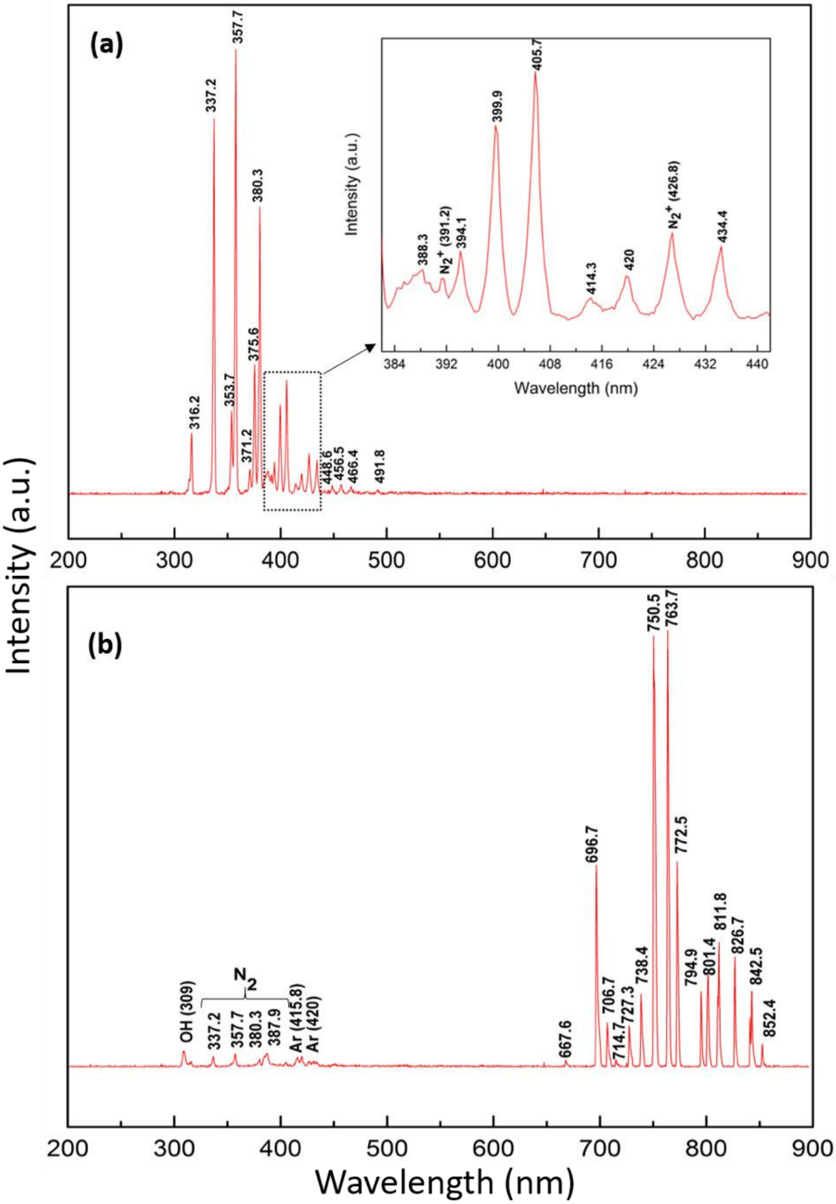

Figure 6.2 OES spectrum of (a) the applied N_2 plasma and (b) the used Ar plasma.

6.3.2.1 N_2 plasma spectral analysis

In case of the N_2 plasma, intense OES peaks in the range 316-466 nm can be observed, which can be attributed to the N_2 second positive system, transition $C^3\Pi_u - B^3\Pi_g$ [193]. These intense molecular N_2 bands in the OES spectrum thus indicate the presence of electronically and vibrational excited N_2 molecules in the used N_2 plasma. Considering that vibrational excitation of N_2 by electron impact is the most effective at an electron energy between 1.7 and 3.5 eV, it was to be expected that considerable amounts of N_2 vibrational excited states would be present in the used N_2 discharge [194]. Furthermore, as indicated by the research group of Bogaerts et al. [195], the electron impact dissociation of vibrational excited N_2 states is the primary process for the formation of atomic nitrogen through the reaction pathway described below (in its general form) [196]:

$$e^- + N_2 \rightarrow N_2\ (a^1\Pi_g),\ N_2\ (B^3\Pi_g),\ N_2\ (b^1\Pi_u) + e^- \rightarrow e^- + N + N \qquad (6.1)$$

The generation of both vibrational and electronically excited molecular states of N_2 and the subsequent generation of N atoms is of key importance for the effective surface activation of polymers and is the primary source for the incorporation of new N-containing functional groups at polymer surfaces [197]. The emission spectrum, shown in Figure 6.2 (a), also indicates the presence of ionized nitrogen molecules (N_2^+) in the discharge, which is confirmed by the appearance of emission lines at wavelengths of 391.2 and 426.8 nm. These spectral lines are known to correspond to the first negative system of the N_2^+ transition $B^2\Sigma_u$-$X^2\Sigma_g$ [181,182]. Additionally, no evidence for the presence of N^+ ions in the N_2 discharge is found in the OES spectrum, leading to the conclusion that N_2^+ is the dominant ionic species in the DBD sustained in N_2 at sub-atmospheric pressure. These N_2^+ species may be possibly generated in the discharge through direct electron impact of ground state N_2 molecules, however, this reaction is less likely to occur as the required electron energy is relatively high (> 15.6 to 18.5 eV) [198]. More likely is the stepwise generation of N_2^+ through electron impact ionization processes with vibrational excited N_2 states [193,199]. Figure 6.3 also shows that the formation of excited N_2^+ species is more pronounced when the plasma reactor base pressure is lowered to 10^{-7} kPa. Finally, it is also important to mention that at the working pressure of 5.0 kPa, the plasma source operates in the recombination mode and diffusion loss of N_2^+ could be neglected [182,200]. A portion of the N_2^+ ions will thus probably recombine with free electrons through dissociative recombination, resulting in the formation of $N(^4S)$ (atomic state), $N(^2D)$ and $N(^2P)$ (metastables) with a relative abundance of ~1, ~ 0.9 and < 0.1 respectively [201]. This process is considered to be important as the N metastable states ($N(^2D)$ and $N(^2P)$) and nitrogen atoms, generated by dissociative recombination as well as by the reaction 6.1, are known to play a major role in altering the surface chemistry [197] as will be discussed later in this work.

6.3.2.2 Ar plasma spectral analysis

The OES spectrum of the DBD sustained in Ar is characterized by intense Ar I lines (4p-4s) found in the wavelength range 696-852 nm [184,202], and less intensive Ar I lines (5p-4s) which appear in the wavelength region between 415 and 420 nm [6,184,202]. As can be seen in Figure 6.2 (b) and also in Figure 6.3, a small emission line attributed to OH radicals is also visible in the OES spectrum of the Ar discharge at 309 nm. Additionally, also a set of emission lines is present in the wavelength range 337-399 nm which can be attributed to the N_2 second positive system. The appearance of other peaks besides Ar emission lines thus indicates the presence of trace amounts of contamination in the Ar discharge, even when reaching a base reactor pressure of 10^{-7} kPa. Nevertheless, it can also be observed from Figure 6.3 that the amount of the contaminants in the Ar discharge can be considerably reduced when the base reactor pressure is decreased to its lowest attainable value (10^{-7} kPa). It is also important to note that not a single trace contaminant, such as for example OH radicals (309 nm), atomic oxygen (777 nm) or atomic hydrogen H_α (656 nm) could be observed in the OES spectrum of the N_2 discharge, not even at high plasma reactor base pressures of 10^{-5} or 10^{-6} kPa (Figure 6.3). This can be related to the fact that all above-mentioned impurities (OH, O and H_α) are created by dissociation of trace molecules, namely H_2O and O_2. This dissociation process followed by excitation is however very inefficient in case of an N_2 discharge due to the low electron temperature as the dissociation process typically requires high energy values above 10 eV. Consequently, no trace contaminations derived from H_2O and O_2 could be observed in the OES spectrum of the used N_2 discharge, although they are definitely present in the discharge reactor. On the other hand, in the Ar discharge, highly energetic Ar metastables with energies above 13 eV are present, which can effectively dissociate trace impurities, resulting in the presence of OH radicals in the OES spectrum of Ar (Figure 6.2 (b) and Figure 6.3).

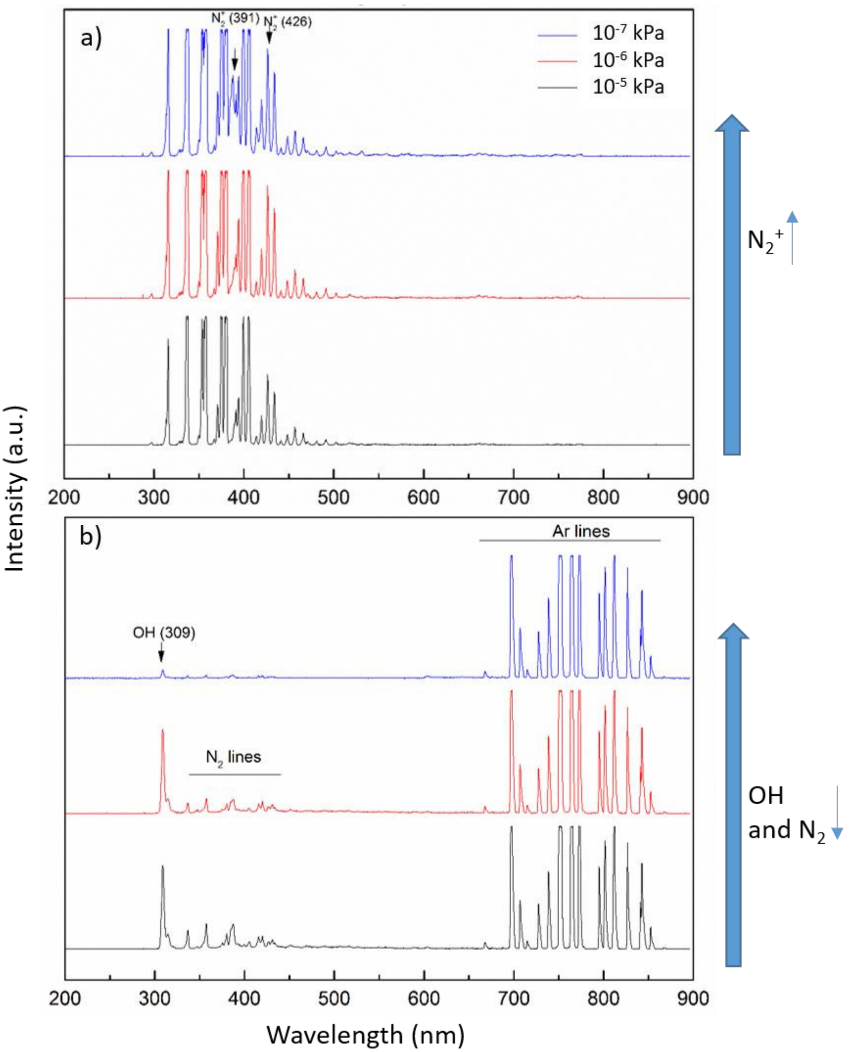

Figure 6.3 OES spectra of the used N_2 (a) and argon (b) discharges when using a plasma reactor base pressure of 10^{-5} ,10^{-6} and 10^{-7} kPa

Finally, it is also important to mention that OES is a recognized technique capable of detecting excited states which are emitting photons due to radiative decay. In both Ar and N_2 discharges, there are considerable amounts of metastables being generated which are considered to be key species in both plasma chemistry and polymer-surface interactions [203]. In order to get more insight in the plasma properties, the electron excitation temperature (T_{exc}) of the discharges under study was also determined from OES spectra. The results of these measurements are provided in the next section.

6.3.3 Electron excitation temperature (T_{exc}) measurements

To be able to measure the T_{exc} in the N_2 plasma under study, a small amount of ammonia gas (<1 %) was added to the N_2 plasma, after which the excitation temperature was calculated using the H_α (656 nm) and H_β (486 nm) atomic lines occurring in the OES spectrum of the discharge. Figure 6.4 (a) shows the Boltzmann plot for the relative populations of the H Balmer states [204] from which a T_{exc} value of 0.84 eV could be determined. To confirm the calculated T_{exc} value of the used N_2 plasma, a second calculation method was also applied using the N_2^+ lines at 391.2 and 426.8 nm (Figure 6.4 (b)) as described by Nassar et al. [205]. The second method confirms the result of the first calculation method as in this case a T_{exc} value of 0.85 eV is found, which is very close to the previously obtained T_{exc} value. As previously mentioned, this electron excitation temperature can be seen as an approximation of the electron temperature (T_e) of the nitrogen DBD used in this work.

In case of the Ar plasma, atomic Ar transitions were used to determine the T_{exc} value by comparing the line intensities of various upper-states as presented in the Boltzmann plot depicted in Figure 6.4 (c). From the obtained Boltzmann plot, it was calculated that the T_{exc} of the N_2 plasma is almost similar to the T_{exc} of the used Ar plasma (0.82 eV) revealing that both discharges under study have an almost identical T_e. Considering that electron impact ionization is one of the dominant processes in sustaining the discharge and that n_e is exponentially depending on T_e [205]:

$$n_e \propto \exp(E_i/k_B T_e) \qquad (6.2)$$

it can be concluded that the ionization degree in both plasmas is very similar.

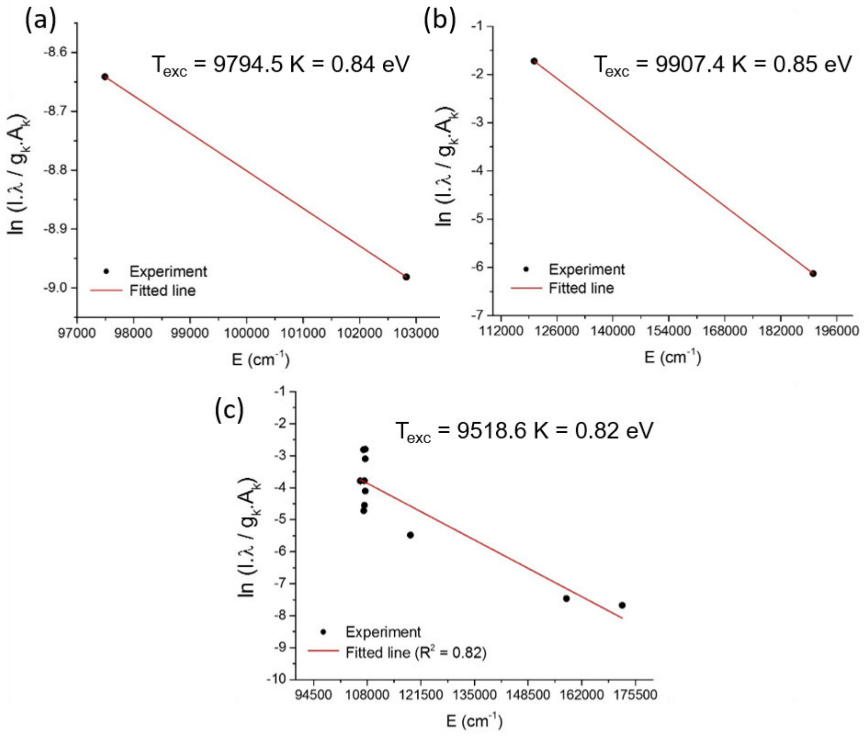

Figure 6.4 Boltzmann plot used for the determination of T_{exc} of (a),(b) the used N_2 plasma and (c) the applied Ar plasma.

6.3.4 WCA results as a function of energy density

Figure 6.5 represents the WCA evolution of the Ar and N_2 plasma-treated UHMWPE films as a function of energy density. Within this context, it is worth mentioning that WCA measurements were carried out solely on plasma-treated samples which were exposed to ambient air after plasma modification (referred to as "indirect" samples in this work) because it was not possible to determine the treatment efficiency with WCA analysis without any exposure to ambient air. This WCA analysis was performed to select the optimal energy density values (or the optimal plasma exposure time) for both discharges under study as only the samples exposed to these optimal conditions will be subjected to XPS analysis.

Figure 6.5 reveals that the WCA on the UHMWPE samples progressively decreases with increasing energy density for both N_2 and Ar plasma treatments until a rather constant, so-called saturated WCA value was reached (N_2 = 41.3 ±

3.3°; Ar = 61.5 ± 3.4°), similar to what was observed in earlier work [53,65,206]. Figure 6.5 also shows that the treatment in N_2 plasma appears to be more effective in reducing the WCA values on the UHMWPE substrates compared to the Ar plasma treatment. Furthermore, the energy density required for reaching the minimal attainable WCA was higher for the Ar discharge than in case of the N_2 discharge, as can be seen from the values mentioned in Table 6.1. According to literature, N_2 plasma treatments typically lead to the simultaneous incorporation of oxygen- and nitrogen-containing polar groups such as amines, amides, peroxides, alcohols, aldehydes, esters… onto the surface of a plasma-exposed polymer [15,75]. In contrast, in case of an Ar plasma treatment, typically only oxygen-containing polar groups are being incorporated, leading to a less profound increase in polymer surface wettability [17,42,53,82,97]. Additionally, as oxygen species are only present as contamination in the Ar and N_2 discharge and nitrogen species are abundantly present in the N_2 plasma (see OES results), it also appear logic that longer plasma treatment times are needed in case of Ar plasma to reach the highest attainable surface wettability. To obtain a deeper knowledge on the UHMWPE surface chemistry after plasma treatment, XPS measurements have been performed on untreated and plasma-treated UHMWPE surfaces exposed to the optimal energy density values, which are indicated in Table 6.1, as the largest differences in surface chemical composition are to be expected for these samples. The obtained XPS results will be extensively described in the following results section.

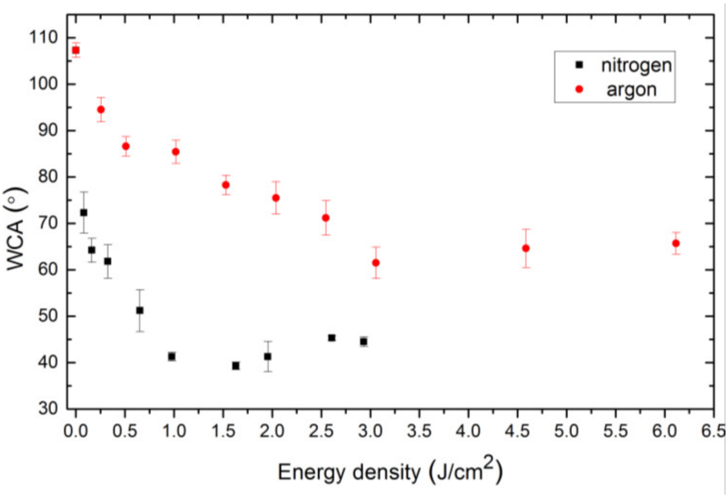

Figure 6.5 WCA evolution on UHMWPE samples as a function of energy density in case of Ar and N_2 plasma treatment.

6.3.5 XPS results

6.3.5.1 N_2 plasma treatment

Table 6.2 represents the atomic composition, determined from XPS survey spectra of the untreated and the N_2 plasma-treated UHMWPE sample for 2 particular conditions: (1) without exposure to ambient air between plasma treatment and XPS analysis (so-called direct XPS analysis) and (2) with exposure to ambient air for different durations ranging from 5 minutes to 21 days (so-called indirect XPS analysis). From Table 6.2, it can be seen that the untreated UHMWPE film already contains a small amount of oxygen, which could be mainly attributed to surface contamination. Table 6.2 also shows that N_2 plasma treatment itself results in a significant nitrogen incorporation on the UHMWPE sample (20.6 ± 0.8 at% for the plasma-treated sample compared to 0 at% for the untreated sample). The abundant incorporation of nitrogen-containing functional groups on the surface can be explained by the following mechanism: excited nitrogen molecules in the discharge are able to break C-C and/or C-H bonds on the polymer surface resulting in the formation of polymer radicals. These radicals will in turn rapidly react with atomic and metastable nitrogen states, namely $N(^4S)$, $N(^2p)$… and N_2^+ ions present in the discharge resulting in the grafting of nitrogen-containing functional groups on the polymer surface [42,197].

Table 6.2 also reveals that during the N_2 plasma treatment, a small amount of oxygen is also incorporated into the UHMWPE samples as the surface oxygen content increases from 1.1 ± 0.1 at% to 2.8 ± 0.4 at% resulting in an O/C ratio of 0.03 after plasma modification. When comparing the observed oxygen incorporation with other studies available in literature, it can be concluded that the N_2 plasma treatment in this work only introduces a very small amount of oxygen to the UHMWPE surface. Indeed, in other studies, authors have reported O/C ratios varying between 0.12 and 0.24 after N_2 plasma treatment of UHMWPE [65,75,206]. The lower oxygen incorporation in this particular work can be mainly attributed to the presence of less oxygen impurities in the used plasma reactor as the reactor base pressure is set to 10^{-7} kPa. In the work of Aziz et al., a much higher reactor base pressure of 0.05 kPa was used [76], while in the paper of Borcia et al. plasma treatment was performed at atmospheric pressure using high nitrogen gas flows to maximally eliminate oxygen contamination [75]. Thanks to the low oxygen contamination in the N_2 discharge used in this work, considerably large amounts of nitrogen could also be incorporated at the UHMWPE substrate resulting into an N/C ratio of 0.26. In contrast, when N_2 plasma treatments were performed in reactors containing high levels of oxygen contamination, much lower N/C ratios have been reported (0.08 to 0.17) [65,75,76]. Oxygen, present even at very low levels, is indeed known to be a very surface reactive species and can thus strongly hamper the incorporation of nitrogen at the polymer surface [15,75]. This work thus clearly reveals the large impact of oxygen traces inside a nitrogen discharge: the more oxygen contamination can be removed from the discharge, the more nitrogen can be incorporated at the polymer surface. In fact, the chemical composition of UHMWPE samples subjected to N_2 plasma treatment was also assessed when using different plasma reactor base pressures. The obtained results depicted in Table 6.3 have indeed revealed that the oxygen incorporation becomes more pronounced and the nitrogen incorporation less intense when higher plasma reactor base pressures were used.

Table 6.2 Surface chemical composition of the N_2 plasma-modified UHMWPE samples without and with exposure to ambient air during different time periods ranging from 5 min to 21 days.

Sample	**C1s (at%)**	**N1s (at%)**	**O1s (at%)**	**O/C**	**(N+O)/C**	**N/C**
Untreated	98.9 ± 0.0	0	1.1 ± 0.1	0.01	0.01	0
Direct	76.6 ± 0.5	20.6 ± 0.8	2.8 ± 0.4	0.03	0.30	0.26
5 min	74.1 ± 0.9	19.8 ± 0.5	6.1 ± 0.2	0.08	0.34	0.26
30min	75.2 ± 1.8	18.6 ± 2.1	6.2 ± 0.3	0.08	0.33	0.24
1 h	75.3 ± 1.6	17.3 ± 2.0	7.4 ± 0.7	0.09	0.33	0.23
3h	73.9 ± 1.9	18.8 ± 2.0	7.3 ± 0.2	0.09	0.35	0.25
4h	74.0 ± 0.7	18.7 ± 0.6	7.3 ± 0.04	0.09	0.35	0.25
5h	74.7 ± 0.6	17.5 ± 0.3	7.8 ± 0.3	0.10	0.33	0.23
6h	74.4 ± 0.5	17.3 ± 0.5	8.3 ± 0.5	0.11	0.34	0.23
24 h	73.8 ± 1.7	17.6 ± 1.2	8.6 ± 1.1	0.11	0.35	0.23
21 days	84.0 ± 1.4	8.1 ± 1.3	7.9 ± 0.6	0.09	0.19	0.09

Table 6.3 Surface chemical composition of the N_2 and Ar plasma-modified UHMWPE samples without ambient air exposure at different base pressures.

Working gas	**Base pressure (kPa)**	**C1s (at%)**	**N1s (at%)**	**O1s (at%)**	**O/C**	**(N+O)/C**	**N/C**
N_2	10^{-5}	75.9 ± 2.3	15.9 ± 1.3	8.2 ± 1.6	0.10	0.31	0.20
N_2	10^{-6}	75.2 ± 1.9	18.2 ± 1.5	6.6 ± 0.4	0.08	0.32	0.24
N_2	10^{-7}	76.6 ± 0.5	20.6 ± 0.8	2.8 ± 0.4	0.03	0.30	0.26
Ar	10^{-5}	88.6 ± 1.0	0	11.4 ± 1.0	0.12	0.12	0
Ar	10^{-6}	90.8 ± 0.6	0	9.2 ± 0.6	0.10	0.10	0
Ar	10^{-7}	94.1 ± 0.6	0	5.9 ± 0.6	0.06	0.06	0

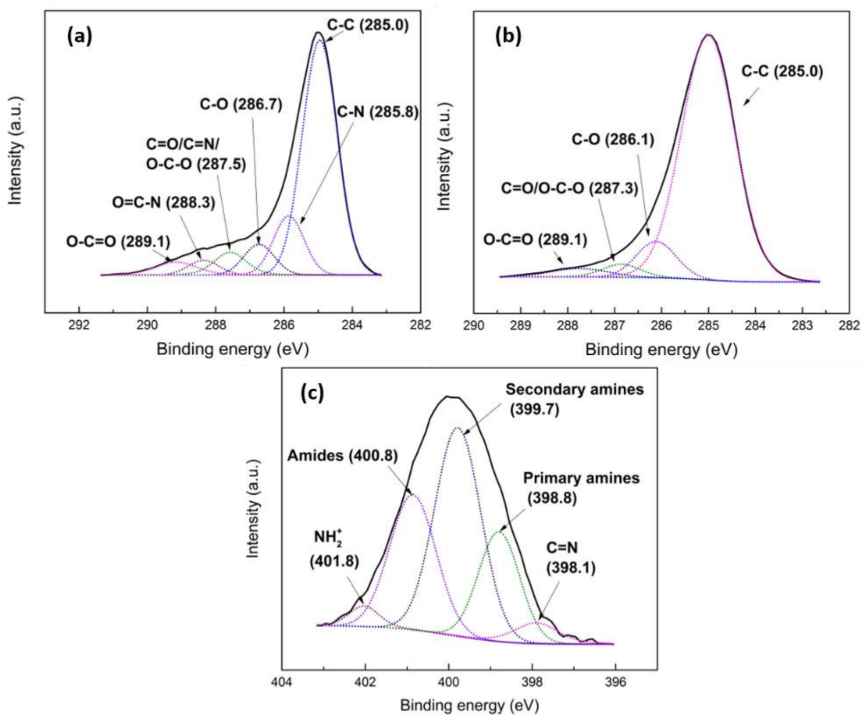

Figure 6.6 Representation of a C1s curve fit in case of N_2 plasma treatment for direct sample (experimental data represented in Table 6.4) (a), Ar plasma treatment for in direct sample- 24h (experimental data represented in Table 6.7) (b) and a N1s fitting of an N_2 plasma-activated UHMWPE sample after storage in ambient air for 6 hours (experimental data represented in Table 6.5) (c).

To reveal more information on the type of functional groups incorporated on the UHMWPE surface upon N_2 plasma treatment, high resolution C1s and N1s peaks have also been fitted according to the procedure described in the materials & methods section. In case of the untreated UHMWPE sample, **C-**C and **C-**O peaks at 285.0 and 286.7 eV (the latter due to surface contamination) were used to obtain a good C1s fit. In contrast, the C1s peaks of the N_2 plasma-modified samples were fitted using 6 different peaks, as shown in Figure 6.6 (a): **C-**C, **C-**N, **C-**O, **C=**O/**C**=N/O-**C**-O, O**=C-**N and O**-C=**O at 285.0, 285.8, 286.7, 287.5, 288.3 and 289.1 eV respectively [60,82,104,193] Based on these C1s XPS fittings, the relative concentration of each carbon-containing surface functional group could be obtained and the results are presented in Table 6.4. These results clearly reveal that the performed N_2 plasma treatment results in the simultaneous incorporation of different polar functionalities including C-N, C-O, C=O/C=N/O-C-

O and O=C-N groups on the UHMWPE surface. After storing the N_2 plasma modified sample in ambient air for 5 min, no significant differences can be seen in the concentration of C-N, C-O, C=O/C=N/O-C-O and O=C-N functional groups. On the other hand, a notable increase in O=C-O groups after a short exposure to ambient air is observable: this increase could be explained by the reaction of remaining free carbon-centered surface radicals ($C^{\bullet}$) after N_2 plasma treatment with ambient oxygen leading to the formation of metastable peroxy radicals and hydroperoxides, which can further decompose to generate a variety of stable functional groups, such as hydroxyl, carbonyl and carboxylic functional groups [63]. In this particular case, mainly carboxylic functional groups seem to appear due to the post-plasma oxidation processes.

Besides fitting the high resolution C1s peaks of the N_2 plasma-modified samples, also the high resolution N1s peaks have been curve fitted in an effort to reveal more information on the type and concentration of the nitrogen containing functional groups. The N1s peaks have been fitted making use of 5 different peaks, as depicted in Figure 6.6 (c): C=**N**, **N**H_2 (primary amines), **N**H (secondary amines), **N**-C=O (amides) and **N**H_2^+ at 398.1, 398.8, 399.7, 400.8 and 401.8 eV respectively [207–209]. From these fittings, the relative concentrations of the nitrogen functional groups have been determined and the results are presented in Table 6.5.

Table 6.4 Relative concentrations (in %) of carbon-containing functional groups on UHMWPE samples after N_2 plasma treatment.

Bands	**Untreated**	**Direct**	**5 min**	**30 min**	**1 h**	**3 h**	**4 h**	**5h**	**6 h**	**24 h**	**21 days**
C-C	95.3 ± 0.5	70.6 ± 0.7	63.8 ± 2.6	68.4 ± 2.5	67.4 ± 1.1	69.5 ± 2.5	66.9 ± 3.7	65.8 ± 0.8	66.1 ± 2.6	67.0 ± 3.3	75.2 ± 1.4
C-N	-	14.7 ± 2.6	15.4 ± 2.3	13.6 ± 2.7	13.5 ± 1.8	14.8 ± 3.3	13.5 ± 4.9	14.9 ± 1.3	15.0 ± 2.6	13.9 ± 1.2	13.5 ± 2.1
C-O	4.6 ± 0.5	6.3 ± 2.2	8.5 ± 0.6	6.2 ± 1.4	7.9 ± 1.6	6.6 ± 1.4	7.6 ± 1.4	6.2 ± 1.0	6.4 ± 1.7	7.0 ± 0.9	7.7 ± 2.2
C=O/C=N/ O-C-O	-	5.7 ± 0.7	6.1 ± 0.7	5.8 ± 1.1	4.1 ± 2.0	4.0 ± 1.0	5.4 ± 1.0	6.8 ± 2.3	4.6 ± 0.8	4.9 ± 0.8	2.1 ± 0.3
O=C-N	-	2.6 ± 0.5	3.4 ± 0.8	3.8 ± 0.8	4.3 ± 2.0	3.6 ± 0.6	3.7 ± 0.3	2.5 ± 0.8	5.1 ± 0.8	4.4 ± 1.3	1.2 ± 0.2
O=C-O	-	0.1 ± 0.2	2.8 ± 0.9	2.2 ± 0.7	2.8 ± 0.6	1.5 ± 0.6	2.9 ± 0.5	3.7 ± 0.3	2.6 ± 0.8	2.8 ± 1.2	0.1 ± 0.2

Table 6.5 Relative concentrations (in %) of nitrogen-containing functional groups on UHMWPE samples after N_2 plasma treatment.

Bands	**Untreated**	**Direct**	**5 min**	**30 min**	**1 h**	**3 h**	**4 h**	**5 h**	**6 h**	**24 h**	**21 days**
C=N	-	7.7 ± 2.1	5.7 ± 2.1	6.9 ± 2.0	5.9 ± 1.5	4.8 ± 3.2	4.3 ± 1.7	6.0 ± 1.4	5.3 ± 1.6	5.9 ± 2.0	4.7 ± 1.7
Primary amines	-	29.9 ± 3.3	25.4 ± 3.9	24.4 ± 3.7	22.2 ± 2.8	24.6 ± 6.4	22.2 ± 2.3	20.8 ± 4.6	22.1 ± 2.7	19.9 ± 2.5	29.5 ± 4.9
Secondary amines	-	39.2 ± 2.3	40.1 ± 1.8	41.6 ± 2.4	42.9 ± 1.8	42.7 ± 5.0	43.5 ± 3.1	41.4 ± 3.0	39.4 ± 2.5	42.9 ± 3.5	37.3 ± 3.1
Amides	-	17.5 ± 0.8	21.9 ± 1.3	21.3 ± 2.2	25.2 ± 1.4	24.6 ± 3.1	25.7 ± 0.9	26.9 ± 2.7	28.0 ± 3.4	25.9 ± 1.4	23.9 ± 1.0
NH_2^+	-	5.7 ± 0.9	6.9 ± 2.7	5.8 ± 1.6	3.8 ± 1.3	3.3 ± 1.7	4.3 ± 0.9	4.9 ± 2.1	5.2 ± 1.8	5.1 ± 1.8	4.4 ± 2.7

According to this table, the actual N_2 plasma treatment mainly results in the incorporation of primary and secondary amines and to a lesser extent amides, which is consistent with the results from the C1s curve fitting. Table 6.5 also reveals that upon 5 min exposure to ambient air, a significant increase in the amount of amides occurs, which was not well observed in the C1s curve fitting due to the low contribution of the amide groups to the total C1s peak. Post-plasma oxidation processes therefore do not only result into the incorporation of O-C=O groups on the UHMWPE substrates, but also lead to the formation of additional amide groups. This additional amide incorporation can be explained as follows: N_2 plasma treatment can result in the cleavage of C-H bonds on the UHMWPE surface leading to the formation of polymer chain radicals at the α-amino carbons. These radicals can rapidly react with oxygen molecules in the atmosphere leading to the formation of peroxy radicals, as indicated in Figure 6.7. Recombination of 2 peroxy radicals can then in turn result into the formation of amides [210].

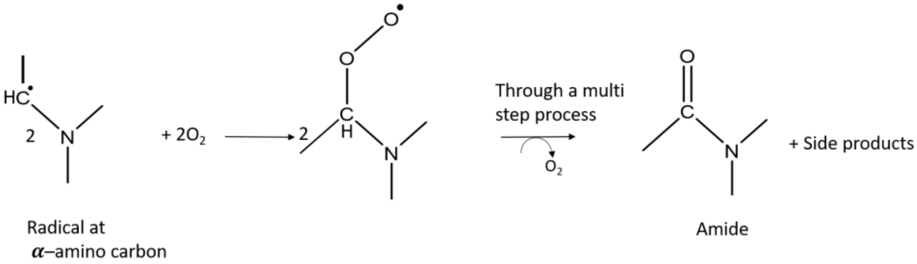

Figure 6.7 Mechanism responsible for the formation of amides on N_2 plasma-treated UHMWPE samples upon exposure to ambient air.

6.3.5.2 Ar plasma treatment

Table 6.6 shows the atomic composition of the Ar plasma-modified UHMWPE samples without air exposure between plasma treatment and XPS analysis (direct sample) as well as after air exposure for time periods ranging from 5 min to 21 days. As can be seen in Table 6.6, as a result of the Ar plasma exposure, the oxygen concentration on the UHMWPE surface strongly increases from 1.1 ± 0.1 at% for the untreated sample to 5.9 ± 0.6 at% after Ar plasma treatment. The XPS results reveal that although the plasma reactor base pressure was set to 10^{-7} kPa, still a considerable amount of oxygen was incorporated on the polymer surface directly during Ar plasma exposure. Nevertheless, at higher base pressures, even higher amounts of oxygen were detected on the UHMWPE surface (Table 6.3).

Moreover, the direct oxygen incorporation was found to be more efficient in case of the Ar plasma treatment compared to the N_2 plasma treatment, where only approximately 3 at% of oxygen was detected on the plasma-treated sample. This observation is in agreement with the fact that large amounts of Ar metastables with high energy are present in the Ar discharge used in this work, as already previously mentioned [211]. These metastables can very effectively break surface C-C and C-H bonds thus creating more surface radicals that can react with the highly reactive O_2 impurities. Based on the OES spectrum of the Ar discharge (Figure 6.2 (b)), it can be concluded that mainly OH radicals will contribute to the oxygen incorporation processes on the UHMWPE substrates. In fact, Ar metastables can as well efficiently dissociate the H_2O molecules present in the feed gas thus producing OH radicals known to play a major role in the chemical processes leading to the incorporation of O-containing groups onto UHMWPE. The oxygen-rich impurities in the discharge can come from air traces remaining in the plasma reactor, from outgassing of the electrodes/dielectrics or from impurities being present in the Ar discharge gas. As already reported in literature, even small concentrations of oxygen impurities in the discharge gas (< 1 ppm) can have an large impact on the final surface chemical composition of polymers [15,42]. When examining the O/C ratio of the Ar plasma-modified UHMWPE sample obtained in this work (0.06) with other O/C values mentioned in literature, it can be concluded that the oxygen incorporation in this work is considerably low. For example, in the work of Aziz et al., where a reactor base pressure of 0.05 kPa was used, a much higher O/C ratio of 0.22 was observed [76]. The considerably low oxygen incorporation in this chapter can be mainly attributed to the low oxygen contamination in the plasma reactor thanks to the low reactor base pressure used and the specific sample introduction procedure applied in this particular chapter (see Table 6.3). On the other hand, some studies have also reported almost no oxygen incorporation after Ar plasma treatment, however, in this case, a very special procedure was followed prior to plasma modification including baking of the plasma reactor above 100°C for 12 hours and flushing with Ar gas for 24 hours [47]. If this extended procedure was not followed, an O/C ratio of 0.04 was detected, which is slightly lower than the value observed in this work due to the fact that a lower reactor base pressure was used (10^{-9} kPa).

Table 6.6 Surface chemical composition of the Ar plasma-modified UHMWPE samples without and with exposure to ambient air during different time periods ranging from 5 min to 21 days.

Sample	**C1s (at%)**	**O1s (at%)**	**O/C**
untreated	98.9 ± 0.6	1.1 ± 0.1	0.01
direct	94.1 ± 0.6	5.9 ± 0.6	0.06
5 min	93.3 ± 0.5	6.7 ± 0.5	0.07
30 min	92.8 ± 0.7	7.2 ± 0.7	0.07
1h	92.5 ± 0.7	7.5 ± 0.7	0.08
3h	92.4 ± 0.7	7.6 ± 0.7	0.08
4h	91.4 ± 0.9	8.6 ± 0.9	0.09
6h	91.7 ± 0.4	8.3 ± 0.4	0.09
24h	88.4 ± 0.9	11.6 ± 0.9	0.13
21 days	95.7 ± 0.3	4.3 ± 0.3	0.04

Table 6.6 also reveals that in contrast to the N_2 discharge, where nitrogen atoms are being added to the polymer surface, active Ar plasma species are not incorporated onto the polymer surface as Ar atoms are not detected on the plasma-modified samples. In the case of Ar plasma treatment, the Ar plasma species most likely break C-C and/or C-H bonds present on the polymer surface, leading to the production of radical sites on the polymer backbone [26]. These radicals will subsequently react with the highly reactive oxygen species (like atomic oxygen and OH radicals) present in the Ar discharge resulting in the formation of oxygen-containing functionalities on the UHMWPE surface. Table 6.6 also shows that after exposing the Ar plasma-treated sample to ambient air for only 5 minutes, a small, but rather non-significant, increase in oxygen content can be observed. This small increase may be due to the fact that some of the carbon-centered radicals formed on the UHMWPE surface remain dangling after Ar plasma exposure: when these radicals are exposed to ambient air, they can react with oxygen molecules present in ambient air resulting in post-

plasma oxidation. This result is in agreement with literature in which post-plasma oxidation processes of Ar plasma-modified polyethylene samples have also been observed upon exposure to ambient air [47].

To reveal more information on the type and the relative concentration of functional oxygen groups incorporated on the UHMWPE surface upon Ar plasma treatment, high resolution C1s peaks have also been fitted according to the procedure described in the materials & methods section. In the case of Ar plasma treatment, the high resolution C1s peaks are decomposed into 4 distinct peaks as shown in Figure 6.6 (b): **C-**C, **C-**O, **C=**O/O-**C**-O and O**-C=**O at 285.0, 286.1, 287.3 and 289.1 eV respectively. Based on the performed C1s XPS fittings, the relative concentration of each carbon-containing surface functional group has been obtained and the results are presented in Table 6.7.

This table reveals that Ar plasma treatment simultaneously introduces different oxygen-containing groups, such as C-O, C=O/O-C-O and O-C=O bonds. Most oxygen is however incorporated in the form of C-O bonds on the Ar plasma-modified UHMWPE samples, which is consistent with other XPS results available in literature [76,212]. When exposing the Ar plasma-modified sample to ambient air for 5 min, a very small increase in O-C=O functionalities can be observed combined with a considerable increase in C-O functionalities, meaning that mainly C-O groups are being incorporated during post-plasma oxidation. Again, as described in the XPS section of the N_2 plasma treatment, remaining free carbon-centered surface radicals react with ambient oxygen leading to the formation of metastable peroxy radicals ($COO^\bullet$) as indicated in Figure 6.8. The reaction of $COO^\bullet$ with water in ambient air can then result in the formation of hydroperoxides (C-O-O-H). Additionally, combination of $COO^\bullet$ radicals with other $C^\bullet$ radicals can lead to the formation of peroxides (C-O-O-C), which can in turn decompose into $CO^\bullet$ radicals. Subsequent reactions between $CO^\bullet$ and $C^\bullet$ radicals can then finally result in the generation of hydroxyl or carbonyl functional groups [63]. The metastable peroxy radicals ($COO^\bullet$) can be also converted into $^\bullet COOH$ radicals via ion-radical chain reactions under particular circumstances [213]. In a subsequent step, $^\bullet COOH$ radicals can then react with CH resulting in the formation of O-C=O, H_2 and $C^\bullet$ radicals (Figure 6.8). In this particular case, mainly C-O and to a lesser extent O-C=O functional groups seem to appear due to the post-plasma oxidation processes, which is in contrast to the N_2 plasma-treated samples on which mostly O-C=O and amide groups were post-plasma incorporated.

Table 6.7 Relative concentration (in %) of carbon-containing functional surface groups on UHMWPE films after Ar plasma treatment.

Bands	**Untreated**	**Direct**	**5 min**	**30 min**	**1 h**	**3 h**	**4 h**	**5 h**	**6 h**	**24 h**	**21 days**
C-C	95.3 ± 0.5	87.9 ± 0.5	83.5 ± 1.7	85.5 ± 2.1	84.3 ± 1.7	80.6 ± 1.5	82.6 ± 0.2	78.6 ± 1.4	82.6 ± 1.7	78.7 ± 3.8	88.7 ± 0.3
C-O	4.6 ± 0.5	7.5 ± 0.6	10.8 ± 1.6	7.7 ± 1.3	11.1 ± 1.4	15.2 ± 0.8	11.7 ± 0.4	12.6 ± 1.0	13.6 ± 1.8	14.3 ± 2.2	7.9 ± 0.2
C=O/O-C-O	-	2.9 ± 0.2	3.3 ± 0.2	5.0 ± 2.4	3.0 ± 0.7	3.2 ± 0.5	2.9 ± 0.2	5.8 ± 0.4	3.1 ± 0.7	4.3 ± 0.6	2.2 ± 0.2
O-C=O	-	1.7 ± 0.2	2.4 ± 0.3	1.8 ± 0.7	1.6 ± 0.5	1.0 ± 0.3	2.8 ± 0.3	3.0 ± 0.5	0.7 ± 0.6	2.7 ± 2.1	1.1 ± 0.1

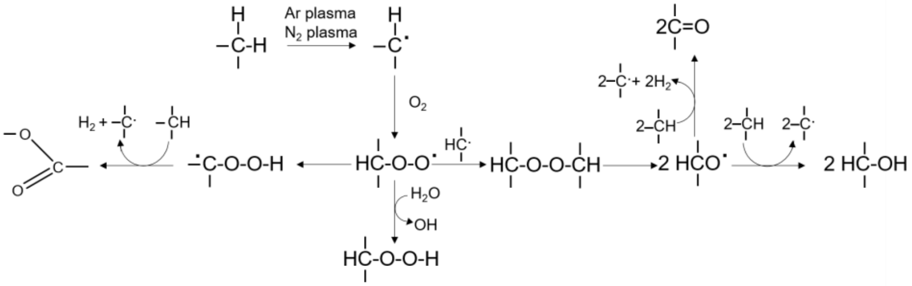

Figure 6.8 Possibly occurring reactions for the post-plasma oxidation of Ar and N_2 plasma-treated UHMWPE samples (formation of C-O functional groups is the most pronounced in case of Ar plasma treatment; formation of O-C=O groups is the most pronounced in case of N_2 plasma treatment).

6.4 Ageing study of N_2 and Ar plasma-treated UHMWPE samples

It is well known from literature that plasma-treated polymers are susceptible to hydrophobic recovery during storage in air (the so-called ageing effect) [26,129]. The induced plasma modification is not permanent since the surface tries to reduce its surface free energy by returning as much as possible to its untreated state. In other words, the behavior of the plasma-induced polar functional groups onto the surface of plasma-modified polymers is known to be dynamic. The reduction in surface free energy can be possible through both reactions with ambient air as well as polymer chain reorientation/migration [26,125,129,130]. In what follows next, the objective was to find out until which time point post-plasma oxidation of the UHMWPE samples takes place and from what time point onwards the reorientation/migration of functional groups and reduction of oxygen takes the upper hand. To do so, WCA and XPS results will be discussed in the following sections and correlated with each other.

6.4.1 WCA results of aged N_2 and Ar plasma-treated UHMWPE samples

In a first step, an ageing study of the saturated plasma-treated UHMWPE surfaces was performed by repeating WCA measurements on samples stored in ambient air over a total period of 21 days and the WCA evolution as a function of storage time for N_2 and Ar plasma-treated samples is presented in Figure 6.9 (a) and (b) respectively.

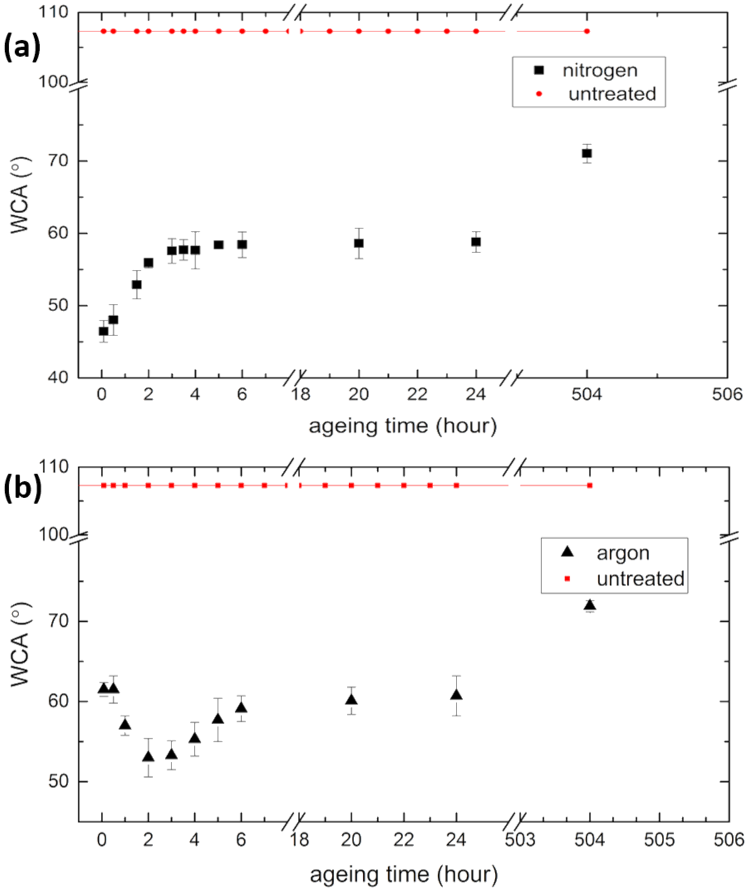

Figure 6.9 WCA variation as a function of ageing time for (a) N_2 and (b) Ar plasma-treated UHMWPE samples.

It can be observed from Figure 6.9 (a) that the WCA value of the N_2 plasma-treated samples almost directly increases after exposing these to ambient air, similar to what has been observed by other research groups [75]. Moreover, the increase in WCA is most pronounced in the first few hours after plasma treatment, stabilizing after 5-6 hours of storage time at approximately 58.4 ± 1.8°. This WCA value is further maintained until 24 hours after plasma treatment. However, after a storage time of 21 days, it seems that the surface hydrophobic recovery does slowly progress upon longer storage, as a WCA value of 71.0 ± 1.3°

is reached in this case. The observed increase in WCA values upon storage in ambient air may be attributed to the reorientation of the plasma-induced polar groups into the polymer bulk or to the migration of small polymer chain fragments into the polymer matrix [26,130].

Figure 6.9 (b) presents the WCA evolution of Ar plasma-treated samples as a function of storage time in ambient air. In this case, it can be seen that the WCA value decreases during the first 2 storage hours reaching a minimal WCA value of 53.0 ± 2.4° after 2 hours of storage in ambient air. This result is very surprising as in most cases, increases in WCA values as a function of storage time are reported for plasma-modified polymers [26,129]. The decrease in WCA value during the first 2 storage hours may be due to post-plasma reactions with oxygen molecules present in ambient air resulting in the introduction of additional polar groups to the surface of the UHMWPE sample which can in turn result in the formation of a more hydrophilic surface [214]. However, after 2 hours of storage in ambient air, the WCA value starts to increase as a function of storage time until a storage time of 6 hours, after which the WCA value stabilizes at a WCA value close to the unaged Ar plasma-modified sample (61.5 ± 0.8°). This stable WCA value is maintained until 24 hours after plasma treatment, after which an increase in WCA value is again noticed reaching a WCA value of 71.9 ± 0.7° after 21 days of storage. As such, after initial post-plasma reactions taken place on the Ar plasma-modified samples within the first 2 hours of exposure to ambient air, the Ar plasma-modified samples start to age in a similar way as the N_2 plasma-treated samples.

In this results section, it is also worth mentioning that even after 21 days of ageing, the WCA values of the Ar and N_2 plasma-treated samples are still considerably lower than the value of the untreated UHMWPE sample, as can be observed in Figure 6.9. WCA analysis thus indicates that a good UHMWPE surface wettability is preserved up until 21 days after plasma treatment, which is in close agreement with previous observations in literature [26,75,82,129,130]. Figure 6.9 also reveals that the ageing behavior is much more pronounced in case of the N_2 plasma-treated sample as after 21 days of storage an almost similar WCA value is reached on the N_2 and Ar plasma-treated samples while the N_2 plasma-treated sample is much more hydrophilic prior to storage. Based on this, it could be concluded that the nitrogen-containing functional groups incorporated during plasma exposure are maybe much more prone to ageing than the oxygen-containing groups introduced on the polymer surface during or after plasma exposure.

6.4.2 XPS analysis of N_2 and Ar plasma-treated UHMWPE samples during storage

6.4.2.1. N_2 plasma-treated samples

Table 6.2 shows the elemental composition of the N_2 plasma-treated samples as a function of storage time. As can be seen in Table 6.2, when storing the samples in ambient air, the nitrogen amount slightly decreases with increasing storage time from 19.8 ± 0.5 at% to 17.6 ± 1.2 at% after 24 hours of storage. This is in agreement with literature, in which a decrease in nitrogen content during ageing has also been previously observed on N_2 plasma-treated polymer films [26,61,62,82] In this work, however, during ageing, also a small increase in oxygen amount can be seen during the first 24 hours of storage in ambient air. Table 6.2 also reveals that after 21 days of ageing, the surface nitrogen content strongly decreases to 8.1 ± 1.3 at% compared to the 1 day aged sample, while the oxygen content remains more or less the same.

To find possible correlations between the increase in WCA angle value observed in Figure 6.9 (a) and the atomic chemical composition of the UHMWPE surface during the storage of the samples in air, the O/C, (N+O)/C and N/C ratios of the N_2 plasma-treated samples have also been calculated as a function of storage time and the results are given in Table 6.2. As expected, during the first storage day, the O/C ratio slightly increases with storage time in combination with a small decrease in N/C ratio. On the other hand, the (O+N)/C ratio remains more or less constant during the first 24 hours after plasma treatment meaning that the total amount of grafted oxygen and nitrogen atoms at the surface is not affected by 1 day of ambient exposure. As the surface wettability does decrease upon storage during the first day, this result thus suggests that the loss in very polar nitrogen-containing functional groups at the polymer surface during storage can probably not be compensated by the incorporation of additional oxygen. Table 6.2 also shows that after 21 days of storage, a strong decrease in N/C and (N+O)/C can be seen in combination with a slightly decreased O/C ratio compared to the 1 day aged sample. The very pronounced loss of mainly the nitrogen-containing functional groups at the UHMWPE surface, which can be highly polar, can in this case explain the strongly decreased wettability when comparing the 1 day and 21 days aged samples.

In this chapter, the high resolution C1s and N1s peaks of the N_2 plasma- treated samples have also been examined as a function of storage time and the resulting relative concentrations of the carbon- and nitrogen-containing functional groups can be seen in Table 6.4 and Table 6.5 respectively. Results reveal that during the first day of storage, the concentrations of all carbon- containing bonds remain quite stable. On the other hand, when looking at the relative concentrations of the nitrogen-containing bonds, some differences as a function of storage time can be seen during the first day. More specifically, the amount of primary amines decreases with increasing storage time, while the concentration of amides simultaneously increases. Other nitrogen functional groups such as C=N, secondary amides and NH_2^+ groups are almost not affected during the first storage day. This result thus suggests that during the first 24 hours of storage in air, the primary amines located at the UHMWPE surface are progressively oxidized to amides. Oxidation of primary amines to amides has already been observed by multiple other researchers when examining the ageing behavior of amino-rich plasma polymers [215,216]. Apparently, this oxidation process also occurs on N_2 plasma-activated UHMWPE samples. The formation of amides at the expense of primary amines can also explain the decreased surface wettability during the first 24 hours of storage as amides are known to be less hydrophilic than primary amines [82].

When comparing the relative concentrations of the carbon-containing functional groups after 1 and 21 days of ageing, large differences can be seen as very strong decreases in the amount of C=O/C=N/O-C-O, O-C=N and O-C=O functional groups occur. On the other hand, the concentration of the C-O and C-N functional groups seem to remain rather unaffected. This observation can be explained as follows: during longer storage periods, the ageing behavior is no longer dominated by chemical oxidative reactions, but by the physical process of surface rearrangement in response to interfacial forces. Indeed, in contact with air, the presence of polar groups at the polymer surface is energetically unfavorable and thus polymer segments carrying such groups tend to move from the top surface into the bulk of the material [26,216,217]. As these groups migrate away from the interface, they are less detected by XPS resulting in an apparent reduction in their relative concentrations. In this particular work, mainly the polymer segments containing C=O/C=N/O-C-O, O-C=N and O-C=O bonds migrate away from the UHMWPE surface, while the C-O and C-N functional groups remain in the top surface. Most likely, these functional groups are more effectively immobilized against transport from the top surface during the N_2 plasma treatment. Moreover, the remaining of some C-O and C-N functional groups at the top surface can also explain the still enhanced surface wettability of the N_2 plasma-modified sample after 21 days of storage in comparison to the untreated sample. When examining the relative concentrations of the nitrogen-containing functional groups after 21 days, it can be concluded that the relative concentration of the primary amines increases, while all other nitrogen-containing functional groups decrease in concentration. This result is thus in agreement with the previously shown XPS results, suggesting that all nitrogen-containing functional groups move away from the top surface, except for the remaining primary amine groups, which are more restricted from transport into the polymer bulk.

6.4.2.2 Ar plasma-treated samples

Table 6.6 represents the atomic composition of the untreated and Ar plasma-treated UHMWPE samples as characterized by XPS with varying ageing time. As shown there, the oxygen content and the corresponding O/C ratio considerably increases during the first 24 hours of storage suggesting that post-plasma oxidation processes not only occur within the first 5 minutes after plasma exposure, but continue to proceed during the first day after Ar plasma exposure. Table 6.6 also reveals that after 21 days of storage, the total post-plasma and some of the in-plasma incorporated oxygen at the polymer surface is diffused into deeper layers as the surface oxygen content is in this case slightly lower than in case of the direct UHMWPE sample. The high resolution C1s peaks of the Ar plasma-treated samples have also been examined as a function of storage time and the resulting relative concentrations of the carbon-containing functional groups can be seen in Table 6.7. According to this table, the concentration of C-O functional groups not only increased during the first 5 minutes of air exposure, but continues to increase within the first 24 hours of storage. On the other hand, the concentration of the other oxygen-containing functional groups (C=O/O-C-O and O-C=O groups) remains more or less stable during the first 24 hours of storage in ambient air.

When comparing the WCA results of the Ar plasma-treated samples with their chemical composition during the first day of storage in ambient air, not a good correlation between the 2 parameters can be found. In fact, XPS measurements performed during the first 24 hours of storage show a gradual increase in surface oxygen content that should normally increase the surface wettability. However, the WCA values only decrease during the first 2 hours, after which the WCA again increases. This apparent contradiction could be explained by the different surface analyzing depth of WCA analysis and XPS: while contact angles are mostly determined by the outer few most angstroms of the polymer surface, the penetration depth of XPS is in the range of 5 to 10 nm [35,37,66]. It could therefore be possible that a high amount of C-O groups incorporated due to post-plasma oxidation processes are present at the top surface during the first 2 hours after Ar plasma treatment and that in this case only a very small amount of C-O groups is present in the subsurface layers. This situation could indeed lead to a considerably low WCA value in combination with a rather low O/C ratio. Upon further oxidation during storage, more C-O functional groups are being incorporated but it may be that more and more polymer segments containing C-O functional groups also continuously diffuse into the subsurface layers leaving only a low amount of C-O functional groups at the top surface. In this particular case, the O/C ratio of the subsurface layer can continue to increase, while the WCA value can increase.

When examining the concentrations of the carbon-containing functional groups on the 1 day and 21 days aged sample, large differences in concentrations can be seen showing considerable decreases in the concentration of all plasma- induced oxygen-containing functionalities. This observation can be explained in a similar way as for the N_2 plasma-treated samples: during longer storage periods, the ageing behavior is no longer affected by chemical oxidative reactions, but is driven by the physical process of surface rearrangement. In case of the Ar plasma-treated sample, during longer storage periods, most polymer segments containing polar C-O, C=O/O-C-O and O-C=O bonds re-orientate from the UHMWPE surface into the bulk or migrate into deeper surface layers, which can in turn explain the considerably increased WCA value of the 21 days aged sample compared to the 1 day aged sample.

6.5 Conclusion

The present study profoundly highlighted the relative importance of in-plasma and post-plasma surface interactions on UHMWPE samples treated with N_2 and Ar DBDs at a medium pressure of 5.0 kPa. OES results revealed that the N_2 discharge was predominantly composed of exited molecular N_2 and N_2^+ states. The OES spectrum of the Ar discharge was predominantly composed of excited Ar lines but also a barely detectable line corresponding to OH radicals as trace amounts of contamination. *In situ* XPS analysis showed a substantially high nitrogen incorporation (20.6 %) onto the polymer surface upon N_2 plasma treatment. This high nitrogen incorporation was accompanied by only a negligible oxygen incorporation (1.1→ 2.8 %) leading to a highly enhanced nitrogen selectivity when comparing to the current state-of-the-art. In fact, nonreactive species present in the discharge are able to generate surface polymer radicals that in turn will react with the chemically active species such the exited N_2^+ ions and atomic N thus grafting N-containing groups onto the surface. More oxygen (5.8 %) was however detected on the Ar-treated samples which is presumably due to the high energy Ar metastables more efficiently breaking surface bonds thus creating more surface radicals that can react with the highly reactive O_2 impurities. Moreover, Ar metastables can as well efficiently dissociate the H_2O molecules present in the feed gas thus producing OH radicals thus leading to the incorporation of O-containing groups onto UHMWPE. Indirect XPS analysis confirmed the occurrence of post-plasma oxidation processes illustrated by reactions between carbon-centered free radicals and ambient oxygen: O-C=O and N-C=O bonds were mainly formed on N_2-treated surfaces while C-O bonds were mostly created on Ar-treated surfaces. From a certain storage time onwards, surface polymeric chain reorientation took over the oxidation processes leading to a decreased surface wettability as a result of the migration of some pre-induced oxygen and nitrogen-containing groups away from the surface. Overall, this work sorts out basic understandings on in-plasma and post-plasma processes occurring on the surface of UHMWPE subjected to Ar and N_2 plasma activation and represents a good reference for future treatment of other polymers.

Chapter 7. Unravelling exclusive in-plasma initiated oxidation processes occurring at polymeric surfaces upon O_2 admixtures to medium pressure Ar and N_2 DBD treatments

7.1 Introduction

The unremitting debate between plasma scientists on the relative implication of in-plasma and post-plasma surface interactions in the oxidation of surfaces subjected to non-oxygen containing discharges has been partly resolved by a number of studies involving *in situ* XPS measurements. The majority of those studies has shed the light on the fact that in-plasma oxidation processes stemming from highly reactive oxygen impurities lingering inside plasma reactors largely contribute to the final surface oxygen content [20,89]. This deduction was confirmed by the study performed in Chapter 6 in which oxygen contaminations could be maximally eliminated by pumping the plasma chamber to a base pressure of 10^{-7} kPa before subjecting UHMWPE to medium pressure N_2 and Ar plasma treatments. In fact, the extent of nitrogen surface uptake that is normally significantly or even completely depleted by the presence O_2 in N_2 discharges could reach an unprecedented value of more than 20 % with less than 3 % of surface oxygen. A slightly higher surface oxygen content was however observed upon Ar plasma treatment because of the highly energetic Ar metastables that were able to generate more surface radicals able to react with O_2 impurities in the plasma chamber. Nonetheless, despite these interesting findings, some important fundamental aspects have not been yet examined. All reported *in situ* XPS analyses were focused on discerning surface chemistries induced by discharges sustained in pure gases such as N_2 and Ar. No study has investigated, to the best of our knowledge, in-plasma initiated oxidation processes by purposely admixing oxygen to the feed gas in order to elucidate its exclusive influence on the surface chemistry without the interference of post-plasma oxidation. By varying the concentration of the added oxygen, this strategy is believed to deliberately decorticate the exact phenomena behind unwanted or desired degrees of plasma-induced surface oxidation. As such, this chapter aims at examining in-plasma initiated oxidation processes occurring at UHMWPE surfaces when exposed to plasmas sustained in Ar and N_2 feed gases admixed with different concentrations of O_2 ranging from 6.2×10^{-3} % to 5 %. In contrast to the available literature focused on low and atmospheric pressures, a DBD operating at a medium pressure of 5.0 kPa is used for the different treatments that are performed after evacuating the plasma chamber to a base pressure of 10^{-7} kPa. A detailed OES characterization of the different discharges is then carried out to unravel insights into the befalling plasma/pure gas and plasma/gas mixture interactions. As such, the active species present in the different discharges are identified which permits to shortlist the possible candidates that could be involved in the surface modifications.

Thereafter, an extensive *in situ* XPS analysis of the plasma-treated surfaces is carried out and careful correlations with the OES diagnostic results are executed. Similarly to the previous chapter, UHMWPE is chosen as model polymer given its simple chemical structure ($-(CH_2-)_n$) and high chemical inertness (little spontaneous surface oxidation or water adsorption). As such, possible side-effects on the polymer surface will be limited, making it easier to identify and distinguish which surface phenomena are exactly taking place.

7.2 Experimental conditions

All experimental details can be found in Chapter 5. The parameters that are specifically used in this chapter are summarized in Table 7.1.

Table 7.1 Specific experimental conditions adopted in this chapter.

Base material	UHMWPE
Plasma gas	Ar, N_2, N_2/O_2 with 6.2×10^{-3} %, 6.2×10^{-2} %, 1 %, 2 %, 3 %, 4 %, 5 % of O_2 and Ar/O_2 with 6.2×10^{-3} %, 6.2×10^{-2} %,1 %, 2 %, 3 %, 4 %, 5 % of O_2
Discharge power (W)	Ar: 1.2 N_2: 2.1 All N_2/O_2 mixtures: 2.4 All Ar/O_2 mixtures: 1.8
Treatment time (s)	Ar: 0-90 N_2: 0-60 All N_2/O_2 mixtures: 0-60 All Ar/O_2 mixtures: 0-50
Energy density at saturated point (J/cm^2)*	Ar: 14.6 N_2: 12.8 N_2/O_2 (O_2: 6.2×10^{-3} %): 14.6 N_2/O_2 (O_2: 6.2×10^{-2} %): 14.6 N_2/O_2 (99/1): 9.7, N_2/O_2 (98/2): 9.7, N_2/O_2 (97/3): 14.6, N_2/O_2 (96/4):14.6, N_2/O_2 (95/5): 19.5 Ar/O_2 (O_2: 6.2×10^{-3} %): 22.0 Ar/O_2 (O_2: 6.2×10^{-2} %): 22.0 Ar/O_2 (99/1): 7.3, Ar/O_2 (98/2): 3.6, Ar/O_2 (97/3): 7.3, Ar/O_2 (96/4): 7.3, Ar/O_2 (95/5): 14.6

Gas flow rate (sccm)	800
Electrode distance (mm)	1
Frequency (kHz)	20
Base pressure (kPa)	10^{-7}
Working pressure (kPa)	5
Surface characterization techniques	WCA: - 2.0 µl-drops of distilled water - Reported value: average of 10 values measured on 2 different samples XPS: - Reported value: average of 6 measurements points for *in situ* XPS measurements

7.3 Results and discussion

7.3.1 Electrical measurements

In order to determine the discharge power and the mode in which the DBDs sustained in pure and mixed gases are (operating, Lissajous plots are acquired. Figure 7.1. depicts the time-averaged Lissajous figures over 10 voltage cycles for N_2, Ar, N_2/O_2 (95/5) and Ar/O_2 (95/5) plasmas. The discharge power is calculated by multiplying the frequency of the feeding voltage (20 kHz) by the electric energy that is actually equal to the area enclosed by the acquired Lissajous figures [135]. It is noticed that by adding oxygen to the discharge, a higher power is required to provoke an electrical breakdown and as such ignite plasma. The reason for this observation presumably resides in the fact that the energy needed to trigger vibrational and rotational excitations of the present oxygen molecules leads to disturbances of the plasma itself. As a consequence, more input power will be necessitated to be able to ignite plasma [218]. Moreover, given the fact that O_2 is an electronegative gas, it can absorb electrons present in the active zone of the discharge via attachment processes through the following reaction [181]:

$$O_2 + e \rightarrow O_2^- \qquad (7.1)$$

This process leads to the formation of negative ions thus causing a reduction in the electron density in the discharge [84]. Therefore, to be able to sustain the discharge in N_2/O_2 and Ar/O_2 mixtures, higher input power and electrical fields are required. In this work, the highest powers that could be applied before the formation of arcs in the plasma chamber are adopted for the pure N_2 and Ar discharges and their counterparts containing an oxygen admixture of 5 %. In order to enable a more accurate comparison between the different tested O_2 admixtures, the same power as the one considered for the highest oxygen concentration (5 %) is applied to ignite the discharges sustained in different N_2/O_2 (2.4 W) and Ar/O_2 (1.8 W) mixtures. All used powers are reported in Table 7.1.

When taking a look at the shape of the plotted Lissajous parallelogram, one can determine in which mode the different discharges are operating. The Lissajous figures of the pure N_2 and the mixed N_2/O_2 discharges (Figure 7.1 (a) & (c)) show both a parallelogram with a rather straight but non-smooth left-hand and right-hand sides distinguished by very small and numerous step-like spikes. This specific shape corresponds to a filamentary discharge that is normally characterized by numerous current pulses of a nanosecond duration at every half-cycle of the applied voltage. In fact, each current pulse indicates a time-dependent spurt of charges on the electrodes and is visualized by a step on the sides of the Lissajous figures. The high number of current pulses present in a filamentary discharge explains the numerous steps of small amplitude observed on the sides of the parallelogram [191]. In contrast, the plotted parallelogram of the Ar plasma exhibits more smooth left-hand and right-hand sides with a barely seen evolution of one or a few depressions corresponding to wider steps (Figure 7.1 (b)). Since the number of steps is equal to the number of the current peaks at every half cycle of the applied voltage, one can deduce that the Ar DBD operates in a glow or multi-pulse glow discharge [191,219]. When adding oxygen to the Ar discharge, a quite similar shape of the Lissajous figure is observed but with a slightly more visible steps especially on the right-hand side of the parallelogram thus elucidating the fact that the discharge operates in a pseudo-glow mode (Figure 7.1 (d)).

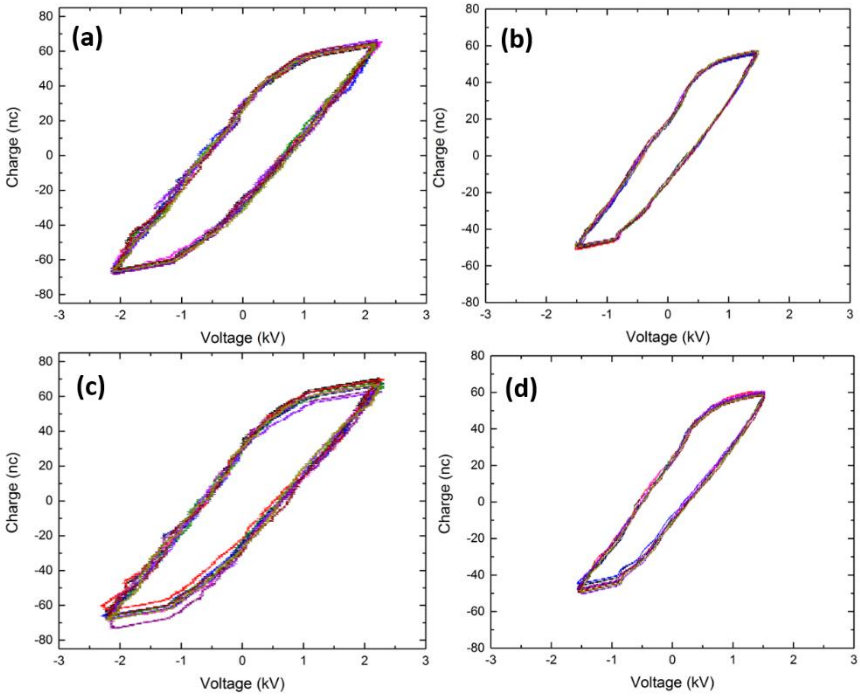

Figure 7.1 Lissajous figures of the discharges sustained in N_2 (a), Ar (b) N_2/O_2 (95/5) (c), and Ar/O_2 (95/5) (d).

7.3.2 OES analyses of the different discharges

Comparative basic optical diagnostics between pure Ar and N_2 discharges and their O_2 admixed counterparts are carried out via OES measurements to decorticate the insights into the implicated gas/plasma interactions. As such, different excited species could be identified thus picking out the potential candidates that are involved in the obtained very diverse surface chemical modifications. Therefore, performing OES measurements for further correlations with *in situ* XPS data is of primordial relevance in this study. The spectra that are shown and analyzed in this section correspond only to plasmas sustained in pure Ar and N_2 and in gas mixtures containing the highest oxygen concentration (5 %). The other gas mixtures containing lower oxygen concentrations are not shown given the fact that the intensity of some of the peaks that appeared due to the presence of oxygen in the discharge was so low that those peaks could be barely visualized.

7.3.2.1 N_2 and N_2 / O_2 plasma spectral analyses

In case of the N_2 plasma, the OES spectrum is dominated by intense peaks located in the wavelength range between 316 nm and 466 nm and attributed to the second positive system of N_2 which is due to the transition $C^3\Pi_u$-$B^3\Pi_g$ [181,193]. Moreover, lower intensity emission lines corresponding to the first negative system of N_2^+ transition $B^2\Sigma_u$-$X^2\Sigma_g$ are visualized at wavelengths between 391 nm and 427 nm. Additionally, an emission of the first positive system of N_2 based on the transition $B^3\Pi_g$ -$A^3\Sigma_u^+$ is perceived in the wavelength range 550 nm–800 nm and is characterized by the lowest peak intensity compared to the other bands [220] (Figure 7.2 (a)). Direct electron impact excitation of relatively low energy of 6.17 eV is presumably giving rise to the population of the excited N_2 ($A^3\Sigma_u^+$) state via the following reaction [181]:

$$e + N_2 (X^1\Sigma_g^+) \rightarrow N_2 (A^3\Sigma_u^+) + e \qquad (7.2)$$

Moreover, inter-vibrational collisions between N_2 molecules can also contribute to the production of the excited N_2 ($A^3\Sigma_u^+$) state as seen in reaction (7.3) [181]:

$$N_2 (\upsilon_1)+ N_2 (\upsilon_2) \rightarrow N_2 (A^3\Sigma_u^+) + N_2 (X^1\Sigma_g^+) \qquad (7.3)$$

The N_2 ($C^3\Pi_u$), N_2 ($B^3\Pi_g$) and N_2^+ ($B^2\Sigma_u$) states can be generated by numerous excitations including electron impact processes of the ground N_2 ($X^1\Sigma_g^+$) state and the first N_2 ($A^3\Sigma_u$) metastable state, pooling reactions, associative excitation and transfer of energy upon interparticle collisional processes. In fact, the ground state of N_2 molecules present in plasma can be excited upon electron impact ionization (7.4) to form the N_2 ($B^3\Pi_g$) state that can be also generated via the pooling reaction (7.5) [221]:

$$e + N_2 (X^1\Sigma_g^+) \rightarrow N_2 (B^3\Pi_g) + e \qquad (7.4)$$

$$N_2 (A^3\Sigma_u^+) + N_2 (A^3\Sigma_u^+) \rightarrow N_2 (B^3\Pi_g) + N_2 (X^1\Sigma_g^+) \qquad (7.5)$$

Moreover, given the fact that the emission peaks of the strongest intensity correspond to the transition $C^3\Pi_u$-$B^3\Pi_g$, the excited N_2 ($C^3\Pi_u$) state is also presumably spawned by direct electron impact processes (7.6) and collision reactions such as the polling reaction of the N_2 ($A^3\Sigma_u^+$) state (7.7) [181,221]:

$$e + N_2 (X^1\Sigma_g^+) \rightarrow N_2 (C^3\Pi_u) + e \qquad (7.6)$$

$$N_2\ (A^3\Sigma_u^+) + N_2\ (A^3\Sigma_u^+) \rightarrow N_2\ (C^3\Pi_u) + N_2\ (X^1\Sigma_g^+) \qquad (7.7)$$

The generation of all the pre-stated excited molecular states of N_2 is known to play an important role in the surface activation of polymers as will be more detailed in the following XPS section [20,222].

Concerning the N_2^+ $(B^2\Sigma_u^+)$ state, it can be potentially formed by impact ionization of electrons via the following reaction [221,223]:

$$e + N_2\ (X^1\Sigma_g^+) \rightarrow N_2^+\ (B^2\Sigma_u^+) + 2e \qquad (7.8)$$

Nonetheless, given the fact that the electron energy required to initiate reaction (7.8) is rather high (> 15.6 to 18.5 eV), the N_2^+ $(B^2\Sigma_u^+)$ excitation is more likely to occur via the collision with N_2 $(X^1\Sigma_g^+)$ molecules having high vibrational states (7.9) [221]:

$$N_2\ (X^1\Sigma_g^+)\ \upsilon_{\geq 12} + N_2^+\ (X^2\Sigma_g^+) \rightarrow N_2^+\ (B^2\Sigma_u^+) + N_2\ (X^1\Sigma_g^+)\ \upsilon_{-12} \qquad (7.9)$$

It is worth mentioning that a discharge sustained at a medium working pressure of 5.0 kPa pressure operates in a the recombination mode, which means that one can neglect the diffusion loss of N_2^+ [182,200]. Interestingly, it was previously reported that these N_2^+ ions have a major impact on the effective incorporation of nitrogen-containing functionalities on an exposed polymeric surface as will be discussed later in this chapter [197]. Since no evidence for the presence of N^+ ions is percieved in the OES spectrum, one can conclude that N_2^+ state is the dominant ionic species in the DBD sustained in N_2 at sub-atmospheric pressure. The occurrence of similar excited species following similar intensity trends was previously detected by Liu et al. who optically characterized a N_2 DBD operating at low and medium pressures [221].

When taking a look at the OES spectrum of the N_2/O_2 plasma, one can distinguish 2 main differences compared to the spectrum of the pure N_2 plasma: 1) the intensity of the emitted N_2 $(B^3\Pi_g - A^3\ \Pi_u)$ peaks is considerably lower and 2) an additional emission of an $NO\gamma$ peak due to the transition $A^2\Sigma^+$-$X^2\Pi_r$ is detected at a wavelength of 297.7 nm (Figure 7.2 (c)). These 2 occurrences are presumably partly connected to each other given the fact that N_2 $(A^3\Sigma_u^+)$ can act as a precursor for the formation of NO when O_2 is present via the following reaction [224–226]:

$N_2\ (A^3\Sigma_u^+) + O_2\ (X^3\Sigma_g^-) \rightarrow NO\ (X^2\Pi_r) + NO\ (X^2\Pi_r)$ (7.10)

Two other frequently reported NO formation pathways are based on: 1) reactions between O atoms and $N_2\ (X^1\Sigma_g^+)$ state producing NO and N atoms and 2) reactions between N atoms and $O_2\ (X^3\Sigma_g^-)$ state generating NO and O atoms [181,226,227]. Nonetheless, Gatilova et al. have demonstrated based on numerical computation that NO formation is more likely to occur via the excited metastable $N_2\ (A^3\Sigma_u^+)$ state [227]. Ono et al. have experimentally confirmed this finding by also showing that NO is mainly sourced from reactions between $N_2\ (A^3\Sigma_u^+)$ state and exited atomic or molecular oxygen [226]. Since the OES spectrum of the N_2/O_2 plasma does not contain any visible peak attributed to atomic oxygen, one can conclude that the formed NO is most probably only attributed to reaction (7.10) that was described in detail by Thomas et al [224]. In fact, the absence of an atomic oxygen peak (777 nm) in the OES spectrum of N_2 and air discharges was also reported by other authors due to the fact that O_2 dissociation requires a relatively high electron energy above 10 eV to occur [20,181].

Once NO is formed, $N_2\ (A^3\Sigma_u^+)$ is also reported to be the principal cause of NO $(A^2\Sigma^+)$ excitation responsible for the characteristic $NO\gamma$ band via the reaction (7.11) [225,228]:

$NO\ (X^2\Pi_r) + N_2\ (A^3\Sigma_u^+) \rightarrow NO\ (A^2\Sigma^+) + N_2\ (X^1\Sigma_g^+)$ (7.11)

Moreover, the ground state NO $(X^2\Pi_r)$ can be electronically excited to generate NO $(A^2\Sigma^+)$ level via the following reaction [228]:

$NO\ (X^2\Pi_r) + e \rightarrow NO\ (A^2\Sigma^+) + e$ (7.12)

Regardless of the formation of NO, adding O_2 to a N_2 discharge was revealed to quench $N_2\ (A^3\Sigma_u^+)$ leading to a decrease in its concentration. The following reaction can for instance occur [227]:

$N_2\ (A^3\Sigma_u^+) + O_2 \rightarrow N_2 + O_2$ (7.13)

It is worth mentioning that no peaks attributed to atomic N can be detected in the OES spectra of both N_2 and N_2/O_2 plasmas. Nonetheless, these N atom transitions are normally known to be very weak when compared to the transition peaks of molecular nitrogen. As such, atomic N could be potentially present but at low concentrations [197]. Such atomic N is known to be primarily produced by electron impact dissociation of excited vibrational N_2 state via the following pathway [20,195]:

$$e^- + N_2 \rightarrow N_2\,(a^1\Pi_g),\ N_2\,(B^3\Pi_g),\ N_2\,(b^1\Pi_u) + e^- \rightarrow e^- + N + N \qquad (7.14)$$

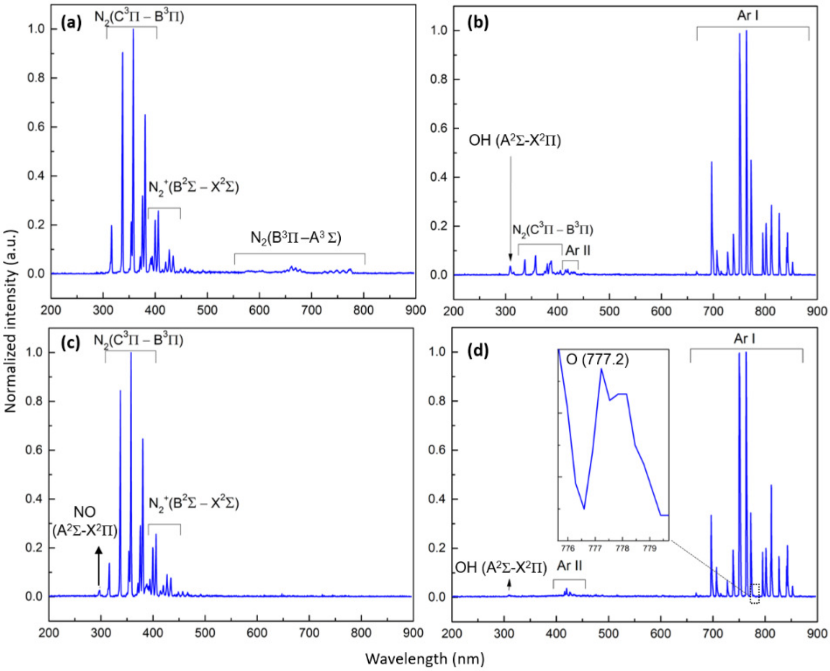

Figure 7.2 OES spectra of (a) N_2 plasma; (b) Ar plasma; (c) N_2/O_2 (95/5) plasma, and (d) Ar/O_2 = (95/5) plasma.

7.3.2.2 Ar and Ar / O_2 plasma spectral analyses

The OES spectrum of the pure Ar plasma, presented in Figure 7.2 (b), is primarily characterized by intense atomic Ar I lines associated with the 4p → 4s transition (Racah notation) at: 696.5 nm ($2p^2 \rightarrow 1s^5$), 706.7 nm ($2p^3 \rightarrow 1s^5$), 727.3 nm ($2p^2 \rightarrow 1s^4$), 738.4 nm ($2p^3 \rightarrow 1s^4$), 750.4 nm ($2p^1 \rightarrow 1s^2$), 763.5 nm ($2p^6 \rightarrow 1s^5$), 772.4 nm ($2p^2 \rightarrow 1s^3$), 794.8 nm ($2p^4 \rightarrow 1s^3$), 801.5 nm ($2p^8 \rightarrow 1s^5$), 811.5 nm ($2p^9 \rightarrow 1s^5$), 826.5 nm ($2p^2 \rightarrow 1s^2$), 842.5 nm ($2p^8 \rightarrow 1s^4$) and 852.1 ($2p^4 \rightarrow 1s^2$) (Paschen notation) [229,230] . The $1s^2$ and $1s^4$ states corresponds to the Ar resonant states, while the $1s^3$ and $1s^5$ states are accredited to Ar metastable [231]. The dominant generation processes of these Ar excited species are the following [230]:

$$Ar + e \rightarrow Ar(4p) + e \quad \text{with } \Delta E \approx 13\text{ eV} \qquad (7.15)$$

$Ar + e \rightarrow Ar(4s) + e$ with $\Delta E \approx 11$ eV (7.16)

$Ar(4s) + e \rightarrow Ar(4p) + e$ with $\Delta E \approx 2$ eV (7.17)

Moreover, Ar II lines are also observed at 415.9 nm ($3p^6 \rightarrow 1s^5$) and 420.1 nm ($3p^9 \rightarrow 1s^5$) but at a much lower intensity. In fact, several authors have also reported a very high emission intensity of Ar I lines compared to Ar II lines in different Ar discharges [229,232]. The generation of the observed Ar(4p) is actually a crucial step in the formation of plasma given the fact that Ar(4p) species are a primordial station in the stepwise generation of electron–ion pairs [232]. Next to the presence of Ar emission lines, emission bands corresponding to the N_2 second positive system due to the transition $C^3\Pi_u$-$B^3\Pi_g$ are detected at a wavelength range of 337 nm-399 nm. Moreover, the spectrum also exhibits an emission band corresponding to OH transition $A^2\Sigma^+$-$X^2\Pi$ at a wavelength of 309.9 nm. These extra N_2 and OH optical emissions that were also previously detected in several other N_2 discharges were attributed to the presence of impurities in plasma [20,230,233]. OH band is most probably accredited to H_2O impurities in the Ar gas and N_2 bands are presumably due to air traces lingering in the reactor or diffusing in the Ar gas flow. A complete evacuation of the reaction is in reality quasi-impossible even when reaching a base pressure of 10^{-7} kPa. As such, N_2 molecules present in the air traces can be excited to the N_2 ($C^3\Pi_u$) state via electron impact as shown in reaction (7.6) or Ar(4s)/Ar(4p) as follows [230,232]:

$N_2 (X^1\Sigma_g^+) + Ar(4s)/Ar(4p) \rightarrow N_2 (C^3\Pi_u) + Ar$ (7.18)

The OH ($A^2\Sigma^+$) is most likely originated from H_2O molecules via the following reactions:

$H_2O + e \rightarrow OH (A^2\Sigma^+) + H + e$ (7.19)

$H_2O + Ar(4s)/Ar(4p) \rightarrow OH (A^2\Sigma^+) + H + Ar$ (7.20)

Despite the fact that the energy needed to excite the ground H state is below the energy level of the Ar(4p) state, the absence of H emission lines in the spectrum was previously accredited by Xiong et al. to the very fast quenching rate of H* by N_2 and O_2 that exceeds the de-excitation time [230].

When having a look at the OES spectrum of the Ar/O_2 discharge, one can notice the disappearance of the N_2 second positive system and a lower OH emission band intensity (309.9 nm). After careful inspection of the spectrum, one can also notice the appearance of a weak emission of O I lines ($3p^5P \rightarrow 3s^5S$) at a wavelength of 777.2 nm (Figure 7.2 (d)) [234]. Therefore, one can deduce that when the concentration of O_2 in the Ar discharge reaches at certain threshold, a small amount of O atoms can be formed either by Penning ionization between Ar metastable and O_2 ($Ar^* + O_2 \rightarrow 2O + Ar$) or by dissociative collisions of O_2 molecules by electrons ($e + O_2 \rightarrow 2O + e$) [84,235]. In contrast, the O_2 admixture triggers a quenching of N_2 and OH lines as a consequence of a total or partial suppression of their excitation and production mechanisms: a phenomenon that was previously observed in other studies upon adding O_2 to an Ar discharge [218,236]. This can be actually due to the high reactivity of O_2 that can absorb electrons via the attachment reaction (7.1) resulting in a certain loss of electrons in plasma [84]. This can as such be partly responsible for the decrease in OH emission line and the suppression of the N_2 lines as their formation through electron impact (reactions (7.6) and (7.19)) will compete with the O_2 attachment processes. Additionally, fewer electrons are expected to collide and excite Ar thus reducing the production of Ar metastable. This will in turn reduce the probability of the occurrence of reactions (7.18) and (7.20) and as such the generation of excited N_2 and OH bands via energy transfer from Ar metastable. In fact, when taking a closer look at the OES spectra, one can notice that the O_2 admixture to Ar plasma causes a decrease in the emission line at 696.5 nm and 772.5 nm corresponding to Ar metastable and an increase in the emission line at 811.5 nm due to an Ar state whose production is sensitive to low-energy electrons [237].

7.3.3 WCA results

In order to evaluate the degree of surface hydrophilicity induced upon the exposure of UHMWPE to plasmas sustained in pure N_2 and Ar and those admixed with 1 % to 5 % of O_2, WCA measurements are performed. Within this context, it should be noted that these measurements were carried out immediately after plasma modification. Moreover, given the unfeasibility of achieving such measurements without exposing the samples to the ambient air, the results are to a certain extent affected by post-plasma surface oxidation. Nonetheless, the comparison between *in situ and ex situ* XPS results done in our previous chapter indicated a dominance of in-plasma processes over post-plasma processes (occurring within 5 min post-treatment) in chemically modifying the surface. As such, although not totally spot-on, the WCA analysis is believed to provide a roughly accurate estimation on the optimal plasma exposure time (or energy density) leading to an exclusive in-plasma saturation of the surface chemical treatment effects. As such, the subsequent *in situ* XPS analysis will be limited to the obtained (sub)optimal conditions.

7.3.3.1 N_2 and N_2 / O_2 plasma case

Figure 7.3 (a) represents the WCA evolution of the N_2 and N_2/O_2 plasma-treated UHMWPE films as a function of plasma exposure time. In case of the N_2 plasma treatment, results reveal that the WCA progressively decreases from a value of 106.8° for the untreated surface to a value of 41.3° after 30 s of plasma exposure. No additional variations in the WCA are noticed at longer treatment times which suggests a saturation of the surface modification processes. Significant differences in the WCA behavior are perceived when adding O_2 to the discharge gas. Generally, the minimal attainable WCA values turn out to be notably higher than the lowest WCA value obtained upon the pure N_2 plasma treatment. Moreover, the so-called saturated WCAs resulting from the saturation of the treatment effects are revealed to be reached at shorter treatment times. When closely examining the results of the different O_2 admixtures, one can distinguish gradual changes accompanying the increase in the O_2 concentration from 1 % to 5 %. These changes are characterized by a progressive increase in the minimal reachable WCA values from 49.5° to 55.8° for O_2 admixtures of 1 % and 5 % respectively. Comparable trends in the WCA results were obtained by Massines et al who subjected PP surfaces to N_2 and N_2/O_2 plasmas [42]. As it was previously reported in literature, N_2 plasma modification normally leads to the concurrent incorporation of N- and O-containing polar groups such as amides, amines, aldehydes, alcohols, esters and peroxides onto the surface [15,75]. Nonetheless, given the fact that oxygen is only present under the form of contamination in the pure N_2 discharge that is characterized by the abundance of exited nitrogen species (as revealed by the OES results), one can assume that considerably more N-containing polar groups would be grafted on the N_2 plasma-treated surface compared to the N_2/O_2 plasma-treated surfaces. Moreover, it also appear logic that when increasing the O_2 concentration in the N_2/O_2 discharge, more O-containing functionalities would be grafted on the surface at the expense of N-containing groups. This probable decrease in the N/O ratio occurring on the UHMWPE surface when increasing the O_2 concentration in the N_2 discharge is presumably responsible for the observed reduced wettability. In fact, N-containing groups were reported to exhibit a higher polarity compared to O-containing groups [11,97]. Moreover, the overall reduction in the saturation time upon O_2 addition to the N_2 discharge suggests that the incorporation of O-containing groups on the surface is faster than that of N-containing groups and might competitively oppress the latter. In order to obtain a deeper knowledge on the UHMWPE surface chemistry after N_2 and N_2/O_2 plasma treatments, extensive *in situ* XPS analysis has been performed in the next sections.

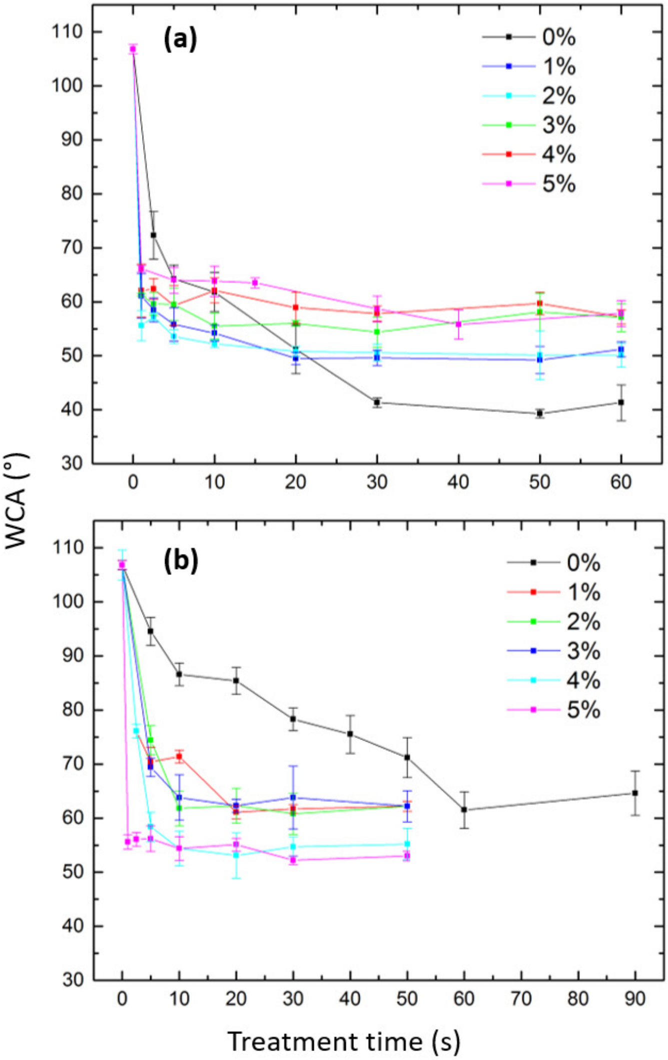

Figure 7.3 WCA evolution as a function of the treatment time upon exposure to: (a) N_2 and different N_2/O_2 plasmas and (b) Ar and different Ar/O_2 plasmas with O_2 admixtures ranging from 0 % to 5 %.

7.3.3.2 Ar and Ar / O_2 plasma treatment

The WCA evolution of the Ar and Ar/O_2 plasma-treated UHMWPE films as a function of treatment time is presented in Figure 7.3 (b). An opposite trend to the one detected for the N_2 and N_2/O_2 plasma-treated surfaces is perceived in this case. In fact, a progressive decrease in the WCA is also observed as the plasma treatment time increases but the minimal attainable value for pure Ar plasma treated surfaces (61.5°) is higher than the one reached in case of Ar/O_2 (95/5) plasma (52.2°). This clearly shows that the hydrophilicity of the surface increases when O_2 is added to an Ar discharge. Moreover, the majority of plasma induced effects take place within the first 20 s of the Ar/O_2 plasma exposure after which a WCA plateau is reached for all mixture ratios. However, in case of Ar plasma modification, the saturated value is attained only after an extended treatment time of 60 s. These observations are in-line with the study performed by Chen et al. in which PS surfaces were subjected to Ar and Ar/O_2 plasmas [238]. In theory, the pure "non-reactive" Ar plasma is only expected to trigger potential changes in the surface topology without any surface functionalization. Nonetheless, given the inevitable presence of oxygen contamination in the reactor, Ar plasma was recurrently reported to exclusively graft O-containing polar groups onto treated surfaces thus enhancing their surface wettability. The non-reactive excited species present in the discharge are able to break C-C and C-H bonds that can subsequently react with O_2 (and OH radicals as detected in OES) thus grafting polar O-containing functionalities onto UHMWPE surfaces [20,33,239]. The very low amount of O_2 traces present in the pure Ar discharge is probably associated with a slower surface functionalization characterized by an ultimate lower amount of grafted functionalities and hence the longer saturation time and reduced wettability. The more the discharge contains O_2, the more O-containing polar groups are incorporated onto its surface leading to the detected enhanced hydrophilicity. In order to confirm these hypotheses, *in situ* XPS characterization has been performed on UHMWPE surfaces after exposure to Ar and Ar/O_2 plasmas for the optimal times giving saturated WCA values. Given the fact that the saturation times of both N_2 and Ar plasmas treatments are longer compared to the mixed plasma treatments, similar exposure times are considered for the samples treated with O_2 admixtures of 6.2×10^{-3} % and 6.2×10^{-2} %. One can therefore ensure that the WCA plateau is already attained at the chosen exposure times. The corresponding optimal energy densities that are adopted in the subsequent XPS analysis are indicated in Table 7.1 for N_2, Ar and all N_2/O_2 and Ar/O_2 plasma treatments.

7.3.4 *In situ* XPS results

7.3.4.1 N_2 and N_2 / O_2 plasma case

Figure 7.4 (a) represents the surface N and O contents, determined from *in situ* XPS survey spectra of the N_2 and N_2/O_2 plasma-treated UHMWPE samples, as a function of the concentration of the added O_2 in the feed gas. It is worth mentioning that a very small amount of surface O (≈1.1 %) is already detected on the surface of the untreated UHMWPE, which could be primarily due to the inevitable surface contamination. Interestingly, plasma modification in the pure N_2 discharge triggers a surface incorporation of an unprecedented large percentage of atomic N reaching 29.1 %. Two successive in-plasma occurring mechanisms are excepted to eventually lead to this abundant N incorporation. The first mechanism involves photons, electrons and the nonreactive excited N_2 species that were detected in the OES spectrum (N_2 ($B^3\Pi_g$), N_2 ($C^3\Pi_g$) and N_2 ($A^3\Sigma_u^+$)). Depending on their energies, all these species were previously reported to excite the polymer surface or break C-C and/or C-H bonds thus engendering the generation of surface polymer radicals. The second mechanism implicates the reaction between these radicals and the chemically active species present in the discharge such as atomic nitrogen states and exited N_2^+ ions which eventually grafts N-containing groups onto the surface [42,197,221]. As already mentioned, very weak non visible OES transitions attributed to atomic N states namely N(^{4}S), N(^{2}p),… known to play an important role in the surface functionalization, could be potentially present [20]. Moreover, exited N_2^+ species, abundantly present in the discharge, were previously reported to also have a major implication in incorporating N onto polymer surfaces. Firstly, N_2^+ ions can acquire a sufficiently high energy to break surface chemical bonds when in proximity to the substrate. Moreover, when N_2^+ ions recombine with the UHMWPE's electrons, a dissociation of N_2^+ can befall via the following reaction:

$$N_2^+ + e_{surface} \rightarrow 2N \qquad (7.21)$$

Reaction (7.21) is exothermic and releases an energy that is also able to break surface chemical bonds. The spawned N atoms can react with the activated sites triggered by the surface initiated dissociative collision of N_2^+ ions thus enhancing the N surface uptake [221]. Figure 7.4 also reveals that a small amount of oxygen is inserted onto the surface as its content increases from 1.1 % to 2.8 % upon N_2 plasma treatment. This perceived slight oxygen incorporation can be originated from the presence of oxygen traces in the used plasma reactor. This means that, despite using a base pressure of 10^{-7} kPa, not all air impurities inside the plasma chamber could be depleted. This was actually further confirmed by the appearance of excited N_2 states in the Ar discharge (Figure 7.2 (b)). Nonetheless, when comparing to other studies involving N_2 plasma treatment of UHMWPE, significantly higher incorporated oxygen amounts and in return lower nitrogen amounts were reported [65,75,206].

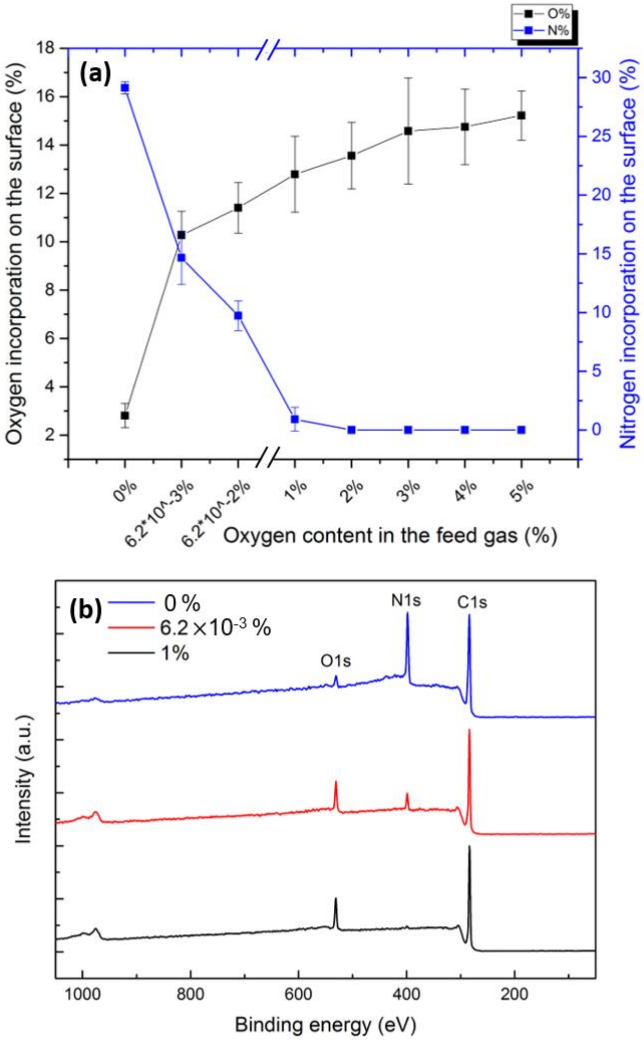

Figure 7.4 (a) N and O contents on the surface of UHMWPE samples subjected to plasma ignited in pure N_2 and different N_2/O_2 mixtures; (b) Example of some of the recorded XPS survey scan spectra.

When taking a closer look at quantitative data, these differences can be clearly highlighted by N/O ratios ranging between 0.11 and 1.04 in literature versus 10.39 in the present study [65,75,76]. This can be attributed to the presence of significantly lower concentrations of oxygen traces remaining in the DBD chamber due to the relatively very low base pressure of 10^{-7} kPa. The importance of low base pressures and their primordial effect on the depletion of surface oxygen was elaborately discussed in the previous chapter: the lower the oxygen contamination in the reactor is, the more nitrogen can be incorporated on the surface [20]. This shows the very high reactivity of O_2 and its strong capacity in obviating the incorporation of surface nitrogen. The very high amount of surface nitrogen (29.1 %) that is reached in this work is, to the best of our knowledge, never attained in previous studies available in literature. Despite using a similar base pressure, a lower but still remarkably high surface nitrogen content of 20.6 % was obtained in the previous chapter. This can be attributed to the difference in the used discharge powers between the previous (0.16 W) and the present study (2.1 W). In fact, by increasing the power a more energetic plasma is ignited thus breaking more surface bonds and triggering the formation of higher densities of excited species such as N_2^+ species which in turn enhances the surface nitrogen uptake [221,240].

The high reactivity of O_2 in N_2 plasmas is actually confirmed by the extreme changes in the surface elemental composition upon the deliberate addition of O_2 to the N_2 flow. Figure 7.4 reveals that when the discharge atmosphere contains only 6.2×10^{-3} % of O_2, about 10.2 % of O is bonded to the surface of UHMWPE at the expenses of the N content that drops to 14.6 %. A progressive increase in the oxygen content to a value exceeding 14 % is thereafter observed when the oxygen portion in the gas mixture is further increased from 6.2×10^{-2} % to 5 %. In return, the nitrogen incorporation onto the surface decreases significantly and becomes completely quenched when the added O_2 in the feed gas exceeds 1 %. Massines et al. have also revealed that by adding only 1.7×10^{-4} % of O_2 to N_2 in a DBD chamber used to treat PP substrates, the surface N content decreased by a factor of 5 while the O content doubled [42]. The main difference between the OES spectra of N_2 and N_2/O_2 discharges is the emission of an $NO\gamma$ peak upon the addition of O_2. This excited NO state could participate in the breakage of the C-C/C-H bonds [222]. Nonetheless, given the high stability of the ground NO state, it is most likely not implicated in the direct surface functionalization. No other excited O-containing species or atomic O could be detected in the OES results. As such, one can conclude that the high surface O content is mainly due to reactions between O_2 molecules and plasma-induced surface radicals. Normand et al. have actually studied the respective effects of atomic and molecular oxygen on the surface functionalization of PE and have come up with the following conclusions: 1) oxygen atoms act as initiators generating surface radicals while 2) oxygen molecules are mainly implicated in the surface functionalization upon reaction with the formed radicals [241]. In case of the N_2/O_2 plasma, the initiation of the functionalization is actually driven by photons, electrons and nonreactive excited NO and N_2 species breaking surface bonds. Thereafter, the added highly reactive O_2 molecules seem to be attracted to the surface radicals faster than N-containing species thus depleting their effects and ending up with a pure oxygen surface functionalization rather than a nitrogen uptake. As such only extremely small amount of O_2 traces in the reactor (6.2×10^{-3} % and 6.2×10^{-2} %) could still allow some N-containing groups to be inserted on the surface. Figure 7.4 (b) depicts the big changes in the N peak intensity of the XPS survey scan spectra recorded on UHMWPE treated with pure N_2 plasma and N_2 discharges admixed with 6.2×10^{-3} % and 1 % of oxygen.

To further investigate the types of functional groups incorporated on UHMWPE surfaces upon N_2 and N_2/O_2 plasma treatments, high resolution C1s and N1s peaks are recorded and analyzed. According to literature, the C1s envelope of the untreated UHMWPE is composed of 2 peaks corresponding to **C**-C/C-H bonds and **C**-O bonds positioned at 285.0 eV and 286.7 respectively with the latter attributed to the detected low-level of oxidation [20]. Following N_2 and N_2/O_2 plasma modifications, the C1s peak exhibits additional contributions at the higher binding energy side due to the probable incorporation of different types of nitrogen- and/or oxygen-containing functionalities displaying the following extra bonds: **C-**N (285.8 eV), **C**=N/ **C**=O/O-**C**-O (287.5 eV) and O**=C-**N (288.3 eV) and O-**C=**O (289.1) eV [20,104,193]. Nonetheless, given the abundance of these bonds and the significant overlap between their binding energies, the C1s envelope is not fitted by separate peaks as the resulting fittings would lead to an erroneous quantification of the different functionalities. The analysis is therefore restricted to a visual comparison between the C1s envelopes of the surfaces subjected to the different plasma treatments. For the sake of clarity, a qualitative comparison between the different N1s envelopes encompassing the following peaks is also carried out: C=**N (**398.1), **N**H_2 (primary amines - 398.8 eV), **N**H (secondary amines - 399.7 eV), **N**-C=O (amides - 400.8 eV and **N**H_2^+ (401.8 eV) [20,208]. The N1s spectra normally exhibit a broad symmetric peak which makes their fitting by separate peaks rather arbitrary and misguiding for the extraction of meaningful data. However, it is very clear from Figure 7.5 (b) that the N1s spectrum of the N_2 plasma-treated UHMWPE is shifted towards the lower binding energy side whereas those corresponding to the treatments with small amounts of O_2 in the feed gas (6.2×10^{-3} % and 6.2×10^{-2} %) are rather shifted towards the higher binding energy side. This means that the pure N_2 treatment incorporates mainly imine and amine groups while the N_2/O_2 treatments tend to incorporate more amide groups on UHMWPE surfaces. The N1s peaks of the samples treated with N_2/O_2 plasmas containing 1 to 5 % of O_2 in the feed gas are not shown as a very small amount or even no nitrogen was inserted onto the surface. The findings deduced from the N1s peaks are actually confirmed when taking a look at the C1s peaks (Figure 7.5 (a)). A close inspection of the C1s envelope of the N_2 plasma-activated substrate additionally reveals that a higher density of imine groups (C=N) compared to amine groups (C-N) is presumably inserted onto the surface. This dominance of C=N groups over C-N groups on UHMWPE surfaces subjected to N_2 plasma in in agreement with a previous study conducted by Wagner et al. [197] The insertion of amides upon the addition of small amounts of oxygen (6.2×10^{-3} % and 6.2×10^{-2} %) can be explained as follows: the non-reactive species in the discharge can trigger the generation of polymer chain radicals at α-amino carbons. Thereafter, a rapid reaction between these radical and the O_2 added to the feed gas takes place thus forming peroxy radicals. Each 2 peroxy radicals can then recombine resulting in the formation of an amide group [20,210]. The corresponding reaction is shown in Figure 6.7 of chapter 6. When adding higher O_2 concentrations (1-5 %) to the feed gas, oxygen-containing functionalities such as C-O and O=C-O are solely incorporated onto the surface via reactions between O_2 and plasma-induced surface radicals. Some of these possible reactions are shown in Figure 6.8 of Chapter 6.

Overall, the surface reactions occurring upon the exposure of UHMWPE to N_2 and N_2/O_2 plasmas can be categorized in 3 different pathways:

- In pure N_2 plasma, reactions of carbon-centered surface radicals ($C^{\bullet}$) with active species (N atoms and N_2^+ ions) result in the formation of N-containing functional groups namely C-N and C=N on the surface.
- In N_2/O_2 plasmas containing very low amounts of O_2 (6.2×10^{-3} % and 6.2×10^{-2} %), the formed polymer radicals react with reactive nitrogen species and O_2 in the feed gas inserting N- and O-

containing functional groups such as C-O, C=N and O=C-N onto the surface.

- In N_2/O_2 plasmas sustained in gas mixtures containing O_2 concentrations exceeding 1 %, the plasma-induced surface radicals solely react with O_2 molecules that completely deplete the incorporation of N onto the surface. In fact, O_2 molecules are highly reactive thus rapidly reacting with the surface radicals in a way overpowering the reactions with nitrogen species.

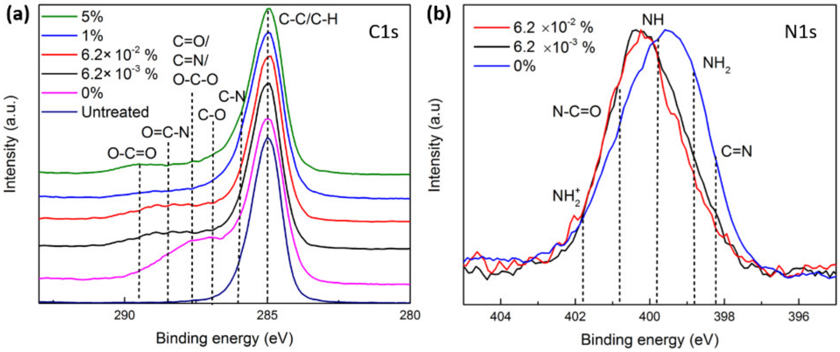

Figure 7.5 High resolution C1s and N1s spectra of untreated and plasma-treated UHMWPE in pure N_2 and different N_2/O_2 mixtures

7.3.4.2 Ar and Ar / O_2 plasma treatments

Figure 7.6 depicts the surface O content of the samples modified with Ar and Ar/O_2 plasmas as a function of the concentration of the added O_2 in the feed gas, as determined from *in situ* XPS survey scans. Upon plasma modification in the pure Ar discharge, the surface oxygen concentration remarkably increases from 1.1 % (pristine sample) to 7.8 %. In theory, a pure Ar atmosphere should not contain chemical reactive species leading to an oxygen incorporation onto the surface. However, this notable amount of inserted surface oxygen can be to a big extent attributed to the presence of residual air lingering in the plasma chamber in addition to impurities present in the Ar feed gas and potential outgassing of the electrodes [20]. The incomplete evacuation of the plasma chamber was actually confirmed by the emission of excited N_2 lines in the OES spectrum (Figure 7.2 (b)). As such, given the fact that the base pressure pre-plasma treatment was set to 10^{-7} kPa, one can conclude that the presence of oxygen traces is sufficient to induce oxygen-based surface functionalization. This finding is actually in agreement with previous literature studies showing that the effect of even very small concentrations of impurities in the feed gas (< 3ppm) is associated with pronounced variations in the surface chemical composition upon plasma modification [15,20,42,242]. Nonetheless, it is worth emphasizing on the fact that in this chapter, the O/C (0.08) ratio of Ar plasma-treated UHMWPE is substantially lower than the ones obtained in other studies in which higher plasma base pressures were adopted. For instance, Teodoru et al. and Aziz et al. have subjected UHMWPE to Ar DBD treatments where higher base pressures were used and have obtained a surface O/C ratios of 0.17 and 0.22 respectively [76,243]. When comparing between the surface oxygen incorporation occurring in pure Ar plasma (O content: 2.8 %) and pure N_2 plasma (O content: 7.8 %), one can clearly notice its more prominent incidence in Ar plasma. This can be presumably attributed to the more energetic Ar metastables generated in Ar plasma compared to the excited species produced in N_2 plasma. These metastables that were detected in the OES together with some excited N_2 species, can very efficiently break surface C-C and C-H bonds thus creating more surface radicals that can react with O_2 [244]. As already mentioned, oxygen molecules are highly reactive which leads to a rapid initiation of reactions between them and the plasma-induced radicals thus functionalizing the surface [241]. Moreover, Ar metastables could as well efficiently dissociate the H_2O molecules present in the feed gas and plasma chamber thus producing OH radicals as was seen in the OES spectrum. These radicals are known to play a major role in the chemical processes leading to the incorporation of O-containing groups onto UHMWPE; hence the higher surface O content [20].

The moment 6.2×10^{-3} % of oxygen is added to the gas flow, a sharp increase in the surface oxygen content is detected (12.3 %). Moreover, by adding more oxygen to the feed gas (from 6.2×10^{-3} to 5 %), a further progressive and less steep increase in the O content reaching a value of 16.3 % is perceived. This shows that the evolution of the incorporated oxygen amount onto the surface runs in parallel with the amount of the added O_2 in the gas mixture. This evolution is nicely represented by the decrease in the O peak intensity in the XPS survey scan spectra (Figure 7.6 (b)). These results are in-line with a previous study performed by Gerenser et al. [61]. In fact when more O_2 is present in the discharge, more surface radicals are excepted to react with O_2 molecules instead of interacting with each other which eventually leads to more O-containing functionalities inserted on the surface with a lower degree of cross-linking. When taking a look at the OES spectrum of the Ar/O_2 discharge, one can detect the disappearance of the excited N_2 emission lines that is compensated by the appearance of a small atomic O line (Figure 7.2 (d)). This atomic O was reported to be very powerful in initiating the surface functionalization by generating surface radicals [241].

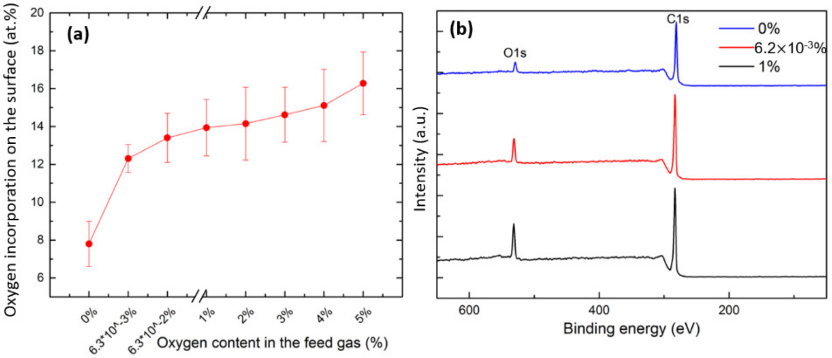

Figure 7.6 (a) O content on the surface of UHMWPE samples subjected to plasma ignited in pure N_2 and different N_2/O_2 mixtures; (b) Example of some of the recorded XPS survey scan spectra.

In order to get more insight into the types and relative concentrations of the different oxygen-containing functionalities inserted on the surface of UHMWPE upon Ar and Ar/O_2 plasma treatment, high resolution C1s peaks have been recorded and analyzed. Such C1s envelopes induced by Ar and Ar/O_2 plasma treatments can be decomposed into 4 distinctive bonds as shown in Figure 7.7 (a): **C**-C, **C**-O, **C**=O/O-**C**-O and O-**C**=O at 285.0, 286.1, 287.3 and 289.1 eV respectively [13,20,33,114]. Given the fact that no nitrogen-containing functionalities are incorporated onto the surface, the C1s envelope is fitted by the different peaks attributed to the abovementioned bonds. Since these peaks are relatively distant from each other, a quite accurate quantification of the different functional groups can be obtained.

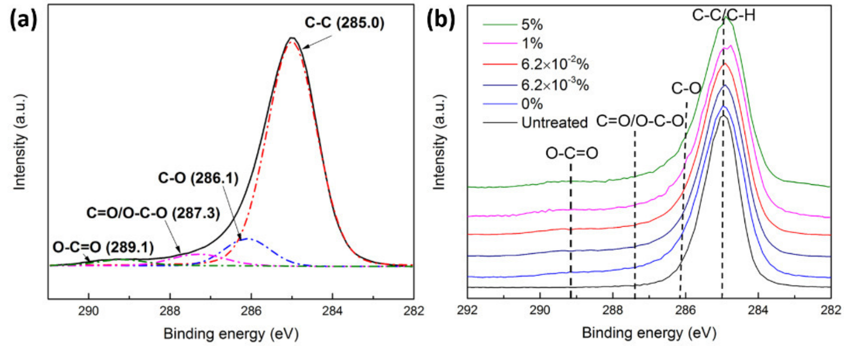

Figure 7.7 a) Representation of a characteristic C1s curve fitting in case of Ar and Ar/O_2 plasma treatments; b) High resolution C1s spectra of untreated and plasma-treated UHMWPE in pure Ar and different Ar/O_2 mixtures.

Based on the carried out C1s XPS fittings, the relative concentration of each carbon-containing group has been acquired and the results are presented in Table 7.2. Result reveal that Ar and Ar/O_2 plasma treatments simultaneously introduce different oxygen-containing functional groups, such as C-O, C=O/O-C-O and O-C=O bonds. However, most oxygen is incorporated in the form of C-O bonds (≈ 10 %) on all Ar and Ar/O_2 plasma-modified UHMWPE samples, which is consistent with other *ex situ* XPS results available in literature [76,212]. It is worth mentioning that the relative concentration of all added groups is more or less similar as the oxygen concentration increases in the feed gas. As such, one can conclude that by adding more oxygen to the feed gas, the overall surface O content increases but this oxygen is incorporated under the form of relatively equal portions of chemical bonds going along with the following order of descending concentrations: C-O (≈ 10 %), C=O/O-C-O (≈ 3.5 %) and O-C=O (≈ 2 %). These groups are inserted on the surface upon different chemical processes triggered by the reaction of O_2 with the plasma-induced carbon-centered surface radicals [20]. Some of these reactions is shown in Figure 6. 8 of Chapter 6.

Table 7.2 Relative concentration (in %) of carbon containing functionalities on UHMWPE films after Ar and Ar/O_2 plasma treatments.

Bands	**Untreated**	**Pure Ar**	**6.2×10^{-3} %**	**6.2×10^{-2} %**	**1 %**	**2 %**	**3 %**	**4 %**	**5 %**
C-C	95.3 ± 0.5	83.8 ± 1.3	84.3 ± 0.5	84.4 ± 1.1	82.7 ± 1.8	85.1 ± 1.7	83.6 ± 0.8	83.3 ± 1.1	82.1 ± 1.7
C-O	4.6 ± 0.5	10.7 ± 0.9	10.1 ± 0.3	9.8 ± 0.6	10.9 ± 1.6	9.4 ± 09	10.9 ± 1.0	10.9 ± 1.3	10.8 ± 1.5
C=O/O-C-O	-	3.6 ± 0.1	3.3 ± 0.3	3.3 ± 0.2	3.8 ± 0.4	3.2 ± 0.3	3.9 ± 0.4	3.5 ± 0.3	4.3 ± 0.5
O-C=O	-	1.6 ± 0.3	2.1 ± 0.2	2.2 ± 0.3	2.3 ± 0.5	2.1 ± 0.5	2.1 ± 0.3	2.1 ± 0.4	2.7 ± 0.4

7.4 Conclusion

In the present chapter, an extensive comparative study on in-plasma processes occurring at UHMWPE surfaces subjected to plasmas sustained in pure Ar and N_2 versus different Ar/O_2 and N_2/O_2 mixtures (O_2 concentration ranging from 6.2×10^{-3} % to 5 %) was conducted. As such, exclusive in-plasma initiated oxidation processes and their effects on the final surface chemical composition were examined without the interference of post-plasma oxidation. To do so, OES measurements were firstly carried out to decorticate the influence of the different gas compositions on the generation of excited species playing a major role in the subsequent surface chemical modifications. Results revealed the predominant presence of different excited molecular nitrogen species (N_2 ($C^3\Pi_u$), N_2 ($B^3\Pi_g$) and N_2 ($A^3\Sigma_u^+$)) and ionic nitrogen states (N_2^+ ($B^2\Sigma_u$) in the pure N_2 discharge. When O_2 is added to N_2, an additional OES emission line attributed to excited NOγ was detected. The pure Ar discharge was primarily characterized by Ar resonant states and metastables in addition to excited OH ($A^2\Sigma^+$) and N_2 ($C^3\Pi_u$-$B^3\Pi_g$). The latter 2 excited species were attributed to the presence of air and H_2O traces in the plasma reactor. The moment O_2 is added to the Ar flow, a weak emission of an atomic O line and the disappearance of the excited N_2 species were noticed. Thereafter, profound correlations between OES results and *in situ* XPS measurements were carefully conducted to shortlist the species interacting with the surface and leading to the obtained diverse surface chemistries. Interestingly, plasma modification in the pure N_2 discharge triggers a surface incorporation of an unprecedented large percentage of atomic N reaching 29.1 %. In fact, photons, electrons and excited N_2 molecules present in the discharge are able to generate surface polymer radicals that will in turn react with the chemically active species namely atomic nitrogen, nitrogen metastables and the exited N_2^+ species thus grafting N-containing groups onto the surface. The used very low reactor base pressure of 10^{-7} kPa is actually behind the very low surface oxygen incorporation (2.8 %). More surface oxygen is however detected after Ar activation which is probably due to the high energy Ar metastables more efficiently breaking surface C-C and C-H bonds thus creating more surface radicals that can react with the highly reactive O_2 impurities. Moreover, Ar metastables can as well efficiently dissociate H_2O molecules present in the feed gas thus producing OH radicals known to play a major role in the incorporation of O-containing groups onto surfaces. A very high reactivity of O_2 in N_2 plasmas was perceived via the detected extreme changes in the surface elemental composition upon the deliberate addition of O_2 to the N_2 flow. In fact, a steep rise in the O surface content at the expenses of N content (14.6 %) was detected upon the addition of only 6.2×10^{-3} % of O_2 to the feed gas. When the added O_2 exceeded 1 %, the nitrogen incorporation onto the surface becomes completely quenched. In this case, the surface radicals created by the non-reactive plasma species are probably rapidly reacting with the highly reactive O_2 molecules in a way overpowering the reactions with nitrogen species. The moment a small concentration of O_2 is added to the Ar gas flow, a sharp increase in the surface oxygen content is also detected. Thereafter, the evolution of the surface oxygen amount runs in parallel with the amount of the extra O_2 added in the gas mixture. In fact when more O_2 is present in the discharge, more surface radicals are excepted to react with O_2 molecules instead of interacting with each other which eventually leads to more O-containing functionalities inserted on the surface. Overall, one can conclude that in-plasma oxidation processes initiated by the presence of O_2 in the plasma reactor can, depending on the O_2 concentration, strikingly change the surface chemistry of UHMWPE exposed to N_2 and Ar plasmas.

Chapter 8. Integrative effects of coral particles addition and plasma treatment on the properties of chitosan/polyethylene oxide NFs intended for bone tissue engineering

The results of Chapter 8 were published in the following peer-reviewed journal:

Parinaz Saadat Esbah Tabaei, Mahtab Asadian, Rouba Ghobeira, Pieter Cools, Monica Thukkaram, Parviz Gohari Derakhshandeh, Sara Abednatanzi, Pascal Van Der Voort, Kim Verbeken, Chris Vercruysse, Heidi Declercq, Rino Morent and Nathalie De Geyter. "Combinatorial effects of coral addition and plasma treatment on the properties of chitosan/polyethylene oxide nanofibers intended for bone tissue engineering." *Carbohydrate Polymers* 253: Art. No. 117211 (2021).

8.1 Introduction

After fundamentally analyzing the chemical processes occurring at polymeric surfaces in-plasma and post-plasma activation, this experimental chapter is actually directed towards the application of plasma treatment in BTE. The previously stated benefits of electrospinning and plasma activation are underlined by their joint use in the engineering of the used scaffolds. The base materials forming the scaffolds have been carefully selected for an optimal outcome paving the way towards a complete bone tissue recovery. Both natural and synthetic polymers, such as poly (lactide-co-glycolide) (PLGA), PLLA, PCL, gelatin, collagen and CS have been successfully utilized to produce electrospun NFs that demonstrated enhancement in bone formation [24,45,142,245–248]. Among the mentioned polymers, CS, the deacetylated form of chitin, has been widely used, mainly due to its biocompatibility, biodegradability, bioresorption and non-toxicity. Additionally, its specific interactions with components of the bECM and growth factors make CS an ideal candidate for use in bone regeneration [140]. Moreover, the molecular structure of CS contains hydroxyl (-OH) and amino (-NH_2) groups that facilitate cell adhesion, proliferation, and differentiation. Although CS-containing NFs already showed promising results for numerous BTE systems [24,142], the CS electrospinnability is still challenging due to the limited solubility of CS as a result of the formation of a polyelectrolyte in an acidic solution [24,140,249]. To circumvent the abovementioned issue, blending of CS with other polymers such as PEO, PCL and PVA prior to electrospinning has been utilized to improve the electrospinnability of CS, among which PEO (a hydrophilic, biocompatible synthetic polymer) is by far the most widely used blending polymer [136,249–251]. Adding PEO to CS solutions was not only found to improve the electrospinnability of CS, but also further improved the hydrophilicity of the CS-containing NFs [140,250,251]. However, by following this approach, the required bioactivity of the CS/PEO NFs was still not fully achieved, because CS does not have sufficient bioactive sites and shows only limited osseointegrative capacity to facilitate cell growth [24].

To further improve cell-surface interactions on and osteoinductivity of NFs, the incorporation of additional biocomponents has been suggested, among which coral particles has been considered as a promising reinforcement agent to enhance NF bioactivity [147,252,253]. More than 98 % of natural coral consists of calcium carbonate ($CaCO_3$) which could serve as an effective substrate for bone regeneration [147,254]. According to literature, $CaCO_3$ can be converted into hydroxyapatite (HA) ($Ca_{10}(PO_4)_6(OH)_2$), which is one of the main mineral components of bone [147,253]. It has been reported that when coral particles is added to CS-based scaffolds, an enhancement in cell viability in addition to yielding a more well-defined cell morphology occurs in comparison to pristine CS-based scaffolds [147]. As a result, the combination of appropriate organic (CS, PEO) and inorganic (coral) materials provides an excellent alternative choice to gather the best properties of each phase while overcoming many of their deficiencies (when used as unblended materials) [147].

In view of the above, the main objective of this chapter is to adopt an exclusive integrative strategy in the development of a bone tissue-engineered scaffold encompassing refined surface chemical, topographical and biomolecular cues thus successfully repairing bone defects. In fact, taking all previous findings into account, it is hypothesized that adding coral particles to CS-containing nanofibrous meshes together with subsequent plasma surface modifications may enhance osteoblast-surface interactions, apatite mineralization and osseointegration and therefore bone regeneration. To the best of our knowledge, this advanced approach has not been examined yet. As such, the present study will investigate the effects of a non-thermal plasma treatment on electrospun CS/PEO and Coral/CS/PEO NFs by means of a DBD sustained in N_2, air and Ar. Subsequently, the plasma-induced effects will be examined in detail making use of WCA, tensile measurements, XPS, SEM, and FTIR on both sets of NFs. Moreover, the *in vitro* performance of CS/PEO and Coral/CS/PEO NFs will be investigated by seeding MC3T3 cells on untreated and plasma-treated NFs followed by live/dead fluorescence imaging and MTT assays. Finally, to further investigate the bioactivity of the fabricated NFs, the deposition of CaP minerals will also be evaluated after immersing the samples in SBF.

8.2 Experimental methods

All experimental details can be found in Chapter 5. The parameters that are specifically used in this chapter are summarized in Table 8.1.

Table 8.1 Specific experimental conditions adopted in this chapter.

Base material	CS/PEO Coral/CS/PEO
Plasma gas	Ar, air, N_2
Discharge power (W)	Ar: 0.2 Air: 0.6 N_2: 0.7
Treatment time (s)	Ar: 0-180 Air: 0-180 N_2: 0-180
Energy density range (J/cm^2)	Ar: 0-7.3 Air: 0-22.0 N_2: 0-25.7
Energy density at saturated point for CS/PEO NFs (J/cm^2)	Ar: 4.9 Air: 9.8 N_2: 5.7
Energy density at saturated point for Coral/CS/PEO NFs (J/cm^2)	Ar: 4.9 Air: 9.8 N_2: 17.1
Gas flow rate (sccm)	800
Electrode distance (mm)	1
Frequency (kHz)	20
Base pressure (kPa)	10^{-5}
Working pressure (kPa)	5
Surface characterization techniques	WCA: - 2.0 µL-drops of distilled water. - Reported value: average of 5 values measured on 3 different samples. XPS: - Reported value: average of 4 values measured on 2 different samples.

8.3 Results and discussion

8.3.1 Characterization of coral powder via XRD and SEM/EDS measurements

In order to evaluate the crystalline phase of coral, XRD measurements were performed on the powder (Figure 8.1). The XRD spectrum revealed that coral particles are composed of calcium carbonate with major peaks associated with aragonite phase and fewer peaks ascribed to trace amounts of the calcite phase [255,256]. Similar results were previously obtained for natural marine coral particles obtained from different sources such as Brazilian and Irish coral particles [255,257]. It is worth mentioning that aragonite crystals in particular trigger a fast cell invasion, adhesion and proliferation. In fact, it was previously reported that the architectural configuration of the aragonite crystalline particles provides better adhesion sites for cells than other configurations and thus faster cell invasion [147,258]. A fast cell invasion is actually beneficial as it means rapid integration into the bone structure [259]. In fact, cells grown on coralline aragonite can directly make use of the present calcium ions which in turn affects their behavior and allow a control over their differentiation [147,258].

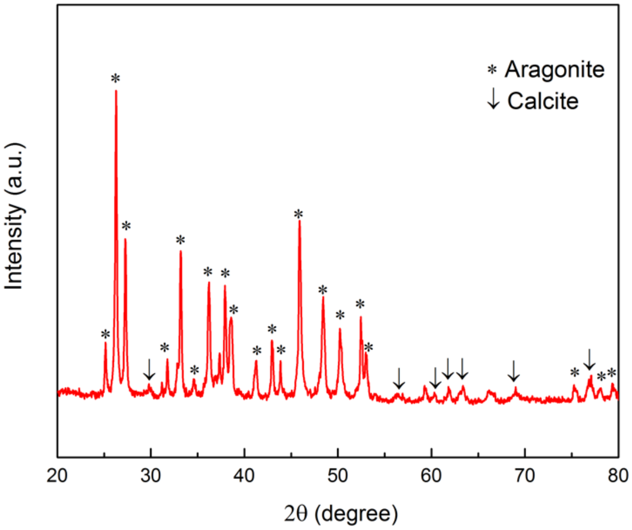

Figure 8.1 XRD spectrum of coral powder.

Besides XRD measurements, SEM-EDS measurements are acquired and can be found in Figure 8.2. The EDS elemental spectrum reveals the presence of Ca, C, and O elements forming the coral particles. Moreover, the micro-analysis of each elemental map indicates a completely homogeneous distribution of these 3 elements in the material.

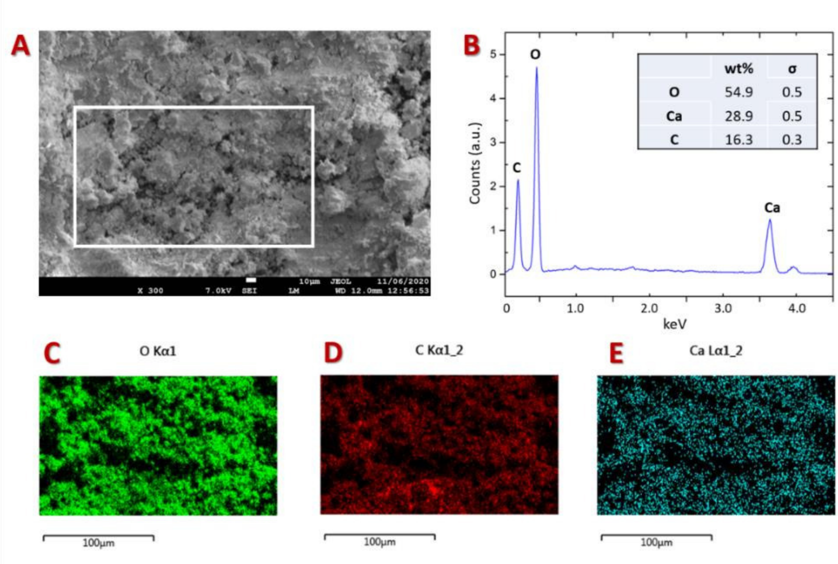

Figure 8.2 SEM image (A), EDS spectrum (B), and EDS elemental maps (C-E) of coral powder.

8.3.2 Size of coral particles before and after immersion in the solvent system acetic acid/water

Coral particles used for the electrospinning have sizes in the micrometer range and the aim of this study is to electrospin fibers having a nanometer scale. As such, it is quite crucial to ensure that the coral microparticles get well dissolved in the used solvent system to decrease in size and be able to accommodate nanofibers. Luckily, the aragonite polymorph of $CaCO_3$ that was detected in the XRD measurements as the main constituent forming the used coral powder has a higher solubility than the calcite counterpart found in trace amounts and would probably easily accommodate nanofibers [256]. In order to confirm this hypothesis, coral powder was immersed in the same solvent system as the one used during electrospinning (acetic acid/water), after which the powder was then allowed to dry under the fume hood. Figure 8.3 represents the SEM images of coral powder before and after immersion in the electrospinning solvent system. It can be clearly seen that the initial powder contains particles in the micrometer range whereas the size of the observed particles after immersion becomes more homogenous and in the nanometer range. As a consequence, coral particles could easily accommodate the NFs without causing an increase in their diameter.

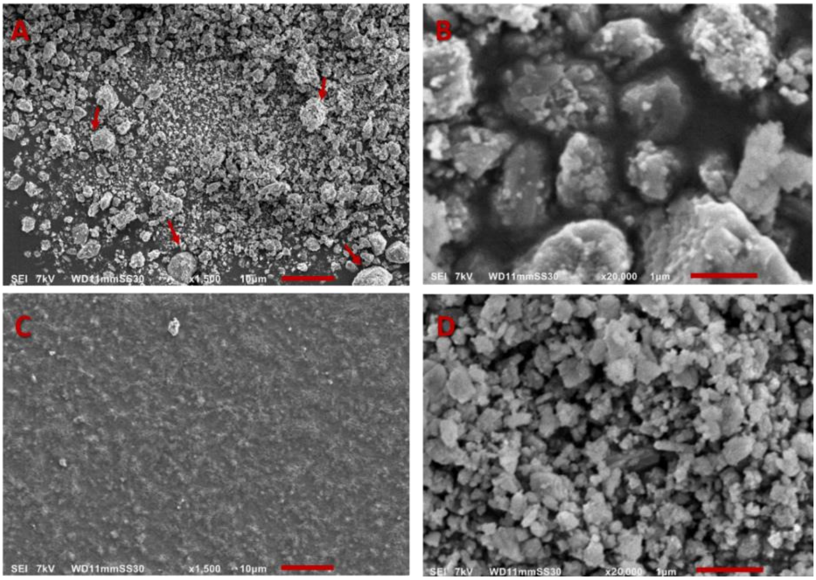

Figure 8.3 SEM images of coral particles before (A-B) and after (C-D) immersion in the solvent system acetic acid/water. A and C: scale bar = 10 µm (magnification: 1500 x); B and D: scale bar = 1 µm (magnification: 20,000 x). red arrows show big-sized coral particles.

8.3.3 WCA measurements

The obtained WCA values of CS/PEO and Coral/CS/PEO NFs before and after applying the plasma treatment in different discharge gases are represented in Figure 8.4. As previously discussed, the WCA values are reported as a function of energy density, due to the fact that the average discharge power is not the same for the different discharge gases under study. The WCA values for untreated CS/PEO and Coral/CS/PEO NFs were observed to be 53.7 ± 2.6° and 33.9 ± 2.4° respectively, showing that pristine CS/PEO NFs are more hydrophobic compared to Coral/CS/PEO NFs. This behavior can be attributed to the highly hydrophilic native structure of coral, which is mainly composed out of $CaCO_3$. Consequently, its incorporation into the NFs will result in a more hydrophilic surface [254,260]. Upon plasma treatment in different discharge gases, a further reduction in WCA values was observed for both NF sample groups with increasing energy density until a plateau value was reached. The obtained WCA plateau value implies that further increasing energy density for plasma-treated samples was not effective in reducing the WCA values.

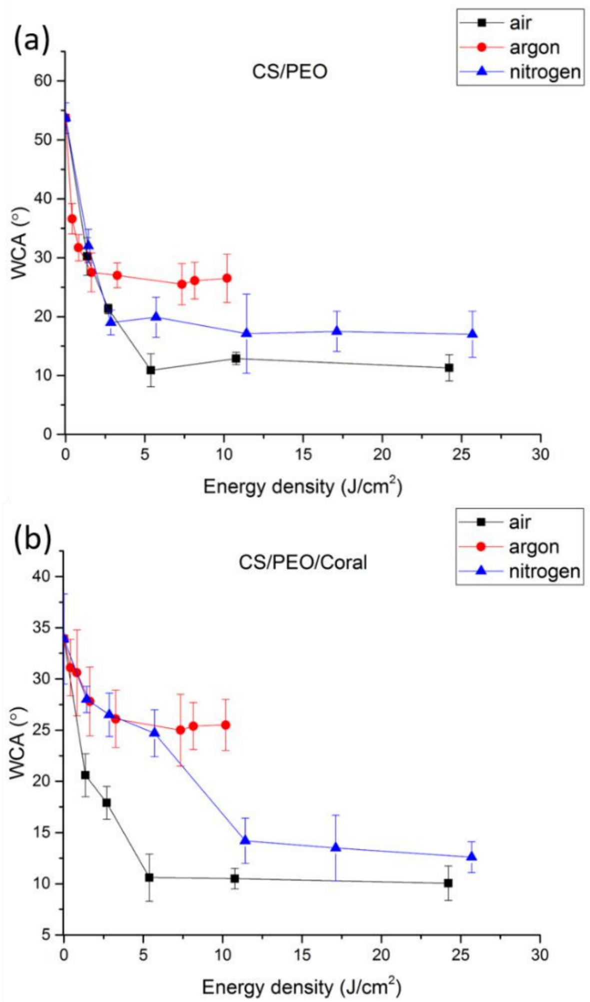

Figure 8.4 Evolution of the WCA on electrospun CS/PEO NFs (a), and Coral/CS/PEO NFs (b) as a function of energy density for plasma treatments in air, Ar and N_2 discharges.

Figure 8.4 also reveals that, among all plasma treatments, for both groups of NFs, the air and N_2 plasma-treated NFs exhibited a higher degree of hydrophilicity compared to the Ar plasma-treated samples. The lowest WCA values after air and N_2 plasma treatment were 11.3 ± 2.2° and 17.0 ± 3.9° respectively for CS/PEO NFs and 10.0 ± 1.6° and 12.6 ± 1.5° respectively for Coral/CS/PEO NFs. On the other hand, after Ar plasma treatment, the lowest attainable WCA values were found to be 25.5 ± 3.5° and 25.0 ± 2.5° for CS/PEO and Coral/CS/PEO NFs respectively, which were notably higher WCA values compared to the values on the air and N_2 plasma-treated samples. Similar differences in surface wettability were also observed in literature, stating that N_2 and air plasma treatments on polymeric substrates could more strongly improve the surface hydrophilicity in comparison to an Ar plasma treatment [24,34,42,97,242]. Moreover, as can be seen in Figure 8.4, the energy densities required to reach the saturated WCA value region for CS/PEO NFs were 9.8, 4.9 and 5.7 J/cm^2 after air, Ar and N_2 plasma treatments respectively. For the coral-containing NFs, the corresponding energy density values were similar (with the exception of N_2 plasma treatment), namely 9.8, 4.9 and 17.1 J/cm^2 after air, Ar and N_2 plasma treatments respectively. It can thus be concluded that plasma treatments in air and N_2 discharges require more input energy to make the surface more hydrophilic compared to an Ar plasma. The pronounced decrease in WCA values observed in Figure 8.4 with increasing energy density for both NF groups can be attributed to a significant increase in nitrogen- and/or oxygen-containing polar groups on the surface of the CS/PEO and Coral/CS/PEO NFs [24,49] which will be discussed in detail in section 8.3.6. Moreover, this great hydrophilic behavior is also due to the nanofibrous porous topography affecting the solid-liquid interface to a high extent. In fact, at a certain threshold of moderate chemical hydrophilicity, a highly pronounced wettability is observed on the fibers due to the massive penetration of water molecules inside the pores. This is triggered by the fact that water drops of low tension prevail over the air entrapment in the inter-fibrous pores by their inability to be held on a structurally hydrophilic surface [33,135]. Several other studies have also revealed a super-hydrophilic behavior of electrospun fibers subjected to a plasma treatment [33,135,164,261]. Based on the WCA results presented in this part, optimized energy density values were chosen (see Table 8.1) to further investigate the NFs morphology, surface chemistry, CaP deposition and cell adhesion and proliferation on samples possessing the maximal plasma treatment effect (so-called saturated samples).

8.3.4 Morphological visualization of NFs by SEM

Figure 8.5 represents the morphology of the untreated and plasma-treated electrospun CS/PEO and Coral/CS/PEO NFs. The obtained SEM micrographs for both types of pristine NFs (Figure 8.5 (a) & (e)) revealed that the untreated nanofibrous meshes were composed out of randomly aligned, smooth, ultra-fine and beadless NFs while possessing a highly interconnected porous structure. Based on the SEM images, the fiber diameters of the untreated CS/PEO and Coral/CS/PEO NFs were found to be 241 ± 79 nm and 263 ± 90 nm respectively. This result shows that the incorporation of coral micro particles did not notably change the NFs diameter. This was attributed to the dissolution of the micro particles in the used solvent system and the consequent formation of nanoparticles easily accommodating the NFs without increasing their diameter (see Figure 8.3).

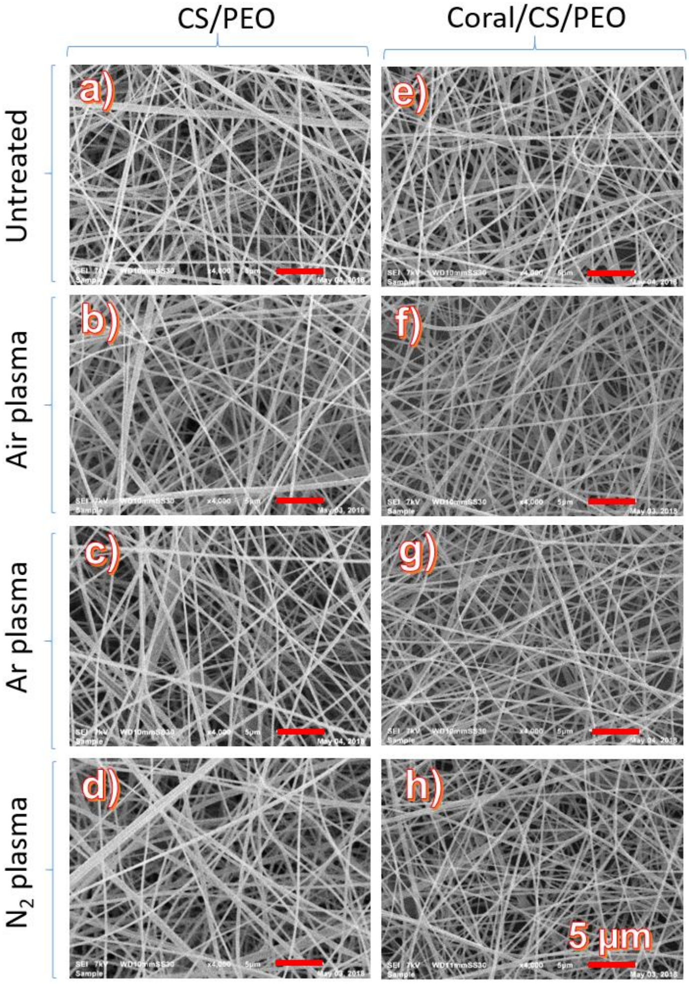

Figure 8.5 SEM images of CS/PEO NFs before plasma treatment (a) and after plasma treatment in air (b), Ar (c) and N_2 (d) and SEM images of Coral/CS/PEO NFs before plasma treatment (e) and after plasma treatment in air (f), Ar (g) and N_2 (d) (Magnification: 4000 x; scale bar = 5 µm).

As can be seen in Figure 8.5 (b-d) & (f-h), no significant changes in fiber diameters or fiber morphology could be observed after performing the plasma treatments in different working gases. Indeed, the observed fiber diameters after plasma modification in Ar, air and N_2 on CS/PEO NFs were found to be 274 ± 64 nm (Ar), 252 ± 83 nm (N_2) and 257 ± 87 nm (air), which were similar to the NF diameter of the untreated CS/PEO sample. In case of plasma-treated Coral/CS/PEO NFs, the following fiber diameters were obtained: 253 ± 119 nm (Ar), 248 ± 143 nm (N_2) and 257 ± 90 nm (air), which are not significantly different fiber diameters than the fiber diameter of the untreated sample. In addition, Figure 8.5 also reveals that no extra open spaces and/or melted fiber to fiber joints were observed following plasma treatments. As a result, it can be concluded that after conducting plasma treatment in all discharge gases, the NFs retained their morphological features. This conclusion is in agreement with Liu et al. who found that plasma modifications did not notably alter the topography of NFs when the diameter of the NFs was larger than 80 nm [262]. The preserved morphological structure of the NFs after the conducted plasma treatments showed that the expected etching effects of plasma modification were neglectable in this work. Based on the obtained WCA and SEM results, plasma treatments using the saturated energy density values given in Table 8.1 were thus sufficiently mild to preserve the bECM-like appearance while efficiently improving the surface hydrophilicity.

Additionally, in order to confirm that the UV sterilization performed before the cell tests is not damaging the morphology of Coral/CS/PEO and CS/PEO NFs, SEM images were taken after the sterilization that involves an exposure to UV light (Sylvania; 254 nm wavelength) for 30 min. As can be seen in Figure 8.6, no damage was observed post-UV exposure on both groups of NFs.

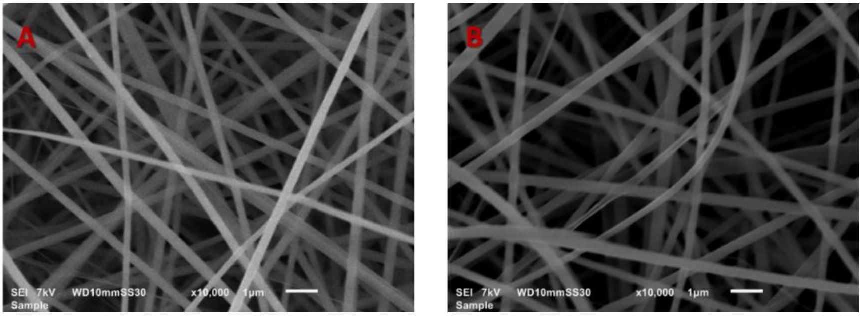

Figure 8.6 SEM images of (A) Coral/CS/PEO and (B) CS/PEO NFs after UV exposure (Magnification: 10000 x; scale bar = 1 μm).

8.3.5 Mechanical properties of the NFs

In order to evaluate the mechanical properties of the electrospun meshes and examine whether the addition of coral particles and/or the different plasma treatments compromise or reinforce such properties, the tensile strength and the Young’s modulus were measured for all fiber conditions and the results are reported in Figure 8.7. Next to the challenges accompanying the electrospinning of pure chitosan, the enhancement of the mechanical properties of the fibers was another crucial reason driving bone tissue engineers to blend chitosan with synthetic polymers prior to electrospinning [143]. The mixture of CS/PEO used in this thesis has led to an ultimate tensile strength and a Young’s modulus of 4.8 MPa and 51.8 MPa for the untreated fibers respectively. When comparing these results with the mechanical properties of other chitosan-containing fibers blended with PCL or PLGA for instance, one can notice the higher mechanical performance of CS/PEO (3:1) fibers. In fact, Yang et al. have found a considerably lower ultimate tensile strength (0.8 MPa) and Young’s modulus (9.8 MPa) of CS/PCL fibers prepared with a similar ratio of CS/synthetic polymer (3:1) and used for BTE [263]. Semnani et al. have also obtained chitosan/PCL (3:7) fibers with mediocre tensile strength (1.3 MPa) and Young’s modulus (7.4 MPa) despite the higher content in PCL [264]. Duan et al. have revealed that different compositions of PLGA/CS fibers give rise to weaker tensile strengths ranging between 1.2 and 3.2 MPa [265]. Luckily, the different plasma treatments did not compromise the mechanical properties of CS/PEO fibers since no significant statistical differences between the tensile strength values between untreated and air (4.3 MPa) , Ar (4.4 MPa) and N_2 (5.4 MPa) treated samples is observed. On top of that, Ar and N_2 plasma treatments have improved the elasticity of the fibers since the Young’s modulus increased significantly to 64.3 MPa and 71.4 MPa, respectively. This improvement was however not perceived for air plasma-treated fibers that preserved almost the same Young’s modulus (54.2 MPa) compared to the untreated samples. This observation is presumably attributed to the combination of an increased fiber-to-fiber friction as a result of plasma surface etching and cross-linking reactions occurring at the surface of the NFs upon N_2 and Ar plasmas [24]. Cross-linking reactions are believed to be more actively implicated in the elasticity enhancement since air plasma treatment, known by its predominant etching effect over cross-linking effects, did not significantly increase the Young’s modulus of the fibers. In fact, cross-linking mechanisms are probably leading to a certain fastening of the molecular chains accommodating the fibers which enhances their elasticity.

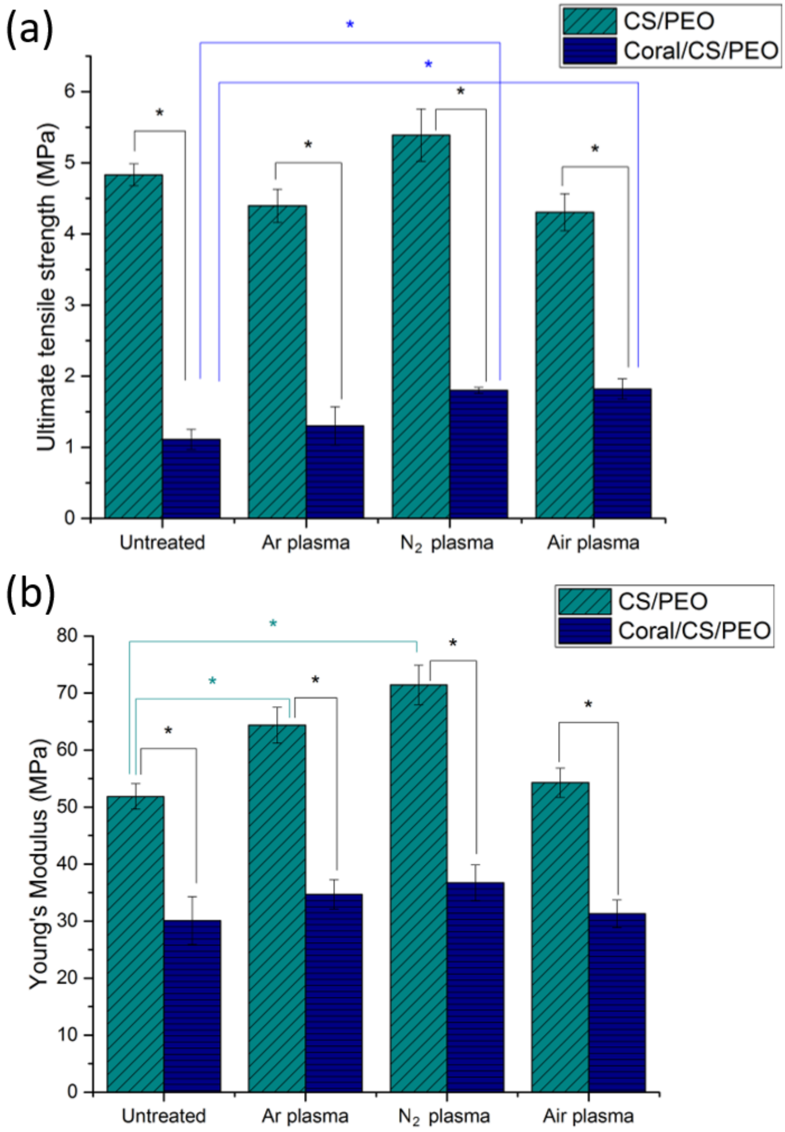

Figure 8.7 Mechanical properties of CS/PEO and coral/CS/PEO before and after Ar, N_2 and air plasma treatments. (a) Histograms of stress at maximal load and (b) Histograms of Young's modulus ((*) shows statistically significant differences; $P < 0.05$).

When examining the mechanical properties of coral-containing NFs, one can clearly discern that the addition of coral particles has led to a significant decrease in both the tensile strength (1.1 MPa) and the Young's modulus (30.1 MPa). This was to be expected since coral particles are probably disrupting the ordered arrangement of the polymeric molecular chains forming the fibers [142]. In fact, when these macromolecular chains are highly aligned and more densely packed, the tensile strength and Young's modulus of the fibers increase [55]. Moreover, the presence of coral particles in the polymeric solution could presumably interfere with the stretching effect of the polymer jet during its whipping motion towards the collector leading to the deposition of lamellar molecular chain structures rather than fibrillary ordered structures. A poor interface bonding between coral nanoparticles and CS/PEO might also translate into poor mechanical properties [266]. Several previous studies have also reported that electrospun composite NFs containing HA nanoparticles exhibit considerably poorer mechanical properties than their nanoparticle-free counterparts [142,267,268]. For instance, Venugopal et al. have shown that PCL/HA fibers that mineralized osteoblast cells for BTE applications were characterized by an almost similar tensile strength (1.0 MPa) as the Coral/CS/PEO fibers in this study but at the same time also showed a much lower Young's modulus (3.5 MPa) [268]. This indicates that coral-containing fibers still outperform some of the previously used nanoparticle-containing fibers used in BTE in terms of elasticity. Interestingly, N_2 and air plasma treatments have increased the tensile strength of coral-containing fibers to 1.8 MPa. A slight but statistically not significant increase in the tensile strength to 1.3 MPa was also perceived upon Ar plasma treatment. This might be attributed to the more pronounced etching effect of N_2 and air plasmas enhancing the friction between coral nanoparticles and CS/PEO thus strengthening the adhesion between them and improving their interface bonding. No significant differences in the Young's modulus were however distinguished before and after the different plasma treatments.

8.3.6 XPS results

Since no clear plasma-induced morphological changes were observed on both CS/PEO and Coral/CS/PEO NFs, the observed variations in WCA values after plasma modification can only be attributed to plasma-induced chemical changes on the surface. As such, for further investigation of the plasma-induced effects, the chemical composition of untreated and plasma-treated NFs under the optimized plasma conditions (see Table 8.1) were analyzed making use of XPS. The elemental composition of CS/PEO and Coral/CS/PEO NFs are presented in Tables 8.2. The table show that the O/C ratio of the pristine CS/PEO sample was significantly lower than the O/C ratio of Coral/CS/PEO NFs (0.39 versus 0.71), which was mainly due to the existence of carbonates in the coral-containing samples.

After applying Ar plasma treatment on the CS/PEO NFs, the O/C ratio increased from 0.39 to 0.49, while the N/C ratio remained unaffected. Similar trends were observed on the Ar plasma-treated Coral/CS/PEO NFs: an increase in O/C ratio from 0.71 to 0.75 and an unchanged N/C ratio. In case of the air plasma-treated CS/PEO NFs, the O/C ratio also remarkably increased after plasma treatment. Moreover, a very small increase in N/C ratio could also be observed for this sample. A similar increase in oxygen incorporation after air plasma treatment was also observed in case of the Coral/CS/PEO NFs (from 0.71 to 0.87). In contrast to the CS/PEO NFs, no significant change in N/C ratio was however observed for the coral-containing sample.

To explain the abovementioned changes in surface elemental composition after Ar plasma treatment, it should be noted that since Ar is an inert gas, its pure plasma cannot directly introduce a significant oxygen content on the surface of NFs. However, the observed oxygen incorporation could be explained as followed: Ar plasma contains excited atoms, photons, electrons, ions and Ar metastables. When these species interact with the surface of NFs, they excite the surface by breaking C-C/C-H chemical bonds and creating carbon radicals [26,34]. Subsequently, when these highly reactive surface radicals are exposed to ambient conditions after removing the samples from the plasma reactor, they will rapidly react with oxygen present in the atmosphere [47]. Moreover, the increase in oxygen incorporation (1.1% for Coral/CS/PEO, and 4.5% for CS/PEO samples) that was detected by XPS after Ar plasma exposure compared to untreated samples can also be (partly) explained by the presence of oxygen impurities in the plasma chamber or in the gas supply. As it mentioned in chapters 6 and 7 (section 6.3.2.2, 6.3.5.2, 7.3.4.1, and 7.3.4.2), this oxygen contamination is very difficult to overcome, even after installing additional pumping systems and will thus also directly graft oxygen atoms to the nanofibrous samples during plasma exposure [15,20].

In case of air plasma treatment, the observed oxygen incorporation directly occurs in the plasma reactor as in case of an air discharge, an abundant number of chemically reactive plasma species such as atomic oxygen, ozone, nitrogen oxides… are present in the plasma phase [34]. These active plasma species directly interact with the surface of the NFs, thereby increasing the surface energy of the samples by introducing oxygen-containing polar groups, resulting in the enhanced hydrophilicity of the CS/PEO and Coral/CS/PEO NFs after air plasma treatment (see Figure 8.4). Table 8.2 also shows that the conducted N_2 plasma treatments led to a notable increase in N/C ratio (from 0.03 to 0.19 and from 0.02 to 0.14 for CS/PEO and Coral/CS/PEO NFs respectively). Simultaneously, the N_2 plasma treatments also resulted into a small increase in O/C ratio for both sample groups. The abundant nitrogen incorporation on the surface of both studied NFs can be explained by the interaction between the excited nitrogen molecules present in the discharge and the surface chemical groups thereby turning the latter into surface polymer radicals. These formed polymer radicals in turn rapidly react with plasma-induced excited atomic and ionic (N_2^+) nitrogen states resulting in the grafting of nitrogen-containing functional groups onto the polymer surface as was previously discussed in chapters 6 and 7 (section 6.3.5.1 and 7.3.4.1) [42,197]. Additionally, the observed oxygen grafting can be attributed to the presence of oxygen impurities in the used DBD reactor [20]. This is quite probable given the fact that a lower reactor base pressure of 10^{-5} kPa is used in this chapter compared to the base pressure used in chapters 6 and 7 (10^{-7} kPa) where an in-plasma surface oxidation also occurred. Moreover, by exposing the N_2 plasma-treated NFs to ambient air, rapid reactions between oxygen and/or water vapor present in the ambient air and surface radicals and/or nitrogen-containing functional groups can also occur, thereby resulting in post-plasma oxygen functionalization. Finally, when comparing the total oxygen + nitrogen incorporation between the differently prepared plasma-modified samples (N+O/C ratio shown in Table 8.2), it can be concluded that the oxygen + nitrogen incorporation was significantly larger in air and N_2 discharges compared to the Ar discharge for both CS/PEO and Coral/CS/PEO samples. This can in turn explain the lower saturated WCA values obtained after air and N_2 plasma exposure compared to Ar plasma treatment (see Figure 8.4). Table 8.2 also reveals that, unlike the CS/PEO NFs, the coral-containing NFs contain a very small amount of phosphorus (P) and approximately 7 at% of Ca which could be attributed to the presence of coral particles at the surface of these NFs. After all conducted plasma treatments, the P content did not notably vary on the surface of the Coral/CS/PEO NFs. However, when conducting air plasma treatment, a slight increase in Ca content was observed. The reason for this particular behavior can be the plasma etching effect which is known to be more pronounced in an air plasma compared to other plasmas due to the particular presence of high amounts of atomic O in an air discharge. This etching effect probably resulted into a preferential depletion of soft polymer segments rather than Ca-containing bonds thereby resulting in a small increase in the Ca content.

Table 8.2 Elemental composition of CS/PEO and of Coral/CS/PEO NFs before and after plasma treatment in N_2, air and Ar.

Sample	**Plasma treatment**	**C (%)**	**N (%)**	**P (%)**	**Ca (%)**	**O (%)**	**O/C**	**N/C**	**N+O/C**
CS/PEO NFs	untreated	69.8 ± 1.4	2.3 ± 0.6	-	-	27.9 ± 0.9	0.39	0.03	0.43
	N_2	58.7 ± 0.6	11.2 ± 0.7	-	-	30.1 ± 1.1	0.51	0.19	0.7
	air	54.7 ± 1.9	3.6 ± 0.9	-	-	41.7 ± 1.1	0.76	0.06	0.82
	Ar	65.2 ± 0.7	2.4 ± 0.8	-	-	32.4 ± 0.6	0.49	0.03	0.53
Coral/ CS/PEO NFs	untreated	53.5 ± 0.8	1.2 ± 0.2	0.3 ± 0.2	6.7 ± 0.2	38.3 ± 1.0	0.71	0.02	0.73
	N_2	47.3 ± 1.1	6.8 ± 0.2	0.3 ± 0.1	6.9 ± 0.1	38.7 ± 1.1	0.81	0.14	0.96
	air	48.2 ± 1.8	1.7 ± 1.5	0.3 ± 0.2	7.6 ± 0.3	42.2 ± 0.3	0.87	0.03	0.91
	Ar	52.0 ± 1.2	1.3 ± 1.1	0.5 ± 0.2	6.8 ± 0.2	39.4 ± 0.8	0.75	0.02	0.78

To investigate the type of carbon-containing functional groups that were grafted onto the surface of the NFs after the different plasma treatments, high resolution C1s spectra for both groups of NFs were studied in more detail using peak deconvolution. These deconvoluted C1s spectra are shown in Figure 8.8 (a) & Figure 8.9 (a) for all nanofibrous meshes under study, presenting the position of the used peaks and their corresponding binding energies. According to literature, the untreated C1s peak of the CS/PEO NFs could be deconvoluted into 5 distinct peaks (see Figure 8.8 (a)): a peak at 285.0 eV corresponding to **C**-C bonds, a peak at 286.1 eV attributed to **C**-N bonds, a peak at 286.7 eV assigned to **C**-O bonds, a peak at 288.0 eV corresponding to O-**C**-O (acetate) /**C**=O (aldehyde or ketone) /O=**C**-NH bonds, and finally a peak at 289.1 eV attributed to O-**C**=O bonds in carboxylic acids or esters [269]. For the untreated coral-containing NFs, similar peaks as for the CS/PEO NFs can be seen, however, also an additional peak at the higher binding energy side located at 289.3 eV was required to obtain a good curve fit. This observation is logic as this particular peak can be attributed to carbonate (CO_3), which is the main constituent of coral particles (see Figure 8.9 (a)) [62,104,139,269–271]. As it is shown in Figure 8.8 (a) & Figure 8.9 (a), a clear difference between the C1s peaks for CS/PEO and Coral/CS/PEO NFs could be observed, which could be attributed to the presence of coral particles at the surface of the latter NFs. Moreover, Figure 8.8 (a) & Figure 8.9 (a) also revealed that after plasma modification of CS/PEO and Coral/CS/PEO NFs, remarkable differences in peak intensities, depending on the working gas, could be noted.

Based on these C1s fittings, quantitative information on the relative prevalence of the carbon-containing chemical bonds on the surface of the NFs after plasma treatment can be obtained and the results are presented in Figure 8.8 (b) & Figure 8.9 (b) for CS/PEO and Coral/CS/PEO NFs respectively. Ar and air plasma modification of CS/PEO NFs result into an increase in the relative concentration of all oxygenated carbon groups (**C**-O, O-**C**-O/**C**=O/O=**C**-NH and O-**C**=O), combined with a relative decrease in the amount of **C**-C functional groups. Figure 8.8 (b) also shows that the increase in oxygen-containing carbon bonds was more pronounced in case of air plasma treatment, which is in close agreement with the larger increase in O/C ratio observed after air plasma treatment (see Table 8.2). A small increase in the amount of **C**-N functional groups could also be noticed after air plasma treatment, which is in agreement with the increased N/C ratio observed for this particular sample. In contrast, N_2 plasma treatment of CS/PEO NFs results not only into a small increase in the amount of O-**C**-O/**C**=O/O=**C**-NH groups, but also causes a notable increase in the **C**-N group concentration.

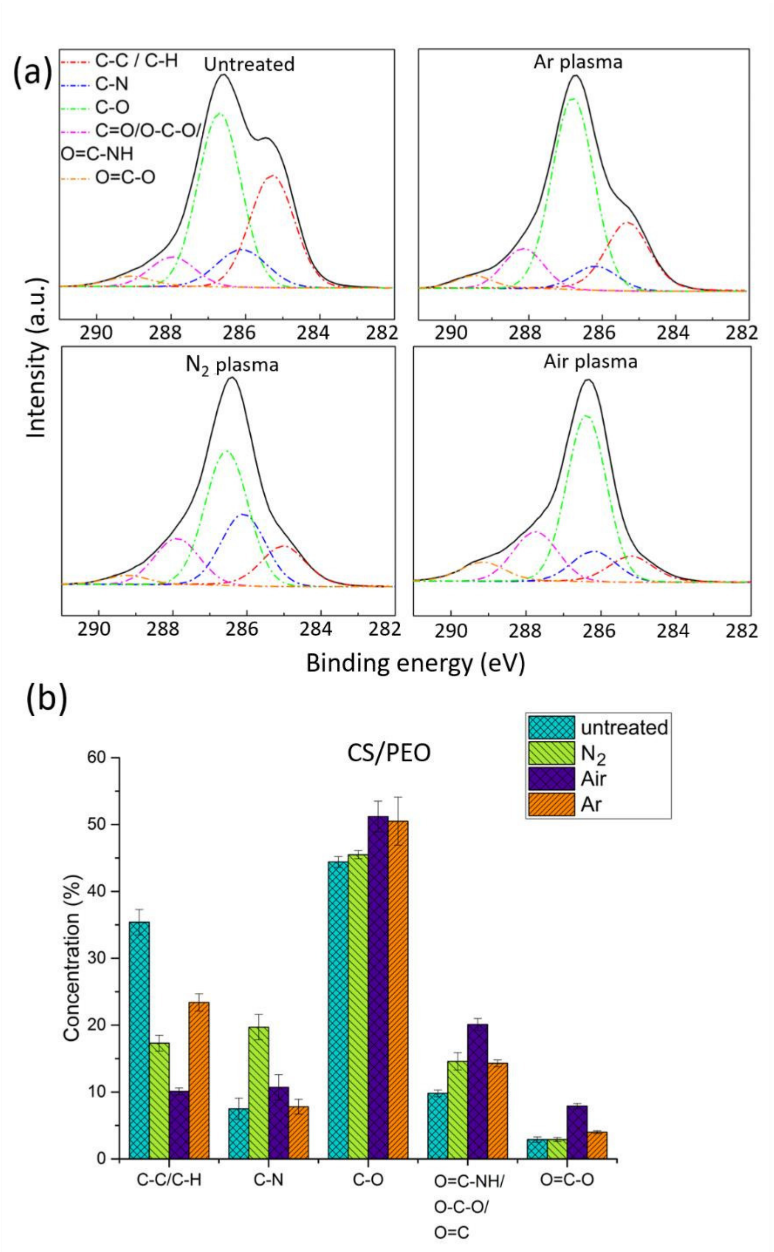

Figure 8.8 Deconvolution of the high resolution C1s spectra of CS/PEO NFs before and after plasma treatment in Ar, N_2, and air (a). Relative concentrations of different carbon-containing functional groups on CS/PEO before and after plasma modification (b).

This result is also consistent with the atomic composition presented in Table 8.2, as N_2 plasma treatment was found to increase both the O/C and N/C ratio. When examining the results on the Coral/CS/PEO NFs, it was noticed that Ar plasma treatment mainly increases the relative concentration of the O-**C**=O groups, while the concentrations of the other nitrogen- and oxygen-containing functional groups remain largely unaffected. In contrast, an air plasma treatment is observed to result not only in an increase in the relative concentration of O-**C**=O, but also in an increase in the relative amounts of **C**-O, O-**C**-O/**C**=O/O=**C**-NH and $\mathbf{C}\mathrm{O}_3$ functionalities. The incorporation of oxygenated carbon groups is thus more pronounced in case of air plasma treatment compared to Ar plasma which is in agreement with the O/C ratio values mentioned in Table 8.2. Nitrogen plasma treatment of Coral/CS/PEO NFs mainly causes a strong increase in the relative concentration of **C**-N functionalities combined with a less pronounced increase in the relative amount of O-**C**-O/**C**=O/O=**C**-NH and $\mathbf{C}\mathrm{O}_3$ groups. These results are again consistent with the O/C and N/C ratios given in Table 8.2. Figure 8.9 (b) also shows that the incorporation of CO_3 functionalities was the most pronounced when performing an air plasma treatment on Coral/CS/PEO NFs. This behavior is most likely the result of the more pronounced etching effect of an air plasma due to the presence of more atomic oxygen known to be an etching component [97,272]. However, as no significant damage of the morphological structure of Coral/CS/PEO NFs was observed after air plasma modification, this gradual etching probably mainly occurrs on a molecular level.

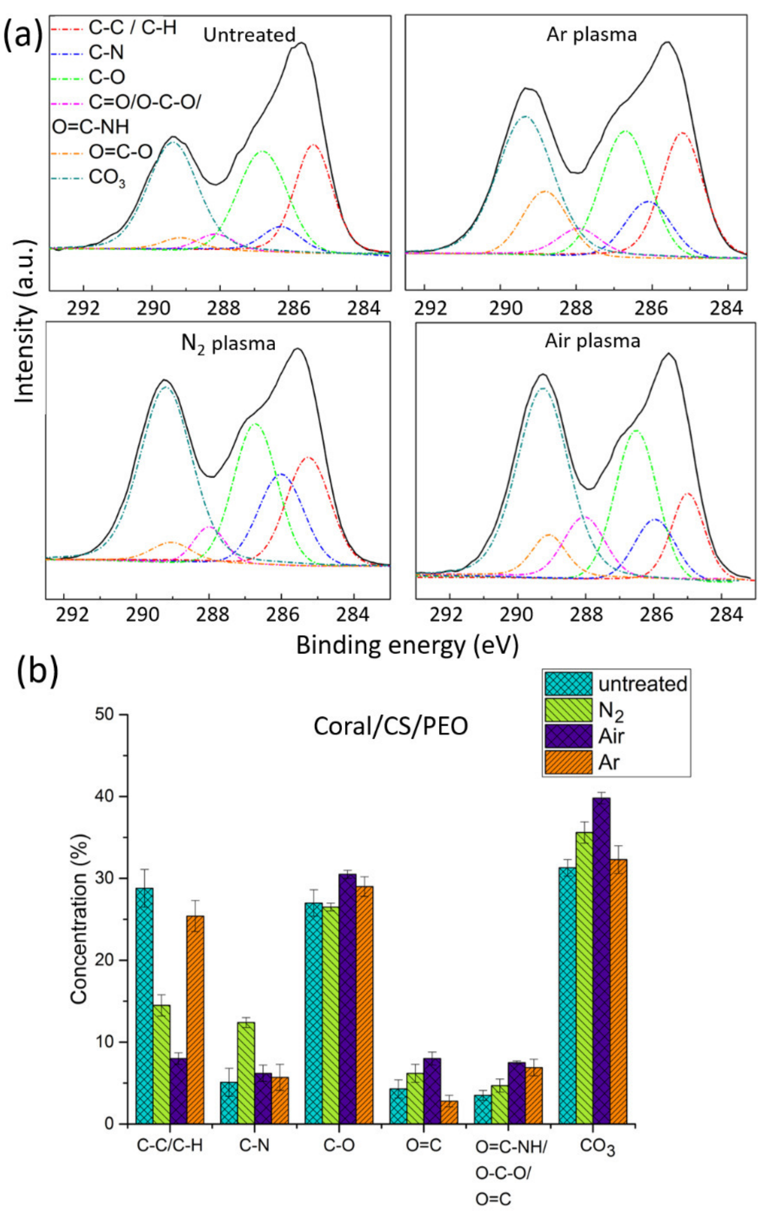

Figure 8.9 Deconvolution of the high resolution C1s spectra of Coral/CS/PEO NFs before and after plasma treatment in Ar, N_2, and air (a). Relative concentrations of different carbon-containing functional groups on Coral/CS/PEO before and after plasma modification (b).

8.3.7 Ageing effect of plasma-treated CS/PEO and coral/CS/PEO fibers

As already previously mentioned, the chemical surface changes induced by plasma treatment are not always permanent as the surface has a tendency to retrogress again towards the untreated state post-treatment in an unfavorable phenomenon so-called ageing effect [20,33]. This phenomenon is caused by 2 previously described pathways that could come into play: 1) the reorientation of the implanted polar groups towards the bulk of the fibers to acquire a more energetically stable position and 2) the occurrence of post-plasma treatment reactions between atmospheric minorities such as H_2O and CO_2 and the incorporated chemical groups that become therefore neutralized [20,33]. Nonetheless, we have previously shown that the ageing effect is trivial on electrospun NFs due to: 1) the highly packed arrangement of the molecular chains accommodating the small nano-dimensional size of the fibers which limits the practicability of the plasma-induced functional groups to reorientate and find room inside the fibers and 2) the confined exposure of the fibrous network to the ambient air as neighboring fibers are covering and protecting each other [33,135]. In order to verify if the ageing effect is also negligible on CS/PEO and Coral/CS/PEO fibers subjected to air, Ar and N_2 plasmas, XPS measurements were performed on the treated fibers after storage in ambient air for 7 days (Table 8.3). When comparing these results with the XPS results obtained directly after plasma treatment (Table 8.2), one can indeed notice the minor (or inexistent) ageing effect generally occurring on all fiber conditions with some distinctions between different plasma treatments. A small decrease in the O/C ratio form 0.76 to 0.69 was detected on air plasma-modified CS/PEO NFs. In contrast, Ar plasma-treated CS/PEO samples did not show any notable difference in the O/C ratio 7 days post-treatment thus confirming the high stability of these samples. The O/C ratio also remained constant on N_2 plasma-treated CS/PEO fibers but the N/C ratio drastically decreased from 0.19 to 0.05. The higher loss in treatment efficiency for air and N_2 plasma treatments compared to Ar plasma treatment is due to the higher degree of cross-linking achieved upon Ar plasma treatment. The highly cross-linked structure restricts the polymer chain mobility and therefore the reorientation towards the bulk. The low cross-linking degree engendered upon air and N_2 treatments results in a higher fraction of mobile groups and thus in a more pronounced ageing effect [26,114,129]. The reorientation of N-containing groups seems to overtake the one of O-containing groups probably because of their less complex conformation and/or lower molecular weight. When taking a look at the XPS results of Coral/CS/PEO fibers, one can detect an almost unchanged O/C ratio for all treatments and a smaller decrease in the N/C ratio of N_2-plasma-treated samples from 0.14 to 0.07. This less pronounced or even completely absent loss in the treatment efficiency could be explained by the presence of coral nanoparticles inside the fibers further hindering the free movement of plasma-induced functional groups towards the bulk.

Table 8.3 Elemental composition of plasma-treated CS/PEO and Coral/CS/PEO NFs after storage in ambient air for 7 days.

Sample	**Plasma treatment**	**C (%)**	**N (%)**	**P (%)**	**Ca (%)**	**O (%)**	**O/C**	**N/C**	**N+O/C**
CS/PEO NFs	N_2	63.9 ± 0.9	3.5 ± 0.7	-	-	32.5 ± 1.0	0.5	0.05	0.56
	air	56.9 ± 1.0	3.5 ± 0.4	-	-	39.5 ± 0.7	0.69	0.06	0.75
	Ar	64.6 ± 1.0	1.0± 0.5	-	-	34.3 ± 0.9	0.53	0.01	0.54
Coral/CS/PEO NFs	N_2	49.9 ± 0.4	3.7 ± 0.1	0.3 ± 0.3	6.2 ± 0.1	39.9 ± 0.7	0.79	0.07	0.87
	air	48.5 ± 1.3	0.7 ± 0.5	0.5 ± 0.3	7.4 ± 0.5	42.9 ± 0.9	0.88	0.01	0.89
	Ar	52.3 ± 0.4	0.7 ± 0.4	0.5 ± 0.3	6.6 ± 0.1	39.9 ± 0.5	0.76	0.01	0.77

8.3.8 Biological performance of CS/PEO and Coral/CS/PEO NFs

8.3.8.1 MC3T3 cellular interactions

To elucidate the effect of the incorporated coral particles and of the various plasma treatments on the biological performance of the NFs, detailed cell studies were conducted. For this examination, plasma-treated NFs with the highest possible hydrophilicity (so-called saturated samples) were selected for cell tests using the energy density values mentioned in Table 8.1. Fluorescence imaging and SEM micrographs were utilized to visualize MC3T3 cell behavior on CS/PEO and Coral/CS/PEO NFs 1 day and 7 days after cell seeding. The obtained images are shown in Figures 8.10 & 8.11 for CS/PEO and Coral/CS/PEO NFs respectively. According to Figures 8.10 & 8.11, 1 day post-cell seeding, a very low amount of viable MC3T3 cells (green color) with a round morphology attached on the surface of untreated CS/PEO NFs (Figure 8.10 (a & A*)). In addition, the clusters and aggregates of MC3T3 cells indicate that cell-cell interactions were favored over cell-NFs interactions. In comparison, for untreated coral-containing NFs, a notably higher amount of viable cells spread onto the surface 1 day after cell seeding (see Figure 8.11 (a & A*)). The abovementioned results indicate that incorporating coral particles into the NFs structure resulted in an improvement in osteoblast adhesion and a higher degree of cell spreading. The enhanced biological performance of coral-containing chitosan composite scaffolds has already been reported in literature [253].

One day after cell seeding, cell adhesion notably increased on all plasma-modified CS/PEO and Coral/CS/PEO NFs compared to their corresponding pristine samples (Figures 8.10 & 8.11). For all plasma-modified samples, very high amounts of viable cells with an elongated morphology were observed 1 day after cell seeding. The fluorescence images thus clearly indicate excellent initial MC3T3 cell adhesion on the surface of the plasma-treated NFs compared to their untreated counterparts. On the other hand, no significant differences in cell adhesion could be observed among the applied plasma treatments. When evaluating the impact of coral particles addition on the plasma-modified samples, Figures 8.10 and 8.11 also show that more cells adhered on the coral-containing plasma-treated NFs, suggesting that coral particles incorporation positively affected cell adhesion.

As can be seen in Figures 8.10 and 8.11, fluorescent and SEM micrographs have also been obtained one week after cell seeding to investigate cell proliferation. Figure 8.10 (e & E*) clearly reveals that one week after MC3T3 cell seeding on untreated CS/PEO NFs, only small amounts of aggregated cells were present on the surface. Similar observations were reported in previous work, which also indicated poor cell proliferation on the surface of CS/PEO NFs originating from the lack of negatively charged functional groups on the surface [24]. In contrast, a notable higher amount of living cells, compared to pristine CS/PEO NFs, were observed on untreated coral-containing NFs 7 days after cell seeding (Figure 8.11 (e & E*)), confirming that incorporating coral particles improves the bioactivity of CS-based NFs.

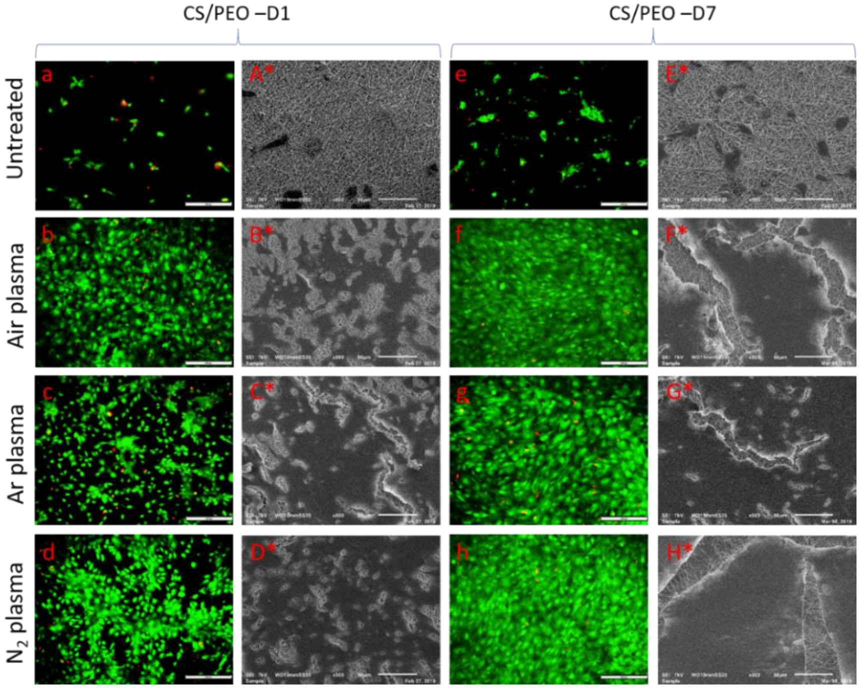

Figure 8.10 Fluorescent and SEM images of MC3T3 cells one day and seven days after cell seeding on untreated and plasma- treated CS/PEO NFs (magnification: x10, scale bar = 200 µm) and SEM imaging (magnification: x500 and scale bar = 50 µm).

Moreover, after one week, both SEM and live/dead fluorescent imaging revealed the presence of much higher amounts of viable cells on both groups of NFs compared to the first day after cell seeding, thereby confirming successful cell proliferation. In addition, cell proliferation was also notably improved after conducting plasma treatments on both CS/PEO and Coral/CS/PEO NFs, with no clear differences in cell proliferation behavior among the different applied discharge gases or among the different sample groups (CS/PEO versus

Coral/CS/PEO NFs). On all plasma-treated samples, the MC3T3 cells highly spread out over the surface, thereby almost completely covering the sample surfaces. In conclusion, all applied plasma exposures thus strongly improved cell adhesion and proliferation on both CS/PEO and Coral/CS/PEO NFs.

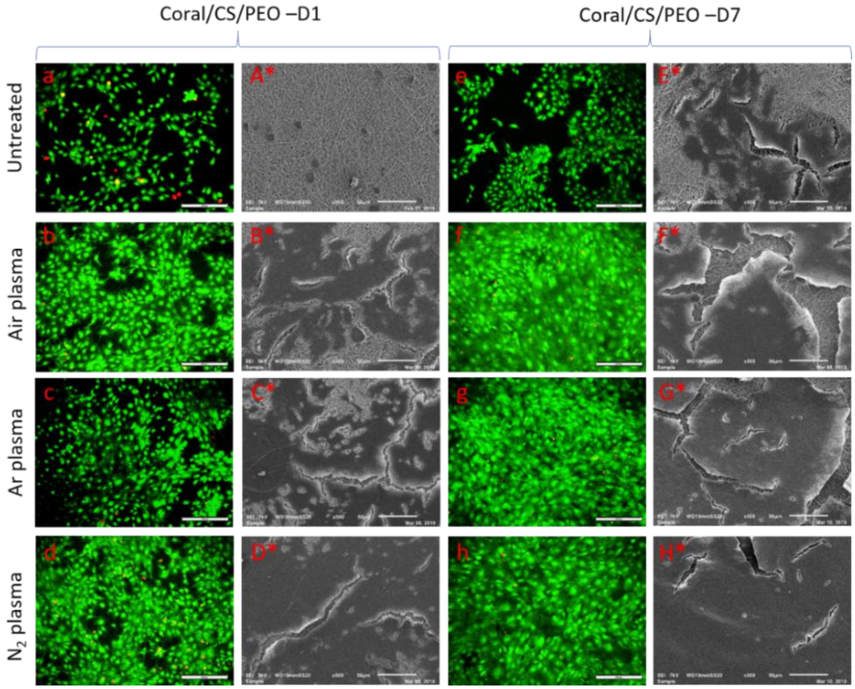

Figure 8.11 Fluorescent and SEM images of MC3T3 cells one day and seven days after cell seeding on untreated and plasma-treated Coral/CS/PEO NFs (magnification: x10, scale bar = 200 µm) and SEM imaging (magnification: x500 and scale bar = 50 µm).

Although Figures 8.10 & 8.11 provide important insights into the cellular behavior of MC3T3s on plasma-treated CS/PEO and Coral/CS/PEO NFs, they only give qualitative information. To quantify the number of viable cells on both groups of NFs, MTT assays were performed one day and seven days after MC3T3 cell seeding and the obtained results are presented in Figure 8.12. According to this figure, the incorporation of coral particles into the untreated NFs led to a significantly higher cell viability 1 day after cell seeding, which is in accordance with the previously shown fluorescence images. On the other hand, cell proliferation seem to be less affected by the addition of coral particles into the untreated NFs despite the fact that the fluorescence images show considerably more viable cells on the untreated Coral/CS/PEO sample 7 days after cell seeding.

Additionally, Figure 8.12 also shows that cell viability is higher on all plasma-modified samples in comparison to their untreated counterparts both 1 day and 7 days after cell seeding. However, no large differences in cell viability can be observed among the different applied discharge gases within each sample group (CS/PEO and Coral/CS/PEO). Moreover, the addition of coral particles into the plasma-modified NFs seemed to mainly positively affect initial cell adhesion, while the impact on cell proliferation was less pronounced, which is in agreement with the images shown in Figures 8.10 & 8.11. The results of the cell-material studies thus clearly show that all conducted plasma modifications strongly improved cell adhesion and proliferation onto the nanofibrous samples, while the addition of coral particles into the NFs mainly enhanced initial osteoblast adhesion.

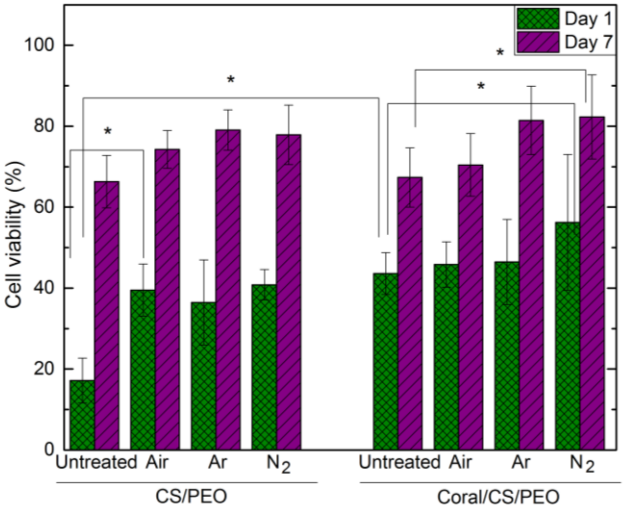

Figure 8.12 Cell viability results one day and seven days after cell seeding on untreated and plasma-modified CS/PEO and Coral/CS/PEO NFs ((*) shows statistically significant differences; $P < 0.05$).

8.3.8.2 CaP deposition

As the goal of this chapter was to produce appropriate scaffolds for bone defects, the capability of the NFs to form bone-like apatite needs to be investigated as well. To do so, the osteo-bioactivity of untreated and plasma-treated NFs was investigated by immersing the samples in an SBF solution. It is known that during immersion bone-like apatite can be formed on the surface of the NFs [46,172], however, the precipitation rate of CaP is reported to be relatively slow [35].

Therefore, to be able to make a clear distinction between untreated and plasma-treated samples in both groups of NFs under study, the possible formation of an apatite coating was studied over a period of 4 weeks. An initial assessment of the formation of CaP crystals was performed by SEM micrograph analysis. Subsequently, FTIR spectra were also recorded to show possible differences in chemical composition between immersed untreated and plasma-treated samples.

8.3.8.3 SEM analysis

SEM images taken post-SBF immersion reveal that the different fibrous mesh conditions exhibit diverse effects in inducing CaP deposition and dictating the crystals dispersion and morphology (Figure 8.13). Firstly, one can clearly visualize significant differences between untreated and plasma-treated CS/PEO samples. As can be seen in Figure 8.13 (a-A), CaP was scarcely deposited on a few dispersed surface spots of the untreated CS/PEO NFs in the form of smooth beads or island-shaped coatings not having the characteristic shape and nano-dimension of bone-like CaP crystals. Moreover, these fused deposits were seen to partially block the pores of the fibrous mesh when their size was sufficiently large. Similar CaP deposit shapes but with the occurrence of more agglomerated beads cover larger areas of the CS/PEO NFs plasma-treated with argon (Figure 8.13 d-D). In contrast to argon, air and nitrogen plasma treatments were revealed to trigger the deposition of numerous spherically shaped nano-dimensional CaP crystals nicely growing around each fiber. Interestingly, the nanocrystal deposition was not only limited to the outer fibers but also to deeper fibers without clogging the inter-fiber pores thus forming a uniformly CaP coated 3D fibrous scaffold (Figure 8.13 b-B and c-C). The number of the deposited crystals appear to be higher in case of the air plasma-treated samples with some fibers fully covered with nanocrystals (Figure 8.13 b-B). In order to understand the positive influence of plasma treatments on CaP deposition onto CS/PEO NFs, it is essential to elucidate that the initial key step in this biomimetic process is the crucial CaP nucleation occurring on specific binding sites of the polymeric chains [172,273]. One can therefore assume that the oxygen- and nitrogen-containing functionalities that were incorporated after plasma activation are the reason why plasma-treated fibers present a better and more homogeneous CaP deposition than the untreated NFs. Several studies have previously compared the ability of different functional groups to nucleate CaP and have indeed concluded that carboxyl groups are one of the most potent nucleation sites followed by hydroxyl groups [46,172,274]. This finding clarifies why air plasma-treated CS/PEO fibers presenting the most COOH-rich surface compared to nitrogen and argon plasma-treated fibers have the higher amount of deposited CaP crystals. In fact, CaP nucleation can take place only when a certain activation energy threshold is surpassed. This energy can be reduced by increasing the super-saturation or by decreasing the surface energy [35,172]. Plasma-induced surface functionalities play significant roles in governing the solid/ion interfacial energies and each functional group can therefore have a different nucleation capability for CaP. When the plasma-treated fibers are immersed in SBF solution, the carboxyl groups become negatively charged (carboxyl anions) at a pH of 7.4 and attract the surrounding Ca^{2+} ions. Therefore, the binding of the ions effectively decreases the interfacial energy and activates the surface nucleation [46,172]. Hydroxyl groups were revealed in some studies to be also important in CaP nucleation through different less recognized reactions [172]. Hydroxyl ions might for instance bind phosphate groups via a hydrogen bond triggering their concentration around the fibers surface [275]. Since untreated and argon plasma-treated NFs have a lower oxygen content on their surface than air and nitrogen plasma-treated samples, the nucleation was not effectively stimulated which explains the absence of nano-sized nuclei. Nonetheless, argon plasma-treated fibers exhibiting a slightly higher surface oxygen content could trigger the attachment of more spread out CaP deposits. A question mark about the nucleation ability of the plasma-induced nitrogen-containing groups still lingers given the presence of a discrepancy in literature about this subject. Some researchers have stated that amine groups for example have a weak nucleation capacity and others have reported that they cannot induce CaP nucleation [172,274,276]. This can again explain the lower amount of CaP nuclei on nitrogen plasma-treated fibers compared to air plasma-treated samples.

When comparing the SEM images of coral-free and coral-containing NFs, one can notice that the amount of CaP crystals was significantly higher when coral particles were present even on untreated fibers. Actually, the untreated coral-containing NFs still showed similar but more agglomerated beads and island-shape CaP deposits with the extra occurrence of some CaP crystals covering some individual fibers (Figure 8.13 e-E). Interestingly, plasma-treated coral-containing fibers were one by one completely covered with flake-like CaP nanocrystals while still conserving the fibrous mesh architecture (Figure 8.13 f-F, g-G and h-H). In addition to the plasma-induced functional groups, the initial presence of calcium in the coral-containing fibers is most probably also inducing CaP nucleation and greatly enhancing the growth of CaP crystals. Once the nucleation is triggered, the CaP nuclei that are generated start to grow spontaneously by attaching phosphate and calcium ions from the surrounding SBF via further ionic deposition [173,275]. This CaP precipitation was remarkably fast as the thickness of the plasma-treated NFs increased considerably especially after air and argon treatments. Plasma treatment sustained in argon exhibited noticeably improved CaP nucleation and nanocrystal deposition in coral-containing fibers than in coral-free fibers. This can be linked back, in addition to the extra presence of calcium, to the incorporation of more plasma-induced carboxylic groups in coral-containing fibers. Nitrogen plasma-treated Coral/CS/PEO samples showed a slower CaP growth around each fiber compared to air and argon plasma-treated Coral/CS/PEO fibers, which was illustrated by slightly thinner fibers and larger interfibrous pores. This can be again correlated to the weaker or event absent nucleation capacity of the induced nitrogen-containing functionalities.

The noticeable preservation of the porous structure of the nanofibrous meshes is due to the nano-metric aspect of the formed CaP crystals which is in fact the biologically active size of CaP crystals in bone [273]. The occurrence of these nanocrystals is aided by 2 previously demonstrated facts: 1) the presence of numerous homogeneously dispersed nucleation sites, which were induced by plasma in this present thesis, led to the formation of a large number of tiny particles rather than agglomerated large deposits and 2) an increased surface roughness or surface-to-volume ratio, afforded by the NFs in this case, induced a free crystal growth not limited by space restrictions thus preventing the particles from fusing together and forming plate-like crystals rather than globular nanocrystals [273,275].

To conclude, plasma treatments mainly generating carboxyl groups on the surface of the fibers stimulated CaP nucleation and the homogeneous growth of numerous nanocrystals around each fiber. This finding was also observed during the mineralization of plasma-treated PCL NFs and an UHMWPE polymer film after SBF incubation [35,46]. Moreover, the synergistic effect of plasma treatment and the presence of coral particles in the fibers accelerated the growth of CaP, which is known to be a rather slow process.

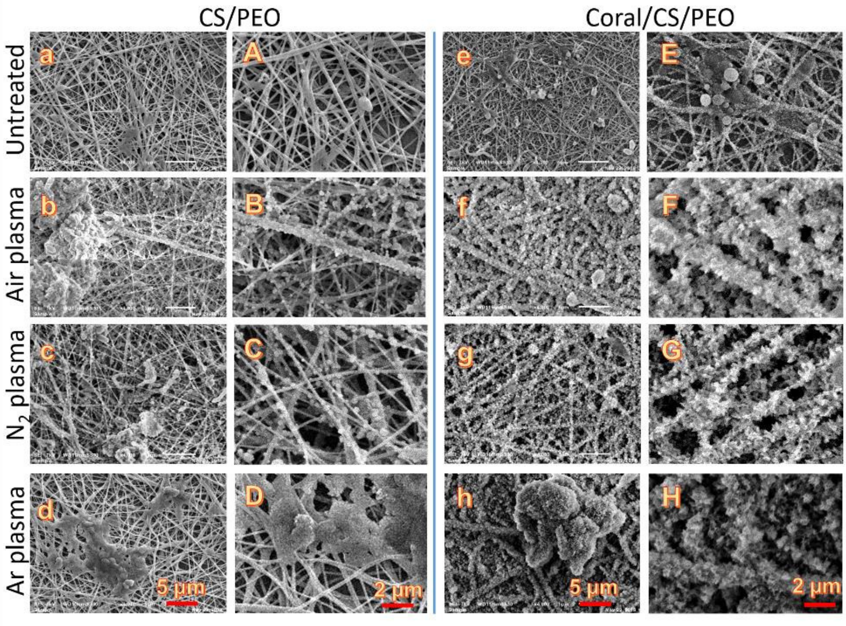

Figure 8.13 SEM images of CS/PEO NFs after immersion in SBF for 4 weeks before plasma treatment (a, A) and after plasma treatment in air (b, B), N_2 (c, C) and Ar (d, D). SEM images of Coral/CS/PEO NFs after immersion in SBF for 4 weeks before plasma treatment (e, E) and after plasma treatment in air (f, F), N_2 (g, G) and Ar (h, H). (a-h: scale bar = 5 µm; A-H: scale bar = 2 µm).

8.3.8.4 FTIR analysis

Different CaP phases can be found in normal and pathological calcifications occurring in the body with apatite being the characteristic CaP phase of naturally calcified bones. Biological apatite corresponds to the following formula: $Ca_{10}(PO_4, HPO_4, CO_3)_6(OH,Y)_2$ where Y can be fluoride (F) or chloride (Cl) substituting OH [277]. In order to get an insight on the chemistry of the deposited CaP crystals and to know if the apatitic phase is actually the one involved, FTIR measurements were performed. Figure 8.14 (a & b) represents the obtained FTIR spectra for untreated and plasma-treated CS/PEO and Coral/CS/PEO NFs after immersion in SBF for 4 weeks. The spectra of the immersed samples consisted, besides a broad band in the high wavenumber region due to absorbed water and OH$^-$, of characteristic peaks at 560, 600, and 1030 cm^{-1} attributed to PO_4^{3-} groups.

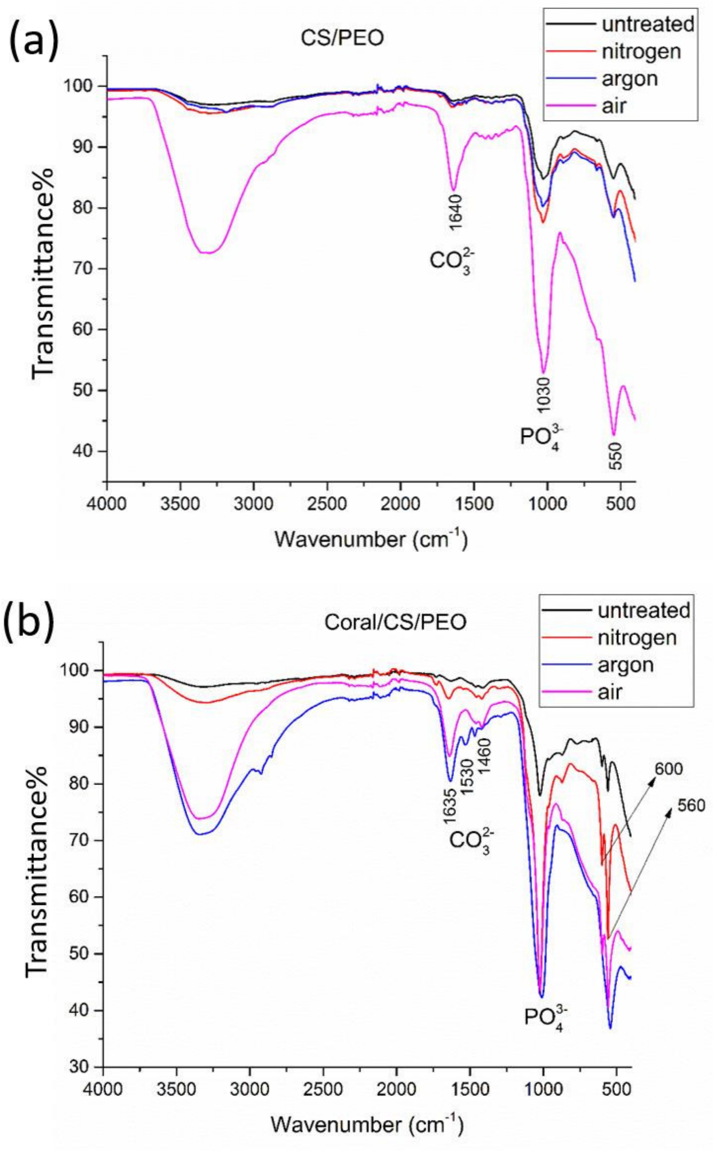

Figure 8.14 FTIR spectra after immersing in SBF for 4 weeks of untreated and air, Ar and N_2 plasma-treated CS/PEO NFs (a) and Coral/CS/PEO NFs (b).

Additionally, peaks between 1460 and 1640 cm^{-1}, corresponding to CO_3^{2-} groups, were also present in the FTIR spectra [35,46,278]. Based on several previous studies, the occurrence of these bands is indeed representative of apatite and in particular type B carbonate apatite in which CO_3^{2-} substitutes PO_4^{3-} [35,278]. FTIR spectra of other CaP peaks were revealed to have slightly different peaks such as the typical presence of two intense peaks at 3541 and 3488 cm^{-1} in case of dicalcium phosphate dehydrate for instance [46,278]. When concurrently analyzing the FTIR spectra (Figure 8.14 (a & b)) and the SEM images (Figure 8.13 (a-H)), one can further confirm that carbonate apatite, represented by the following formula $Ca_{10-x/2}(PO_4)_{6-x}(CO_3)_x(OH)_2$, is the CaP phase deposited on the fibers [277,279]. In fact, LeGeros has shown that this specific phase exhibits, in contrast to the other phases, nanosized particles similar to the crystals formed on the fibers in this chapter. Carbonate substitution is indeed known to cause a reduction in the crystal size which further resulted in the prevention of interfibrous pore blockage. Interestingly, carbonate addition into biological apatite is a natural mechanism that highly occurs in bones thus making the CaP-coated fibers perfect candidates for BTE [277].

When closely examining the FTIR spectra of untreated and plasma-treated CS/PEO NFs (Figure 8.14 (a)), significantly more intense peaks attributed to PO_4^{3-} and CO_3^{2-} groups could be visualized after air plasma treatment compared to no and other plasma modifications. This correlates with the SEM images in which one can visualize the increased amount of deposited CaP crystals on the air-plasma-treated NFs having a COOH-rich surface. A clear distinction could also be noticed between the different FTIR spectra of Coral/CS/PEO fibers with PO_4^{3-} and CO_3^{2-} peaks increasing in intensity in the following order: untreated, nitrogen, argon and air plasma-treated NFs (Figure 8.14 (b)). These results can be again linked back to the SEM images showing the enhanced and accelerated CaP growth on air- and argon-plasma-treated fibers on which surface oxygen-containing functionalities were significantly increased. FTIR results further confirmed that the Ca-enriched aspect of coral-containing fibers is very beneficial in CaP deposition. In fact, in addition to the boosted PO_4^{3-} peaks intensity, coral-containing fibers also exhibited additional and intensified peaks assigned to CO_3^{2-} groups when comparing with coral-free fibers. This finding suggests that the carbonate substitution occurs more frequently in coral-containing fibers which might accelerate CaP growth and have an influence on the morphology of the CaP crystals. Indeed, coral-containing fibers presented a more flake-like crystal shape rather than the globular crystal shape observed on the coral-free fibers.

8.3.8.5 XRD measurements on plasma-treated CE/PEO and Coral/CS/PEO NFs immersed in SBF

In a final step of this experimental chapter, XRD measurements have been performed on the NFs post-immersion in SBF in order to investigate the degree of crystallization of the deposited calcium phosphate. Unfortunately, the crystal structure of the mineral deposition could not be identified as can be seen in the XRD spectra below (Figure 8.15). The reason for this observation is that the formed calcium phosphate layer on the NFs was too thin to be identified. A similar amorphous structure with a broad peak at ∼25° has also been reported in previous studies involving chitosan NFs [280,281]. Moreover, Jin et al. could also not identify the crystal structure of the mineral deposition on composite chitosan fibers post-immersion in SBF by the obtained XRD patterns [282]. However, the deposition of CaP crystals via nucleation and growth mechanisms [282] was clearly visualized in the previously shown SEM images.

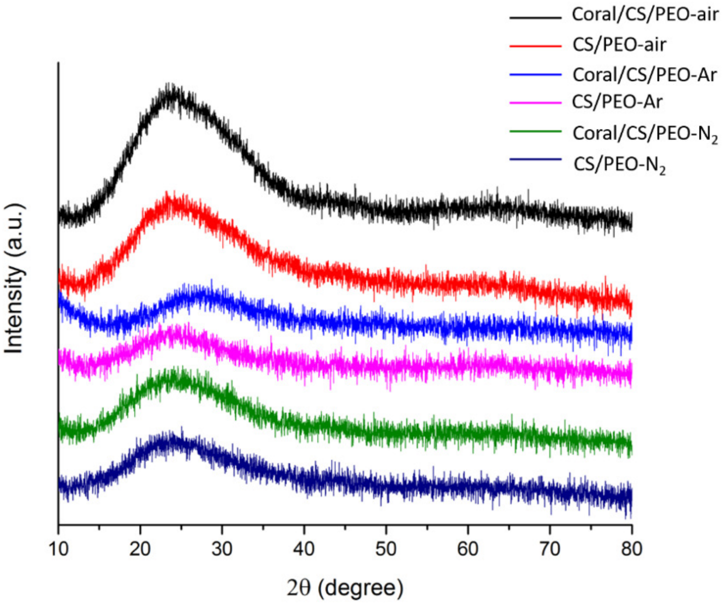

Figure 8.15 XRD spectra of the air, Ar and N_2 plasma-treated CS/PEO and Coral/CS/PEO NFs post-immersion in SBF.

8.4 Conclusion

This chapter adopted an integrative strategy merging topographical cues with bulk and surface biochemical diversity in the design of bone tissue-engineered scaffolds. In fact, natural coral having a bone-like Ca-enriched structure was added to electrospun CS/PEO nanofibrous scaffolds mimicking the bECM architecture. Coral-free and coral-containing fibers were then subjected to plasma surface modifications using Ar, Air or N_2 DBDs operating at medium pressure (5.0 kPa) to further enhance the scaffolds osseoinduction, osteoconduction and osteointegration. Afterwards, an extensive comparative study of the physicochemical properties, cytocompatibility and CaP growth capacity was performed. Results revealed that all plasma treatments significantly enhanced the fibers wettability by incorporating polar groups onto their surface. XPS spectra have in particular shown that oxygen-containing functionalities in the form of C-O, O-C=O and C=O were mainly inserted on air and argon plasma-treated samples. Nitrogen plasma activation have triggered the grafting of nitrogen-containing groups represented by C-N and O=C-N in addition to similar oxygen-containing groups. It is worth mentioning that the relative amount of each chemical group was different on the different fiber conditions with air plasma incorporating the highest amount of C-O, C=O and O-C=O bonds for instance. SEM images have indicated the absence of any morphological or dimensional alterations of the fibers post-plasma treatments. The improved plasma-induced surface chemistry has strikingly enhanced the adhesion and proliferation of MC3T3 osteoblasts that were fully spread out on the plasma-activated fibers regardless of the used discharge gas. The interplay between the plasma treatment and the presence of coral particles in the fibers was shown to further boost the density and the initial adhesion of the cells. Finally, the *in vivo* capacity of the fibers to trigger CaP growth onto their surface was predicted via a biomimetic method illustrated by an immersion in SBF. Oxygen-containing functionalities mainly COOH groups were shown to stimulate the CaP nucleation and constitute the main CaP nuclei binding sites. As such, globular nano-dimensional CaP crystals were deposited on air and nitrogen plasma-treated CS/PEO NFs while thicker layers of flake-like CaP nanocrystals were fully and individually covering each plasma-treated Coral/CS/PEO fiber without blocking the pores of the fibrous mesh architecture. The initial Ca-enriched aspect of coral particles were therefore responsible of the accelerated CaP nucleation and growth. FTIR measurements post-SBF immersion have indicated that the deposited CaP phase is the type B carbonate apatite occurring in normal bone calcification. Overall, the unique integrative characteristics of plasma-treated coral-containing CS/PEO NFs constitute a promising approach to effectively repair bone defects and revolutionize the field of BTE.

Chapter 9. General Conclusions and Outlook

9.1 Conclusions

The current dissertation is built on two main goals revolving around novel unraveled aspects of non-thermal plasma activation of polymers: the first tackles fundamental plasma/surface chemical processes and the second is application-oriented and perfectly situated in the particularly dynamic field of bone TE.

To date, numerous advanced fundamental studies have attempted to apprehend the exact plasma/surface interactions occurring upon plasma activation of polymers. However, a clear distinction between particular mechanisms occurring in-plasma and post-plasma treatment performed at medium pressure is up-to-the-minute missing and has therefore constituted the first aim of this thesis. In **Chapter 6**, UHMWPE films were subjected to N_2 and Ar plasma using a DBD operating at 5.0 kPa with a highly controlled and minimally oxygen-contaminated chamber pre-evacuated to a base pressure of 10^{-7} kPa. A distinctive combination of OES and *in situ* XPS was then used to characterize the in-plasma species/surface interactions. Post-plasma surface oxidation and ageing were unraveled by exposing plasma-treated samples to ambient air from 5 min to 21 days and performing comparative *ex situ* XPS measurements. Results revealed that Ar and N_2 discharges were predominantly composed of exited Ar species and molecular N_2 and N_2^+ states respectively, with discernable low intensity OES emission lines attributed to OH radicals and excited N_2 molecules in the Ar discharge. *In situ* XPS analysis showed a remarkably high nitrogen incorporation (20.6 %) with only negligible oxygen content (2.8 %) on the polymer surface thus leading to a significantly enhanced N-selectivity when comparing to the current state-of-the-art. In fact, nonreactive plasma species of which the excited N_2 molecules are able to generate surface polymer radicals that will in turn react with the chemically active species namely the exited N_2^+ ions and atomic N thus grafting N-containing groups onto the surface. More surface oxygen (5.9 %) was however detected after Ar activation which is probably due to the high energy Ar metastables more efficiently breaking surface C-C and C-H bonds thus creating more surface radicals that can react with the highly reactive O_2 impurities. Moreover, Ar metastables can as well efficiently dissociate H_2O molecules present in the feed gas thus producing OH radicals known to play a major role in the incorporation of O-containing groups onto UHMWPE. Indirect XPS analysis confirmed the occurrence of post-plasma oxidation processes illustrated by reactions between carbon-centered free radicals and ambient oxygen: O-C=O and N-C=O bonds were mainly formed on N_2-treated surfaces while C-O bonds were mostly created on Ar-treated surfaces. From a certain storage time onwards, surface polymeric chain reorientation took over the oxidation processes leading to a decreased surface wettability as a result of the migration of some pre-induced oxygen and nitrogen-containing groups away from the surface. **Chapter 7** further advanced in complexity and purposely investigated exclusive in-plasma initiated oxidation processes by deliberately adding different concentrations of oxygen (ranging from 6.2×10^{-3} % to 5 %) to the previously studied non-oxygen containing feed gases (N_2 and Ar). A very high reactivity of O_2 was perceived in N_2 plasmas via the detected extreme changes in the surface elemental composition. In fact, a steep rise in the O surface content at the expenses of N content was detected upon the addition of only 6.2×10^{-3} % of O_2 to the feed gas. When the added O_2 exceeded 1 %, the nitrogen incorporation onto the surface was fully depleted. In this case, the surface radicals created by the non-reactive plasma species are probably rapidly reacting with the highly reactive O_2 molecules in a way overpowering the reactions with nitrogen species. The moment a small concentration of O_2 is added to the Ar gas flow, a sharp increase in the surface oxygen content is also detected. Thereafter, the evolution of the surface oxygen amount runs in parallel with the amount of the extra O_2 added in the gas mixture. In fact when more O_2 is present in the discharge, more surface radicals are excepted to react with O_2 molecules instead of interacting with each other which eventually leads to more O-containing functionalities inserted on the surface.

Overall, several in-depth fundamental acquaintances on in- and post-plasma surface interactions were discriminated in this thesis that constitutes a perfect-picture reference for Ar and N_2 plasma activation of polymers. The light was shed on the fact that in-plasma oxidation processes stemming from highly reactive oxygen impurities lingering inside plasma reactors largely contribute to the final surface oxygen content. In fact, the presence of O_2 in the plasma reactor can, depending on its concentration, strikingly change the surface chemistry of surfaces exposed to N_2 and Ar plasmas: oxygen-containing functionalities will be dominantly incorporated onto the surface which suppresses the surface nitrogen uptake normally occurring in N_2 plasma and the cross-linking typically occurring in Ar plasma.

After deeply uncovering the fundamentals of in-plasma and post-plasma chemical processes occurring at polymeric surfaces, the reaped knowledge was used to plasma-treat bone TE scaffolds for a synergistic enhancement of cell/material interactions and biomineralization. Bone TE is in particular selected because of the high alerting incidence of bone defects occurring nowadays which triggers an urgent need for artificial implants sufficiently boosting bone regeneration. As such, in **Chapter 8** of the thesis, an integrative approach merging the advantages of previous scaffolds and implementing novel topographical and plasma-induced chemical cues was adopted in the design of a novel bone TE scaffold. Natural coral having a bone-like calcium-enriched structure was added to electrospun CS/ PEO nanofibrous scaffolds mimicking the bone ECM architecture. In order to further enhance the scaffolds osseoinduction, osteoconduction and osteointegration, coral-free and coral-containing fibers were then subjected to plasma surface modifications using Ar, Air or N_2 DBD operating at medium pressure (5.0 kPa). A profound comparative study of the physicochemical surface properties, cytocompatibility and CaP growth capacity was performed. Results revealed that the synergetic effects of coral particles and plasma-induced surface chemistry strikingly improved the performances of osteoblasts and led to the deposition of bone-like carbonate apatite nanocrystals without blocking the pores of the nanofibrous architecture.

Overall, the joint use of plasma activation together with refined topographical and biomolecular cues in the design of bone implants is believed to effectively repair bone defects and revolutionize the field of bone TE.

9.2 Outlook

9.2.1 Future fundamental research perspectives

In this thesis, the distinctive use of *in situ* XPS measurements combined with OES analysis has successfully allowed to resolve the unremitting debate between plasma scientists on the relative implication of in-plasma and post-plasma surface interactions in the oxidation of surfaces subjected to Ar and N_2 discharges. The next planned step is to apply the same methodology in unravelling in-plasma and post-plasma mechanisms upon exposure of polymers to plasmas sustained in other non-oxygen containing feed gases such as He, Ne and NH_3. This approach will provide answers to the numerous fundamental questions that still remain unresolved to this day in a broader range of the plasma activation field.

It is generally agreed within the scientific community that plasma activation is a non-invasive method inducing effects limited to the top few (sub)surface layers of an exposed substrate. Nevertheless, the experimental acquisition of precise information regarding the penetration depth and the vertical spatial distribution of plasma-induced functionalities into a surface is believed to provide extra useful acquaintances on plasma treatments. As such, a great value that can be added to the conducted research in this thesis, would be to examine different plasma-treated polymer films making use of *in situ* XPS in combination with C_{60} sputtering. The acquired chemical depth profiles will thus enable to clearly define the exact plasma penetration depth and the spatial distribution of plasma-induced functionalities without the interference of post-plasma oxidation. A similar approaches performed through *ex situ* measurements would also allow to check via a comparative study the exclusive penetration depth of post-plasma oxidation.

Next to the plasma activation, a very interesting research pathway would be to investigate, via *in situ* XPS analyses, the exclusive in-plasma chemical mechanisms occurring in the more complex plasma polymerization of non-oxygen containing monomers such as allylamine, cyclopropylamine, propanethiol and thiophenol. Such plasma polymerizations are performed to deposit thin cross-linked coatings rich in a desired functionality (e.g. amine and thiol) onto polymeric substrates. An undesirable oxidation of such coatings depleting or sheltering its characteristic functionality is sometimes detected. As such, the examination of the relative involvement of in-plasma initiated oxidation versus post-plasma oxidation would constitute a major breakthrough towards a deeper understanding and subsequent refinement of plasma polymerization processes.

9.2.2 Future applied research perspectives

The results of the second application-oriented part of this thesis showed that the plasma activation of electrospun fibrous scaffolds would constitute a very powerful tool in enhancing bone regeneration. The next logical step would be therefore to translate from *in vitro* to *in vivo* tests to check this hypothesis.

In order to widen the functionalization spectrum and more adequately control the specificity of the grafted functional groups, plasma polymerization on the electrospun scaffolds is planned. Several plasma polymers can be considered for the subsequent immobilization of particular biomolecules that are known to enhance the performance of osteoblasts. A careful fine-tuning of all process parameters should be carried out to allow the deposition of stable plasma-polymerized coatings on the nanofibrous meshes without damaging their relatively fragile structure.

The final results of the thesis have shown a successful biomineralization of the plasma-activated scaffolds upon their incubation in SBF. Nonetheless, the sufficient growth of CaP crystals on the scaffolds demanded a relatively long time (one month) to occur. As such, in order accelerate the biomineralization, a direct deposition of hydroxyapatite nanoparticles on the surface of the plasma-treated nanofibers will be explored in the near future.

Appendix

A. XPS characterization of plasma-activated polymeric surfaces (techniques not used in the thesis)

A.1 Quantification of target surface functionalities via a combination of derivatization reactions and XPS analyses

Several plasma-induced surface chemical functionalities such as amino, carboxyl, hydroxyl and epoxy groups are frequently aimed to be incorporated onto polymeric surfaces with a high selectivity [24,48,68,208,283,284]. On the one hand, specific functionalities are sometimes desired for certain applications as they have different polarities and can therefore affect the surface wettability differently [20,33,285]. On the other hand, when particularly considering the biomedical field, such polar groups act as very efficient and specific binding sites for proteins and biomolecules and were shown to distinctively enhance cell performances in a cell-type and cell activity-dependent aspect [48,135]. As such, a precise identification and quantification of such surface groups is highly needed. In order to overcome the previously stated limitations associated with the fitting of high resolution XPS curves, several authors have combined chemical derivatization techniques with XPS analyses thus enabling the labelling and the more precise density determination of the looked-for functional groups [36,48,68,208,283,284]. The basic principle of derivatization is to allow a very specific reaction to occur between the target functionality and a special marker molecule (usually containing fluorine atoms). In fact, the marker must have at least one element that is not present in the original sample. After the derivatization reaction, XPS survey scans can be measured on the derivatized polymers to identify and quantify the one extra element of the marker molecule and link back the obtained results to the density of the target functionalities by simple mathematical calculations [36,99]. This integrative derivatization/XPS method was mainly conducted in studies implicating plasma polymerization processes in which cross-linked coatings rich in the specific target functionality are deposited on polymeric substrates [32,68,208,286,287]. Nonetheless, a special interest in determining the density of surface NH_2 groups was also perceived in case of plasma-activated polymeric substrates. This interest was largely associated with the particular ability of primary amines to covalently but also electrostatically bind proteins and signaling biomolecules which in turn significantly enhances different vital cell activities such as adhesion and growth [24,48,99]. As such, several research groups have conducted a derivatization of amino groups on plasma-activated surfaces using 4-(trifluoromethyl) benzaldehyde (TFBA) as target marker [36,48,99,288–290]. This marker was confirmed to selectively react with primary amines leading to the incorporation of CF_3 groups onto the surface as depicted in Figure A.1. After the assessment of fluorine, nitrogen and carbon contents via XPS measurements, the amino selectivity and amino grafting efficiency of the performed plasma treatment can be calculated as follows [99]:

$$\text{Amino selectivity (\%)} = \frac{[NH_2]}{[N]} = \frac{\left({[F]}/{3}\right)}{[N]} \times 100$$

$$\text{Amino grafting efficiency (\%)} = \frac{[NH_2]}{[C]} = \frac{\left({[F]}/{3}\right)}{\left([C] - 8{[F]}/{3}\right)} \times 100$$

The derivatized amine groups can be as well distinguished by the CF_3 component peak of the C1s spectrum [36,99,290].

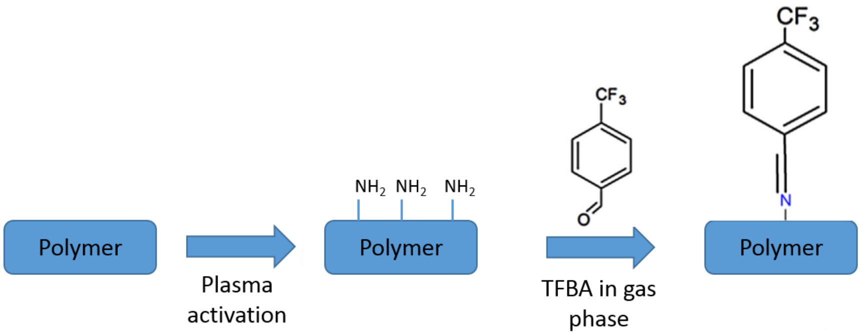

Figure A.1 Chemical derivatization occurring between TFBA and plasma-induced primary amines.

Table A.1 portrays the N/C ratio, amino grafting efficiency (NH_2/C) and amino selectivity (NH_2/N) that were detected on the surface of plasma-activated polymers via TFBA derivatization and subsequent XPS analysis. The corresponding most influential parameters that have led to the reported results are also displayed. This table has revealed that the amino grafting efficiency (NH_2/C) in all the reviewed papers was generally quite low while the amino selectivity (NH_2/N) varied depending on the used working parameters. Favia et al. have for instance revealed that the addition of H_2 to an NH_3 RF glow discharge resulted in an enhanced amino grafting selectivity but a reduced grafting efficiency on plasma-treated PE surfaces [289]. Meyer-Plath et al. have also investigated the effect of H_2 admixtures to nitrogen-containing discharges in an extensive comparative study with the aim to generate mono-functional surfaces. In fact, PS substrates were subjected to several plasma treatments having different parametric arrangements including N_2 + H_2 MW, NH_3 MW, NH_3 + H_2 RF and N_2 + H_2 RF discharges. Moreover, changes in the treatment time, sample-to-plasma distance and pressure were also tested. Results have generally revealed that generating plasma in nitrogen and hydrogen atmospheres allows to control the selectivity of amino grafting in the full range from 0 to 100 %. This study has therefore underlined that besides the key role of hydrogen in grafting amino groups, the optimization of the process parameters is very important in reaching the desired surface amino selectivity [48]. Nonetheless, Kràl' et al. have shown that the amino group selectivity on PE sheets treated with MW discharges sustained in NH_3 or various N_2/H_2 gas mixtures has reached 100 % only after the NH_3 treatment. This could be probably related to the more limited variation of parameters that entered into play [291]. In order to better comprehend the chemical processes standing behind the preferential grafting of NH_2 groups on plasma-treated surfaces, Cicala et al. have complemented the XPS analyses performed post-derivatization with OES measurements. They have observed that when the emission intensity of NH_x radicals is more pronounced than that of excited N_2 molecules in an NH_3-fed RF discharge, a high density of NH_2 functionalities could be incorporated on PE surfaces through, amongst others, the reduction by H atoms. Interestingly, the study has also shown that the modulation of the active species in-plasma can be purposely done via plasma power adjustments for a high amino selectivity [288]. Ogino et al. have also noticed that an increase in the OES emission intensity of NH_x radicals in an Ar/NH_3 MW plasma could lead to a heightened amino group concentration onto polyurethane (PU) surfaces. In fact, the addition of Ar to NH_3 was the reason behind the increased intensity of NH_x species that were generated by the Penning effect. Nonetheless, the amino group selectivity turned out to be higher in the case of pure NH_3 plasma given the fact that the enhanced decomposition of NH_3 by Ar metastables in Ar/NH_3 plasma can also incorporate secondary and tertiary amino groups in parallel with primary amines [290].

More recently, Asadian et al. have exposed PCL and CS/PEO nanofibers (NFs) to N_2 and NH_3/He DBD plasma ignited at medium pressure [36,99]. Paradoxical results were obtained between both substrates. A significantly higher NH_2 grafting efficiency and selectivity was perceived on PCL fibers subjected to a He/NH_3 plasma treatment compared to those treated with N_2 plasma while an opposite trend was detected in case of CS/PEO fibers. The relatively high amino density on N_2 plasma-activated CS/PEO fibers was correlated to the higher N/C ratio (10.6) suggesting the incorporation of more primary amine groups together with other types of N-containing functional groups [36]. It is worth highlighting the fact that CS/PEO fibers initially contain NH_2 groups which can potentially explain the contradictory results obtained on both polymers and draw the attention again on the importance of the base polymer structure in the final plasma-induced surface chemistry.

After conducting XPS analyses post-TFBA derivatization applied to aminated surfaces, Yegen et al. have actually shed the light on a limitation of this approach. An unexpected fluorine peak was detected at a binding energy attributed to F in fluorides with higher intensities after prolonged derivatization times. This inspection emphasized the existence of unanticipated reaction pathways in addition to the one shown in Figure A.1. Such extra reactions seemed to induce C–F bond cleavages. As such, an amine quantification based on the F surface content or on the CF_3 component peak area of the C1s curve can underestimate the amine content. This suggests the need of more reliable derivatization reactions [292]. Another general limitation of the derivatization/XPS approaches is the steric hindrance that has to be taken into consideration in case of surfaces with a high density of the target functional groups [293]. Nonetheless, the grafting efficiency of NH_2 groups on plasma-activated polymers was perceived to be relatively low thus not triggering a steric hindrance upon derivatization reactions.

Other reagents such as trifluoroacetic anhydride (TFAA) were comprehensively investigated for the derivatization and determination of surface hydroxyl groups [283,293]. Nonetheless, contrary to the large number of available papers on amine group derivatization, a limited number of papers is dealing with hydroxyl group derivatization. As such, the application of this approach on plasma-activated surfaces is very rare. On the one hand, this can be due to the fact that some authors have reported that amines are more effective in improving cell-material interactions than hydroxyl groups [294]. On the other, the derivatization using TFAA is not as straightforward as the one with TFBA. The main problem is that TFAA does not only react with OH but also with other nucleophilic groups such as amines or thiols. TFAA can be bonded to OH groups to form trifluoroacetate and to NH_2 groups generating trifluoroacetamide. Both reactions will therefore graft CF_3 groups onto the surface with the carbon atom bonded to 3 fluorine atoms and to another carbon atom. This adjacent carbon has a double bond to oxygen in case TFAA has reacted with OH groups and a single bond to a nitrogen when TFAA has reacted with an amine. This would lead to 2 CF_3 component peaks at slightly different binding energies in the high resolution C1s curve: one peak corresponding to a carbon atom in a trifluoroacetate and another peak attributed to a carbon atom in a trifluoroacetamide. Holländer et al. have indeed proven that the C1s curve of a TFAA-labeled PP surface pre-subjected to a nitrogen DBD plasma treatment could be successfully used to distinguish different types of functional groups from the CF_3 component. Nonetheless, the analysis was purely quantitative [283].

Table A.1 Overview of literature on nitrogen grafting efficiency and selectivity results obtained upon TFBA derivatization reaction and XPS analysis performed on plasma-activated polymers using nitrogen-containing discharges.

Authors (Year)	**Polymeric substrate**	**Reactor and working pressure**	**Working gas/ gas mixture**	**Maximum surface density**		
				N/C (%)	**NH_2/C (%)**	**NH_2/N (%)**
Favia et al. (1995) [289]	PE	RF, 66.6 Pa	NH_3+H_2	22.0	3.5	75.0
Meyer-Plath et al. (2003) [48]	PS	MW and RF, 0-120 Pa	NH_3+H_2, N_2+H_2	25.0	3.5	100.0
Cicala et al. (1999) [288]	PE	RF, 66.6 Pa	NH_3	10.0	-	60.0
Kràl’ et al. (2008) [291]	PE	MW, 13.3 Pa	NH_3	3.5	2.1	100.0
Ogino et al. (2011) [290]	PU	MW, 13 Pa	NH_3+Ar	-	2.1	34.0
Asadian et al. (2018) [36]	CS/PEO	DBD, 5 kPa	N_2	10.6	5.6	53.3
	CS/PEO	DBD, 5 kPa	NH_3/He	9.0	3.5	39.2
Asadian et al. (2018) [99]	PCL	DBD, 5 kPa	N_2	36.4	1.2	3.2
	PCL	DBD, 5 kPa	NH_3/He	16.7	2.6	15.6

Several authors have used trifluoroethanol (TFE) as a derivatization agent prior to XPS analysis to distinguish between and to precisely quantify carboxylic and ester groups but mainly in the context of plasma polymerization rather than plasma activation [295,296].

A.2 Chemical depth profiling via angle-resolved XPS measurements

It is generally agreed within the scientific community that plasma activation is a non-invasive method inducing effects limited to the top few (sub)surface layers of an exposed substrate [16,33,34,38]. Nevertheless, the experimental acquisition of precise information regarding the penetration depth and the vertical spatial distribution of plasma-induced functionalities into a surface is believed to provide extra useful acquaintances on plasma treatments. Interestingly, XPS can be used in this context to acquire chemical depth profiles via 2 methods: 1) the use of ion guns to sputter away organic layers from the polymeric substrate in combination with XPS measurements after each sputtering cycle and 2) angle-resolved XPS (ARXPS) measurements [134,297–299]. In the first approach, it is well known that monatomic ion guns such as Ar^+ and Ga^+ lead to a harsh etching and to the penetration of individual ions relatively deep into the surface thus triggering major chemical damages within and beyond the exposed organic subsurface [300–302]. As such, the usefulness of such guns in thin surface analyses of polymeric materials in general and plasma-activated substrates in particular is limited. The development of C_{60} ion sources came to solve this issue. In fact, when a C_{60} ion cluster impacts a surface, it collapses and releases energy in the near surface thus only exposing a subsurface layer that has undergone a minimal chemical damage. Given the high sputtering efficiency and shallow penetration of the C_{60} sputtering process, unbiased depth chemical profiles could be acquired on polymeric substrates [300,302]. Nonetheless, to the best of our knowledge, C_{60} sputtering has been only employed so far for the XPS analysis of plasma-polymerized coatings deposited on different substrates but not yet in the context of plasma-activated polymeric substrates [14,59]. The second approach involving ARXPS measurements was however widely used to get information about the elemental composition and the grafted functionalities upon plasma activation as a function of the analytical depth [79,131,132,146,303,304]. It is a non-destructive method that is perfectly suitable for plasma-activated surfaces as it is only affected by a sufficient shallow depth range of approximately 2 to 10 nm and allows to get a differentiated chemical vertical distribution within the first atomic layers of a sample. ARXPS data are actually acquired by tilting the sample placed on the XPS plate to vary the angle of emission at which the electrons are collected and ejected, thereby allowing their detection from a specific depth [298]. When repeatedly changing the take-off angle over a certain range and performing each time an XPS measurement, a chemical depth profile can be obtained. The fundamentals of ARXPS are depicted in Figure A.2 where α corresponds to the take-off angle between the sample plane and the photoelectron emission direction, *l* to the attenuation depth or the inelastic mean free path of the electron and *d* to the vertical sampling depth [131]. According to the equation presented in Figure A.2, when α= 90° the analysis depth reaches a maximum.

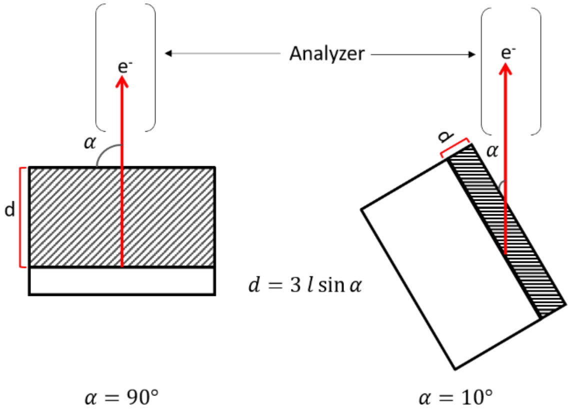

Figure A.2 Principle of angle-resolved XPS. The given equation determines the analysis depth (d) that is dependent on the photoemission angle (α) and the electron attenuation length (l).

In a trial to reveal the vertical distribution of plasma-induced oxygen into an LDPE surface, Dufour et al. have performed ARXPS measurements at take-off angles varying between 15° and 75° after exposing the substrate to an atmospheric RF He/O_2 discharge. The resulting chemical depth profile covering a range of 2 nm to approximately 8 nm has revealed that the oxygen content progressively decreased from 33 % 29 % when increasing the analysis depth (Figure A.3). The fact that the oxygen variations stayed lower than 5 % over a depth of 8 nm was attributed to the high O_2 flow rate (200 $ml.min^{-1}$) that was adopted during the treatment. The authors have stated that O_2 flow rates comprised between 1 and 5 $ml.min^{-1}$ might be required to trigger a shallower plasma penetration depth and thus significant variations in O content over an 8 nm depth [134]. In contrast, when subjecting PS surfaces to a low pressure RF O_2 discharge, ARXPS measurements revealed a more pronounced vertical gradient with larger oxygen content variances between escape depths of 2.6 nm and 10.2 nm. At a plasma exposure time of 1 s, the oxygen content decreased from approximately 30 % at a depth of 2.6 nm to 21 % at a depth of 10.2 nm. Nonetheless, when increasing the treatment time to 50 s, plasma penetration depth seemed to increase as can be confirmed by a similar oxygen content at a depth of 2.6 nm (30 %) but a considerably higher oxygen content at a depth of 10.6 nm (24 %) [303]. Similar trends were obtained by Haïdopoulos et al. who have also subjected PS substrates to a low pressure O_2 RF treatment and then reconstructed the oxygen depth profiles based on ARXPS. In fact, for plasma exposure times between 6 s and 90 s, the depth profiles depicted approximately the same oxygen contents on the outer layers with thicker O profiles reaching 6 nm as the treatment time increases. However, when further increasing the treatment times to 150 s, the oxidized layer thickness was significantly decreased to 3 nm and a higher overall O concentration was perceived. Such interesting observations have made evidence that some outer layers were removed and newly exposed layers were oxidized again within a competition between 2 mechanisms namely plasma etching and functionalization [132]. Besides the treatment time, the working gas seems to also have an influence on the plasma-induced oxygen depth profiles. In this context, Lopez-Santos et al. have performed ARXPS measurements on PS substrates subjected to RF and MW nitrogen-containing discharges. The inevitable presence of oxygen traces in all discharges has led to a surface oxygen enrichment that is only restricted to the topmost surface layers (2-3 nm) [79].

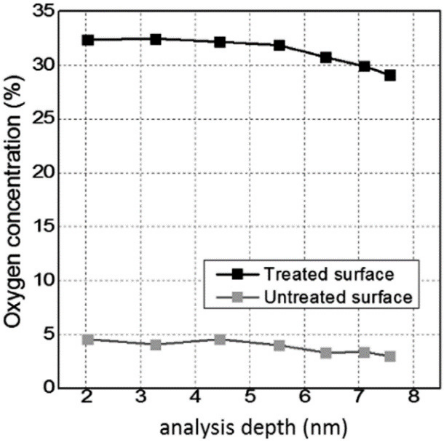

Figure A.3 Depth profile of the oxygen content in the subsurface of untreated and He/O_2 plasma-treated LDPE substrates [134].

Some authors have also noticed that, in addition to the plasma parameters, the type of the treated polymer or its degree of crystallinity can also influence the plasma penetration depth and as such the depth and distribution of plasma-induced functionalities. For instance, Reznickova et al. have subjected UHMWPE, LDPE and high density PE (HDPE) to a low pressure Ar plasma treatment and have compared the surface chemistry of the 3 substrates. ARXPS data recorded at take-off angles of 0° and 81° have shown a significantly higher oxygen concentration on UHMWPE (34 %) at the angle of 81° (≈ 8-10 atomic layers) compared to LDPE and HDPE in which the oxygen concentration was 31 %. This difference was attributed to the fact that UHMWPE exhibited a higher polymeric chain motility on its surface which can be triggered by an excessive surface ablation. This chain motility is believed to be limited by the polymer crystallinity and surface cross-linking which can also justify the lower oxygen content in the deep surface layers of LDPE and HDPE [146]. This statement was actually approved by Kim et al. who have firstly exposed LDPE substrates having different degrees of crystallinity namely quenched LDPE and annealed LDPE to an O_2 plasma and then performed ARXPS measurements (take-off angles: 20°, 50° and 90°). For both polymers, a linear decrease in oxygen content was perceived with the increase in the measurement depth thus confirming again that the reactions of plasma excited species with the polymeric chains occurred in a very shallow region. In fact, for the oxygen functionalization to occur, carbon radicals have to be generated on the surface by accelerated excited species such as oxygen ions in plasma and to react with molecular oxygen. Nonetheless, oxygen ions are unable to penetrate deep into the surface layers and molecular oxygen cannot easily diffuse away from the top surface thus explaining the declining O depth profiles. Interestingly, an overall lower oxygen content and higher decreasing rate of oxygen throughout the depth were observed in the annealed LDPE compared to the quenched LDPE. This can actually reflect the less prominent chemical reactivity of the annealed LDPE having a higher crystallinity and thus a lower free volume for the diffusion of molecular oxygen. In contrast, the lower crystallinity of the quenched LDPE confers it with a higher motion freedom of the plasma species and plasma-induced functional groups. The fitting of high resolution C1s spectra have revealed that there were actually no large variations in the concentrations of C=O and O-C=O bonds all over 8 nm in depth. The observed differences in the oxygen depth profiles were because of the more concentrated C-O bonds on the outer surface region and their lower concentration in the deep surface region especially for the annealed LDPE (Figure A.4) [133]. Jacobs et al. have carried out ARXPS measurements on 2 different types of polymers namely PP and PET after exposing them to an atmospheric pressure air plasma treatment. Opposite results were obtained in terms of the location of the oxygen enrichment throughout the surface regions: as the depth increases, increasing and decreasing oxygen contents were detected for PP and PET respectively. Moreover, a much lower oxygen concentration was perceived in the first few atomic layers of PP compared to deeper locations with a difference of around 17 % between take-off angles of 45° and 85°. These results drew the attention to the fact that the type of polymer might affect the location of the highest plasma reactivity throughout the surface layers [304].

ARXPS measurements were also performed after a TBFA derivatization of plasma-induced NH_2 groups on PS substrates pre-subjected to nitrogen-containing discharges. Results revealed that fluorine density profiles were shallower (2-3 nm) than their nitrogen counterparts (6-8 nm). These observations could reveal a probable underestimation of the amino density in the surface region. As such, questions marks on whether the derivatization method failed to label all amino groups or weather the plasma treatment did not initially graft them have emerged [48].

ARXPS has also constituted a very efficient method to understand some of the main underlying reasons associated with the frequently observed ageing effects post-plasma activation [66,131]. Several authors have perceived that when the storage time increases, the density profiles change as the plasma-induced functionalities progressively accommodate deeper locations inside the polymer surface. This was attributed to the re-orientation and migration of the polar groups from the top surface regions into deeper layers in order to occupy more energetically favorable positions [131–133]. A detailed discussion on the plasma ageing effect accompanied with several examples will be given in the next chapter.

Despite the beneficiary features of ARXPS measurements, sample degradation induced by a prolonged X-ray exposure can occur [297]. This problem can specifically arise when performing measurements at small angles. In fact, the intensity of the elemental peaks generally decline when decreasing the photoemission angle. Therefore, in order to obtain a good signal from different depths, a higher number of scans and subsequently longer X-ray exposure times are often required. In order to restrict the risk of sample damaging, Meyer-Plath et al. have set a reduced X-ray beam power with a short acquisition time to perform ARXPS measurements [48].

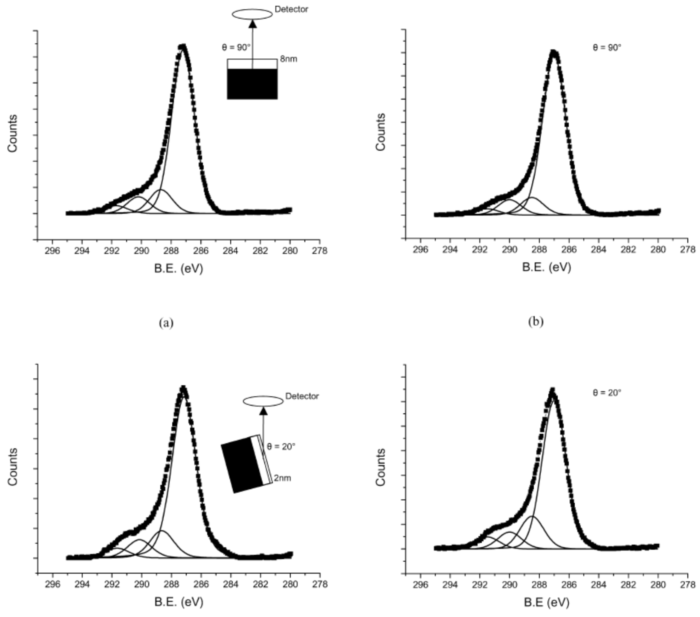

(a) (b)

(c) (d)

Figure A.4 Curve-fitted C1s spectra recorded at take-off angles of 20° and 90° for quenched (a, c) and annealed (b, d) LDPE samples subjected to an oxygen plasma treatment [133].

A.3 Determination of the lateral distribution of elements and chemical states via XPS mapping

In the early 1980's, XPS imaging has emerged as an established method for the determination of the lateral distribution of chemical species across a sample surface [305]. In fact, the advancements implemented to the XPS instrumentation have conferred it with the ability of acquiring 2D images depicting the variations in the elemental composition and chemical states over a determined surface area. This method can deliver complete XPS spectral information at every pixel of a selected area, thus providing a final chemical map of this “imaged” area [306]. To do so, the XPS manufacturers have adopted different ways based on: 1) a localization of the incident X-ray beam on the surface via specific micro-focusing, 2) a reduction of the analysis area or 3) the use of array detectors equipped with imaging optics [307]. As such, spectra with a lateral spatial resolution that can potentially reach, depending on the used instrument, a few micrometers can be acquired. The detailed principle of XPS imaging with the associated developments were extensively discussed in previous review papers [305,307].

In spite of the interesting additional findings that XPS mapping can provide, its use in the context of plasma surface activation has been often overlooked. This can be attributed to three main issues: 1) limited spatial resolution (µm range), 2) long acquisition time and 3) deficiency in the interpretation of very large spectral image data leading to a difficulty in the extraction of the needed information within a realistic time scale and without generating bias (the latter is being tackled by software developers [307,308]). As such, the implementation of XPS mapping in the framework of plasma surface activation was, to the best of our knowledge, only restricted to the elucidation of 2 incidents: 1) the resolution and micro-scale accuracy of a microplasma needle set-up locally activating polymeric surfaces on pre-defined patterns [41,272] and 2) the reactivity zones created on polymers activated using an atmospheric pressure plasma jet [309,310].

In the first case, Bitar et al. have investigated the minimal resolution of an atmospheric pressure microplasma DBD equipped with small needle electrodes (diameter: 200 µm) by plasma activating PP surfaces on a pre-defined line. In this initial study, XPS mapping measurements have been performed to detect the distribution of plasma-induced oxygen functionalities across the plasma-treated tracks and eventually determine the width of the modified lines.

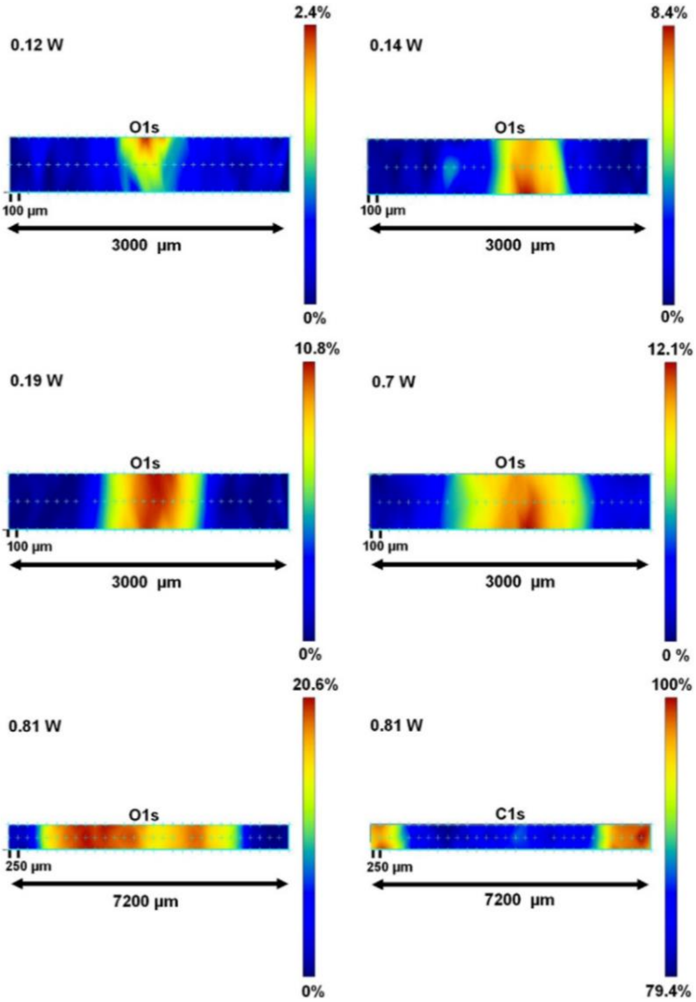

Figure A.5 Evolution of the XPS maps measured across horizontal cross-sections of a plasma-activated line on PP surfaces as a function of the plasma applied power [41].

The obtained cross-sectional maps of the treated tracks have spotted that an increase in the plasma power and treatment repeats triggered wider activated lines ranging from 0.8 mm to 5 mm with progressively higher oxygen contents. Moreover, the central part of the treated area exhibited the highest oxygen content that gradually decreased on both sides in a Gaussian distribution (Figure A.5). As such, a careful fine-tuning of the process parameters is required to get the desired dimension and concentration of plasma-induced functionalities on the treated area. Overall, one can notice that the plasma treatment effect was not all restricted to the expected size of the needle but typically expanded over a much larger area of the sample. This observation was mainly attributed to the renowned spreading of ignited microdischarges on dielectric surfaces occurring in DBDs [272].

In a subsequent study, a more sophisticated pattern implicating 3 parallel lines was adopted to locally activate PS substrates using the same microplasma device. This pattern that can ultimately trigger the occurrence of alternating hydrophilic and hydrophobic regions was applied to selectively adhere cells on the pre-defined hydrophilic lines thus showing evidence for the use of the microplasma reactor in the biomedical field. XPS maps have shown similar trends as the ones observed in the previous study in terms of track line width, oxygen content and lateral distribution as function of the treatment repeats and plasma power. Moreover, the selected distance between the 3 lines was revealed as a major parameter in delineating the plasma effect on the treated surface. In fact, when decreasing the pre-defined inter-line distance to 0.4 mm, the plasma treatment effect befell in a way leading to the overlap and connection of the 3 vertical lines that could not be any more distinguished separately. In contrast, when the distance was increased to 2 and 3 mm, three clearly distinguished lines with high oxygen content could be visualized [41] (Figure A.6).

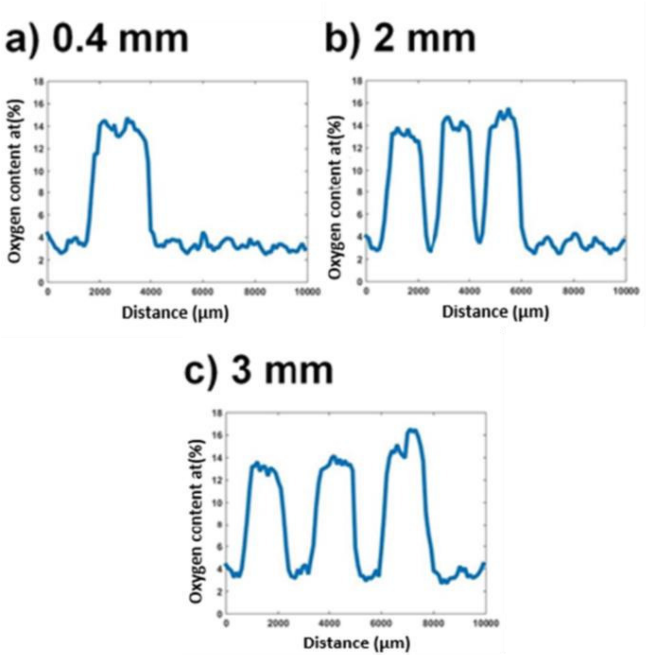

Figure A.6 Distribution of the oxygen content across 3 parallel plasma-treated lines on PS surfaces as a function of the pre-defined inter-line width [41].

In the second case, Birer et al. have aimed to demonstrate the presence of reactivity zones around a He plasma jet by performing XPS mapping of the chemical functionalities incorporated on an exposed PE surface. The measured XPS maps have reflected that the area facing the reactor tube and directly struck by the plasma jet got initially oxidized. Nonetheless, at prolonged treatment times, this central part experienced an etching effect and the local oxidation underwent an expansion outwards in the form of ring patterns. Such radial patterns were shown to exhibit different spatial potencies depending on the treatment time and gas composition. For instance, after a plasma exposure of 10 min, clear-cut ring patterns corresponding to $–NO_3$, –CO, –NO and –COO groups could be visualized with respectively decreasing diameters. The plasma-induced chemical changes could reach regions located at several millimeters from the center. The distinct radial distribution of oxidized and nitrogenized species could indeed evidence the manifestation of chemical reactivity zones upon plasma jet treatment. The admixture of nitrogen to the helium plasma jet enriched the reactivity zones with higher densities of nitrogen-containing functionalities and accelerated their incorporation on the surface. For instance, the nitrate generation was already detected on the outer perimeter at early stages and experienced a progressive expansion outwards when increasing the exposure time (Figure A.7). The authors have finally stated that the radial patterns discerned for most of the plasma-induced functionalities were presumably due to an interchange between etching processes and peripheral reactions [310]. Vesel et al. have also visualized, via XPS mapping, a large circular spot (≈2 cm) of high surface oxygen density on PET surfaces subjected to an atmospheric pressure argon plasma jet. The high reactivity spot was actually characterized by a radial gradient of decreasing oxygen density towards the outer perimeter [309].

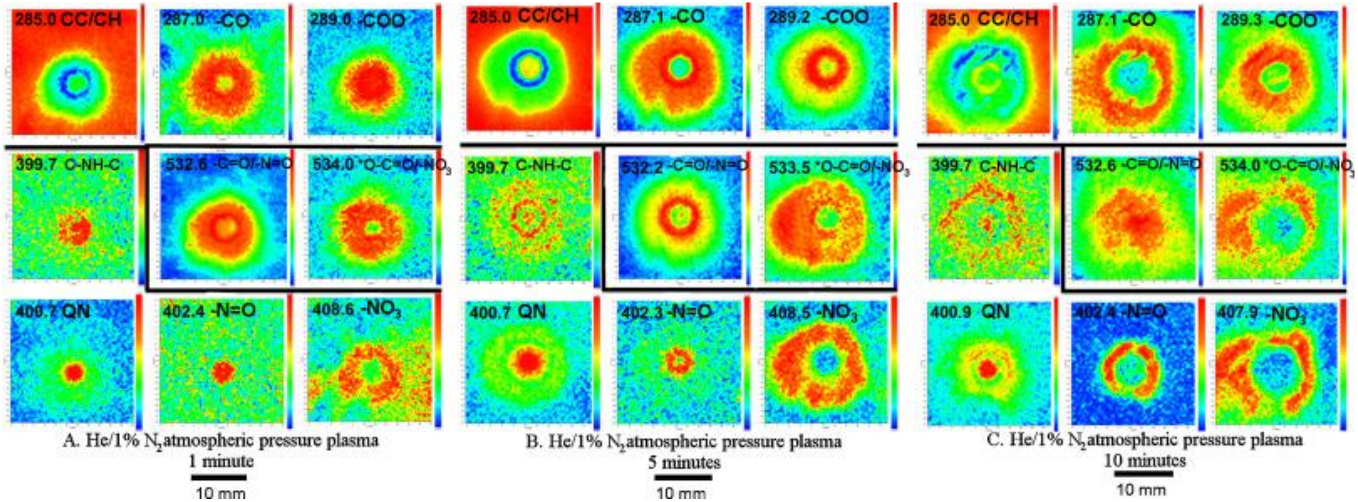

A. He/1% N_2 atmospheric pressure plasma
1 minute

B. He/1% N_2 atmospheric pressure plasma
5 minutes

C. He/1% N_2 atmospheric pressure plasma
10 minutes

Figure A.7 XPS maps of chemical functionalities incorporated on PE surfaces subjected to a 1, 5 and 10 min atmospheric He/1 % N_2 plasma treatment. The numbers indicate the binding energy of the used peaks [310].

A.4 Homogeneity evaluation of the surface chemistry across 3D microporous scaffolds via a SEM-like imaging capability of XPS

As already noticed, extensive literature on the plasma treatment of 2D polymeric samples is actually available. Nonetheless, its application on microporous 3D scaffolds used in the TE field is up-to-the-minute quite challenging and sometimes unsuccessful [311–313]. This is largely caused by the limited penetration of excited plasma species inside scaffolds because of their collisions with each other and with the scaffold struts. As such, active plasma species tend to lose their modifying ability during their diffusive travelling across 3D scaffolds. Therefore, if not carefully optimized, plasma activation processes will lead to a preferential incorporation of polar groups on the outer parts. This has frequently triggered the adhesion of cells forming dense layers only on the periphery of scaffolds that eventually ended up collapsing once the base material started to degrade [11,313]. The complexity in accurately reaching the inner struts to characterize their surface chemistry during the optimization processes of the plasma treatment accounts for a large part of this ultimate treatment non-uniformity. Some authors have actually performed XPS measurements on different sections of porous 3D scaffolds in a trial to get an insight on the penetration depth of the plasma-induced surface modification [313–315]. Nonetheless, given the small scaffold features (micrometer range), the accurate demarcation of the measurement areas on precise locations along the scaffold depth is quite challenging. Moreover, the risk of a measurement area ending up in the bulk of the struts that were cut during the scaffold sectioning pre-XPS measurements is high.

Recently, some XPS apparatuses were appended with an extra SEM-like capability allowing the generation of X-ray induced secondary electron images (SXIs) of the sample to be measured by scanning a finely focused X-ray beam characterized by a sub-10 µm size across the surface. Such images are very useful to navigate to features of interest on the sample and to precisely select the spot locations for analysis in real time. Therefore, this approach can locate small features with a 100 % confidence while avoiding unwanted areas such as zones of contamination or inhomogeneity [144,316]. Lately, the SXI camera was interestingly used to accurately define measurement spots into porous 3D-printed scaffolds and foams for an unbiased investigation of the plasma treatment homogeneity across such structures [11,144,316–318]. To do so, plasma-treated scaffolds were cross-sectioned using a sharp blade and subsequently placed on the XPS platen with the inner scaffold part exposed outwards. Once the XPS plate was moved to the analyzing chamber, the SXI camera was engaged in the delicate selection of analysis areas on desired scaffold struts. Thereafter, XPS measurements (survey scans or high resolution spectra) were performed on the selected spots (Figure A.8) [144]. For instance, Cheng et al. have followed this procedure after subjecting 3D-printed PCL scaffolds to N_2 and NH_3/He DBD plasma activations. The ensuing XPS results have revealed a more uniform distribution of plasma-induced nitrogen across the scaffolds treated with NH_3/He plasma compared to N_2 plasma. This was attributed to the higher amount of excited nitrogen species in the NH_3/He plasma which led to more particles attaining the inner struts while still upholding their modifying effect. The authors have then tried to further optimize the treatment uniformity by varying the plasma exposure time and NH_3/He flow rate. An increase in the treatment time was shown to enhance the homogeneity of nitrogen incorporation. This observation was presumably due to the fact that more inner positions could reach a saturation of the treatment effect after long plasma exposures. Figure A.9 depicted that when the flow rate was increased, the average nitrogen content had a tendency to generally increase while the homogeneity of the nitrogen content throughout the scaffolds decreased. In fact, high flow rates drove the active species to efficiently penetrate into the scaffolds' pores which could explain the higher averaged nitrogen density. Nonetheless, the high turbulence accompanying the high flow rates was presumably the cause of the decreased treatment uniformity. No clear trend in the oxygen density distributions were however observed [11].

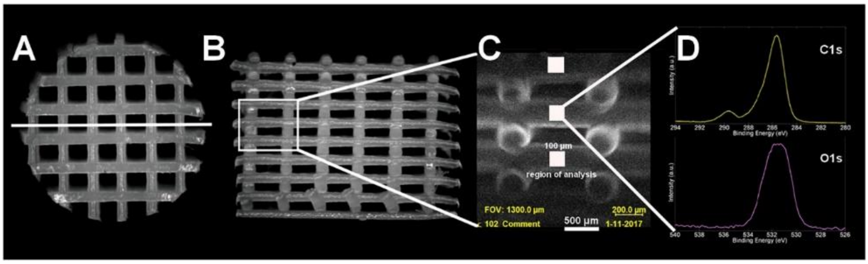

Figure A.8 Steps followed to perform XPS measurements on a pre-defined inner strut of a 3D-printed scaffold using SXI. (A: Stereomicroscopic image of the scaffold's plane; B: Stereomicroscopic image of the scaffold's cross-section; C: SXI of the scaffold's cross-section taken in the XPS chamber (C). Recorded C1s and O1s high resolution spectra of the pre-defined analysis region [144].

Cools et al. have also used SXI imaging pre-XPS measurements to unbiasedly assess the homogeneity of the surface oxygen content on PEOT/PBT 3D-printed scaffolds activated with a He DBD plasma. A relatively homogeneous modification throughout the scaffold with a slight gradient of decreasing O content towards the middle of the scaffold was perceived. The authors have attributed this observation to the fact that inner parts generally experience a lower feed gas flow and are therefore exposed to less plasma excited species having a high modifying capacity [317]. Armenise et al. have also employed SXIs of porous PU foams pre-subjected to a He/O_2 DBD treatment to precisely locate XPS measurement areas all over the scaffold. No significant differences in the XPS results obtained from all the analyzed scaffold regions were discerned. The authors have therefore concluded that an optimized plasma process can ultimately lead to a uniform chemical modification on both the inner and outer surfaces of porous scaffolds [318].

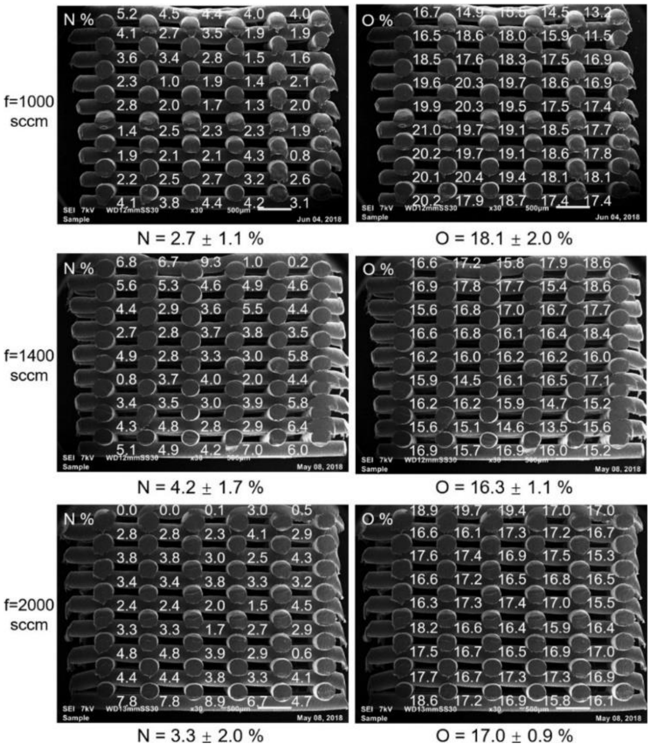

Figure A.9 Feed gas flow rate influence on the nitrogen and oxygen surface concentrations throughout PCL scaffolds subjected to an NH_3/He plasma treatment [11].

References

[1] H. Conrads, M. Schmidt, Plasma generation and plasma sources, Plasma Sources Sci. Technol. 9 (2000) 441–454. https://doi.org/10.1088/0963-0252/9/4/301.

[2] A.F. Aleksandrov, L.S. Bogdankevich, A.A. Rukhadze, Principles of plasma electrodynamics, 1978.

[3] L.A. Rosocha, G.K. Anderson, L.A. Bechtold, J.J. Coogan, H.G. Heck, M. Kang, W.H. McCulla, R.A. Tennant, P.J. Wantuck, Treatment of Hazardous Organic Wastes Using Silent Discharge Plasmas, in: Non-Thermal Plasma Tech. Pollut. Control, Springer Berlin Heidelberg, Berlin, Heidelberg, 1993: pp. 281–308. https://doi.org/10.1007/978-3-642-78476-7_21.

[4] D. Xiao, Fundamental Theory of Streamer and Leader Discharge, in: Springer, Berlin, Heidelberg, 2016: pp. 89–121. https://doi.org/10.1007/978-3-662-48041-0_4.

[5] A. Chirokov, A. Gutsol, A. Fridman, Atmospheric pressure plasma of dielectric barrier discharges, Pure Appl. Chem. 77 (2005) 487–495. https://doi.org/10.1351/pac200577020487.

[6] R. Brandenburg, J. Ehlbeck, M. Stieber, T. v. Woedtke, J. Zeymer, O. Schlüter, K.-D. Weltmann, Antimicrobial Treatment of Heat Sensitive Materials by Means of Atmospheric Pressure Rf-Driven Plasma Jet, Contrib. to Plasma Phys. 47 (2007) 72–79. https://doi.org/10.1002/ctpp.200710011.

[7] A.D. Kramar, B.M. Obradović, A. Vesel, M.M. Kuraica, M.M. Kostić, Surface cleaning of raw cotton fibers with atmospheric pressure air plasma, Cellulose. 25 (2018) 4199–4209. https://doi.org/10.1007/s10570-018-1820-5.

[8] S. Bhatt, J. Pulpytel, S. Mori, M. Mirshahi, F. Arefi-Khonsari, Cell Repellent Coatings Developed by an Open Air Atmospheric Pressure Non-Equilibrium Argon Plasma Jet for Biomedical Applications, Plasma Process. Polym. 11 (2014) 24–36. https://doi.org/10.1002/ppap.201300076.

[9] P. Cools, N. De Geyter, R. Morent, PLA Enhanced via Plasma Technology: A Review, Nova Science Publishers, inc, 2015. https://doi.org/hdl.handle.net/1854/LU-5831939.

[10] A.H. Khoja, A. Mazhar, F. Saleem, M.T. Mehran, S.R. Naqvi, M. Anwar, S. Shakir, N.A. Saidina Amin, M.B. Sajid, Recent developments in catalyst synthesis using DBD plasma for reforming applications, Int. J. Hydrogen Energy. 46 (2021) 15367–15388. https://doi.org/10.1016/J.IJHYDENE.2021.02.043.

[11] L. Cheng, R. Ghobeira, P. Cools, Z. Liu, K. Yan, N. De Geyter, R. Morent, Comparative study of different nitrogen-containing plasma modifications applied on 3D porous PCL scaffolds and 2D PCL films, Appl. Surf. Sci. 516 (2020) 146067. https://doi.org/10.1016/j.apsusc.2020.146067.

[12] X. Wang, Q. Huang, S. Ding, W. Liu, J. Mei, Y. hunag, J. Luo, L. Lei, F. He, Micro hollow cathode excited dielectric barrier discharge (DBD) plasma bubble and the application in organic wastewater treatment, Sep. Purif. Technol. 240 (2020) 116659. https://doi.org/10.1016/J.SEPPUR.2020.116659.

[13] P.S. Esbah Tabaei, M. Asadian, R. Ghobeira, P. Cools, M. Thukkaram, P.G. Derakhshandeh, S. Abednatanzi, P. Van Der Voort, K. Verbeken, C. Vercruysse, H. Declercq, R. Morent, N. De Geyter, Combinatorial effects of coral addition and plasma treatment on the properties of chitosan/polyethylene oxide nanofibers intended for bone tissue engineering, Carbohydr. Polym. 253 (2021). https://doi.org/10.1016/j.carbpol.2020.117211.

[14] K.V. Chan, Y. Onyshchenko, M. Asadian, A.Y. Nikiforov, H. Declercq, R. Morent, N. De Geyter, Investigating the stability of cyclopropylamine-based plasma polymers in water, Appl. Surf. Sci. 517 (2020) 146167. https://doi.org/10.1016/j.apsusc.2020.146167.

[15] R. Morent, N. De Geyter, L. Gengembre, C. Leys, E. Payen, S. Van Vlierberghe, E. Schacht, Surface treatment of a polypropylene film with a nitrogen DBD at medium pressure, in: EPJ Appl. Phys., EDP Sciences, 2008: pp. 289–294. https://doi.org/10.1051/epjap:2008076.

[16] N. De Geyter, R. Morent, C. Leys, Surface modification of a polyester non-woven with a dielectric barrier discharge in air at medium pressure, Surf. Coatings Technol. 201 (2006) 2460–2466. https://doi.org/10.1016/j.surfcoat.2006.04.004.

[17] N. De Geyter, R. Morent, T. Desmet, M. Trentesaux, L. Gengembre, P. Dubruel, C. Leys, E. Payen, Plasma modification of polylactic acid in a medium pressure DBD, Surf. Coatings Technol. 204 (2010) 3272–3279. https://doi.org/10.1016/j.surfcoat.2010.03.037.

[18] A.S. Chiper, G. Popa, Temporally, spatially, and spectrally resolved barrier discharge produced in trapped helium gas at atmospheric pressure, J. Appl. Phys. 113 (2013) 213302. https://doi.org/10.1063/1.4809764.

[19] L. Cheng, R. Ghobeira, P. Cools, B. Luthringer, M. Asadian, N. De Geyter, Z. Liu, K. Yan, R. Morent, Comparing medium pressure dielectric barrier discharge (DBD) plasmas and classic methods of surface cleaning/activation of pure Mg for biomedical applications, Surf. Coatings Technol. 410 (2021) 126934. https://doi.org/10.1016/J.SURFCOAT.2021.126934.

[20] P.S. Esbah Tabaei, R. Ghobeira, P. Cools, F. Rezaei, A. Nikiforov, R. Morent, N. De Geyter, Comparative study between in-plasma and post-plasma chemical processes occurring at the surface of UHMWPE subjected to medium pressure Ar and N2 plasma activation, Polymer (Guildf). (2020) 122383. https://doi.org/10.1016/j.polymer.2020.122383.

[21] C. Penache, C. Gessner, T. Betker, V. Bartels, A. Hollaender, C.-P. Klages, Plasma printing: patterned surface functionalisation and coating at atmospheric pressure, IEE Proc. - Nanobiotechnology. 151 (2003) 139–144. https://doi.org/10.1049/ip-nbt:20040836.

[22] O. V. Penkov, M. Khadem, W.-S. Lim, D.-E. Kim, A review of recent applications of atmospheric pressure plasma jets for materials processing, J. Coatings Technol. Res. 12 (2015) 225–235. https://doi.org/10.1007/s11998-014-9638-z.

[23] J. Van Durme, J. Dewulf, C. Leys, H. Van Langenhove, Combining non-thermal plasma with heterogeneous catalysis in waste gas treatment: A review, Appl. Catal. B Environ. 78 (2008) 324–333. https://doi.org/10.1016/J.APCATB.2007.09.035.

[24] M. Asadian, I. Onyshchenko, M. Thukkaram, P.S. Esbah Tabaei, J. Van Guyse, P. Cools, H. Declercq, R. Hoogenboom, R. Morent, N. De Geyter, Effects of a dielectric barrier discharge (DBD) treatment on chitosan/polyethylene oxide nanofibers and their cellular interactions, Carbohydr. Polym. 201 (2018) 402–415. https://doi.org/10.1016/J.CARBPOL.2018.08.092.

[25] P. Favia, R. D’Agostino, Plasma treatments and plasma deposition of polymers for biomedical applications, (1998) 1102–1106. https://doi.org/10.1016/S0257-8972(97)00285-5.

[26] R. Morent, N. De Geyter, M. Trentesaux, L. Gengembre, P. Dubruel, C.

Leys, E. Payen, Influence of discharge atmosphere on the ageing behaviour of plasma-treated polylactic acid, Plasma Chem. Plasma Process. 30 (2010) 525–536. https://doi.org/10.1007/s11090-010-9233-8.

[27] J.F. Friedrich, R. Mix, R. Schulze, A. Meyer-Plath, R. Joshi, S. Wettmarshausen, New Plasma Techniques for Polymer Surface Modification with Monotype Functional Groups, Plasma Process. Polym. 5 (2008) 407–423. https://doi.org/10.1002/ppap.200700145.

[28] C.-L. Fan, Y.-Z. Lin, P.-C. Chiu, S.-J. Wang, W.-D. Lee, Teflon/SiO2 bilayer passivation for improving the electrical reliability of pentacene-based organic thin-film transistors, Org. Electron. 14 (2013) 2228–2232. https://doi.org/10.1016/J.ORGEL.2013.05.031.

[29] R. Ghobeira, N. De Geyter, R. Morent, Plasma surface functionalization of biodegradable electrospun scaffolds for tissue engineering applications Biomimetic scaffolds and intraperitoneal drug delivery View project Smart contact lenses View project, in: G. Rohman (Ed.), Biodegrad. Polym., Recent Developments and New Perspectives, IAPC Publishing, Zagreb Croatia, 2017: pp. 191–236. https://doi.org/10.5599/obp.14.4.

[30] B. Bharti, S. Kumar, H.-N. Lee, R. Kumar, Formation of oxygen vacancies and Ti3+ state in TiO2 thin film and enhanced optical properties by air plasma treatment, Sci. Rep. 6 (2016) 1–12. https://doi.org/10.1038/srep32355.

[31] S.I. Tverdokhlebov, E.N. Bolbasov, E.V. Shesterikov, L.V. Antonova, A.S. Golovkin, V.G. Matveeva, D.G. Petlin, Y.G. Anissimov, Modification of polylactic acid surface using RF plasma discharge with sputter deposition of a hydroxyapatite target for increased biocompatibility, Appl. Surf. Sci. 329 (2015) 32–39. https://doi.org/10.1016/j.apsusc.2014.12.127.

[32] M. Asadian, I. Onyshchenko, D. Thiry, P. Cools, H. Declercq, R. Snyders, R. Morent, N. De Geyter, Thiolation of polycaprolactone (PCL) nanofibers by inductively coupled plasma (ICP) polymerization: Physical, chemical and biological properties, Appl. Surf. Sci. 479 (2019) 942–952. https://doi.org/10.1016/J.APSUSC.2019.02.178.

[33] R. Ghobeira, C. Philips, L. Liefooghe, M. Verdonck, M. Asadian, P. Cools, H. Declercq, W.H. De Vos, N. De Geyter, R. Morent, Synergetic effect of electrospun PCL fiber size, orientation and plasma-modified surface chemistry on stem cell behavior, Appl. Surf. Sci. 485 (2019) 204–221. https://doi.org/10.1016/J.APSUSC.2019.04.109.

[34] N. De Geyter, R. Morent, C. Leys, L. Gengembre, E. Payen, Treatment of polymer films with a dielectric barrier discharge in air, helium and argon at medium pressure, Surf. Coatings Technol. 201 (2007) 7847–7854. https://doi.org/10.1016/j.surfcoat.2007.03.018.

[35] S. Van Vrekhem, K. Vloebergh, M. Asadian, C. Vercruysse, H. Declercq, A. Van Tongel, L. De Wilde, N. De Geyter, R. Morent, Improving the surface properties of an UHMWPE shoulder implant with an atmospheric pressure plasma jet, Sci. Rep. 8 (2018) 4720. https://doi.org/10.1038/s41598-018-22921-6.

[36] M. Asadian, I. Onyshchenko, M. Thukkaram, P.S. Esbah Tabaei, J. Van Guyse, P. Cools, H. Declercq, R. Hoogenboom, R. Morent, N. De Geyter, Effects of a dielectric barrier discharge (DBD) treatment on chitosan/polyethylene oxide nanofibers and their cellular interactions, Carbohydr. Polym. 201 (2018). https://doi.org/10.1016/j.carbpol.2018.08.092.

[37] R. Morent, N. De Geyter, C. Leys, L. Gengembre, E. Payen, Comparison between XPS- And FTIR-analysis of plasma-treated polypropylene film surfaces, in: Surf. Interface Anal., 2008. https://doi.org/10.1002/sia.2619.

[38] T. Shao, C. Zhang, K. Long, D. Zhang, J. Wang, P. Yan, Y. Zhou, Surface modification of polyimide films using unipolar nanosecond-pulse DBD in atmospheric air, Appl. Surf. Sci. 256 (2010) 3888–3894. https://doi.org/10.1016/j.apsusc.2010.01.045.

[39] P. Cools, L. Astoreca, P.S. Esbah Tabaei, M. Thukkaram, H. De Smet, R. Morent, N. De Geyter, Surface Treatment of Polymers by Plasma, in: Surf. Modif. Polym., Wiley-VCH Verlag GmbH & Co. KGaA, Weinheim, Germany, 2019: pp. 31–65. https://doi.org/10.1002/9783527819249.ch2.

[40] K.S. Siow, L. Britcher, S. Kumar, H.J. Griesser, Plasma Methods for the Generation of Chemically Reactive Surfaces for Biomolecule Immobilization and Cell Colonization - A Review, Plasma Process. Polym. 3 (2006) 392–418. https://doi.org/10.1002/ppap.200600021.

[41] R. Bitar, M. Asadian, S. Van Vrekhem, P. Cools, H. Declercq, R. Morent, N. De Geyter, Local plasma activation of PS films with a defined design for biomedical use, Surf. Coatings Technol. 350 (2018) 985–996. https://doi.org/10.1016/J.SURFCOAT.2018.03.041.

[42] F. Massines, G. Gouda, N. Gherardi, M. Duran, E. Croquesel, The role of dielectric barrier discharge atmosphere and physics on polypropylene

surface treatment, Plasmas Polym. 6 (2001) 35–49. https://doi.org/10.1023/A:1011365306501.

[43] X.-F. Zhang, H.-X. Liu, L.S. Ortiz, Z.-D. Xiao, N.-P. Huang, Laminin-modified and aligned poly(3-hydroxybutyrate-co-3-hydroxyvalerate)/polyethylene oxide nanofibrous nerve conduits promote peripheral nerve regeneration, J. Tissue Eng. Regen. Med. 12 (2018) e627–e636. https://doi.org/10.1002/term.2355.

[44] C.H. Jang, H. Lee, M.S. Kim, G.H. Kim, Effect of polycaprolactone/collagen/hUCS microfiber nerve conduit on facial nerve regeneration, Int. J. Biol. Macromol. 93 (2016) 1575–1582. https://doi.org/10.1016/j.ijbiomac.2016.04.031.

[45] E. Seyedjafari, M. Soleimani, N. Ghaemi, I. Shabani, Nanohydroxyapatite-Coated Electrospun Poly(l -lactide) Nanofibers Enhance Osteogenic Differentiation of Stem Cells and Induce Ectopic Bone Formation, Biomacromolecules. 11 (2010) 3118–3125. https://doi.org/10.1021/bm1009238.

[46] F. Yang, J.G.C. Wolke, J.A. Jansen, Biomimetic calcium phosphate coating on electrospun poly(ε-caprolactone) scaffolds for bone tissue engineering, Chem. Eng. J. 137 (2008) 154–161. https://doi.org/10.1016/J.CEJ.2007.07.076.

[47] S.K. Øiseth, A. Krozer, B. Kasemo, J. Lausmaa, Surface modification of spin-coated high-density polyethylene films by argon and oxygen glow discharge plasma treatments, Appl. Surf. Sci. 202 (2002) 92–103. https://doi.org/10.1016/S0169-4332(02)00928-5.

[48] A.. Meyer-Plath, K. Schröder, B. Finke, A. Ohl, Current trends in biomaterial surface functionalization—nitrogen-containing plasma assisted processes with enhanced selectivity, Vacuum. 71 (2003) 391–406. https://doi.org/10.1016/S0042-207X(02)00766-2.

[49] N. Dorraki, N.N. Safa, M. Jahanfar, H. Ghomi, S.-O. Ranaei-Siadat, Surface modification of chitosan/PEO nanofibers by air dielectric barrier discharge plasma for acetylcholinesterase immobilization, Appl. Surf. Sci. 349 (2015) 940–947. https://doi.org/10.1016/J.APSUSC.2015.03.118.

[50] P. Jelínek, K. Polášková, F. Jeník, Z. Jeníková, L. Dostál, E. Dvořáková, J. Cerman, H. Šourková, V. Buršíková, P. Špatenka, L. Zajíčková, Effects of additives on atmospheric pressure gliding arc applied to the modification of polypropylene, Surf. Coatings Technol. 372 (2019) 45–55. https://doi.org/10.1016/J.SURFCOAT.2019.04.035.

[51] C. Ma, L. Wang, A. Nikiforov, Y. Onyshchenko, P. Cools, K. (Ken) Ostrikov, N. De Geyter, R. Morent, Atmospheric-pressure plasma assisted engineering of polymer surfaces: From high hydrophobicity to superhydrophilicity, Appl. Surf. Sci. 535 (2021) 147032. https://doi.org/10.1016/j.apsusc.2020.147032.

[52] S. Sui, L. Li, J. Shen, G. Ni, H. Xie, Q. Lin, Y. Zhao, J. Guo, W. Duan, Plasma treatment of polymethyl methacrylate to improve surface hydrophilicity and antifouling performance, Polym. Eng. Sci. 61 (2021) 506–513. https://doi.org/10.1002/pen.25595.

[53] P. Cools, S. Van Vrekhem, N. De Geyter, R. Morent, The use of DBD plasma treatment and polymerization for the enhancement of biomedical UHMWPE, Thin Solid Films. 572 (2014) 251–259. https://doi.org/10.1016/j.tsf.2014.08.033.

[54] D. Cho, S. Chen, Y. Jeong, Y.L. Joo, Surface hydro-properties of electrospun fiber mats, Fibers Polym. 16 (2015) 1578–1586. https://doi.org/10.1007/s12221-015-5258-1.

[55] R. Ghobeira, M. Asadian, C. Vercruysse, H. Declercq, N. De Geyter, R. Morent, Wide-ranging diameter scale of random and highly aligned PCL fibers electrospun using controlled working parameters, Polymer (Guildf). 157 (2018) 19–31. https://doi.org/10.1016/j.polymer.2018.10.022.

[56] A. Marmur, Soft contact: Measurement and interpretation of contact angles, Soft Matter. 2 (2006) 12–17. https://doi.org/10.1039/b514811c.

[57] D.G. Castner, B.D. Ratner, Polymer surface analysis: The leadership and contributions of David Briggs, Surf. Interface Anal. 52 (2020) 1122–1127. https://doi.org/10.1002/sia.6754.

[58] F.M. Petrat, D. Wolany, B.C. Schwede, L. Wiedmann, A. Benninghoven, In situ ToF-SIMS/XPS investigation of nitrogen plasma-modified polystyrene surfaces, Surf. Interface Anal. 21 (1994) 274–282. https://doi.org/10.1002/sia.740210503.

[59] T. Egghe, P. Cools, J.F.R. Van Guyse, M. Asadian, D. Khalenkow, A. Nikiforov, H. Declercq, A.G. Skirtach, R. Morent, R. Hoogenboom, N. De Geyter, Water-Stable Plasma-Polymerized N, N-Dimethylacrylamide Coatings to Control Cellular Adhesion, ACS Appl. Mater. Interfaces. 12 (2020) 2116–2128. https://doi.org/10.1021/acsami.9b19526.

[60] N. Vandencasteele, F. Reniers, Plasma-modified polymer surfaces: Characterization using XPS, J. Electron Spectros. Relat. Phenomena. 178–179 (2010) 394–408.

https://doi.org/10.1016/J.ELSPEC.2009.12.003.

[61] L.J. Gerenser, XPS studies of in situ plasma-modified polymer surfaces, J. Adhes. Sci. Technol. 7 (1993) 1019–1040. https://doi.org/10.1163/156856193X00556.

[62] L.J. Gerenser, X-Ray photoemission study of plasma modified polyethylene surfaces, J. Adhes. Sci. Technol. 1 (1987) 303–318. https://doi.org/10.1163/156856187X00319.

[63] T.R. Gengenbach, Z.R. Vasic, R.C. Chatelier, H.J. Griesser, A multi-technique study of the spontaneous oxidation of N-hexane plasma polymers, J. Polym. Sci. Part A Polym. Chem. 32 (1994) 1399–1414. https://doi.org/10.1002/pola.1994.080320801.

[64] A.J. Roberts, C.E. Moffitt, Trends in XPS instrumentation for industrial surface analysis and materials characterisation, J. Electron Spectros. Relat. Phenomena. 231 (2019) 68–74. https://doi.org/10.1016/j.elspec.2018.03.002.

[65] S. Van Vrekhem, P. Cools, H. Declercq, A. Van Tongel, C. Vercruysse, M. Cornelissen, N. De Geyter, R. Morent, Application of atmospheric pressure plasma on polyethylene for increased prosthesis adhesion, Thin Solid Films. 596 (2015) 256–263. https://doi.org/10.1016/J.TSF.2015.08.055.

[66] R. Morent, N. De Geyter, F. Axisa, N. De Smet, L. Gengembre, E. De Leersnyder, C. Leys, J. Vanfleteren, M. Rymarczyk-Machal, E. Schacht, E. Payen, Adhesion enhancement by a dielectric barrier discharge of PDMS used for flexible and stretchable electronics, J. Phys. D. Appl. Phys. 40 (2007) 7392–7401. https://doi.org/10.1088/0022-3727/40/23/021.

[67] N. Sanada, A. Yamamoto, R. Oiwa, Y. Ohashi, Extremely low sputtering degradation of polytetrafluoroethylene by C60 ion beam applied in XPS analysis, Surf. Interface Anal. 36 (2004) 280–282. https://doi.org/10.1002/sia.1680.

[68] A. Manakhov, M. Michlíček, A. Felten, J.-J. Pireaux, D. Nečas, L. Zajíčková, XPS depth profiling of derivatized amine and anhydride plasma polymers: Evidence of limitations of the derivatization approach, Appl. Surf. Sci. 394 (2017) 578–585. https://doi.org/10.1016/J.APSUSC.2016.10.099.

[69] G. Greczynski, L. Hultman, X-ray photoelectron spectroscopy: Towards reliable binding energy referencing, Prog. Mater. Sci. 107 (2020) 100591. https://doi.org/10.1016/j.pmatsci.2019.100591.

[70] H. Seyama, M. Soma, B.K.G. Theng, X-Ray Photoelectron Spectroscopy, in: Dev. Clay Sci., Elsevier, 2013: pp. 161–176. https://doi.org/10.1016/B978-0-08-098259-5.00007-X.

[71] Arne Vandenbroucke, Abatement of volatile organic compounds by combined use of non-thermal plasma and heterogeneous catalysis, Doctoral dissertation, Ghent University, 2015.

[72] M.A. Leutenegger, M.E. Eckart, S.J. Moseley, S.O. Rohrbach, J.K. Black, M.P. Chiao, R.L. Kelley, C.A. Kilbourne, F.S. Porter, Simple, compact, high-resolution monochromatic x-ray source for characterization of x-ray calorimeter arrays, Rev. Sci. Instrum. 91 (2020) 083110. https://doi.org/10.1063/5.0005206.

[73] F. Reniers, C. Tewell, New improvements in energy and spatial (x, y, z) resolution in AES and XPS applications, J. Electron Spectros. Relat. Phenomena. 142 (2005) 1–25. https://doi.org/10.1016/j.elspec.2004.07.004.

[74] Z. Zheng, L. Ren, W. Feng, Z. Zhai, Y. Wang, Surface characterization of polyethylene terephthalate films treated by ammonia low-temperature plasma, Appl. Surf. Sci. 258 (2012) 7207–7212. https://doi.org/10.1016/j.apsusc.2012.04.038.

[75] G. Borcia, C.A. Anderson, N.M.D. Brown, Using a nitrogen dielectric barrier discharge for surface treatment, Plasma Sources Sci. Technol. 14 (2005) 259–267. https://doi.org/10.1088/0963-0252/14/2/006.

[76] G. Aziz, P. Cools, N. De Geyter, H. Declercq, R. Cornelissen, R. Morent, Dielectric barrier discharge plasma treatment of ultrahigh molecular weight polyethylene in different discharge atmospheres at medium pressure: A cell-biomaterial interface study, Biointerphases. 10 (2015) 029502. https://doi.org/10.1116/1.4907755.

[77] K.N. Pandiyaraj, V. Selvarajan, R.R. Deshmukh, M. Bousmina, The effect of glow discharge plasma on the surface properties of Poly (ethylene terephthalate) (PET) film, Surf. Coatings Technol. 202 (2008) 4218–4226. https://doi.org/10.1016/j.surfcoat.2008.03.015.

[78] C. López-Santos, F. Yubero, J. Cotrino, A.R. González-Elipe, Nitrogen plasma functionalization of low density polyethylene, Surf. Coatings Technol. 205 (2011) 3356–3364. https://doi.org/10.1016/j.surfcoat.2010.11.038.

[79] C. López-Santos, F. Yubero, J. Cotrino, A.R. González-Elipe, Surface functionalization, oxygen depth profiles, and wetting behavior of PET treated with different nitrogen plasmas, ACS Appl. Mater. Interfaces. 2

(2010) 980–990. https://doi.org/10.1021/am100052w.

[80] N. Recek, M. Resnik, H. Motaln, T. Lah-Turnšek, R. Augustine, N. Kalarikkal, S. Thomas, M. Mozetič, Cell Adhesion on Polycaprolactone Modified by Plasma Treatment, Int. J. Polym. Sci. 2016 (2016). https://doi.org/10.1155/2016/7354396.

[81] M. Tatoulian, F. Arefi-Khonsari, N. Shahidzadeh-Ahmadi, J. Amouroux, Comparison of the efficiency of N2 and NH3 plasma treatments to improve the adhesion of PP films to in situ deposited Al coatings. Study of ageing phenomena in terms of acid-base properties, Int. J. Adhes. Adhes. 15 (1995) 177–184. https://doi.org/10.1016/0143-7496(95)91629-K.

[82] A. Vesel, I. Junkar, U. Cvelbar, J. Kovac, M. Mozetic, Surface modification of polyester by oxygen- and nitrogen-plasma treatment, Surf. Interface Anal. 40 (2008) 1444–1453. https://doi.org/10.1002/sia.2923.

[83] T. Jacobs, H. Declercq, N. De Geyter, R. Cornelissen, P. Dubruel, C. Leys, A. Beaurain, E. Payen, R. Morent, Plasma surface modification of polylactic acid to promote interaction with fibroblasts, J. Mater. Sci. Mater. Med. (n.d.). https://doi.org/10.1007/s10856-012-4807-z.

[84] Z. Fang, X. Wang, T. Shao, C. Zhang, Influence of Oxygen Content on Argon/Oxygen Dielectric Barrier Discharge Plasma Treatment of Polyethylene Terephthalate Film, IEEE Trans. Plasma Sci. 45 (2017) 310–317. https://doi.org/10.1109/TPS.2016.2633063.

[85] R. Wang, Y. Shen, C. Zhang, P. Yan, T. Shao, Comparison between helium and argon plasma jets on improving the hydrophilic property of PMMA surface, Appl. Surf. Sci. 367 (2016) 401–406. https://doi.org/10.1016/j.apsusc.2016.01.199.

[86] N. De Geyter, R. Morent, L. Gengembre, C. Leys, E. Payen, S. Van Vlierberghe, E. Schacht, Increasing the hydrophobicity of a PP film using a helium/CF 4 DBD treatment at atmospheric pressure, Plasma Chem. Plasma Process. 28 (2008) 289–298. https://doi.org/10.1007/s11090-008-9124-4.

[87] R. Wang, C. Zhang, X. Liu, Q. Xie, P. Yan, T. Shao, Microsecond pulse driven Ar/CF 4 plasma jet for polymethylmethacrylate surface modification at atmospheric pressure, Appl. Surf. Sci. 328 (2015) 509–515. https://doi.org/10.1016/j.apsusc.2014.12.076.

[88] M. Resnik, R. Zaplotnik, M. Mozetic, A. Vesel, Comparison of SF6 and CF4 Plasma Treatment for Surface Hydrophobization of PET Polymer, Materials (Basel). 11 (2018) 311. https://doi.org/10.3390/ma11020311.

[89] M. Dhayal, M.R. Alexander, J.W. Bradley, The surface chemistry resulting from low-pressure plasma treatment of polystyrene: The effect of residual vessel bound oxygen, Appl. Surf. Sci. 252 (2006) 7957–7963. https://doi.org/10.1016/J.APSUSC.2005.10.005.

[90] N. Vandencasteele, B. Nisol, P. Viville, R. Lazzaroni, D.G. Castner, F. Reniers, Plasma-Modified PTFE for Biological Applications: Correlation between Protein-Resistant Properties and Surface Characteristics, Plasma Process. Polym. 5 (2008) 661–671. https://doi.org/10.1002/ppap.200700143.

[91] A. Vesel, M. Mozetic, A. Zalar, XPS characterization of PTFE after treatment with RF oxygen and nitrogen plasma, in: Surf. Interface Anal., 2008: pp. 661–663. https://doi.org/10.1002/sia.2691.

[92] C. Vasile, M.C. Baican, C.M. Tibirna, C. Tuchilus, D. Debarnot, E. Pslaru, F. Poncin-Epaillard, Microwave plasma activation of a polyvinylidene fluoride surface for protein immobilization, J. Phys. D. Appl. Phys. 44 (2011) 475303. https://doi.org/10.1088/0022-3727/44/47/475303.

[93] S.J. Cho, T. Nguyen, J.H. Boo, Polyimide surface modification by using microwave plasma for adhesion enhancement of Cu electroless plating, in: J. Nanosci. Nanotechnol., 2011: pp. 5328–5333. https://doi.org/10.1166/jnn.2011.3793.

[94] J. Hnilica, L. Potočňáková, M. Stupavská, V. Kudrle, Rapid surface treatment of polyamide 12 by microwave plasma jet, Appl. Surf. Sci. 288 (2014) 251–257. https://doi.org/10.1016/j.apsusc.2013.10.016.

[95] O.M. Ba, P. Marmey, K. Anselme, A.C. Duncan, A. Ponche, Surface composition XPS analysis of a plasma treated polystyrene: Evolution over long storage periods, Colloids Surfaces B Biointerfaces. 145 (2016) 1–7. https://doi.org/10.1016/j.colsurfb.2016.04.026.

[96] K. Terpiłowski, A.E. Wiącek, M. Jurak, Influence of nitrogen plasma treatment on the wettability of polyetheretherketone and deposited chitosan layers, Adv. Polym. Technol. 37 (2018) 1557–1569. https://doi.org/10.1002/adv.21813.

[97] P. Cools, M. Asadian, W. Nicolaus, H. Declercq, R. Morent, N. De Geyter, Surface Treatment of PEOT/PBT (55/45) with a Dielectric Barrier Discharge in Air, Helium, Argon and Nitrogen at Medium Pressure, Materials (Basel). 11 (2018) 391. https://doi.org/10.3390/ma11030391.

[98] Y. Ren, Z. Ding, C. Wang, C. Zang, Y. Zhang, L. Xu, Influence of DBD plasma pretreatment on the deposition of chitosan onto UHMWPE fiber surfaces for improvement of adhesion and dyeing properties, Appl. Surf.

Sci. 396 (2017) 1571–1579. https://doi.org/10.1016/j.apsusc.2016.11.215.

[99] M. Asadian, M. Dhaenens, I. Onyshchenko, S. De Waele, H. Declercq, P. Cools, B. Devreese, D. Deforce, R. Morent, N. De Geyter, Plasma Functionalization of Polycaprolactone Nanofibers Changes Protein Interactions with Cells, Resulting in Increased Cell Viability, ACS Appl. Mater. Interfaces. 10 (2018) 41962–41977. https://doi.org/10.1021/acsami.8b14995.

[100] G.H. Major, N. Fairley, P.M.A. Sherwood, M.R. Linford, J. Terry, V. Fernandez, K. Artyushkova, Practical guide for curve fitting in x-ray photoelectron spectroscopy, J. Vac. Sci. Technol. A. 38 (2020) 061203. https://doi.org/10.1116/6.0000377.

[101] D. Briggs, Surface Analysis of Polymers by XPS and Static SIMS - D. Briggs - Google Books, Cambridge University Press, 1998.

[102] A. V. Lubenchenko, A.A. Batrakov, A.B. Pavolotsky, O.I. Lubenchenko, D.A. Ivanov, XPS study of multilayer multicomponent films, Appl. Surf. Sci. 427 (2018) 711–721. https://doi.org/10.1016/j.apsusc.2017.07.256.

[103] E. Gonzalez, M.D. Barankin, P.C. Guschl, R.F. Hicks, Remote atmospheric-pressure plasma activation of the surfaces of polyethylene terephthalate and polyethylene naphthalate, Langmuir. 24 (2008) 12636–12643. https://doi.org/10.1021/la802296c.

[104] G. Borcia, C.A. Anderson, N.M.D. Brown, Dielectric barrier discharge for surface treatment: application to selected polymers in film and fibre form, Plasma Sources Sci. Technol. 12 (2003) 335–344. https://doi.org/10.1088/0963-0252/12/3/306.

[105] C. Huang, C.-Y. Tsai, R.-S. Juang, Surface modification and characterization of an H2/O2 plasma-treated polypropylene membrane, J. Appl. Polym. Sci. 124 (2012) E108–E115. https://doi.org/10.1002/app.34049.

[106] S. Nejatbakhsh, A. Anagri, A. Valinataj Omran, J. Pulpytel, C. Bazin, M. Ullah, M. Mirshahi, H. Rezaie, J. Javadpour, F. Arefi-Khonsari, Improvement of the Bioactivity of UHMWPE by Two Different Atmospheric Plasma Treatments, Plasma Chem. Plasma Process. 41 (2021) 245–264. https://doi.org/10.1007/s11090-020-10134-7.

[107] S. Tajima, K. Komvopoulos, Surface modification of low-density polyethylene by inductively coupled argon plasma, J. Phys. Chem. B. 109 (2005) 17623–17629. https://doi.org/10.1021/jp052121x.

[108] A. Van Deynse, P. Cools, C. Leys, R. Morent, N. De Geyter, Surface modification of polyethylene in an argon atmospheric pressure plasma jet, Surf. Coatings Technol. 276 (2015) 384–390. https://doi.org/10.1016/j.surfcoat.2015.06.041.

[109] T. Jacobs, N. De Geyter, R. Morent, T. Desmet, P. Dubruel, C. Leys, Plasma treatment of polycaprolactone at medium pressure, Surf. Coatings Technol. 205 (2011) S543–S547. https://doi.org/10.1016/j.surfcoat.2011.02.012.

[110] A. Sarani, A.Y. Nikiforov, N. De Geyter, R. Morent, C. Leys, Surface modification of polypropylene with an atmospheric pressure plasma jet sustained in argon and an argon/water vapour mixture, Appl. Surf. Sci. 257 (2011) 8737–8741. https://doi.org/10.1016/j.apsusc.2011.05.071.

[111] E. Abdel–Fattah, Surface Activation of Poly(Methyl Methacrylate) with Atmospheric Pressure Ar + H2O Plasma, Coatings. 9 (2019) 228. https://doi.org/10.3390/coatings9040228.

[112] V. Bagiatis, G.W. Critchlow, D. Price, S. Wang, The effect of atmospheric pressure plasma treatment (APPT) on the adhesive bonding of poly(methyl methacrylate) (PMMA)-to-glass using a polydimethylsiloxane (PDMS)-based adhesive, Int. J. Adhes. Adhes. 95 (2019) 102405. https://doi.org/10.1016/j.ijadhadh.2019.102405.

[113] J. Izdebska-Podsiadły, E. Dörsam, Effects of argon low temperature plasma on PLA film surface and aging behaviors, Vacuum. 145 (2017) 278–284. https://doi.org/10.1016/j.vacuum.2017.09.001.

[114] R. Ghobeira, C. Philips, H. Declercq, P. Cools, N. De Geyter, R. Cornelissen, R. Morent, Effects of different sterilization methods on the physico-chemical and bioresponsive properties of plasma-treated polycaprolactone films, Biomed. Mater. 12 (2017). https://doi.org/10.1088/1748-605X/aa51d5.

[115] T.S. Cheng, H.T. Lin, M.J. Chuang, Surface fluorination of polyethylene terephthalate films with RF plasma, Mater. Lett. 58 (2004) 650–653. https://doi.org/10.1016/S0167-577X(03)00586-X.

[116] C. Zhang, Y. Zhou, T. Shao, Q. Xie, J. Xu, W. Yang, Hydrophobic treatment on polymethylmethacrylate surface by nanosecond-pulse DBDs in CF 4 at atmospheric pressure, Appl. Surf. Sci. 311 (2014) 468–477. https://doi.org/10.1016/j.apsusc.2014.05.091.

[117] B. Nisol, F. Reniers, Challenges in the characterization of plasma polymers using XPS, J. Electron Spectros. Relat. Phenomena. 200 (2015) 311–331. https://doi.org/10.1016/j.elspec.2015.05.002.

[118] F. Wieland, R. Bruch, M. Bergmann, S. Partel, G.A. Urban, C. Dincer, Enhanced Protein Immobilization on Polymers—A Plasma Surface Activation Study, Polymers (Basel). 12 (2020) 104–116. https://doi.org/10.3390/polym12010104.

[119] H.S. Yoo, T.G. Kim, T.G. Park, Surface-functionalized electrospun nanofibers for tissue engineering and drug delivery, Adv. Drug Deliv. Rev. 61 (2009) 1033–1042. https://doi.org/10.1016/j.addr.2009.07.007.

[120] K. Chan, Plasma Polymerization of Cyclopropylamine at Sub-Atmospheric Pressure on Flat Films and Nanofibrous Surfaces for Tissue Engineering Applications, 2019.

[121] N.S. Kasálková, P. Slepička, Z. Kolská, P. Hodačová, Š. Kučková, V. Švorčík, Grafting of bovine serum albumin proteins on plasma-modified polymers for potential application in tissue engineering, Nanoscale Res. Lett. 9 (2014) 1–7. https://doi.org/10.1186/1556-276X-9-161.

[122] P. Wang, K.L. Tan, E.T. Kang, K.G. Neoh, Plasma-induced immobilization of poly(ethylene glycol) onto poly(vinylidene fluoride) microporous membrane, J. Memb. Sci. 195 (2002) 103–114. https://doi.org/10.1016/S0376-7388(01)00548-8.

[123] F. Rezaei, M.D. Dickey, M. Bourham, P.J. Hauser, Surface modification of PET film via a large area atmospheric pressure plasma: An optical analysis of the plasma and surface characterization of the polymer film, Surf. Coatings Technol. 309 (2017) 371–381. https://doi.org/10.1016/j.surfcoat.2016.11.072.

[124] P. Nancy, J. Joy, J. James, B. Joseph, S. Thomas, N. Kalarikkal, Spectroscopic and Mass Spectrometry Analyses of Plasma-Activated Polymeric Materials, in: Non-Thermal Plasma Technol. Polym. Mater., Elsevier, 2019: pp. 319–340. https://doi.org/10.1016/b978-0-12-813152-7.00012-3.

[125] T. Desmet, T. Billiet, E. Berneel, R. Cornelissen, D. Schaubroeck, E. Schacht, P. Dubruel, Post-Plasma Grafting of AEMA as a Versatile Tool to Biofunctionalise Polyesters for Tissue Engineering, Macromol. Biosci. 10 (2010) 1484–1494. https://doi.org/10.1002/mabi.201000147.

[126] B. Mutel, J. Grimblot, O. Dessaux, P. Goudmand, XPS investigations of nitrogen-plasma-treated polypropylene in a reactor coupled to the spectrometer, Surf. Interface Anal. 30 (2000) 401–406. https://doi.org/10.1002/1096-9918(200008)30:1<401::AID-SIA826>3.0.CO;2-G.

[127] L. Lianos, D. Parrat, T.Q. Hoc, T.M. Duc, Secondary ion mass

spectrometry time of flight and in situ x-ray photoelectron spectroscopy studies of polymer surface modifications by a remote oxygen plasma treatment, J. Vac. Sci. Technol. A Vacuum, Surfaces, Film. 12 (1994) 2491–2498. https://doi.org/10.1116/1.579199.

[128] M.K. Shi, G. Dunham, M.E. Gross, G.L. Graff, P.M. Martin, Plasma treatment of PET and acrylic coating surfaces - I. In-situ XPS measurements, J. Adhes. Sci. Technol. 14 (2000) 1485–1498. https://doi.org/10.1163/156856100742320.

[129] R. Morent, N. De Geyter, C. Leys, L. Gengembre, E. Payen, Study of the ageing behaviour of polymer films treated with a dielectric barrier discharge in air, helium and argon at medium pressure, Surf. Coatings Technol. 201 (2007) 7847–7854. https://doi.org/10.1016/j.surfcoat.2007.03.018.

[130] A. Van Deynse, P. Cools, C. Leys, R. Morent, N. De Geyter, Influence of ambient conditions on the aging behavior of plasma-treated polyethylene surfaces, Surf. Coatings Technol. 258 (2014) 359–367. https://doi.org/10.1016/J.SURFCOAT.2014.08.073.

[131] Y. Wang, S. Yin, L. Ren, L. Zhao, Surface characterization of the chitosan membrane after oxygen plasma treatment and its aging effect, Biomed. Mater. 4 (2009) 035003–035010. https://doi.org/10.1088/1748-6041/4/3/035003.

[132] M. Haïdopoulos, M. Horgnies, F. Mirabella, J.-J. Pireaux, Angle-Resolved XPS Study of Plasma-Deposited Polystyrene Films after Oxygen Plasma Treatment, Plasma Process. Polym. 5 (2008) 67–75. https://doi.org/10.1002/ppap.200700067.

[133] K.S. Kim, C.M. Ryu, C.S. Park, G.S. Sur, C.E. Park, Investigation of crystallinity effects on the surface of oxygen plasma treated low density polyethylene using X-ray photoelectron spectroscopy, Polymer (Guildf). 44 (2003) 6287–6295. https://doi.org/10.1016/S0032-3861(03)00674-8.

[134] T. Dufour, J. Minnebo, S. Abou Rich, E.C. Neyts, A. Bogaerts, F. Reniers, Understanding polyethylene surface functionalization by an atmospheric He/O2 plasma through combined experiments and simulations, J. Phys. D. Appl. Phys. 47 (2014) 224007–224019. https://doi.org/10.1088/0022-3727/47/22/224007.

[135] R. Ghobeira, C. Philips, V. De Naeyer, H. Declercq, P. Cools, N. De Geyter, R. Cornelissen, R. Morent, Comparative study of the surface properties and cytocompatibility of plasma-treated poly-ϵ-caprolactone nanofibers subjected to different sterilization methods, J. Biomed.

Nanotechnol. 13 (2017) 699–716. https://doi.org/10.1166/jbn.2017.2377.

[136] J. Xu, J. Zhang, W. Gao, H. Liang, H. Wang, J. Li, Preparation of chitosan/PLA blend micro/nanofibers by electrospinning, 63 (2009) 658–660. https://doi.org/10.1016/j.matlet.2008.12.014.

[137] R. Sedghi, A. Shaabani, N. Sayyari, Electrospun triazole-based chitosan nanofibers as a novel scaffolds for bone tissue repair and regeneration, Carbohydr. Polym. 230 (2020) 115707–115719. https://doi.org/10.1016/j.carbpol.2019.115707.

[138] L. Russo, T. Russo, C. Battocchio, F. Taraballi, A. Gloria, U. D'Amora, R. De Santis, G. Polzonetti, F. Nicotra, L. Ambrosio, L. Cipolla, Galactose grafting on poly(ε-caprolactone) substrates for tissue engineering: A preliminary study, Carbohydr. Res. 405 (2015) 39–46. https://doi.org/10.1016/j.carres.2014.07.027.

[139] S.S. Silva, S.M. Luna, M.E. Gomes, J. Benesch, I. Pashkuleva, J.F. Mano, R.L. Reis, Plasma Surface Modification of Chitosan Membranes: Characterization and Preliminary Cell Response Studies, Macromol. Biosci. 8 (2008) 568–576. https://doi.org/10.1002/mabi.200700264.

[140] M. Pakravan, M.-C. Heuzey, A. Ajji, A fundamental study of chitosan/PEO electrospinning, Polymer (Guildf). 52 (2011) 4813–4824. https://doi.org/10.1016/J.POLYMER.2011.08.034.

[141] M. Mohammadi, M. Alibolandi, K. Abnous, Z. Salmasi, M.R. Jaafari, M. Ramezani, Fabrication of hybrid scaffold based on hydroxyapatite-biodegradable nanofibers incorporated with liposomal formulation of BMP-2 peptide for bone tissue engineering, Nanomedicine Nanotechnology, Biol. Med. 14 (2018) 1987–1997. https://doi.org/10.1016/j.nano.2018.06.001.

[142] M.E. Frohbergh, A. Katsman, G.P. Botta, P. Lazarovici, C.L. Schauer, U.G.K. Wegst, P.I. Lelkes, Electrospun hydroxyapatite-containing chitosan nanofibers crosslinked with genipin for bone tissue engineering, Biomaterials. 33 (2012) 9167–9178. https://doi.org/10.1016/J.BIOMATERIALS.2012.09.009.

[143] K. Balagangadharan, S. Dhivya, N. Selvamurugan, Chitosan based nanofibers in bone tissue engineering, Int. J. Biol. Macromol. 104 (2017) 1372–1382. https://doi.org/10.1016/j.ijbiomac.2016.12.046.

[144] P. Cools, H. Declercq, R. Ghobeira, R. Morent, N. De Geyter, Acrylic acid plasma coatings for enhanced cell migration in PCL 3D additive manufactured scaffolds, Surf. Coatings Technol. 350 (2018) 925–935.

https://doi.org/10.1016/j.surfcoat.2018.03.067.

[145] D. Sankar, K.T. Shalumon, K.P. Chennazhi, D. Menon, R. Jayakumar, Surface plasma treatment of poly(caprolactone) micro, nano, and multiscale fibrous scaffolds for enhanced osteoconductivity, Tissue Eng. - Part A. 20 (2014) 1689–1702. https://doi.org/10.1089/ten.tea.2013.0569.

[146] A. Reznickova, Z. Novotna, Z. Kolska, N.S. Kasalkova, S. Rimpelova, V. Svorcik, Enhanced adherence of mouse fibroblast and vascular cells to plasma modified polyethylene, Mater. Sci. Eng. C. 52 (2015) 259–266. https://doi.org/10.1016/j.msec.2015.03.052.

[147] M. Gravel, T. Gross, R. Vago, M. Tabrizian, Responses of mesenchymal stem cell to chitosan–coralline composites microstructured using coralline as gas forming agent, Biomaterials. 27 (2006) 1899–1906. https://doi.org/10.1016/J.BIOMATERIALS.2005.10.020.

[148] A.R. Amini, C.T. Laurencin, S.P. Nukavarapu, Bone tissue engineering: Recent advances and challenges, Crit. Rev. Biomed. Eng. 40 (2012) 363–408. https://doi.org/10.1615/CritRevBiomedEng.v40.i5.10.

[149] N. Bhattarai, D. Edmondson, O. Veiseh, F.A. Matsen, M. Zhang, Electrospun chitosan-based nanofibers and their cellular compatibility, Biomaterials. 26 (2005) 6176–6184. https://doi.org/10.1016/j.biomaterials.2005.03.027.

[150] Y. Zhang, H. Ouyang, C.T. Lim, S. Ramakrishna, Z.-M. Huang, Electrospinning of gelatin fibers and gelatin/PCL composite fibrous scaffolds, J. Biomed. Mater. Res. 72B (2005) 156–165. https://doi.org/10.1002/jbm.b.30128.

[151] F. Rezaei, A. Nikiforov, R. Morent, N. De Geyter, Plasma Modification of Poly Lactic Acid Solutions to Generate High Quality Electrospun PLA Nanofibers, Sci. Rep. 8 (2018) 2241–2255. https://doi.org/10.1038/s41598-018-20714-5.

[152] J.H. Lee, H.W. Jung, I.-K. Kang, H.B. Lee, Cell behaviour on polymer surfaces with different functional groups, Biomaterials. 15 (1994) 705–711. https://doi.org/10.1016/0142-9612(94)90169-4.

[153] J. Yang, J. Bei, S. Wang, Improving cell affinity of -poly(D,L -lactide) film modified by anhydrous ammonia plasma treatment, Polym. Adv. Technol. 13 (2002) 220–226. https://doi.org/10.1002/pat.177.

[154] N. Udomluck, W.G. Koh, D.J. Lim, H. Park, Recent developments in nanofiber fabrication and modification for bone tissue engineering, Int.

J. Mol. Sci. 21 (2020) 99–115. https://doi.org/10.3390/ijms21010099.

[155] E.S. Place, J.H. George, C.K. Williams, M.M. Stevens, Synthetic polymer scaffolds for tissue engineering, Chem. Soc. Rev. 38 (2009) 1139–1151. https://doi.org/10.1039/b811392k.

[156] M.-H. Ho, J.-J. Lee, S.-C. Fan, D.-M. Wang, L.-T. Hou, H.-J. Hsieh, J.-Y. Lai, Efficient Modification on PLLA by Ozone Treatment for Biomedical Applications, Macromol. Biosci. 7 (2007) 467–474. https://doi.org/10.1002/mabi.200600241.

[157] S.C.J. Loo, C.P. Ooi, Y.C.F. Boey, Radiation effects on poly(lactide-co-glycolide) (PLGA) and poly(L-lactide) (PLLA), Polym. Degrad. Stab. 83 (2004) 259–265. https://doi.org/10.1016/S0141-3910(03)00271-4.

[158] Y. Zhu, C. Gao, X. Liu, J. Shen, Surface modification of polycaprolactone membrane via aminolysis and biomacromolecule immobilization for promoting cytocompatibility of human endothelial cells, Biomacromolecules. 3 (2002) 1312–1319. https://doi.org/10.1021/bm020074y.

[159] T.I. Croll, A.J. O’Connor, G.W. Stevens, J.J. Cooper-White, Controllable surface modification of poly(lactic-co-glycolic acid) (PLGA) by hydrolysis or aminolysis I: Physical, chemical, and theoretical aspects, Biomacromolecules. 5 (2004) 463–473. https://doi.org/10.1021/bm0343040.

[160] Y. Zhu, M.F. Leong, W.F. Ong, M.B. Chan-Park, K.S. Chian, Esophageal epithelium regeneration on fibronectin grafted poly(l-lactide-co-caprolactone) (PLLC) nanofiber scaffold, Biomaterials. 28 (2007) 861–868. https://doi.org/10.1016/j.biomaterials.2006.09.051.

[161] A. Alam, C. Wan, T. McNally, Surface amination of carbon nanoparticles for modification of epoxy resins: plasma-treatment vs. wet-chemistry approach, Eur. Polym. J. 87 (2017) 422–448. https://doi.org/10.1016/J.EURPOLYMJ.2016.10.004.

[162] M.S.K. Chong, C.N. Lee, S.H. Teoh, Characterization of smooth muscle cells on poly(ε-caprolactone) films, Mater. Sci. Eng. C. 27 (2007) 309–312. https://doi.org/10.1016/j.msec.2006.03.008.

[163] D. Yan, J. Jones, X.Y. Yuan, X.H. Xu, J. Sheng, J.C.-M. Lee, G.Q. Ma, Q.S. Yu, Plasma treatment of electrospun PCL random nanofiber meshes (NFMs) for biological property improvement, J. Biomed. Mater. Res. Part A. 101A (2013) 963–972. https://doi.org/10.1002/jbm.a.34398.

[164] A. Martins, E.D. Pinho, S. Faria, I. Pashkuleva, A.P. Marques, R.L. Reis,

N.M. Neves, Surface Modification of Electrospun Polycaprolactone Nanofiber Meshes by Plasma Treatment to Enhance Biological Performance, Small. 5 (2009) 1195–1206. https://doi.org/10.1002/smll.200801648.

[165] J.R.J. Paletta, S. Bockelmann, A. Walz, C. Theisen, J.H. Wendorff, A. Greiner, S. Fuchs-Winkelmann, M.D. Schofer, RGD-functionalisation of PLLA nanofibers by surface coupling using plasma treatment: Influence on stem cell differentiation, J. Mater. Sci. Mater. Med. 21 (2010) 1363–1369. https://doi.org/10.1007/s10856-009-3947-2.

[166] A. Ardeshirylajimi, P. Dinarvand, E. Seyedjafari, L. Langroudi, F. Jamshidi Adegani, M. Soleimani, Enhanced reconstruction of rat calvarial defects achieved by plasma-treated electrospun scaffolds and induced pluripotent stem cells, Cell Tissue Res. 354 (2013) 849–860. https://doi.org/10.1007/s00441-013-1693-8.

[167] J. Lee, G. Ma, Y. Q, Plasma treatment of random and aligned electrospun PCL nanofibers, J. Med. Biol. Eng. 33 (2013) 171–178. https://doi.org/10.5405/jmbe.1072.

[168] A. Nandakumar, Z. Tahmasebi Birgani, D. Santos, A. Mentink, N. Auffermann, K. Van Der Werf, M. Bennink, L. Moroni, C. Van Blitterswijk, P. Habibovic, Surface modification of electrospun fibre meshes by oxygen plasma for bone regeneration, Biofabrication. 5 (2013) 15006–15020. https://doi.org/10.1088/1758-5082/5/1/015006.

[169] I. Unalan, O. Colpankan, A.Z. Albayrak, C. Gorgun, A.S. Urkmez, Biocompatibility of plasma-treated poly(3-hydroxybutyrate-co-3-hydroxyvalerate) nanofiber mats modified by silk fibroin for bone tissue regeneration, Mater. Sci. Eng. C. 68 (2016) 842–850. https://doi.org/10.1016/j.msec.2016.07.054.

[170] G. Birhanu, H. Akbari Javar, E. Seyedjafari, A. Zandi-Karimi, M. Dusti Telgerd, An improved surface for enhanced stem cell proliferation and osteogenic differentiation using electrospun composite PLLA/P123 scaffold, Artif. Cells, Nanomedicine, Biotechnol. 46 (2018) 1274–1281. https://doi.org/10.1080/21691401.2017.1367928.

[171] M. Wang, Y. Zhou, D. Shi, R. Chang, J. Zhang, M. Keidar, T.J. Webster, Cold atmospheric plasma (CAP)-modified and bioactive protein-loaded core-shell nanofibers for bone tissue engineering applications, Biomater. Sci. 7 (2019) 2430–2439. https://doi.org/10.1039/c8bm01284a.

[172] Q. Liu, J. Ding, F.K. Mante, S.L. Wunder, G.R. Baran, The role of surface

functional groups in calcium phosphate nucleation on titanium foil: a self-assembled monolayer technique, Biomaterials. 23 (2002) 3103–3111. https://doi.org/10.1016/S0142-9612(02)00050-9.

[173] H.J. Kim, U.J. Kim, H.S. Kim, C. Li, M. Wada, G.G. Leisk, D.L. Kaplan, Bone tissue engineering with premineralized silk scaffolds, Bone. 42 (2008) 1226–1234. https://doi.org/10.1016/j.bone.2008.02.007.

[174] G.P. Awasthi, V.K. Kaliannagounder, B. Maharjan, J.Y. Lee, C.H. Park, C.S. Kim, Albumin-induced exfoliation of molybdenum disulfide nanosheets incorporated polycaprolactone/zein composite nanofibers for bone tissue regeneration, Mater. Sci. Eng. C. 116 (2020) 111162. https://doi.org/10.1016/J.MSEC.2020.111162.

[175] H. Samadian, H. Mobasheri, M. Azami, R. Faridi-Majidi, Osteoconductive and electroactive carbon nanofibers/hydroxyapatite nanocomposite tailored for bone tissue engineering: in vitro and in vivo studies, Sci. Reports 2020 101. 10 (2020) 1–14. https://doi.org/10.1038/s41598-020-71455-3.

[176] D. Abdelaziz, A. Hefnawy, E. Al-Wakeel, A. El-Fallal, I.M. El-Sherbiny, New biodegradable nanoparticles-in-nanofibers based membranes for guided periodontal tissue and bone regeneration with enhanced antibacterial activity, J. Adv. Res. 28 (2021) 51–62. https://doi.org/10.1016/J.JARE.2020.06.014.

[177] B. Akhavan, T.D. Michl, C. Giles, K. Ho, L. Martin, O. Sharifahmadian, S.G. Wise, B.R. Coad, N. Kumar, H.J. Griesser, M.M. Bilek, Plasma activated coatings with dual action against fungi and bacteria, Appl. Mater. Today. 12 (2018) 72–84. https://doi.org/10.1016/j.apmt.2018.04.003.

[178] B. Akhavan, M. Croes, S.G. Wise, C. Zhai, J. Hung, C. Stewart, M. Ionescu, H. Weinans, Y. Gan, S. Amin Yavari, M.M.M. Bilek, Radical-functionalized plasma polymers: Stable biomimetic interfaces for bone implant applications, Appl. Mater. Today. 16 (2019) 456–473. https://doi.org/10.1016/j.apmt.2019.07.002.

[179] T. Kokubo, H. Takadama, How useful is SBF in predicting in vivo bone bioactivity?, Biomaterials. 27 (2006) 2907–2915. https://doi.org/10.1016/j.biomaterials.2006.01.017.

[180] Y. Ito, H. Hasuda, M. Kamitakahara, C. Ohtsuki, M. Tanihara, I.K. Kang, O.H. Kwon, A composite of hydroxyapatite with electrospun biodegradable nanofibers as a tissue engineering material, J. Biosci. Bioeng. 100 (2005) 43–49. https://doi.org/10.1263/jbb.100.43.

[181] X.L. Deng, A.Y. Nikiforov, P. Vanraes, C. Leys, Direct current plasma jet at

atmospheric pressure operating in nitrogen and air, J. Appl. Phys. 113 (2013) 023305-1-023305–9. https://doi.org/10.1063/1.4774328.

[182] M.A. (Michael A.. Lieberman, A.J. Lichtenberg, Principles of plasma discharges and materials processing, Wiley-Interscience, 2005.

[183] J.J. Camacho, J.M.L. Poyato, L. Díaz, M. Santos, Optical emission studies of nitrogen plasma generated by IR CO2 laser pulses, J. Phys. B At. Mol. Opt. Phys. 40 (2007) 4573–4590. https://doi.org/10.1088/0953-4075/40/24/003.

[184] M.J. Fernández, O. Carabaño, M.J. van de Sande, J. Jonkers, M.C. Quintero, J.J.A.M. van der Mullen, A. Gamero, A. Sola, Preliminary spectroscopic measurements on a low-pressure argon, 2.45 GHz microwave-fed QL-lamp, J. Phys. D. Appl. Phys. 37 (2004) 1228–1233. https://doi.org/10.1088/0022-3727/37/8/011.

[185] J.F.R. Van Guyse, V.R. de la Rosa, R. Hoogenboom, Mechanochemical Preparation of Stable Sub-100 nm γ-Cyclodextrin:Buckminsterfullerene (C60) Nanoparticles by Electrostatic or Steric Stabilization, Chem. - A Eur. J. 24 (2018) 2758–2766. https://doi.org/10.1002/chem.201705647.

[186] M. Jevtić, M. Mitrić, S. Škapin, B. Jančar, N. Ignjatović, D. Uskoković, Crystal Structure of Hydroxyapatite Nanorods Synthesized by Sonochemical Homogeneous Precipitation, Cryst. Growth Des. 8 (2008) 2217–2222. https://doi.org/10.1021/cg7007304.

[187] M. Mujahid, S. Sarfraz, S. Amin, M. Mujahid, S. Sarfraz, S. Amin, On the Formation of Hydroxyapatite Nano Crystals Prepared Using Cationic Surfactant, Mater. Res. 18 (2015) 468–472. https://doi.org/10.1590/1516-1439.298014.

[188] B. Akhavan, S.G. Wise, M.M.M. Bilek, Substrate-Regulated Growth of Plasma-Polymerized Films on Carbide-Forming Metals, Langmuir. 32 (2016) 10835–10843. https://doi.org/10.1021/acs.langmuir.6b02901.

[189] A.. Lemos, J.M.. Ferreira, Porous bioactive calcium carbonate implants processed by starch consolidation, Mater. Sci. Eng. C. 11 (2000) 35–40. https://doi.org/10.1016/S0928-4931(00)00134-X.

[190] T. Kokubo, H. Kushitani, S. Sakka, T. Kitsugi, T. Yamamuro, Solutions able to reproduce in vivo surface-structure changes in bioactive glass-ceramic A-W3, J. Biomed. Mater. Res. 24 (1990) 721–734. https://doi.org/10.1002/jbm.820240607.

[191] Y. Hao, J. Chen, L. Yang, X. Wang, Lissajous figures of glow and filamentary dielectric barrier discharges under high frequency voltage at

atmospheric pressure in helium, in: 2009 IEEE 9th Int. Conf. Prop. Appl. Dielectr. Mater., IEEE, 2009: pp. 626–629. https://doi.org/10.1109/ICPADM.2009.5252353.

[192] Z. Fang, T. Shao, J. Yang, C. Zhang, Discharge processes and an electrical model of atmospheric pressure plasma jets in argon, Eur. Phys. J. D. 70 (2016) 1–8. https://doi.org/10.1140/epjd/e2015-60437-4.

[193] F. Bretagnol, M. Tatoulian, F. Arefi-Khonsari, G. Lorang, J. Amouroux, Surface modification of polyethylene powder by nitrogen and ammonia low pressure plasma in a fluidized bed reactor, React. Funct. Polym. 61 (2004) 221–232. https://doi.org/10.1016/j.reactfunctpolym.2004.06.003.

[194] A. Fridman, L.A. Kennedy, Plasma Physics and Engineering, CRC Press, 2004. https://doi.org/10.1201/9781482293630.

[195] W. Wang, B. Patil, S. Heijkers, V. Hessel, A. Bogaerts, Nitrogen Fixation by Gliding Arc Plasma: Better Insight by Chemical Kinetics Modelling, ChemSusChem. 10 (2017) 2145–2157. https://doi.org/10.1002/cssc.201700095.

[196] R. Snoeckx, S. Heijkers, K. Van Wesenbeeck, S. Lenaerts, A. Bogaerts, CO $_2$ conversion in a dielectric barrier discharge plasma: N $_2$ in the mix as a helping hand or problematic impurity?, Energy Environ. Sci. 9 (2016) 999–1011. https://doi.org/10.1039/C5EE03304G.

[197] A.J. Wagner, D.H. Fairbrother, F. Reniers, A Comparison of PE Surfaces Modified by Plasma Generated Neutral Nitrogen Species and Nitrogen Ions, Plasmas Polym. 8 (2003) 119–134. https://doi.org/10.1023/A:1023942211714.

[198] S.B. Bayram, M. V Freamat, Vibrational spectra of N 2 : An advanced undergraduate laboratory in atomic and molecular spectroscopy, Am. J. Phys. 80 (2012) 664–669. https://doi.org/10.1119/1.4722793.

[199] N. Sewraj, N. Merbahi, J.P. Gardou, P.R. Akerreta, F. Marchal, Electric and spectroscopic analysis of a pure nitrogen mono-filamentary dielectric barrier discharge (MF-DBD) at 760 Torr, J. Phys. D. Appl. Phys. 44 (2011). https://doi.org/10.1088/0022-3727/44/14/145201.

[200] Alexander Fridman, Plasma Chemistry , 2008.

[201] M. Capitelli, C. Ferreira, B. Gordiets, A. Osipov, Plasma kinetics in atmospheric gases, 2013.

[202] NIST Atomic Spectra Database, (2019).

https://doi.org/https://doi.org/10.18434/T4W30F.

[203] X. Fei, S.I. Kuroda, Y. Kondo, T. Mori, K. Hosoi, Influence of additive gas on electrical and optical characteristics of non-equilibrium atmospheric pressure argon plasma jet, Plasma Sci. Technol. 13 (2011) 575–582. https://doi.org/10.1088/1009-0630/13/5/13.

[204] H. Tahara, T. Yonezawa, Y. Andoh, T. Yoshikawa, Emission spectroscopic measurement of ammonia or mixture of nitrogen and hydrogen plasma in a direct-current arc jet generator with an expansion nozzle, IEEE Trans. Plasma Sci. 26 (1998) 1307–1313. https://doi.org/10.1109/27.725163.

[205] H. Nassar, S. Pellerin, K. Musiol, O. Martinie, N. Pellerin, J.-M. Cormier, N2+/N2 ratio and temperature measurements based on the first negative N2+ and second positive N2 overlapped molecular emission spectra, J. Phys. D. Appl. Phys. 37 (2004) 1904–1916. https://doi.org/10.1088/0022-3727/37/14/005.

[206] G. Aziz, N. De Geyter, H. Declercq, R. Cornelissen, R. Morent, Incorporation of amine moieties onto ultra-high molecular weight polyethylene (UHMWPE) surface via plasma and UV polymerization of allylamine, Surf. Coatings Technol. 271 (2015) 39–47. https://doi.org/10.1016/J.SURFCOAT.2015.01.027.

[207] A. Manakhov, P. Skladal, M. Elias, J. Cechal, J. Polak, D. Necas, L. Zajickova, Pulsed Plasma Polymerization of Cyclopropylamine for Deposition of Stable Amine-Rich Films Aimed at the Bio-Immobilization Applications, in: Soc. Vac. Coaters 57th Annu. Tech. Conf. Proc., Society of Vacuum Coaters, 2015: pp. 504–512. https://doi.org/10.14332/svc14.proc.1877.

[208] A. Manakhov, E. Makhneva, P. Skládal, D. Nečas, J. Čechal, L. Kalina, M. Eliáš, L. Zajíčková, The robust bio-immobilization based on pulsed plasma polymerization of cyclopropylamine and glutaraldehyde coupling chemistry, Appl. Surf. Sci. 360 (2016) 28–36. https://doi.org/10.1016/j.apsusc.2015.10.178.

[209] A. Manakhov, L. Zajíčková, M. Eliáš, J. Čechal, J. Polčák, J. Hnilica, Š. Bittnerová, D. Nečas, Optimization of cyclopropylamine plasma polymerization toward enhanced layer stability in contact with water, Plasma Process. Polym. 11 (2014) 532–544. https://doi.org/10.1002/ppap.201300177.

[210] T.R. Gengenbach, H.J. Griesser, Aging of 1,3-diaminopropane plasma-deposited polymer films: Mechanisms and reaction pathways, J. Polym.

Sci. Part A Polym. Chem. 37 (1999) 2191–2206. https://doi.org/10.1002/(SICI)1099-0518(19990701)37:13<2191::AID-POLA34>3.0.CO;2-F.

[211] R.J. Leiweke, B.N. Ganguly, Effects of pulsed-excitation applied voltage rise time on argon metastable production efficiency in a high pressure dielectric barrier discharge, Appl. Phys. Lett. 90 (2007) 241501-1-241501–3. https://doi.org/10.1063/1.2748324.

[212] A. Van Deynse, N. De Geyter, C. Leys, R. Morent, Influence of water vapor addition on the surface modification of polyethylene in an argon dielectric barrier discharge, Plasma Process. Polym. 11 (2014) 117–125. https://doi.org/10.1002/ppap.201300088.

[213] M. Lazár, J. Rychlý, Oxidation of hydrocarbon polymers, Adv. Polym. Sci. 102 (1992) 189–221. https://doi.org/10.1007/3-540-55090-9_7.

[214] F. Rezaei, B. Shokri, M. Sharifian, Atmospheric-pressure DBD plasma-assisted surface modification of polymethyl methacrylate: A study on cell growth/proliferation and antibacterial properties, Appl. Surf. Sci. 360 (2016) 641–651. https://doi.org/10.1016/j.apsusc.2015.11.036.

[215] G. Aziz, M. Thukkaram, N. De Geyter, R. Morent, Plasma parameters effects on the properties, aging and stability behaviors of allylamine plasma coated ultra-high molecular weight polyethylene (UHMWPE) films, Appl. Surf. Sci. 409 (2017) 381–395. https://doi.org/10.1016/j.apsusc.2017.03.027.

[216] T.R. Gengenbach, R.C. Chatelier, H.J. Griesser, Correlation of the nitrogen 1s and oxygen 1s XPS binding energies with compositional changes during oxidation of ethylene diamine plasma polymers, Surf. Interface Anal. 24 (1996) 611–619. https://doi.org/10.1002/(SICI)1096-9918(19960916)24:9<611::AID-SIA169>3.0.CO;2-7.

[217] T.F. Chen, K.S. Siow, P.Y. Ng, B.Y. Majlis, Enhancing the biocompatibility of the polyurethane methacrylate and off-stoichiometry thiol-ene polymers by argon and nitrogen plasma treatment, Mater. Sci. Eng. C. 79 (2017) 613–621. https://doi.org/10.1016/j.msec.2017.05.091.

[218] V. Schulz-von der Gathen, L. Schaper, N. Knake, S. Reuter, K. Niemi, T. Gans, J. Winter, Spatially resolved diagnostics on a microscale atmospheric pressure plasma jet, J. Phys. D. Appl. Phys. 41 (2008) 194004. https://doi.org/10.1088/0022-3727/41/19/194004.

[219] I. Radu, R. Bartnikas, M.R. Wertheimer, Frequency and Voltage Dependence of Glow and Pseudoglow Discharges in Helium Under Atmospheric Pressure, IEEE Trans. Plasma Sci. 31 (2003) 1363–1378.

https://doi.org/10.1109/TPS.2003.820970.

[220] Y. Akishev, M. Grushin, V. Karalnik, A. Petryakov, N. Trushkin, Non-equilibrium constricted dc glow discharge in N2 flow at atmospheric pressure: Stable and unstable regimes, J. Phys. D. Appl. Phys. 43 (2010) 75202. https://doi.org/10.1088/0022-3727/43/7/075202.

[221] D. Liu, J. Niu, N. Yu, Optical emission characteristics of medium- to high-pressure N 2 dielectric barrier discharge plasmas during surface modification of polymers , J. Vac. Sci. Technol. A Vacuum, Surfaces, Film. 29 (2011) 061506. https://doi.org/10.1116/1.3635372.

[222] U. Lommatzsch, D. Pasedag, A. Baalmann, G. Ellinghorst, H.E. Wagner, Atmospheric pressure plasma jet treatment of polyethylene surfaces for adhesion improvement, in: Plasma Process. Polym., John Wiley & Sons, Ltd, 2007: pp. S1041–S1045. https://doi.org/10.1002/ppap.200732402.

[223] D. Xiao, C. Cheng, J. Shen, Y. Lan, H. Xie, X. Shu, Y. Meng, J. Li, P.K. Chu, Characteristics of atmospheric-pressure non-thermal N2 and N2/O2 gas mixture plasma jet, J. Appl. Phys. 115 (2014) 033303. https://doi.org/10.1063/1.4862304.

[224] J.M. Thomas, F. Kaufman, An upper limit on the formation of no(x2hr) in the reactions N2(A3i:) + O(3P) and N2(A) + O2(X3Lg) at 298 K, J. Phys. Chem. 100 (1996) 8901–8906. https://doi.org/10.1021/jp960164v.

[225] S. De Benedictis, G. Dilecce, Rate constants for deactivation of N2(A) v=2-7 by O, O2, and NO, J. Chem. Phys. 107 (1997) 6219–6229. https://doi.org/10.1063/1.474287.

[226] R. Ono, T. Oda, NO formation in a pulsed spark discharge in N2/O2/Ar mixture at atmospheric pressure, J. Phys. D. Appl. Phys. 35 (2002) 543–548. https://doi.org/10.1088/0022-3727/35/6/309.

[227] L. V. Gatilova, K. Allegraud, J. Guillon, Y.Z. Ionikh, G. Cartry, J. Röpcke, A. Rousseau, NO formation mechanisms studied by infrared laser absorption in a single low-pressure plasma pulse, in: Plasma Sources Sci. Technol., IOP Publishing, 2007: p. S107. https://doi.org/10.1088/0963-0252/16/1/S12.

[228] N. Gherardi, G. Gouda, E. Gat, A. Ricard, F. Massines, Transition from glow silent discharge to micro-discharges in nitrogen gas, Plasma Sources Sci. Technol. 9 (2000) 340–346. https://doi.org/10.1088/0963-0252/9/3/312.

[229] T.H. Chung, H. Ra Kang, M.K. Bae, Optical emission diagnostics with electric probe measurements of inductively coupled Ar/O2/Ar-O2

plasmas, Phys. Plasmas. 19 (2012) 113502. https://doi.org/10.1063/1.4765357.

[230] Q. Xiong, A.Y. Nikiforov, X.P. Lu, C. Leys, High-speed dispersed photographing of an open-air argon plasma plume by a grating-ICCD camera system, J. Phys. D. Appl. Phys. 43 (2010) 415201. https://doi.org/10.1088/0022-3727/43/41/415201.

[231] I. Jõgi, J. Raud, K. Hein, M. Laan, Spectral characterization of medium-pressure RF discharge in argon-oxygen mixture, J. Phys. D. Appl. Phys. 47 (2014) 335206. https://doi.org/10.1088/0022-3727/47/33/335206.

[232] L. Taghizadeh, G. Brackman, A. Nikiforov, J. Van Der Mullen, C. Leys, T. Coenye, Inactivation of biofilms using a low power atmospheric pressure argon plasma jet; the role of entrained nitrogen, Plasma Process. Polym. 12 (2015) 75–81. https://doi.org/10.1002/ppap.201400074.

[233] K. Matra, Atmospheric non-thermal argon-oxygen plasma for sunflower seedling growth improvement, Jpn. J. Appl. Phys. 57 (2018) 01AG03. https://doi.org/10.7567/JJAP.57.01AG03.

[234] R. Hippler, M. Cada, V. Stranak, Z. Hubicka, Time-resolved optical emission spectroscopy of a unipolar and a bipolar pulsed magnetron sputtering discharge in an argon/oxygen gas mixture with a cobalt target, Plasma Sources Sci. Technol. 28 (2019) 115020. https://doi.org/10.1088/1361-6595/ab54e8.

[235] G. Park, H. Lee, G. Kim, J.K. Lee, Global model of He/O2 and Ar/O2 atmospheric pressure glow discharges, Plasma Process. Polym. 5 (2008) 569–576. https://doi.org/10.1002/ppap.200800019.

[236] K. Fricke, I. Koban, H. Tresp, L. Jablonowski, K. Schröder, A. Kramer, K.-D. Weltmann, T. von Woedtke, T. Kocher, Atmospheric Pressure Plasma: A High-Performance Tool for the Efficient Removal of Biofilms, PLoS One. 7 (2012) e42539. https://doi.org/10.1371/journal.pone.0042539.

[237] P.J. Cullen, V. Milosavljević, Spectroscopic characterization of a radio-frequency argon plasma jet discharge in ambient air, Prog. Theor. Exp. Phys. 2015 (2015) 63–64. https://doi.org/10.1093/ptep/ptv070.

[238] Y. Chen, Q. Gao, H. Wan, J. Yi, Y. Wei, P. Liu, Surface modification and biocompatible improvement of polystyrene film by Ar, O 2 and Ar + O 2 plasma, Appl. Surf. Sci. 265 (2013) 452–457. https://doi.org/10.1016/j.apsusc.2012.11.027.

[239] T. Egghe, J.F.R. Van Guyse, R. Ghobeira, R. Morent, R. Hoogenboom, N.

De Geyter, Evaluation of cross-linking and degradation processes occurring at polymer surfaces upon plasma activation via size-exclusion chromatography, Polym. Degrad. Stab. 187 (2021) 109543. https://doi.org/10.1016/j.polymdegradstab.2021.109543.

[240] J.M. Grace, L.J. Gerenser, Plasma treatment of polymers, J. Dispers. Sci. Technol. 24 (2003) 305–341. https://doi.org/10.1081/DIS-120021793.

[241] F. Normand, A. Granier, P. Leprince, J. Marec, M.K. Shi, F. Clouet, Polymer treatment in the flowing afterglow of an oxygen microwave discharge: Active species profile concentrations and kinetics of the functionalization, Plasma Chem. Plasma Process. 15 (1995) 173–198. https://doi.org/10.1007/BF01459695.

[242] M.R. Sanchis, O. Calvo, O. Fenollar, D. Garcia, R. Balart, Characterization of the surface changes and the aging effects of low-pressure nitrogen plasma treatment in a polyurethane film, Polym. Test. 27 (2008) 75–83. https://doi.org/10.1016/j.polymertesting.2007.09.002.

[243] S. Teodoru, Y. Kusano, N. Rozlosnik, P.K. Michelsen, Continuous plasma treatment of ultra-high-molecular-weight polyethylene (UHMWPE) fibres for adhesion improvement, in: Plasma Process. Polym., John Wiley & Sons, Ltd, 2009: pp. S375–S381. https://doi.org/10.1002/ppap.200930906.

[244] T. Belmonte, J.M. Thiébaut, D. Mézerette, Role of active species in surface cleaning by an Ar-N2 atmospheric pressure post-discharge, J. Phys. D. Appl. Phys. 35 (2002) 1919–1926. https://doi.org/10.1088/0022-3727/35/16/304.

[245] H. Yoshimoto, Y.M. Shin, H. Terai, J.P. Vacanti, A biodegradable nanofiber scaffold by electrospinning and its potential for bone tissue engineering, Biomaterials. 24 (2003) 2077–2082. https://doi.org/10.1016/S0142-9612(02)00635-X.

[246] Z.X. Meng, Y.S. Wang, C. Ma, W. Zheng, L. Li, Y.F. Zheng, Electrospinning of PLGA/gelatin randomly-oriented and aligned nanofibers as potential scaffold in tissue engineering, Mater. Sci. Eng. C. 30 (2010) 1204–1210. https://doi.org/10.1016/J.MSEC.2010.06.018.

[247] E.J. Chong, T.T. Phan, I.J. Lim, Y.Z. Zhang, B.H. Bay, S. Ramakrishna, Evaluation of electrospun PCL/gelatin nanofibrous scaffold for wound healing and layered dermal reconstitution, Acta Biomater. 3 (2007) 321–330. https://doi.org/10.1016/J.ACTBIO.2007.01.002.

[248] J.A. Matthews, G.E. Wnek, D.G. Simpson, G.L. Bowlin, Electrospinning of Collagen Nanofibers, Biomacromolecules. 3 (2002) 232–238.

https://doi.org/10.1021/BM015533U.

[249] L. Li, Y.-L. Hsieh, Chitosan bicomponent nanofibers and nanoporous fibers, Carbohydr. Res. 341 (2005) 374–381. https://doi.org/10.1016/j.carres.2005.11.028.

[250] J. Li, S. Zivanovic, P.M. Davidson, K. Kit, Characterization and comparison of chitosan/PVP and chitosan/PEO blend films, Carbohydr. Polym. 79 (2010) 786–791. https://doi.org/10.1016/J.CARBPOL.2009.09.028.

[251] B. Duan, C. Dong, X. Yuan, K. Yao, Electrospinning of chitosan solutions in acetic acid with poly(ethylene oxide), J. Biomater. Sci. Polym. Ed. 15 (2004) 797–811. https://doi.org/10.1163/156856204774196171.

[252] J. Vuola, T. Bohling, J. Kinnunen, E. Hirvensalo, S. Asko-Seljavaara, Natural coral as bone-defect-filling material, J. Biomed. Mater. Res. 51 (2000) 117–122. https://doi.org/10.1002/(SICI)1097-4636(200007)51:1<117::AID-JBM15>3.0.CO;2-9.

[253] M. Gravel, R. Vago, M. Tabrizian, Use of Natural Coralline Biomaterials As Reinforcing and Gas-Forming Agent for Developing Novel Hybrid Biomatrices: Microarchitectural and Mechanical Studies, Tissue Eng. 12 (2006) 589–600. https://doi.org/10.1089/ten.2006.12.589.

[254] F. Hejazi, H. Mirzadeh, Roll-designed 3D nanofibrous scaffold suitable for the regeneration of load bearing bone defects, Prog. Biomater. 5 (2016) 199–211. https://doi.org/10.1007/s40204-016-0058-2.

[255] E.J. Sheehy, M. Lemoine, D. Clarke, A. Gonzalez Vazquez, F.J. O'Brien, The Incorporation of Marine Coral Microparticles into Collagen-Based Scaffolds Promotes Osteogenesis of Human Mesenchymal Stromal Cells via Calcium Ion Signalling, Mar. Drugs. 18 (2020) 74–93. https://doi.org/10.3390/md18020074.

[256] T. Foster, P.L. Clode, Skeletal mineralogy of coral recruits under high temperature and pCO2, Biogeosciences. 13 (2016) 1717–1722. https://doi.org/10.5194/bg-13-1717-2016.

[257] H. Mansur, A. Mansur, M. Pereira, XRD, SEM/EDX and FTIR characterization of Brazilian natural coral, Key Eng. Mater. Vol. 284 (2005) 43–46. https://doi.org/10.4028/www.scientific.net/kem.284-286.43.

[258] R.Z. Birk, L. Abramovitch-Gottlib, I. Margalit, M. Aviv, E. Forti, S. Geresh, R. Vago, Conversion of Adipogenic to Osteogenic Phenotype Using Crystalline Porous Biomatrices of Marine Origin, Tissue Eng. 12 (2006)

21–31. https://doi.org/10.1089/ten.2006.12.21.

[259] Y.-T. Sul, Y. Jeong, C. Johansson, T. Albrektsson, Oxidized, bioactive implants are rapidly and strongly integrated in bone. Part 1 – experimental implants, Clin. Oral Implants Res. 17 (2006) 521–526. https://doi.org/10.1111/J.1600-0501.2005.01230.X.

[260] J. Zhang, J. Guo, T. Li, & X. Li, X. Li, Chemical Surface Modification of Calcium Carbonate Particles by Maleic Anhydride Grafting Polyethylene Wax, Int. J. Green Nanotechnol. Phys. Chem. 1 (2010) 65–71. https://doi.org/10.1080/19430871003684341.

[261] D. Yan, J. Jones, X.Y. Yuan, X.H. Xu, J. Sheng, J.C.-M. Lee, G.Q. Ma, Q.S. Yu, Plasma treatment of electrospun PCL random nanofiber meshes (NFMs) for biological property improvement, J. Biomed. Mater. Res. Part A. 101A (2013) 963–972. https://doi.org/10.1002/jbm.a.34398.

[262] W. Liu, J. Zhan, Y. Su, T. Wu, C. Wu, S. Ramakrishna, X. Mo, S.S. Al-Deyab, M. El-Newehy, Effects of plasma treatment to nanofibers on initial cell adhesion and cell morphology, Colloids Surfaces B Biointerfaces. 113 (2014) 101–106. https://doi.org/10.1016/J.COLSURFB.2013.08.031.

[263] X. Yang, X. Chen, H. Wang, Acceleration of osteogenic differentiation of preosteoblastic cells by chitosan containing nanofibrous scaffolds, Biomacromolecules. 10 (2009) 2772–2778. https://doi.org/10.1021/bm900623j.

[264] D. Semnani, E. Naghashzargar, M. Hadjianfar, F. Dehghan Manshadi, S. Mohammadi, S. Karbasi, F. Effaty, Evaluation of PCL/chitosan electrospun nanofibers for liver tissue engineering, Int. J. Polym. Mater. Polym. Biomater. 66 (2017) 149–157. https://doi.org/10.1080/00914037.2016.1190931.

[265] B. Duan, L. Wu, X. Yuan, Z. Hu, X. Li, Y. Zhang, K. Yao, M. Wang, Hybrid nanofibrous membranes of PLGA/chitosan fabricated via an electrospinning array, J. Biomed. Mater. Res. Part A. 83A (2007) 868–878. https://doi.org/10.1002/jbm.a.31408.

[266] V. Thomas, D.R. Dean, M. V. Jose, B. Mathew, S. Chowdhury, Y.K. Vohra, Nanostructured biocomposite scaffolds based on collagen coelectrospun with nanohydroxyapatite, Biomacromolecules. 8 (2007) 631–637. https://doi.org/10.1021/bm060879w.

[267] M.P. Prabhakaran, J. Venugopal, S. Ramakrishna, Electrospun nanostructured scaffolds for bone tissue engineering, Acta Biomater. 5 (2009) 2884–2893. https://doi.org/10.1016/j.actbio.2009.05.007.

[268] J. Venugopal, S. Low, A.T. Choon, A. Bharath Kumar, S. Ramakrishna, Electrospun-modified nanofibrous scaffolds for the mineralization of osteoblast cells, J. Biomed. Mater. Res. - Part A. 85 (2008) 408–417. https://doi.org/10.1002/jbm.a.31538.

[269] J. Kiehl, C. Ben-Azzouz, D. Dentel, M. Derivaz, J.L. Bischoff, C. Delaite, S. Bistac, Grafting process of ethyltrimethoxysilane and polyphosphoric acid on calcium carbonate surface, Appl. Surf. Sci. 264 (2013) 864–871. https://doi.org/10.1016/J.APSUSC.2012.10.166.

[270] M. Ni, B.D. Ratner, Differentiating calcium carbonate polymorphs by surface analysis techniques-an XPS and TOF-SIMS study, Surf. Interface Anal. 40 (2008) 1356–1361. https://doi.org/10.1002/sia.2904.

[271] J. Baltrusaitis, C.R. Usher, V.H. Grassian, Reactions of sulfur dioxide on calcium carbonate single crystal and particle surfaces at the adsorbed water carbonate interface, Phys. Chem. Chem. Phys. 9 (2007) 3011–3024. https://doi.org/10.1039/b617697f.

[272] R. Bitar, P. Cools, N. De Geyter, R. Morent, Atmospheric pressure plasma activation of PP films with a localized µplasma, Surf. Coatings Technol. 307 (2016) 1074–1083. https://doi.org/10.1016/j.surfcoat.2016.06.073.

[273] S. Dorozhkin, Nanodimensional and Nanocrystalline Apatites and Other Calcium Orthophosphates in Biomedical Engineering, Biology and Medicine, Materials (Basel). 2 (2009) 1975–2045. https://doi.org/10.3390/ma2041975.

[274] M. Tanahashi, T. Matsuda, Surface functional group dependence on apatite formation on self-assembled monolayers in a simulated body fluid, J. Biomed. Mater. Res. 34 (1997) 305–315. https://doi.org/10.1002/(SICI)1097-4636(19970305)34:3<305::AID-JBM5>3.0.CO;2-O.

[275] X. Chen, A. Nouri, Y. Li, J. Lin, P.D. Hodgson, C. Wen, Effect of surface roughness of Ti, Zr, and TiZr on apatite precipitation from simulated body fluid, Biotechnol. Bioeng. 101 (2008) 378–387. https://doi.org/10.1002/bit.21900.

[276] K. Sato, Y. Kumagai, J. Tanaka, Apatite formation on organic monolayers in simulated body environment, J. Biomed. Mater. Res. 50 (2000) 16–20. https://doi.org/10.1002/(SICI)1097-4636(200004)50:1<16::AID-JBM3>3.0.CO;2-G.

[277] R.Z. LeGeros, Formation and transformation of calcium phosphates: Relevance to vascular calcification, in: Z. Kardiol., Springer, 2001: pp.

116–124. https://doi.org/10.1007/s003920170032.

[278] S. Meejoo, W. Maneeprakorn, P. Winotai, Phase and thermal stability of nanocrystalline hydroxyapatite prepared via microwave heating, Thermochim. Acta. 447 (2006) 115–120. https://doi.org/10.1016/j.tca.2006.04.013.

[279] M. and D.A.N. Vallet-Regí, Biological apatites in bone and teeth, in: RSC Nanosci. Nanotechnol., Royal Society of Chemistry, 2016: pp. 1–29. https://doi.org/10.1039/9781782622550-00001.

[280] Z. Chen, X. Mo, C. He, H. Wang, Intermolecular interactions in electrospun collagen-chitosan complex nanofibers, Carbohydr. Polym. 72 (2008) 410–418. https://doi.org/10.1016/j.carbpol.2007.09.018.

[281] Z.G. Chen, P.W. Wang, B. Wei, X.M. Mo, F.Z. Cui, Electrospun collagen-chitosan nanofiber: A biomimetic extracellular matrix for endothelial cell and smooth muscle cell, Acta Biomater. 6 (2010) 372–382. https://doi.org/10.1016/j.actbio.2009.07.024.

[282] S. Jin, J. Li, J. Wang, J. Jiang, Y. Zuo, Y. Li, F. Yang, Electrospun silver ion-loaded calcium phosphate/ chitosan antibacterial composite fibrous membranes for guided bone regeneration, Int. J. Nanomedicine. 13 (2018) 4591–4605. https://doi.org/10.2147/IJN.S167793.

[283] A. Holländer, F. Pippig, M. Dubreuil, D. Vangeneugden, Distinguishing Surface OH and NHx Using TFAA Derivatization and XPS, Plasma Process. Polym. 5 (2008) 345–349. https://doi.org/10.1002/ppap.200700167.

[284] U. Hayat, A.M. Tinsley, M.R. Calder, D.J. Clarke, ESCA investigation of low-temperature ammonia plasma-treated polyethylene substrate for immobilization of protein, Biomaterials. 13 (1992) 801–806. https://doi.org/10.1016/0142-9612(92)90022-G.

[285] I. Mrsic, T. Bäuerle, S. Ulitzsch, G. Lorenz, K. Rebner, A. Kandelbauer, T. Chassé, Oxygen plasma surface treatment of polymer films—Pellethane 55DE and EPR-g-VTMS, Appl. Surf. Sci. 536 (2021) 147782. https://doi.org/10.1016/j.apsusc.2020.147782.

[286] K.V. Chan, I. Onyshchenko, A. Nikiforov, G. Aziz, R. Morent, N. De Geyter, Plasma polymerization of cyclopropylamine with a sub-atmospheric pressure DBD, Eur. Polym. J. 103 (2018) 1–10. https://doi.org/10.1016/j.eurpolymj.2018.03.040.

[287] A. Manakhov, P. Kiryukhantsev-Korneev, M. Michlíček, E. Permyakova, E. Dvořáková, J. Polčák, Z. Popov, M. Visotin, D. V. Shtansky, Grafting of carboxyl groups using CO 2 /C 2 H 4 /Ar pulsed plasma: Theoretical

modeling and XPS derivatization, Appl. Surf. Sci. 435 (2018) 1220–1227. https://doi.org/10.1016/j.apsusc.2017.11.174.

[288] G. Cicala, M. Creatore, P. Favia, R. Lamendola, R. D'Agostino, Modulated rf discharges as an effective tool for selecting excited species, Appl. Phys. Lett. 75 (1999) 37–39. https://doi.org/10.1063/1.124269.

[289] P. Favia, M.V. Stendardo, R. D'Agostino, Selective grafting of amine groups on polyethylene by means of NH3-H2 RF glow discharges, Plasmas Polym. 1 (1996) 91–112. https://doi.org/10.1007/BF02532821.

[290] A. Ogino, S. Noguchi, M. Nagatsu, Optimization of amino group introduction onto polyurethane surface using ammonia and argon surface-wave plasma, in: Jpn. J. Appl. Phys., IOP Publishing, 2011: p. 08JF06. https://doi.org/10.1143/JJAP.50.08JF06.

[291] M. Král, A. Ogino, M. Nagatsu, Effect of hydrogen on amino group introduction onto the polyethylene surface by surface-wave plasma chemical modification, J. Phys. D. Appl. Phys. 41 (2008) 105213–105219. https://doi.org/10.1088/0022-3727/41/10/105213.

[292] E. Yegen, U. Zimmermann, W.E.S. Unger, T. Braun, C-F Bond Cleavage during Derivatization Reactions of Amino Groups with TFBA and PFB at Plasma-Processed Organic Surfaces?, Plasma Process. Polym. 6 (2009) 11–16. https://doi.org/10.1002/ppap.200800100.

[293] F. Pippig, S. Sarghini, A. Holländer, S. Paulussen, H. Terryn, TFAA chemical derivatization and XPS. Analysis of OH and NHx polymers, Surf. Interface Anal. 41 (2009) 421–429. https://doi.org/10.1002/sia.3043.

[294] E.A. Vogler, R.W. Bussian, Short-term cell-attachment rates: A surface-sensitives test of cell-substrate compatibility, J. Biomed. Mater. Res. 21 (1987) 1197–1211. https://doi.org/10.1002/jbm.820211004.

[295] J.M. Kelly, R.D. Short, M.R. Alexander, Experimental evidence of a relationship between monomer plasma residence time and carboxyl group retention in acrylic acid plasma polymers, Polymer (Guildf). 44 (2003) 3173–3176. https://doi.org/10.1016/S0032-3861(03)00217-9.

[296] M.R. Alexander, T.M. Duc, A study of the interaction of acrylic acid/1,7-octadiene plasma deposits with water and other solvents, Polymer (Guildf). 40 (1999) 5479–5488. https://doi.org/10.1016/S0032-3861(98)00784-8.

[297] R.W. Paynter, Angle-resolved XPS study of the effect of x-radiation on the aging of polystyrene exposed to an oxygen/argon plasma, Surf. Interface Anal. 33 (2002) 14–22. https://doi.org/10.1002/sia.1155.

[298] R.N.S. Sodhi, P. Brodersen, L. Cademartiri, M.M. Thuo, C.A. Nijhuis, Surface and buried interface layer studies on challenging structures as studied by ARXPS, Surf. Interface Anal. 49 (2017) 1309–1315. https://doi.org/10.1002/sia.6270.

[299] R. Morent, N. De Geyter, F. Axisa, N. De Smet, L. Gengembre, E. De Leersnyder, C. Leys, J. Vanfleteren, M. Rymarczyk-Machal, E. Schacht, E. Payen, Adhesion enhancement by a dielectric barrier discharge of PDMS used for flexible and stretchable electronics, J. Phys. D. Appl. Phys. 40 (2007) 7392–7401. https://doi.org/10.1088/0022-3727/40/23/021.

[300] Z. Postawa, B. Czerwinski, M. Szewczyk, E.J. Smiley, N. Winograd, B.J. Garrison, Enhancement of sputtering yields due to C60 versus Ga bombardment of Ag{111} as explored by molecular dynamics simulations, Anal. Chem. 75 (2003) 4402–4407. https://doi.org/10.1021/ac034387a.

[301] T. Nobuta, T. Ogawa, Depth profile XPS analysis of polymeric materials by C60+ ion sputtering, J. Mater. Sci. 44 (2009) 1800–1812. https://doi.org/10.1007/s10853-009-3274-5.

[302] K. Tanaka, N. Sanada, M. Hikita, T. Nakamura, T. Kajiyama, A. Takahara, Surface depth analysis for fluorinated block copolymer films by X-ray photoelectron spectroscopy using C 60 cluster ion beam, Appl. Surf. Sci. 254 (2008) 5435–5438. https://doi.org/10.1016/j.apsusc.2008.02.089.

[303] A. Vesel, Modification of polystyrene with a highly reactive cold oxygen plasma, Surf. Coatings Technol. 205 (2010) 490–497. https://doi.org/10.1016/j.surfcoat.2010.07.016.

[304] T. Jacobs, E. Carbone, R. Morent, N. De Geyter, F. Reniers, C. Leys, Surface modification of polymer films with a remote atmospheric pressure d.c. glow discharge: influence of substrate location, Surf. Interface Anal. 42 (2010) 1316–1320. https://doi.org/10.1002/sia.3319.

[305] U. Vohrer, C. Blomfield, S. Page, A. Roberts, Quantitative XPS imaging - New possibilities with the delay-line detector, in: Appl. Surf. Sci., Elsevier, 2005: pp. 61–65. https://doi.org/10.1016/j.apsusc.2005.01.114.

[306] D.E. Peebles, J.A. Ohlhausen, P.G. Kotula, S. Hutton, C. Blomfield, Multivariate statistical analysis for x-ray photoelectron spectroscopy spectral imaging: Effect of image acquisition time, J. Vac. Sci. Technol. A Vacuum, Surfaces, Film. 22 (2004) 1579–1586. https://doi.org/10.1116/1.1765134.

[307] D.J. Morgan, Imaging XPS for industrial applications, J. Electron

Spectros. Relat. Phenomena. 231 (2019) 109–117. https://doi.org/10.1016/j.elspec.2017.12.008.

[308] S. Hajati, S. Tougaard, XPS for non-destructive depth profiling and 3D imaging of surface nanostructures, Anal. Bioanal. Chem. 396 (2010) 2741–2755. https://doi.org/10.1007/s00216-009-3401-9.

[309] A. Vesel, R. Zaplotnik, G. Primc, M. Mozetič, Evolution of the Surface Wettability of PET Polymer upon Treatment with an Atmospheric-Pressure Plasma Jet, Polymers (Basel). 12 (2020) 87–112. https://doi.org/10.3390/polym12010087.

[310] Ö. Birer, Reactivity zones around an atmospheric pressure plasma jet, in: Appl. Surf. Sci., Elsevier B.V., 2015: pp. 420–428. https://doi.org/10.1016/j.apsusc.2015.04.100.

[311] F. Intranuovo, D. Howard, L.J. White, R.K. Johal, A.M. Ghaemmaghami, P. Favia, S.M. Howdle, K.M. Shakesheff, M.R. Alexander, Uniform cell colonization of porous 3-D scaffolds achieved using radial control of surface chemistry, Acta Biomater. 7 (2011) 3336–3344. https://doi.org/10.1016/j.actbio.2011.05.020.

[312] J.J.A. Barry, D. Howard, K.M. Shakesheff, S.M. Howdle, M.R. Alexander, Using a Core–Sheath Distribution of Surface Chemistry through 3D Tissue Engineering Scaffolds to Control Cell Ingress, Adv. Mater. 18 (2006) 1406–1410. https://doi.org/10.1002/adma.200502719.

[313] M. Domingos, F. Intranuovo, A. Gloria, R. Gristina, L. Ambrosio, P.J. Bártolo, P. Favia, Improved osteoblast cell affinity on plasma-modified 3-D extruded PCL scaffolds, Acta Biomater. 9 (2013) 5997–6005. https://doi.org/10.1016/j.actbio.2012.12.031.

[314] J.J.A. Barry, M.M.C.G. Silva, K.M. Shakesheff, S.M. Howdle, M.R. Alexander, Using Plasma Deposits to Promote Cell Population of the Porous Interior of Three-Dimensional Poly(D,L-Lactic Acid) Tissue-Engineering Scaffolds, Adv. Funct. Mater. 15 (2005) 1134–1140. https://doi.org/10.1002/adfm.200400562.

[315] T. Jacobs, H. Declercq, N. De Geyter, R. Cornelissen, P. Dubruel, C. Leys, R. Morent, Improved cell adhesion to flat and porous plasma-treated poly-ε-caprolactone samples, Surf. Coatings Technol. 232 (2013) 447–455. https://doi.org/10.1016/j.surfcoat.2013.06.001.

[316] V. Armenise, A. Milella, F. Fracassi, P. Bosso, F. Fanelli, Deposition of thin films containing carboxylic acid groups on polyurethane foams by atmospheric pressure non-equilibrium plasma jet, Surf. Coatings Technol. 379 (2019) 125017–12526.

https://doi.org/10.1016/j.surfcoat.2019.125017.

[317] P. Cools, C. Mota, I. Lorenzo-Moldero, R. Ghobeira, N. De Geyter, L. Moroni, R. Morent, Acrylic Acid Plasma Coated 3D Scaffolds for Cartilage tissue engineering applications, Sci. Rep. 8 (2018) 1–15. https://doi.org/10.1038/s41598-018-22301-0.

[318] V. Armenise, F. Fanelli, A. Milella, L. D'Accolti, A. Uricchio, F. Fracassi, Atmospheric pressure plasma treatment of polyurethane foams with He–O2 fed dielectric barrier discharges, Surfaces and Interfaces. 20 (2020) 100600–100610. https://doi.org/10.1016/j.surfin.2020.100600.

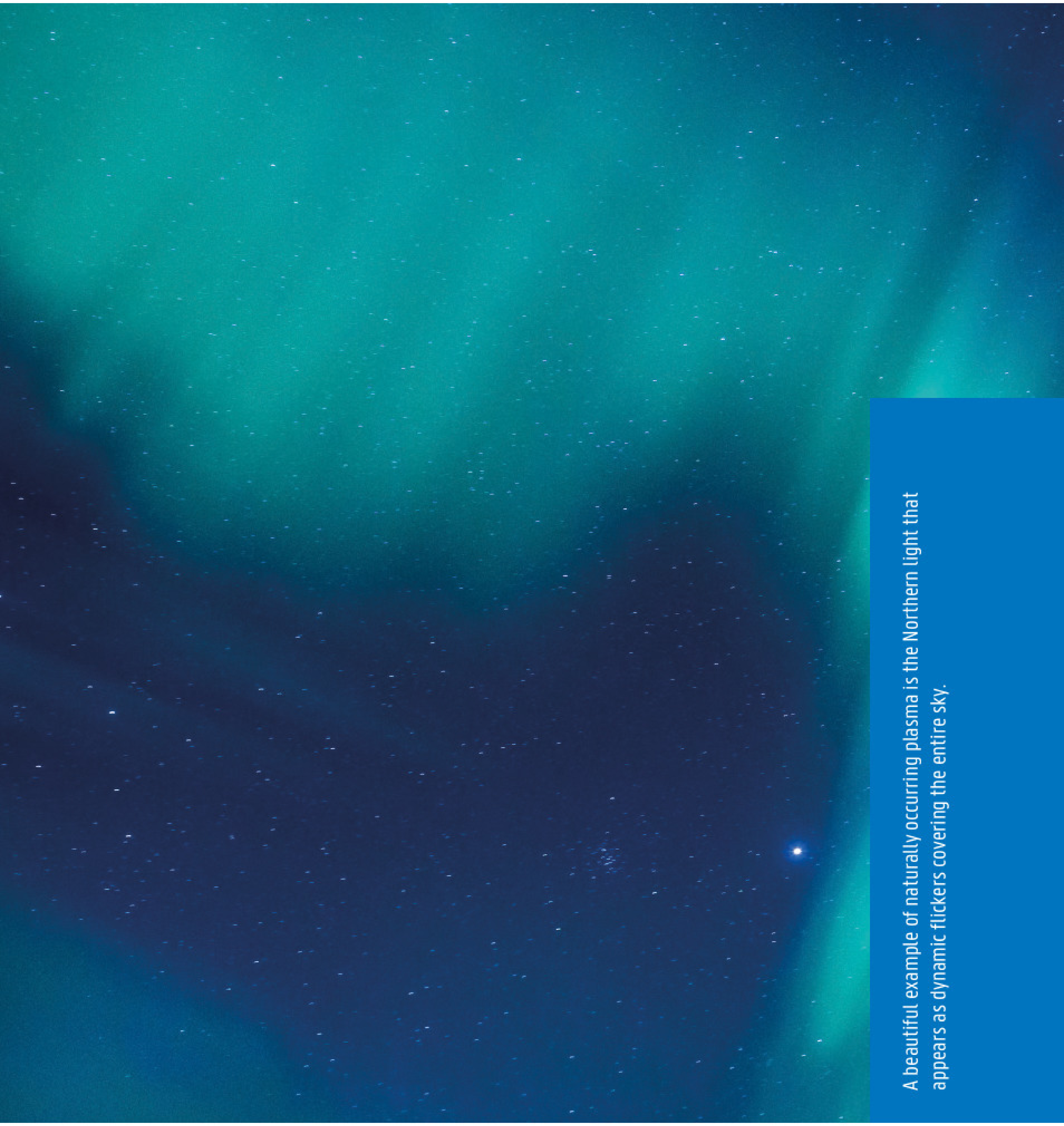

A beautiful example of naturally occurring plasma is the Northern light that appears as dynamic flickers covering the entire sky.